HAL
open science

Influence of the statistical parameters of a random heterogeneous medium on elastic wave scattering : theoretical and numerical approaches

Shahram Khazaie

To cite this version:

Shahram Khazaie. Influence of the statistical parameters of a random heterogeneous medium on elastic wave scattering : theoretical and numerical approaches. Mechanics [physics.med-ph]. Ecole Centrale Paris, 2015. English. NNT : 2015ECAP0021 . tel-01159616

HAL Id: tel-01159616

https://theses.hal.science/tel-01159616

Submitted on 3 Jun 2015

HAL is a multi-disciplinary open access archive for the deposit and dissemination of scientific research documents, whether they are published or not. The documents may come from teaching and research institutions in France or abroad, or from public or private research centers.

L'archive ouverte pluridisciplinaire **HAL**, est destinée au dépôt et à la diffusion de documents scientifiques de niveau recherche, publiés ou non, émanant des établissements d'enseignement et de recherche français ou étrangers, des laboratoires publics ou privés.

École Centrale Paris
Laboratoire de Mécanique des Sols, Structures et Matériaux
CNRS UMR 8579

THÈSE

présentée par

Shahram KHAZAIE

pour l'obtention du garde de

Docteur de l'École Centrale Paris

Spécialité : Mécanique Numérique

Laboratoire d'accueil : Mécanique des Sols, Structures et Matériaux

Influence of the statistical parameters of a random heterogeneous medium on elastic wave scattering: theoretical and numerical approaches

Soutenue le 23 février 2015, devant le jury composé de :

Pr. Didier Clouteau	**École Centrale Paris**	**Directeur de thèse**
Dr. Régis Cottereau	**École Centrale Paris**	**Encadrant de thèse**
Pr. Éric Savin	**Onera**	**Rapporteur**
Pr. Roberto Paolucci	**Politecnico di Milano**	**Rapporteur**
Pr. Geert Lombaert	**KU Leuven**	**Examinateur**
Pr. Jean-François Semblat	**Université Paris-Est**	**Président du jury**

Acknowledgments

It is a great pleasure for me to express my sincere gratitude to Didier Clouteau and Régis Cottereau, who supervised this work. For the amazing amount of knowledge concurrently held, of which they tried to pass some on to me. For their organization in the joint supervision, which lacked the unnecessary inertia sometimes found in this type of collaboration. For their trust to me and the freedom that they gave me. During my Master's thesis Régis revealed to me many new challenges in the domain of probabilistic modeling in mechanics. Although during my undergraduate years I had published some books in this domain, it's truly Régis that initiated me to this domain thanks to his precious knowledge.

I warmly thank Arézou Modaressi and Hachmi Ben Dhia for their supports and care. I appreciate Anne-Sophie Mouronval for her great support in the numerical part of my thesis. I would also like to thank Éric Savin, Ludovic Margerin, Tatiana Okhulkova and Ibrahim Baydoun for our scientific discussions. I especially thank Éric Savin and Roberto Paolucci who carefully reviewed my manuscript and also Jean-Franois Semblat and Geert Lombaert for their positive comments as examiners.

Although a thesis is an individual work and experience, I would have never made it without my colleagues. I appreciate my friend Ahmed Sridi for his care, his availability and for the numerous discussions we had concerning work or personal life. I heartily thank my friends, the lovely couple, Tatiana Okhulkova and Vinicius Alves Fernandes. They were always there for me whenever I was all alone. Among the team of coworkers and former coworkers, I sincerely thank, in no particular order, Luís Berenguer Todo-Bom, Vu Thanh Do, Tran Phuong, Khalil Abene, Yanek Wilorki, Yannick Tampango, Baptiste Durand, Diana Salem, Houda Attia, Bai Xue, Silvana Montoya Noguera, Ahlem Raies, João Camões, Nguyen Van Nghia, Filippo Gatti, Angkeara Svay, Lucio Correa and Luciano De Carvalho.

Special thanks to my best friend, Hossein Jowhari Moghadam, and to my girlfriend, Simonetta, for their unconditional support. And last but not least, although they did not contribute directly to this work, I must thank my parents especially my beloved mother to whom I dedicate this thesis.

Mars 13, 2015, Paris

Résumé

Les phénomènes de diffraction et de diffusion des ondes jouent un rôle important dans l'interprétation de la coda des sismogrammes. Par conséquent, une compréhension approfondie des mécanismes de diffraction et de leurs influences sur la propagation des ondes est une étape fondamentale vers l'identification des propriétés statistiques d'un milieu aléatoire. Cette thèse porte sur la diffraction des ondes élastiques dans des milieux aléatoirement hétérogènes avec un comportement local isotrope. On s'intéresse au régime où: La longueur d'onde est du même ordre de grandeur que la longueur de corrélation, la longueur d'onde est petite comparé à la distance de propagation (haute-fréquence) et l'amplitude des fluctuations est petite. Une approche cinétique basée sur les équations de tranfert radiatif des ondes élastiques est adoptée. La première partie de cette thèse décrit une analyse détaillée de l'influence de la structure de corrélation sur les paramètres de diffraction et sur l'établissement d'un régime de diffusion. La seconde partie présente les simulations éléments spectraux à grande échelle des ondes élastiques afin d'observer numériquement l'apparition d'un régime d'équipartition. Des analyses théoriques ainsi que des simulations montrent également une nouvelle approche pour l'identification des propriétés statistiques du milieu.

Mots-clés : Propagation des ondes élastiques, Équations de transfert radiatif, Milieux aléatoires, Structure de corrélation isotrope, Paramètres de diffraction, Régime d'équipartition

Abstract

Scattering and diffusion phenomena play a crucial role in the interpretation of the coda part of seismograms. Consequently, a profound understanding of scattering mechanisms and their effects on wave propagation is a fundamental step towards the identification of the statistical properties of random media. The focus of this work is on the scattering of elastic waves in a randomly heterogeneous media with locally isotropic material behavior. The weakly heterogeneous regime is considered, in which the wave length is similar to the correlation length, the wave length is small compared to the propagation length (high frequency) and the amplitude of the heterogeneities is small. A kinetic framework based on the transport equations of elastic waves is adopted. The first part of the thesis describes a detailed analysis of the influence of the correlation structure on the scattering parameters and on the arising of the diffusion regime. The second part presents large scale spectral element simulations of elastic waves to observe numerically the onset of the equipartitioning regime. The theoretical analyses and simulations also reveal a novel approach to identify local properties of the heterogeneous medium.

Keywords : Elastic wave propagation, Radiative transfer equations, Random media, Isotropic correlation structure, Scattering parameters, Equipartitioning regime

Contents

Introduction **7**

1 Wave propagation in random media - State of the art **10**

1.1 Different wave types . . . 10
1.1.1 Elastic waves . . . 10
1.1.2 Rayleigh waves . . . 14
1.2 Probabilistic modeling of a geophysical medium . . . 16
1.2.1 Characteristics of a geophysical medium . . . 16
1.2.2 Mathematical description of a random medium . . . 17
1.2.3 Correlation structure . . . 20
1.3 Length scales and scattering regimes . . . 22
1.4 Stochastic scattering regime . . . 25
1.4.1 Radiative transfer equation of acoustic waves . . . 26
1.4.2 Extension to the case of elastic waves . . . 30
1.4.3 Scattering parameters . . . 33
1.5 Diffusion regime . . . 36
1.6 Summary and Conclusion . . . 39

2 Influence of the spatial correlation structure of an elastic random medium on its scattering properties **40**

2.1 Normalizations of parameters . . . 40
2.1.1 Phase velocity contrast parameter K . . . 40
2.1.2 Random model of the mechanical parameters . . . 41
2.1.3 Classical correlation models . . . 43
2.1.4 Normalization of differential scattering cross-section . . . 44
2.2 Influence of the correlation function on the scattering parameters . . . 46
2.2.1 Influence on the differential scattering cross-sections . . . 46
2.2.2 Influence on the total scattering cross-sections . . . 47
2.2.3 Influence on the forward scattering cross-sections . . . 51
2.3 Influence of the correlation function on the diffusion regime . . . 53
2.3.1 Normalized scattering mean free time (path), $\overline{\tau}$ ($\overline{\ell}$) . . . 53
2.3.2 Normalized transport mean free path (time), $\overline{\ell}^*$ ($\overline{\tau}^*$) . . . 55
2.3.3 Normalized diffusion constant, $\overline{D}$ . . . 57
2.3.4 Normalized equipartitioning time . . . 57
2.4 Summary and Conclusion . . . 58

3 Elastic wave propagation in an isotropic randomly heterogeneous medium **60**
3.1 The Spectral Element Code SPEC3D . . . 60
3.1.1 Numerical methods in elastodynamics . . . 60
3.1.2 An introduction to the spectral elements . . . 61
3.1.3 An introduction to the software SPEC3D . . . 67
3.1.4 Adaptations of SPEC3D for different correlation models with isotropic structure . . . 69
3.2 Numerical observation of equipartitioning regime in random elastic media . . . 72
3.2.1 Equipartitioning without free surface . . . 73
3.2.2 Equipartitioning with a free surface . . . 75
3.2.3 Numerical observation of equipartitioning regime . . . 76
3.3 Limitations to reaching numerically the equipartitioning regime . . . 82
3.3.1 Setting of a localization regime . . . 82
3.3.2 Influence of mean free path . . . 85
3.3.3 Influence of inefficient mixture of body waves . . . 86
3.3.4 Influence of the PML layers . . . 87
3.4 Identification of the correlation structure of the medium properties . . . 88
3.4.1 Theory . . . 88
3.4.2 Identification of the correlation structure . . . 91
3.4.3 Limitation to the identification of the correlation structure . . . 93
3.5 Summary and Conclusion . . . 94

Appendices **99**

A Behavior of functions I_n and J_n **100**
A.1 Integral W_n^p . . . 100
A.2 Integral V_n^p . . . 100
A.3 Behavior of function I_n . . . 101
A.4 Behavior of function J_n . . . 102

B Derivation of the correlation matrix **105**
B.1 Weakly varying random media . . . 105
B.2 Highly varying random media . . . 107

C Probabilistic modeling of random heterogeneities **109**
C.1 Maximum Entropy Principle . . . 109
C.2 Probabilistic modeling of matrix-valued random fields . . . 110
C.2.1 Modifications of Soize's probabilistic model for the random elastic matrix . . . 112

D Toward the analytical solution to the RTE of elastic waves propagating in discrete isotropic scattering random media **115**
D.1 Introduction . . . 115
D.2 Isotropic (spherical) source . . . 117
D.3 Non-isotropic (non-spherical) source . . . 119

List of Figures **125**

List of Tables **126**

Introduction

Identifying the mechanical parameters of different layers of the Earth is a central questions for many researchers. The applications range from academic understanding of the interior of the Earth to more industrially-oriented questions related to oil exploration or CO_2 and nuclear waste sequestration. Figure 1 shows a typical seismic exploration which consists of the identification of some desired zones or layers of interest in geological media using the back-propagated surface wave fields. Figure 2 illustrates the typical kind of signals that are used for such identification problems. They typically start with a so-called ballistic or coherent part, with the arrival of the direct compressional (P) wave, direct shear (S) wave and the surface waves (Love and Rayleigh). These coherent waves are followed by a continuous wave train with decaying amplitudes which is called the coda. However, this coda is usually disregarded in classical identification techniques, and the exploration engineers concentrate on the coherent signal rather.

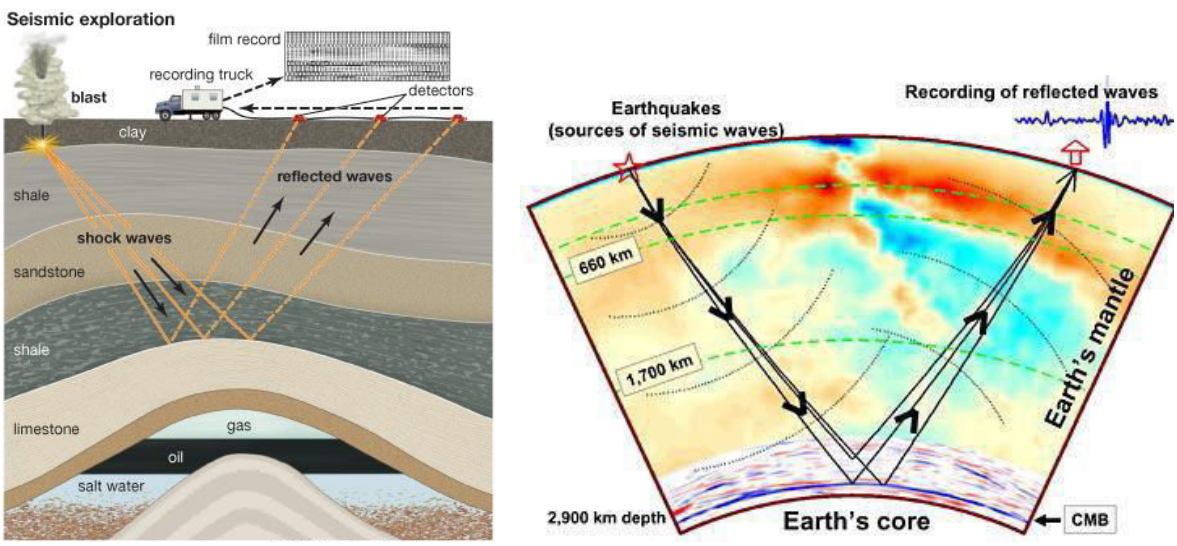

Figure 1: Seismic exploration (left) and Seismic tomography using the recorder wavefield on surface of the Earth (der Hilst et al., 2007) (right).

Aki (1969) and Aki and Chouet (1975) investigated the incoherent coda waves and found that they originate from the multiple scattering of waves in the non-homogeneous structure of the Earth. As a result, the coda waves are a signature of the heterogeneities in the Earth. Another indication of the existence of these heterogeneities can be read in the well-log data obtained in the Earth's crust and in results of seismic reflection experiments. The latter reveal that the crust is heterogeneous on scales of a few kilometers to tens of kilometers (Sato et al., 2012). The existence of these heterogeneities makes the classical identification problem ill-posed as the number of parameters to be inverted for grows rapidly. However, the objective of the identification problem in

such a heterogeneous medium is not necessarily to identify precisely the value of the parameters at a specific location. One may be content with statistical descriptors of these parameters rather than point-wise values. For instance, an oil engineer might be able to detect an area where rocks are prone to contain oil by measuring the amplitude of the fluctuations (variance) of the mechanical parameter field in that area.

To account for the intrinsic spatial variability of the geological medium, as well as uncertainties on their values, we concentrate in this thesis on random models of the soil. The properties of the propagation medium, such as density and elastic moduli, are modeled using random functions of space with given statistical properties, and realizations of the medium can be produced based on that probabilistic model. Note, however, that we only consider single large realizations, and no statistical averaging is performed between samples. We are particularly interested in this work in the onset of the diffusion regime at long lapse times. This regime is characterized by a scalar diffusion equation that can be precisely derived through an asymptotic analysis of the wave equation. Our interest in this regime arises from the observation that the behavior of the envelope of the coda waves is compatible with such a diffusion equation. Aki and Chouet (1975) found that the decay rate of the amplitude of this envelope (the so-called coda quality factor Q_c) is largely independent from the nature of the initial source, which makes it a convenient parameter for identification problems. The radiative transfer theory and asymptotic analysis indeed predicts a Q factor which should only depend on statistical properties of the medium, and not on the details of the source.

Four key parameters influence the scattering of elastic waves in the regime we are interested in:

(i) The ratio between the correlation length and the wavelength,

(ii) The ratio between the mean values of P and S wave velocities,

(iii) The amplitude of fluctuation of the mechanical parameters (covariance matrix),

(iv) The spatial correlation model.

The first objective of this thesis is to describe quantitatively the influence of each of these on the scattering phenomena and on the onset of the diffusion regime. It should be noted that the radiative transfer theory for elastic waves is more complex than for other wave types. Indeed, it

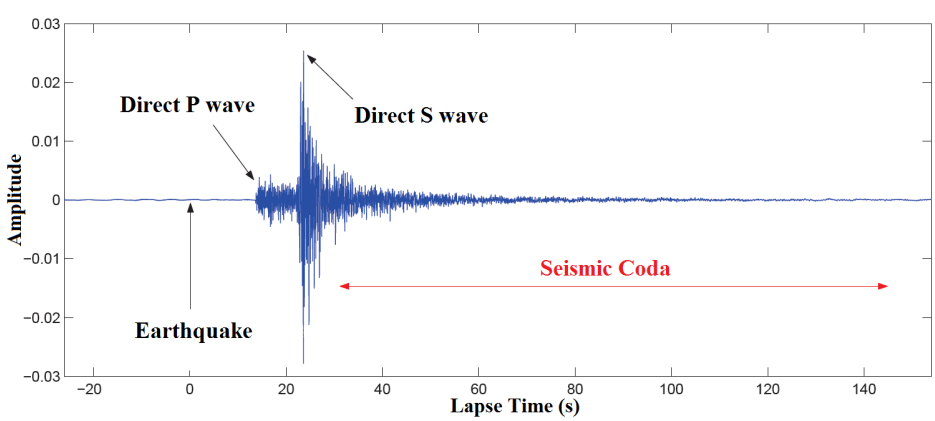

Figure 2: A typical seismogram generated by an earthquake

has to take into account the 2 polarizations of S waves and the mode conversion between P and S waves during scattering events. Most works, in particular in geophysics, concentrate therefore on acoustic approximations, where the P and S waves do not interact (see Zeng (1993), Nakahara and Yoshimoto (2011) and Sato et al. (2012) for example). We consider in this work fully the vectorial nature of the equation. We will however consider only isotropic materials, for simplicity. Also, we will focus particularly on the spatial correlation model, since its influence has been regarded in less detail in the literature. The assessment of its influence, respective to that of the other parameters, should help state in the future whether it can be chosen at will or whether it should be identified explicitly. As it is a function, while the other parameters are scalars, such a possibility would simplify strongly the identification process.

The second objective of this work is to construct a numerical model to reproduce the onset of the diffusion regime. The interest lies in the possibility (i) to test situations in which the theory is not fully developed or (ii) to quantify precisely the limits of different asymptotic regimes. Indeed, asymptotic analysis is only stated in terms of orders of magnitude of certain ratios. There is obviously a range of values of these ratios when the asymptotic analysis is valid, but it is not indicated by the analysis itself. This is however an important parameter in practice. The theory of radiative transfer is fully developed for full spaces and can be extended to include surface waves in the case of a half space. However, no results exist for complex topographies, basins or actual surface configurations. Such a numerical tool allows to investigate these cases. The construction of this numerical model will be presented in this document, and validated with respect to known theoretical results. Its limits will be clearly specified. In particular, the issue of numerical cost will be discussed at length. This cost is related to the size of the domains that have to be simulated before diffusion sets in for most materials.

The third objective of this document will be to propose a preliminary identification process of the spatial correlation of a random medium. This identification is based on measures of the curl and divergence of the displacement field at the surface of a random medium. Time has not allowed to investigate further this identification process but first numerical results will be presented and discussed.

The first chapter introduces a bibliographical study of wave scattering, random media and radiative transfer theory. The second chapter discusses our first objective of evaluating the influence of the correlation structure of the random parameters. All scattering parameters (differential, forward and total scattering coefficients, for PP, PS and SS transformations) as well as the diffusion coefficients are discussed. In the third and last chapter, the numerical model is introduced (second objective). The validation and limitations are described in successive sections. The chapter closes with the preliminary identification results (third objective).

Chapter 1

Wave propagation in random media - State of the art

The study of wave propagation in inhomogeneous media has been applied since longtime in material characterization (Kulkarni et al. (1994), Liu and Turner (2008)), nondestructive testing (Smith (1987), Foley and Rehbein (2000)) and seismic wave analysis (Papanicolaou et al., 1996). Since the studies of Aki at the beginning of 70's, the problem of statistical identification of complex media has seen enormous developments. It has been mentioned that the typical seismograms resulting from earthquakes are not producible using the simplified homogeneous (piece-wise homogeneous) models (Sato et al., 2012). Aki and Chouet (1975) stated that the coda part of seismograms is the direct result of interactions between waves and the existing heterogeneities in the underlying medium.

The main objective of this chapter is to provide the relevant state of the art about the analysis of the interactions between elastic waves and the inhomogeneities or the so-called wave scattering. A profound knowledge about the influences of these interactions can provide relevant tools to investigate the microstructure of a variety of materials such as polycrystals, ceramics, concrete and geological media. For this purpose, transport equations of elastic waves will be discussed. These equations provide fundamental information about the relation between the wave energy in phase space (directional energy) and the statistics of the underlying random medium.

1.1 Different wave types

A wave is a disturbance or oscillation that travels through space and matter, accompanied by a transfer of energy. Mathematically, the waves are the solutions of the wave equation which is a second order partial differential equation. Figure 1.1 depicts schematically the propagation of different wave types which have practical applications on probing of geological media. In this work, we will be concerned only with the case of elastic waves as well as the surface Rayleigh waves which will be elaborated separately in Sections 1.1.1 and 1.1.2.

1.1.1 Elastic waves

The general concepts of the elastic wave propagation in three dimension will be discussed in this section and will be subsequently used in the following parts of the dissertation. In elastic media, the

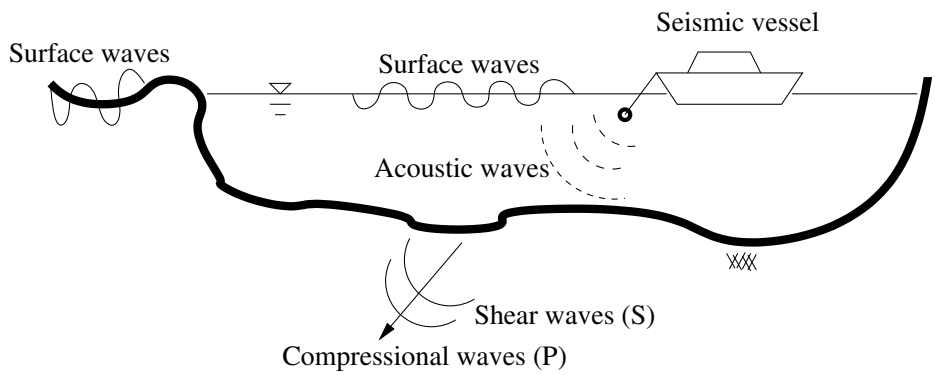

Figure 1.1: Different wave types created during a typical marine survey

wave energy losses due to friction, viscosity and radiation are negligible. The elastodynamic wave equation (equation of motion) describing the elastic wave propagation in elastic (non-dissipative) media states the equilibrium of an open domain $\Omega \subseteq \mathbb{R}^3$:

$$\rho(\mathbf{x})\frac{\partial^2}{\partial t^2}\mathbf{u}(\mathbf{x},t) - \nabla_{\mathbf{x}}.\{C(\mathbf{x}) : \epsilon(\mathbf{u}(\mathbf{x}))\} = 0, \qquad (\mathbf{x},t) \in \Omega \times \mathbb{R}^+ \tag{1.1}$$

in which the properties of the medium $\rho(\mathbf{x})$ and $C(\mathbf{x})$, are respectively the local values of density and the fourth-rank elastic tensor and $\epsilon(\mathbf{u}(\mathbf{x})) = \mathrm{sym}(\nabla_{\mathbf{x}}\mathbf{u}(\mathbf{x})) = (\nabla_{\mathbf{x}}\mathbf{u}(\mathbf{x}) + (\nabla_{\mathbf{x}}\mathbf{u}(\mathbf{x}))^T)/2$ is the local strain tensor. In elastic media, the total energy of the medium will be always conserved as far as the inelastic absorptions are neglected. Equation (1.1) along with its initial and boundary conditions (radiation condition for unbounded domains) provides a unique solution $\mathbf{u}(\mathbf{x},t)$. The vector wave field $\mathbf{u}(\mathbf{x},t)$ is the response of the medium, which is the displacement vector in each point $\mathbf{x}$ at any time t. Detection and monitoring the temporal changes in media like volcanoes (Grêt et al. (2005)), oil reservoirs (Meunier et al. (2001)) and even fault zones (Brenguier et al. (2008)), is one of the challenges of geophysicists and seismologists. Nevertheless, in this presentation we are only concerned with time-independent media in which the temporal variation of the medium properties is neglected. The constitutive law of the medium which relates the stress and strain tensors is:

$$\sigma(\mathbf{x}) = C(\mathbf{x}) : \epsilon(\mathbf{x}) \tag{1.2}$$

In general, the fourth-order elastic tensor $C = C_{ijkl}(1 \leq i,j,k,l \leq 3)$ consists of $3^4 = 81$ parameters. However, due to its symmetries *i.e.* $C_{ijkl} = C_{jikl} = C_{ijlk} = C_{klij}$, it can be described with 21 independent parameters in the form of a 6×6 symmetrical matrix (triclinic material). Subsequently, the Kelvin-Voigt notation can be used to rewrite the reduced form of the equation (1.2) (see Auld (1973) for instance). The number of independent parameters in C decreases when some types of symmetries exist in material. The simplest case in which only 2 independent parameters are needed to describe the stress-strain behavior of a material, is called the isotropy. In terms of Lamé coefficients, the isotropic elasticity matrix reads:

$$C(\mathbf{x}) = \begin{pmatrix} \lambda(\mathbf{x}) + 2\mu(\mathbf{x}) & \lambda(\mathbf{x}) & \lambda(\mathbf{x}) & 0 & 0 & 0 \\ \lambda(\mathbf{x}) & \lambda(\mathbf{x}) + 2\mu(\mathbf{x}) & \lambda(\mathbf{x}) & 0 & 0 & 0 \\ \lambda(\mathbf{x}) & \lambda(\mathbf{x}) & \lambda(\mathbf{x}) + 2\mu(\mathbf{x}) & 0 & 0 & 0 \\ 0 & 0 & 0 & \mu(\mathbf{x}) & 0 & 0 \\ 0 & 0 & 0 & 0 & \mu(\mathbf{x}) & 0 \\ 0 & 0 & 0 & 0 & 0 & \mu(\mathbf{x}) \end{pmatrix} \tag{1.3}$$

Inserting (1.3) into (1.1) results in the following equation of motion in non-dissipative isotropic media:

$$\rho(\mathbf{x})\frac{\partial^2\mathbf{u}}{\partial t^2} = \nabla\lambda(\mathbf{x})(\nabla\cdot\mathbf{u}) + \nabla\mu(\mathbf{x})\cdot[\nabla\mathbf{u} + (\nabla\mathbf{u})^{\mathrm{T}}] + (\lambda(\mathbf{x}) + 2\mu(\mathbf{x}))\nabla\nabla\cdot\mathbf{u} - \mu(\mathbf{x})\nabla\times\nabla\mathbf{u} \quad (1.4)$$

The gradient of the Lamé coefficients in the first two terms of the right hand side make this equation complicated. Most of the classical synthetic seismogram computation methods like the layered homogeneous method, neglect the contribution of these terms and use a simpler version of equation (1.4). When the amplitude of fluctuations is small, the spatial gradient of Lamé coefficients and the density can be neglected which results in the following form of the elastic wave equation in an isotropic medium:

$$\rho(\mathbf{x})\frac{\partial^2\mathbf{u}(\mathbf{x},t)}{\partial t^2} = (\lambda(\mathbf{x}) + 2\mu(\mathbf{x}))\nabla(\nabla\cdot\mathbf{u}(\mathbf{x})) - \mu(\mathbf{x})\nabla\times\nabla\mathbf{u}(\mathbf{x},t) \quad (1.5)$$

Applying the divergence and curl operators to both sides of the equation (1.5) will give two body wave modes in a homogeneous isotropic medium. First, taking the divergence gives:

$$\Delta(\nabla\cdot\mathbf{u}) - \frac{1}{v_p^2(\mathbf{x})}\frac{\partial^2(\nabla\cdot\mathbf{u})}{\partial t^2} = 0, \quad v_p(\mathbf{x}) = \sqrt{\frac{\lambda(\mathbf{x}) + 2\mu(\mathbf{x})}{\rho(\mathbf{x})}} \quad (1.6)$$

Likewise, applying the curl operator to both sides of equation (1.5) results in:

$$\Delta(\nabla\times\mathbf{u}) - \frac{1}{v_s^2(\mathbf{x})}\frac{\partial^2(\nabla\times\mathbf{u})}{\partial t^2} = 0, \quad v_s(\mathbf{x}) = \sqrt{\frac{\mu(\mathbf{x})}{\rho(\mathbf{x})}} \quad (1.7)$$

where p and s subscripts respectively refer to the compressional (P) and shear (S) waves with relative local propagation velocities of $v_p(\mathbf{x})$ and $v_s(\mathbf{x})$. These wave modes are called the *quasi* P and *quasi* S wave modes since the equation (1.5) is an approximate form of the elastodynamic wave equation in weakly-varying media. *Pure* P and S wave modes propagate in a homogeneous isotropic medium in which the spatial variation of elastic coefficients vanishes. Equation (1.6) has the same form as the acoustic wave equation:

$$\left[\Delta - \frac{1}{v^2(\mathbf{x})}\partial_t^2\right]u(\mathbf{x},t) = 0; \quad v(\mathbf{x}) = \sqrt{\frac{\kappa(\mathbf{x})}{\rho(\mathbf{x})}} \quad (1.8)$$

in which density $\rho(\mathbf{x})$ and bulk modulus $\kappa(\mathbf{x})$ are the medium properties. Δ is the Laplacian operator, $v(\mathbf{x})$ is the local propagation speed which is the same as the velocity of sound waves. It should be pointed out that since the scattering theory of acoustic waves is much simpler than that of the elastic waves, the acoustic waves are vastly used for identification problems (see Ramamoorthy et al. (2004) for instance).

A particular solution of the wave equation (1.5) in terms of harmonic plane waves reads:

$$\mathbf{u} = \mathbf{U}\exp\left(i(\boldsymbol{\kappa}\cdot\mathbf{x} - \omega t)\right) \quad (1.9)$$

where $i = \sqrt{-1}$ is the imaginary unit, ω is the circular frequency and $\boldsymbol{\kappa}$ is the wave vector which specifies the wave propagation direction. $\mathbf{U}/||\mathbf{U}||$ is the polarization direction of the wave modes,

i.e. the direction of the particle movements. $||\mathbf{U}(t,\mathbf{x})||$ and $\phi(t,\mathbf{x}) = \boldsymbol{\kappa}\cdot\mathbf{x} - \omega t$ are respectively the amplitude and the phase of the wave. In a general case of a weakly-varying media characterized by local elastic tensor $C_{ijkl}(\mathbf{x})$ and local mass density $\rho(\mathbf{x})$ (with negligible spatial gradients), equation (1.1) can be rewritten as the following equation in which the Einstein convention of summation over repeated indices is assumed:

$$\rho(\mathbf{x})\frac{\partial^2 u_i(\mathbf{x},t)}{\partial t^2} = C_{ijkl}(\mathbf{x})\frac{\partial^2 u_k(\mathbf{x},t)}{\partial x_j \partial x_l} \quad ; \quad 1 \leq i,j,k,l \leq 3 \tag{1.10}$$

Replacing equation (1.9) in (1.10) results in the following so-called Christoffel equation:

$$\begin{bmatrix} \Gamma_{11}-\omega^2 & \Gamma_{12} & \Gamma_{13} \\ \Gamma_{21} & \Gamma_{22}-\omega^2 & \Gamma_{23} \\ \Gamma_{31} & \Gamma_{32} & \Gamma_{33}-\omega^2 \end{bmatrix} \begin{bmatrix} U_1 \\ U_2 \\ U_3 \end{bmatrix} = \begin{bmatrix} 0 \\ 0 \\ 0 \end{bmatrix} \tag{1.11}$$

in which $\Gamma(\boldsymbol{\kappa})$ is a second rank tensor which is often called the acoustic or the Christoffel tensor and is defined as:

$$\Gamma_{ik} = C_{ijkl}\kappa_j\kappa_l \tag{1.12}$$

Equation (1.11) or its equivalent compact form $(\Gamma(\boldsymbol{\kappa}) - \omega^2\boldsymbol{I_3})\,\mathbf{U} = \mathbf{0}$ shows that the polarization vector $\mathbf{U}$ and $\Upsilon = \omega^2$ are respectively the eigenvector and eigenvalue of the acoustic tensor $\Gamma(\boldsymbol{\kappa})$. As a result, the wave modes which can propagate in such a medium can be extracted using the eigenvalues of the medium's acoustic tensor. In the simple case of an isotropic medium with an elastic modulus defined in equation (1.3), the acoustic tensor takes the following form:

$$\Gamma(\boldsymbol{\kappa}) = \frac{\lambda+\mu}{\rho}\boldsymbol{\kappa}\otimes\boldsymbol{\kappa} + \frac{\mu}{\rho}||\boldsymbol{\kappa}||^2\boldsymbol{I_3} = \frac{1}{\rho}\begin{pmatrix} (\lambda+2\mu)\kappa_1^2+\mu(\kappa_2^2+\kappa_3^2) & (\lambda+\mu)\kappa_1\kappa_2 & (\lambda+\mu)\kappa_1\kappa_3 \\ (\lambda+\mu)\kappa_1\kappa_2 & (\lambda+2\mu)\kappa_2^2+\mu(\kappa_1^2+\kappa_3^2) & (\lambda+\mu)\kappa_2\kappa_3 \\ (\lambda+\mu)\kappa_1\kappa_3 & (\lambda+\mu)\kappa_2\kappa_3 & (\lambda+2\mu)\kappa_3^2+\mu(\kappa_1^2+\kappa_2^2) \end{pmatrix} \tag{1.13}$$

it can be shown that this acoustic tensor has three different wave number dependent eigenvalues:

$$\Upsilon_1 = \omega_1^2 = \frac{\lambda+2\mu}{\rho}||\boldsymbol{\kappa}||^2 \tag{1.14a}$$

$$\Upsilon_2 = \omega_2^2 = \frac{\mu}{\rho}||\boldsymbol{\kappa}||^2 \tag{1.14b}$$

$$\Upsilon_3 = \omega_3^2 = \frac{\mu}{\rho}||\boldsymbol{\kappa}||^2 \tag{1.14c}$$

These equations are also called the *dispersion relations* stating the relation between the local frequency and the wave number of each wave mode. Negative frequencies do not correspond to any physical wave mode so that three wave modes, two of which (S modes) have the same frequency are distinguished in a weakly-varying inhomogeneous medium with isotropic material behavior. These P and S wave modes propagate with following local frequencies:

$$\omega_p(\mathbf{x}) = \sqrt{\frac{\lambda(\mathbf{x})+2\mu(\mathbf{x})}{\rho(\mathbf{x})}}\,||\boldsymbol{\kappa}|| = v_p(\mathbf{x})||\boldsymbol{\kappa}|| \tag{1.15a}$$

$$\omega_s(\mathbf{x}) = \sqrt{\frac{\mu(\mathbf{x})}{\rho}}\,||\boldsymbol{\kappa}|| = v_s(\mathbf{x})||\boldsymbol{\kappa}|| \tag{1.15b}$$

in which the phase velocities depend only on the norm of the wave vector and not on the propagation direction. It should be noted that in anisotropic media, the phase velocities become wave vector dependent.

Three different eigenvectors or polarization directions corresponding to different wave modes are:

$$\mathbf{U}_1 = \frac{(\kappa_1, \kappa_2, \kappa_3)}{||\boldsymbol{\kappa}||} = \frac{\boldsymbol{\kappa}}{||\boldsymbol{\kappa}||} \tag{1.16a}$$

$$\mathbf{U}_2 = \frac{(0, -\kappa_3, \kappa_2)}{\sqrt{\kappa_2^2 + \kappa_3^2}} \tag{1.16b}$$

$$\mathbf{U}_3 = \frac{(\kappa_2^2 + \kappa_3^2, -\kappa_1\kappa_2, -\kappa_1\kappa_3)}{||\boldsymbol{\kappa}||\sqrt{\kappa_2^2 + \kappa_3^2}} \tag{1.16c}$$

A direct result of the equations (1.16) is that these polarization directions are mutually orthogonal and the polarization direction of the first wave mode corresponding to a P wave type, coincides exactly to the direction of the wave propagation $\boldsymbol{\kappa}$.

1.1.2 Rayleigh waves

Up to now, the emphasis has been on the propagation of the pure body waves in an unbounded heterogeneous medium. However, in the case of crustal seismic wave propagation, the propagation medium is limited to the Earth's surface (physical boundaries). Moreover, as far as numerical simulations of the seismic waves are concerned, the propagation medium has to be limited to some boundaries (numerical boundaries) because of limited numerical sources. The existence of these bounding surfaces like the ground free surface or the interface between two materials having different elastic properties, will result in:

(1) Appearance of some novel wave modes such as evanescent and surface waves.

(2) Modification on the incident body waves via the reflection/transmission phenomena as well as the wave mode conversion during scatterings on the interface. The scattering mode conversion between body and Rayleigh waves in an inhomogeneous elastic medium has been studied by Maeda et al. (2008).

Generally speaking, the surface Rayleigh waves are a type of guided waves propagating within a layer near the Earth's free surface which satisfy the traction-free boundary condition over the entire surface $\partial\Omega$:

$$\hat{\mathbf{n}} \cdot (C : \mathrm{sym}(\nabla_{\mathbf{x}}\mathbf{u})) = \mathbf{0} \tag{1.17}$$

In a half-space, the motion equations should be therefore coupled with equation (1.17) in which $\hat{\mathbf{n}}$ is the unit outward normal on the surface and the stress tensor σ follows the Hooke's equation: $\sigma = C : \mathrm{sym}(\nabla_{\mathbf{x}}\mathbf{u})$.

The Rayleigh waves can be decomposed as a sum of P and S waves. The amplitude of these waves decays in depth and is determined by the background velocity structure. A complete theoretical analysis of the Rayleigh waves is done in Aki and Richards (2002). Figure 1.2 shows the particle motions for the fundamental Rayleigh mode in a half-space shown over one horizontal

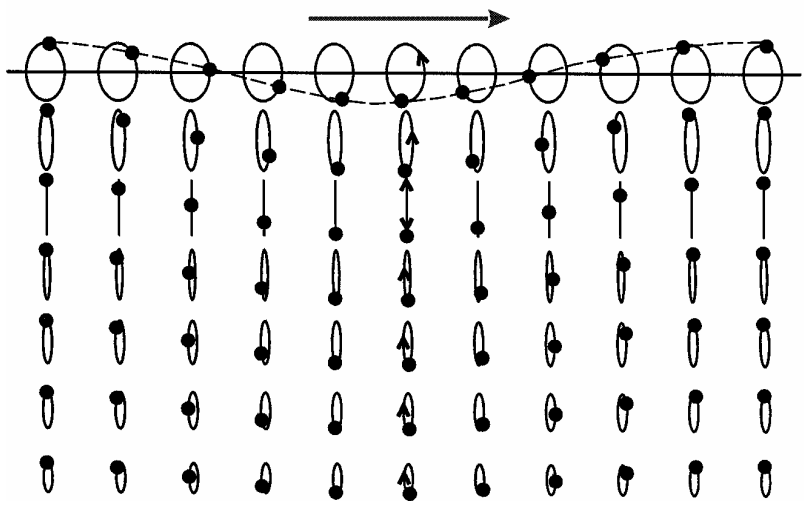

Figure 1.2: Particle motion of Rayleigh waves (Shearer, 2009)

wavelength λ_r. The amplitude decay in depth can be noticed from this figure. The main properties of these waves are:

(1) The wavefield is composed of a longitudinal and a transverse displacement component (perpendicular to the free surface) which will result in an elliptical particle motion.

(2) The propagation velocity of Rayleigh waves is related to the velocity of P and S waves and is frequency-independent in homogeneous media. However, in heterogeneous media it will be dependent on the frequency.

The characteristic equation of the Rayleigh waves propagating in a homogeneous medium is (see Auld (1973) for example):

$$K_r^6 - 8K_r^4 + (24 - 16K^{-2})K_r^2 + (16K^{-2} - 16) = 0 \tag{1.18}$$

in which $K_r = v_r/v_s$ is the ratio between Rayleigh and S wave speeds. Equation (1.18) is also known as Rayleigh equation which gives a unique Rayleigh wave speed for a linear homogeneous elastic medium. It is important to remark that in spatially varying media, the characteristic equation (1.18) can only be expressed in an implicit form as follows (see Foti (2000) for instance):

$$\mathcal{F}_r\left[\rho(\mathbf{x}), \lambda(\mathbf{x}), \mu(\mathbf{x}), \mathbf{k}, \omega\right] = 0 \tag{1.19}$$

which shows that the phase velocity depends on the local frequency ω.

Considering a plane Rayleigh wave propagating in x direction (as shown in Figure 1.2) through a homogeneous medium, the horizontal and vertical components of the displacement wave field can be obtained by:

$$\mathbf{u}_x = Ak\left(e^{-qz} - \frac{2qs}{s^2+k^2}e^{-sz}\right)\sin(\omega t - kx) \tag{1.20a}$$

$$\mathbf{u}_z = Aq\left(e^{-qz} - \frac{2k^2}{s^2+k^2}e^{-sz}\right)\cos(\omega t - kx) \tag{1.20b}$$

in which A is some constant, k is the horizontal wavenumber (or the wavenumber of the Rayleigh waves ($k = \omega/v_r$)) and q and s are related to K and K_r via:

$$\left(\frac{q}{k}\right)^2 = 1 - \frac{K_r^2}{K^2} \quad ; \quad \left(\frac{s}{k}\right)^2 = 1 - K_r^2 \tag{1.21}$$

It should be noted that the Rayleigh equation (1.18) for any given K has three solutions for K_r^2 in which only one of them results in non-imaginary values for q/k and s/k according to the equations (1.21). Inserting equations (1.21) into the equations (1.20) and setting $z = 0$ will give the equations of the Rayleigh plane waves on the free surface:

$$\mathbf{u}_x(z=0) = Ak\frac{2 - K_r^2 - 2\sqrt{1-K_r^2}\sqrt{1-\frac{K_r^2}{K^2}}}{2-K_r^2}\sin(\omega t - kx) \tag{1.22a}$$

$$\mathbf{u}_z(z=0) = -Ak\sqrt{1-\frac{K_r^2}{K^2}}\frac{K_r^2}{2-K_r^2}\cos(\omega t - kx) \tag{1.22b}$$

in which K_r is the solution of the Rayleigh equation knowing the value of K. These equations show that over the free surface, the ratio between the major and minor axes of the ellipses created by the Rayleigh waves is a frequency-dependent constant which depends solely on the medium average properties. This ratio will be denoted by ϱ and will be calculated later in chapter 3.

After this brief introduction about the basic concepts of the elastic and Rayleigh waves and before starting to discuss about the scattering of elastic waves in heterogeneous media, we discuss about the spatial variabilities in geological media in the next section.

1.2 Probabilistic modeling of a geophysical medium

1.2.1 Characteristics of a geophysical medium

Geological processes is one of the factors which can cause variations on the material properties of the media of our interest. Besides, experimental observations also show these spatial fluctuations in almost all of the medium parameters. Log well data are among the direct evidences of the existence of spatial variations. Figure 1.3(a) shows the profiles of the variations in depth of the P and S wave speeds ($\alpha = v_p$, $\beta = v_s$) as well as the medium's mass density ρ in Kyushu, Japan (Shiomi et al., 1997). The velocity profiles are assessed from measurements of travel times of ultrasonic waves and the mass density is determined from the measurements of the gamma rays intensities received at a borehole detector which is a function of the formation density (see Telford et al. (1976) and Sato et al. (2012) for more discussion). An average value of $K = \sqrt{3}$ (Poissonian materials) is often used for geological media. Figure 1.3(b) depicts the scatter plots representing the spatial correlations between these three parameters in some depth intervals. A strong linear correlation is observed between P and S wave velocities whereas these two parameters are seen to have a positive correlation with the mass density. Figure 1.3(a) also shows that in geological media the normalized variance of the density ρ is significantly less than that of the phase velocities (or equivalently the variance of the elastic moduli). Consequently, the mass density of geological media is often considered either a constant or in a perfect positive correlation with the elastic moduli (Figure 1.3(b) shows this correlation).

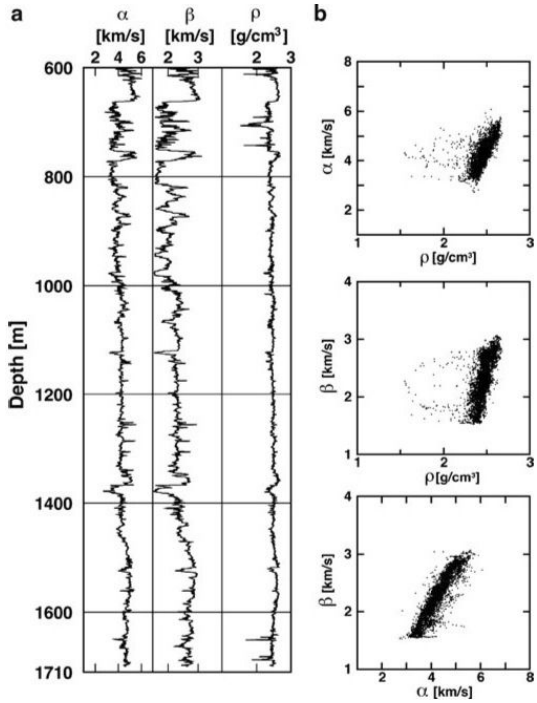

Figure 1.3: (a) Variation of P and S-wave velocity (α, β) and mass density (ρ) in depth. (b) Scattergrams showing the correlations between α, β and ρ at the same depth (Shiomi et al., 1997)

Several researches have been done to investigate the spatial variations of soil parameters as well as to propose some strategies to take them into consideration (see Soulie et al. (1990), Cambardella et al. (1994) and Gallardo (2003) for instance). Considering the medium as different layers in which each layer is homogeneous (piecewise homogeneous medium) could be a way to model these variations. However, it is not possible to reproduce the typical seismograms resulting from the local earthquakes using this type of approach. Another approach is the probabilistic modeling of the medium properties in which the random fields with given probability distributions will be used.

In the next two sections, we briefly discuss the fundamental parameters contributing in probabilistic modeling of random medium parameters. The corresponding theoretical aspects are introduced in Appendix C where a non-parametric probabilistic approach to model the random elasticity matrix is elaborated.

1.2.2 Mathematical description of a random medium

The experimental estimation of the medium parameters is highly limited and can be done locally on some limited points close to the Earth's surface. These estimations are subjected to the measurement errors. The models which are used are also another source of stochasticity. For a more profound discussion about different types of uncertainties, especially in civil and environmental engineering see Ang and Tang (2007). To account for these uncertainties, we can make use of the stochastic functions with given statistical parameters to model the parameters of the propagation medium. Thus, instead of considering a single heterogeneous medium, we imagine an *ensemble* of random media with same *a priori* known statistical parameters such as the same statistical mean and variance, which will be defined later in this section (see Frisch (1968) and Sato et al. (2012) for discussion). Each of the elements of this *a priori* infinite set, is called a realization of the corresponding random medium. To compare the observed quantities with the theoretical results, one

should take the averages over a subset of realizations with sufficiently large cardinality. It should be noted that in this presentation, we always employ only a single realization of a sufficiently large randomly heterogeneous medium. As we will see further in chapter 2, at long lapse times when a diffusion regime sets in, the elastic energies depend only on the statistics of the medium via a simple scalar diffusion equation. Furthermore, we assume that the medium statistics can be deduced from only a single realization which results from the assumption of ergodicity of random fields and will be discussed further in this section.

Now we will briefly elaborate on some of the basic concepts about the random fields. For a deeper study about the theoretical aspects of random fields, see Vanmarcke (2010).

Basic concepts: Let $X(\mathbf{x})$ be a scalar random field defined over *physical space* $\Omega_1 \subset \mathbb{R}^3$ and a *probability space* characterized by the triplet $(\mathcal{A}, \mathcal{F}, \mathcal{P})$ in which $\mathcal{A}$ is the sample space, $\mathcal{F}$ is a set of events and $\mathcal{P}$ is a probability measure. The random field $X(\mathbf{x})$ is defined in $L^2(\mathcal{A}, H^1(\Omega_1))$. A realization of the random medium is a set of the values $x(\mathbf{x})$ of the random field X over the domain Ω_1.

Average and correlation function: The average of a scalar random field $X(\mathbf{x}^{(i)})$ and the covariance or two-point correlation function of two random variables $X(\mathbf{x}^{(i)})$ and $X(\mathbf{x}^{(j)})$ are respectively defined as:

$$\bar{X}(\mathbf{x}^{(i)}) = \mathbb{E}\left\{X(\mathbf{x}^{(i)})\right\} = \int_{\mathbb{R}} X(\mathbf{x}^{(i)})\; p_1\left(X(\mathbf{x}^{(i)})\right)\; dX(\mathbf{x}^{(i)}) \tag{1.23}$$

$$\begin{aligned} C_X(\mathbf{x}^{(i)}, \mathbf{x}^{(j)}) &= \mathbb{E}\left\{\left(X(\mathbf{x}^{(i)}) - \bar{X}(\mathbf{x}^{(i)})\right)\left(X(\mathbf{x}^{(j)}) - \bar{X}(\mathbf{x}^{(j)})\right)\right\} = \\ &\int_{\mathbb{R}}\int_{\mathbb{R}} \left(X(\mathbf{x}^{(i)}) - \bar{X}(\mathbf{x}^{(i)})\right)\left(X(\mathbf{x}^{(j)}) - \bar{X}(\mathbf{x}^{(j)})\right) p_2\left(X(\mathbf{x}^{(i)}), X(\mathbf{x}^{(j)})\right)\; dX(\mathbf{x}^{(i)})\; dX(\mathbf{x}^{(j)}) \end{aligned} \tag{1.24}$$

in which p_1 and p_2 are respectively the first and second order marginal distributions.

Homogeneous, weak-sense homogeneous and isotropic random fields: A random field is called homogeneous if all of its statistical moments are invariant by any translation of all of the space variables. Mathematically, all of the marginal probability distributions of such random fields should be translationally invariant (Frisch, 1968). This implies:

$$\begin{aligned} &p_m\left(X(\mathbf{x}^{(1)} + \boldsymbol{\tau}), X(\mathbf{x}^{(2)} + \boldsymbol{\tau}), \cdots, X(\mathbf{x}^{(m)} + \boldsymbol{\tau})\right) = \\ &\qquad\qquad p_m\left(X(\mathbf{x}^{(1)}), X(\mathbf{x}^{(2)}), \cdots, X(\mathbf{x}^{(m)})\right) \quad \forall \boldsymbol{\tau} \in \mathbb{R}^3; \forall m \in \mathbb{N} \end{aligned} \tag{1.25}$$

A weaker form of homogeneity happens when only the mean value and covariance function of a random field are invariant by translation of the space variables. This type of random fields is called weak-sense homogeneous. From this condition it can be deduced that X is a weak-sense homogeneous random field if its mean is a constant over the whole medium, and its two-point correlation function depends only on the distance between points, *i.e.*:

$$\mathbb{E}\left\{X(\mathbf{x}^{(i)})\right\} = \bar{X} \quad \forall \mathbf{x}^{(i)} \in \Omega_1 \tag{1.26a}$$

$$C_X\left(\mathbf{x}^{(i)}, \mathbf{x}^{(j)}\right) = C_X\left(\mathbf{x}^{(i)} - \mathbf{x}^{(j)}\right) \quad \forall \mathbf{x}^{(i)}, \mathbf{x}^{(j)} \in \Omega_1 \tag{1.26b}$$

A random field is called isotropic if all of its statistical moments are invariant with any simultaneous translation and rotation of all of the space variables. This implies in particular that:

$$C_X\left(\mathbf{x}^{(i)},\mathbf{x}^{(j)}\right) = C_X\left(|\mathbf{x}^{(i)}-\mathbf{x}^{(j)}|\right) \quad \forall \mathbf{x}^{(i)},\mathbf{x}^{(j)} \in \Omega_1 \tag{1.27}$$

Ergodic random fields: One can define the realization-dependent space average random variable:

$$\hat{X}^{(j)}_{\Omega_1} = \frac{1}{V(\Omega_1)}\int_{\Omega_1} X(\mathbf{x},j)\, d\mathbf{x} \quad \forall j \in \mathbb{N} \tag{1.28}$$

in which $X(\mathbf{x},j)$ is the jth realization of the random field X, $V(\Omega_1)$ is the volume occupied by the subspace $\Omega_1 \subseteq \mathbb{R}^3$ and $\hat{X}^{(j)}_{\Omega_1}$ is the sample average estimator corresponding to this realization of the medium. When the medium size is sufficiently large and the random field X is homogeneous, the estimator $\hat{X}^{(j)}_{\Omega_1}$ which is *a priori* a random variable, becomes independent from realizations *i.e.* $\hat{X}^{(j)}_{\Omega_1} = \hat{X}_{\Omega_1}$ and converges to the statistical mean $\bar{X}$. In this case, the random field X is called ergodic. X is called mean-ergodic or mean-square ergodic in the first moment, if it converges in mean square to $\bar{X}$:

$$\lim_{V(\Omega_1)\to\infty} \mathbb{E}\left[\left(\hat{X}_{\Omega_1}-\bar{X}\right)^2\right] = 0 \tag{1.29}$$

The random field X is called covariance-ergodic or mean-square ergodic in the second moment, if the estimator of the covariance, *i.e.*:

$$\hat{C}^{(j)}_{X_{\Omega_1}}(\boldsymbol{\tau}) = \frac{1}{V(\Omega_1)}\int_{\Omega_1}\left[X(\mathbf{x}+\boldsymbol{\tau},j)-\bar{X}(\mathbf{x}+\boldsymbol{\tau})\right]\left[X(\mathbf{x},j)-\bar{X}(\mathbf{x})\right] d\mathbf{x} \quad \forall j \in \mathbb{N} \tag{1.30}$$

becomes independent from realizations and converges in mean-square sense for large medium sizes to the two-point correlation function of the medium $C_X(\boldsymbol{\tau})$ (Papoulis, 1991), *i.e.*:

$$\lim_{V(\Omega_1)\to\infty} \mathbb{E}\left[\left(C_X(\boldsymbol{\tau})-\hat{C}_{X_{\Omega_1}}(\boldsymbol{\tau})\right)^2\right] = 0 \tag{1.31}$$

A random field is called ergodic, if the space-averaged moments of any order converge to the corresponding statistical moment.

In this presentation, we assume that all the random fields $X(\mathbf{x})$ which describe the propagation medium (like density and elastic moduli) are ergodic, so that their statistical moments can be deduced from a single realization of a sufficiently large random medium. For instance, the statistical mean $\bar{X}$ will be estimated using the equation (1.28) for any given realization number j.

In general, two different types of random media can be taken into consideration: continuous random media in which the properties vary randomly and continuously in space, and discrete random media which contain randomly distributed obstacles such as cracks, cavities and inclusions, embedded in a homogeneous matrix. The majority of the studies, especially in Geophysics, are done based on discrete random media (see Sato et al. (1997), Trégourès and van Tiggelen (2002) and Bihan and Margerin (2009) for instance). The extension of the continuous random medium case to that of discrete random medium is straightforward and could be done by considering the density of scatterers in discrete medium (see Turner and Weaver (1996) or Savin (2012) for discussion).

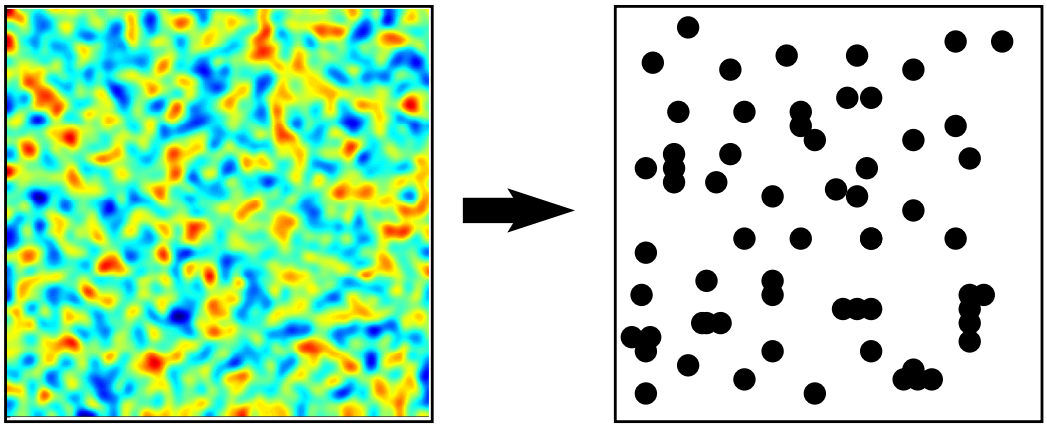

Figure 1.4: Left: A continuous random medium, Right: A discrete random medium consisting in point-like scatterers (heterogeneities) embedded in a homogeneous matrix

1.2.3 Correlation structure

In this section we will look at the covariance function corresponding to the simple case of an isotropic random field (equation (1.27)) which is solely a function of the distance between the points. It is worth noticing that this type of correlation functions will appear in the theory of elastic wave scattering in random media with local isotropy and will be shown in Section 1.4. The amplitude of the fluctuations or the variance of the random field is defined as the value of the covariance function when two points are coincident:

$$\sigma_X^2 = C_X(0) \tag{1.32}$$

The dimensionless correlation function or the autocorrelation function (ACF) of an isotropic random field X is then defined as:

$$\hat{R}_X(\tau) = \frac{C_X(\tau)}{C_X(0)} \tag{1.33}$$

in which τ is the distance between the points. $\hat{R}_X$ is also called the correlation kernel which always satisfies $|\hat{R}_X| \leq 1$ in the case of media with finite variances. In the case of two different scalar random fields X, Y, the adimensional cross-correlation function with isotropic structure is similarly defined as:

$$\hat{R}_{XY}(\tau) = \frac{C_{XY}(\tau)}{\sigma_X \sigma_Y \rho_{XY}} \tag{1.34}$$

in which σ_X and σ_Y denote the standard deviations of the corresponding random fields and ρ_{XY} is their correlation coefficient. Apart from the variance or standard deviation which are measures of the fluctuations magnitude, the correlation functions are characterized by a length scale that is called the correlation length ℓ_c. The latter can be imagined as the distance beyond which the values of the random field are almost uncorrelated. It can be considered as the typical size of the random heterogeneities. Several studies suggest that the Earth's crust should be modeled as containing fluctuations on a continuum of length scales from micro to macro (see Crossley and Jensen (1989) and Pilkington and Todoeschuck (1990) for instance). As a result, more realistic stochastic models, like fractal medium models, should include all these spatial fluctuation scales (Frankel and Clayton (1986), Solna (2003)). As far as the identification of the statistical parameters is concerned, two items will complexify the problem:

- the existence of multiple scales for spatial fluctuations of parameters,
- the fact that C is a *function* so that its identification is much more complex than a *scalar* parameter.

In this work we will be concerned with the scales of fluctuations comparable to the wavelength in which the interactions between the waves and the heterogeneities become more efficient. Therefore, in this study from one hand we will consider only media with a single correlation length (to simplify the first mentioned item) and a finite variance. Another normalization which will be applied hereinafter is that the isotropic correlation kernel $\hat{R}_X$ is considered to be a function of the ratio between the lag distance $x = |\mathbf{x}|$ and the correlation distance ℓ_c. Therefore, the correlation function C_X reads:

$$C_X(x;\ell_c) = \sigma_X^2 \hat{R}_X(x;\ell_c) = \sigma_X^2 \hat{R}_X\left(\frac{x}{\ell_c}\right) \tag{1.35}$$

Different definitions for ℓ_c can be found in literature (see Shinozuka and Deodatis (1988) for example). We define ℓ_c as twice the zeroth-order moment of the function $\hat{R}_X(x/\ell_c)$:

$$\ell_c = 2\int_0^\infty \hat{R}_X\left(\frac{x}{\ell_c}\right)\, dx \tag{1.36}$$

and we normalize the correlation models using this definition. This implies that all correlation models will satisfy the following equations:

$$2\int_0^\infty \hat{R}_X(u)\, du = 1 \tag{1.37}$$

As we will see in chapter 2, the analytical formulas of the wave scattering will be given explicitly in terms of the power spectra of the random heterogeneities which are defined as the Fourier transform of the spatial correlation function C. We adopt the following Fourier transform integral pairs for a random function X defined from $\mathbb{R}^3$ into $\mathbb{R}$:

$$C_X(\mathbf{x}) = \int_{\mathbb{R}^3} e^{+i\mathbf{x}.\mathbf{k}} S_X(\mathbf{k}) d\mathbf{k} \tag{1.38a}$$

$$S_X(\mathbf{k}) = \frac{1}{(2\pi)^3}\int_{\mathbb{R}^3} e^{-i\mathbf{x}.\mathbf{k}} C_X(\mathbf{x}) d\mathbf{x} \tag{1.38b}$$

in which C_X is the autocorrelation function (ACF) and S_X is called the power spectral density function (PSDF) of the scalar random field X. $\mathbf{k}$ is the wave vector corresponding to a $\mathbf{x} \to \mathbf{k}$ Fourier transform. If the correlation function C_X is a real function, it can be shown using equations (1.38) that $S^*(\mathbf{k}) = S(\mathbf{k})$ where $*$ denotes the complex conjugate. As a result, the PSDF and the correlation function are always real. In the case where the correlation function has an isotropic structure, *i.e.* it depends on the radial distance $x = |\mathbf{x}|$ rather than on the distance vector $\mathbf{x}$, it can be shown that the PSDF will also be only a function of the radial wave number $k = |\mathbf{k}| = \sqrt{k_x^2 + k_y^2 + k_z^2}$. Using the spherical coordinates, the Fourier integrals in equations (1.38a) and (1.38b) will be simplified as:

$$C_X(x) = 4\pi\int_0^\infty \mathrm{sinc}(xk) k^2 S_X(k) dk \tag{1.39a}$$

$$S_X(k) = \frac{1}{2\pi^2}\int_0^\infty \mathrm{sinc}(xk) x^2 C_X(x) dx \tag{1.39b}$$

in which $C_X : \mathbb{R}^+ \mapsto \sigma_X^2[-1,+1]$ and $S_X : \mathbb{R}^+ \mapsto \mathbb{R}^+$ and sinc denotes the unnormalized sinc function. Several correlation models that are used particularly in geophysics will be discussed in chapter 2. Studying different approaches to model the medium parameters via stochastic functions is out of the scope of this thesis. However, a non-parametric probabilistic approach based on the maximum entropy principle to model the random fields of scalar or matrix nature is presented in Appendix C.

In the following section we will discuss about the physical phenomenon which happens when elastic waves interact with the random heterogeneities which have been studied in this section.

1.3 Length scales and scattering regimes

The amplitude and phase of elastic waves propagating through a randomly heterogeneous medium ($||\mathbf{U}(t,\mathbf{x})||$ and $\phi(t,\mathbf{x}) = \boldsymbol{\kappa} \cdot \mathbf{x} - \omega t$ in equation (1.9)) are changed due to scattering. Scattering results from the interaction of the elastic waves with the heterogeneities in the medium as it can be seen in Figure 1.5. In this figure an inhomogeneity is illuminated by an incident plane wave and scattered waves with different phases and amplitudes in all directions are produced.

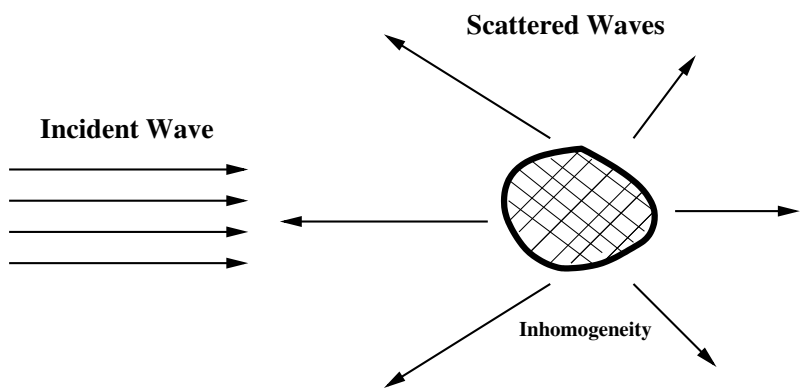

Figure 1.5: Schematic scattering pattern when a typical heterogeneity is illuminated by a plane wave

Scattering phenomenon plays a crucial role in seismogram interpretation. Consequently, a profound understanding of scattering mechanism and its effects on the wave propagation regime could be a fundamental step in the statistical identification of the medium properties. The degree of scattering of the medium or the scattering regime of the waves depends on the ratio between some length scales related to the medium and the waves. Theses length scales are schematically shown in Figure 1.6 in which the propagation/observation distance L, typical size of the heterogeneities or the correlation length ℓ_c and the dominant wave length λ are three fundamental length scales of interest in typical wave propagation problems. Another length scale which is shown in this figure is the mean free path ℓ_{sc} which is the distance over which the scattering of the waves is effective (this parameter will be defined later in this chapter). The dominant wave number could then be defined as $k = \omega/v_0 = 2\pi/\lambda$ in which ω and v_0 are respectively the dominant angular frequency and a reference speed of propagation. For high-frequency seismic waves propagating in rocks, the carrying frequency is at least 1Hz. Typical values of ρ, v_s and v_p in geological media can be found in Figure 1.3. The propagation distances over the Earth's crust is about 15 to 80km. The key adimensional parameters which allow to distinguish different scattering regimes are $\zeta = k\ell_c$, $\varepsilon = kL$ (see Fouque et al. (2007) and Margerin et al. (2000) for instance). Assuming that the boundary effects are negligible, different scattering regimes can be classified as:

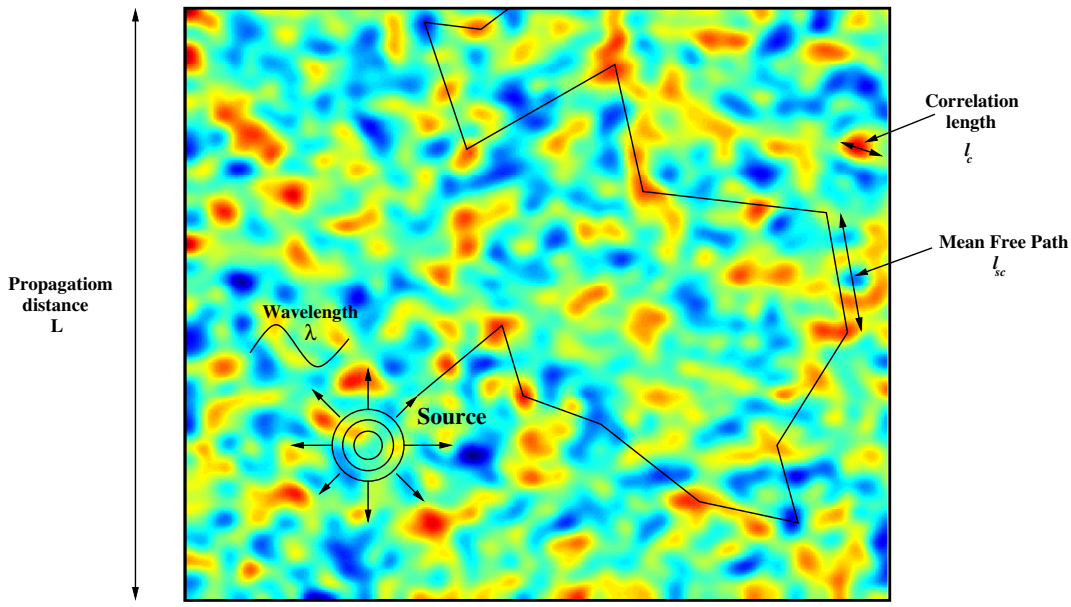

Figure 1.6: Length scales in wave propagation problems

1. The effective medium or homogenization regime happens when $\zeta = k\ell_c \ll 1$. In this low-frequency regime the elastodynamic wave equation is the most appropriate model to describe the wavefield evolution and a deterministic effective wave equation can describe the wave propagation. As a result, the stochastic homogenization methods can be used (see Capdeville et al. (2010) and Fish and Chen (2004) for applications in elastodynamics). These methods are appropriate as long as the propagation distance is comparable to the wavelength, *i.e.* $\varepsilon = kL \simeq 1$ (Savin, 2010).

2. The geometrical optics regime establishes when $\zeta = k\ell_c \gg 1$. The waves will not interact efficiently with the details of the medium so that the medium can be considered as piecewise homogeneous. If the medium's dispersion parameter is weak, the Born approximation can be employed to calculate the wavefield (Born and Wolf, 1965). For example consider the scalar Helmholtz equation (1.8) with a weakly-varying velocity random function described as:

$$v(\mathbf{x}) = v_0 \left[1 + X_v(\mathbf{x})\right] \tag{1.40}$$

in which the zero-mean fractional velocity fluctuation $X_v(\mathbf{x})$ is assumed to have a relatively low variance or equivalently a low spatial gradient. The total wave field u is written as the sum of an incident wave field u_{in} and a scattered wave field u_{sc}:

$$u = u_{in} + u_{sc} \tag{1.41}$$

The incident wave u_{in} satisfies the homogeneous Helmholtz wave equation:

$$\left[\Delta - \frac{1}{v_0^2}\partial_t^2\right] u_{in}(\mathbf{x}, t) = 0 \tag{1.42}$$

Inserting (1.40) into equation (1.8) and neglecting the terms in X_v^2 results in:

$$\left[\Delta - \frac{1}{v_0^2}\partial_t^2\right] u_{sc}(\mathbf{x}, t) = -\frac{2}{v_0^2} X_v(\mathbf{x}) \frac{\partial^2 u_{in}(\mathbf{x}, t)}{\partial t^2} \tag{1.43}$$

in which the right hand side acts as a source term resulting from the interaction between the incident wavefield and the heterogeneities. The weakly coupled equations (1.42) and (1.43) can be solved analytically for simple geometries.

3. The weakly heterogeneous or stochastic scattering regime sets in when (see Ryzhik et al. (1996), Papanicolaou et al. (1996), Bal and Ryzhik (2002) and Baydoun et al. (2014) for instance):

   (i) the amplitude of fluctuations of the medium's mechanical properties is weak,

   (ii) the wavelength is small compared to the propagation distance, *i.e.* $\varepsilon = kL \gg 1$ (high-frequency waves),

   (iii) the scale of heterogeneities is comparable to the wavelength $\zeta = k\ell_c \sim 1$.

   In this high-frequency regime, both the random medium and the waves oscillate at similar frequencies and consequently there will be a significant interaction between the waves and the random heterogeneities (Aki and Richards, 2002). In this case, the transport or the radiative transfer equations (RTE) are the appropriate models to describe the propagation of the wave energy. In highly varying media, a localization regime could occur which means that the energy of the waves will be locally trapped on some regions of the medium so that the transport of the energy does not happen (see Sheng (1995), Larose et al. (2004) and Lobkis and Weaver (2008) for example). Likewise, in highly anisotropic media as in the case of the layered random media a localization regime could be established. The theoretical analysis of the localization regime is out of the scope of this study. The mathematical developments of the scattering theory of elastic waves is the subject of the Section 1.4.

These three regimes are schematically distinguished in Figure 1.7 [1] which shows the variation of the elastic diffusivity of the medium, which is one of the fundamental characteristics of the wave propagation at long lapse times and which appears in the diffusion equation (this parameter will be defined in chapter 2). It should be noted that the elastic diffusivity in weakly-varying media is inversely proportional to the scattering degree of the underlying medium. This means than lower values of this parameters corresponds to highly scattering media and vice versa. It can be observed from this figure that for low and large values of $\zeta = k\ell_c$, the effective medium regime and geometrical optics regime will respectively set in. Between these two regimes there is a transition phase in which the waves have the most efficient interaction with the heterogeneities so that the wavefield becomes randomized more quickly compared to the other scattering regimes. The degree of scattering is often considered to be proportional to the inverse of the elastic diffusivity (see Turner and Weaver (1995) for instance). Consequently, the middle part of the Figure 1.7 corresponds to a highly scattering medium in which the elastic diffusivity has significantly lower values compared to the other two extremes of the curve.

In the next section we introduce the scattering theory of elastic waves in a stochastic scattering regime.

[1] In chapter 2, the elastic diffusivity will be plotted for different correlation models.

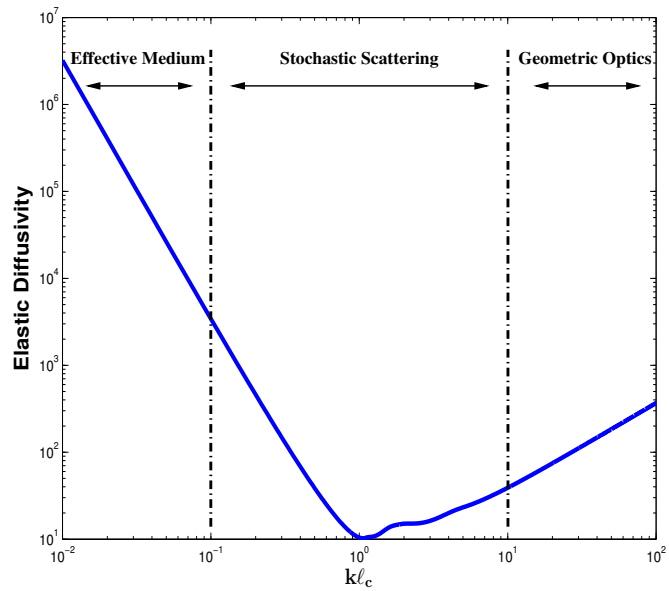

Figure 1.7: Different scattering regimes in terms of the values of $k\ell_c$

1.4 Stochastic scattering regime

The theory of radiative transfer of elastic waves is an approach to study the multiple scattering of seismic waves (Chandrasekhar (1960), Weaver (1990), Zeng (1993), Sato (1994), Turner and Weaver (1994), Ryzhik et al. (1996), Margerin et al. (2000)). The radiative transfer equations (RTE) describe the spatio-temporal evolution of the wave vector dependent energy density of the waves as well as their state of polarization. Chandrasekhar (1960) developed the vector transport equations of the polarized light waves in the case of statistically isotropic media. Assuming a weakly-varying random media with local isotropy, Weaver (1990) and Ryzhik et al. (1996) independently developed the RTEs of elastic waves with two different approaches:

- The derivation of Weaver (1990) is based upon a diagrammatic approach, as introduced by Frisch (1968), in which the mean wave field is governed by Dyson equation (resulting directly from the elastodynamic wave equation). This equation is solved in spatial-Fourier domain with the assumption of the first order smoothing (FOSA) as well as $\zeta = k\ell_c$ which should be below the high-frequency geometric optics limit (Turner and Anugonda, 2001). Then, solving the so-called Bethe-Salpeter equation results in the transport equations.

- Ryzhik et al. (1996) started with the wave equation and used asymptotic expansions to derive the RTEs of elastic waves. Their approach will be detailed further in this chapter.

As far as the materials with locally anisotropic behavior is concerned, Turner (1999) derived the RTEs of elastic waves in a transversely isotropic heterogeneous medium in which there is a plane of symmetry and the elastic matrix could be specified using 5 independent parameters. Margerin (2006) developed the elastic RTEs for the case of anisomeric random media in which the correlation lengths depend on space direction. Recently Baydoun et al. (2014) developed the RTEs of elastic waves for locally anisotropic material behavior and anisotropic background.

In the general case, solving analytically the RTEs of elastic waves is impossible. Margerin et al. (2000) developed a numerical code to solve the RTEs of elastic waves using a random walk

approach. Despite the fact that the scattering of elastic waves is intrinsically anisotropic (*i.e.* the scattered directional energy density varies in different directions) even in low-frequencies (Turner, 1998), the hypothesis of isotropic scattering makes these equations more tractable and allows them to be analytically solved. Consequently, Shang and Gao (1988) and Zeng et al. (1991) assumed that the scattering occurs isotropically and solved the RTEs in the case of scalar waves. In fact, the lowest term in the expansion of the scattering operator (the so-called scattering cross-section) in RTEs of elastic waves using spherical harmonics represents the isotropic scattering. Zeng (1993) and Sato (1994) developed these studies to the case of elastic waves but they neglected the vector nature of elastic waves such as the effect of the polarization of shear waves. In these studies the elastic waves are treated as scalar waves and the scattering is yet assumed to be isotropic.

In the next section, we will briefly discuss the derivation of the RTE of acoustic waves propagating in a low variance random medium with continuous heterogeneities. The same approach leads to the RTEs of elastic waves but for the sake of simplicity, we use the case of acoustic waves to derive the transport equations. The major differences is that the acoustic waves have only one wave mode similar to the compressional mode of elastic waves, so that the effects of the polarization of S waves and possible mode conversions between P and S waves during scattering process will not be taken into consideration in acoustic transport equations. Subsequently, the RTEs corresponding to the case of elastic waves will be introduced without giving the mathematical proofs.

1.4.1 Radiative transfer equation of acoustic waves

In this section, starting with the acoustic wave equations and using a multiscale expansion of the Wigner measure of the wave field as a parameter which is closely related to the wave energy density, the transport equation of acoustic waves will be derived. At first, the acoustic wave equation for the pressure and velocity fields (p and $\mathbf{v}$ respectively) is considered as:

$$\rho(\mathbf{x})\frac{\partial \mathbf{v}(\mathbf{x},t)}{\partial t} + \nabla p(\mathbf{x},t) = \mathbf{0}; \quad \mathbf{v}(\mathbf{x},0) = \mathbf{v}_0(\mathbf{x}) \tag{1.44a}$$

$$\kappa(\mathbf{x})\frac{\partial p(\mathbf{x},t)}{\partial t} + \nabla \cdot \mathbf{v}(\mathbf{x},t) = 0; \quad p(\mathbf{x},0) = p_0(\mathbf{x}) \tag{1.44b}$$

in which $\rho(\mathbf{x})$ and $\kappa(\mathbf{x})$ are respectively the local values of density and bulk modulus of the medium. The acoustic tensor corresponding to the set of wave equations (1.44) has one double eigenvalue corresponding to the non-propagating waves, *i.e.* $\omega_1 = \omega_2 = 0$, and two simple eigenvalues $\omega_+ = v|\mathbf{k}|$ and $\omega_- = -v|\mathbf{k}|$ corresponding respectively to the outgoing and incoming (which is obviously non-physical) longitudinal acoustic waves propagating with the sound speed $v(\mathbf{x}) = \sqrt{\kappa(\mathbf{x})/\rho(\mathbf{x})}$. It should be noted that this wave mode is analogue to the longitudinal elastic wave mode. The corresponding 4×1 eigenvectors are functions of the material properties (κ, μ) and the orthonormal propagation triplet $(\hat{\mathbf{k}}, \mathbf{z}^{(1)}, \mathbf{z}^{(2)})$ where $\hat{\mathbf{k}}$, $\mathbf{z}^{(1)}$ and $\mathbf{z}^{(2)}$ correspond respectively to the unit vectors following the propagation direction and its two perpendiculars.

Let $\mathbf{u}$ be the 4×1 vector wave field containing velocity and pressure fields: $\mathbf{u} = (\mathbf{v}, p)$. The coupled system of equations (1.44) may be written as a first-order symmetric hyperbolic system:

$$\mathcal{A}(\mathbf{x})\frac{\partial \mathbf{u}(\mathbf{x},t)}{\partial t} + \sum_{j=1}^{3} \mathcal{D}^j \frac{\partial \mathbf{u}(\mathbf{x},t)}{\partial x^j} = 0 \quad ; \quad \mathbf{u}(\mathbf{x},0) = \mathbf{u}_0(\mathbf{x}) \tag{1.45}$$

in which $\mathcal{A}(\mathbf{x}) = \text{diag}(\rho(\mathbf{x}), \rho(\mathbf{x}), \rho(\mathbf{x}), \kappa(\mathbf{x}))$ is a symmetric positive-definite matrix containing the material properties and the matrices $\mathcal{D}^j (1 \leq j \leq 3)$ are symmetric and independent from time and space.

The spatial energy density $\mathcal{E}(\mathbf{x}, t)$ and the energy flux $\mathcal{F}(\mathbf{x}, t)$ corresponding to the solutions of (1.45) are given by Ryzhik et al. (1996):

$$\mathcal{E}(\mathbf{x}, t) = \frac{1}{2} \left(\mathcal{A}(\mathbf{x}) \mathbf{u}(\mathbf{x}, t) \cdot \mathbf{u}(\mathbf{x}, t) \right) \quad ; \quad \mathcal{F}_j(\mathbf{x}, t) = \frac{1}{2} \left(\mathcal{D}^j \mathbf{u}(\mathbf{x}, t) \cdot \mathbf{u}(\mathbf{x}, t) \right) \tag{1.46}$$

which satisfy the energy conservation law:

$$\frac{\partial \mathcal{E}(\mathbf{x}, t)}{\partial t} + \nabla \cdot \mathcal{F}(\mathbf{x}, t) = 0 \tag{1.47}$$

Assuming that the overall propagation distance L is much larger than the typical wavelength of the initial excitation, *i.e.* $\varepsilon = \frac{\lambda}{L} \ll 1$, high frequency solutions of (1.45) are of our interest. The rescaled time and space variables are thus defined as $t \to \varepsilon^{-1} t$ and $\mathbf{x} \to \varepsilon^{-1} \mathbf{x}$. Hence, the rescaled wave field $\mathbf{u}_\varepsilon(\mathbf{x}, t) = \mathbf{u}(\varepsilon^{-1}\mathbf{x}, \varepsilon^{-1} t)$ will satisfy:

$$\mathcal{A}(\mathbf{x}) \frac{\partial \mathbf{u}_\varepsilon(\mathbf{x}, t)}{\partial t} + \sum_{j=1}^{3} \mathcal{D}^j \frac{\partial \mathbf{u}_\varepsilon(\mathbf{x}, t)}{\partial x^j} = 0 \quad ; \quad \mathbf{u}_\varepsilon(\mathbf{x}, 0) = \mathbf{u}_0(\mathbf{x}/\varepsilon) \tag{1.48}$$

The following paragraph presents the concept of the Wigner transform of the wave field $\mathbf{u}$ and shows that in high frequencies it becomes closely related to the energy density.

Spatial Wigner transform and its properties: The spatial Wigner transform of the wave field $\mathbf{u}(\mathbf{x}, t)$ is defined on phase space $(\mathbf{x}, \mathbf{k})$ as (**?**):

$$W(\mathbf{x}, \mathbf{k}, t) = \left(\frac{1}{2\pi} \right)^3 \int_{\mathbb{R}^3} e^{i\mathbf{k}\mathbf{y}} \mathbf{u} \left(\mathbf{x} - \frac{1}{2}\mathbf{y}, t \right) \mathbf{u}^* \left(\mathbf{x} + \frac{1}{2}\mathbf{y}, t \right) d\mathbf{y} \tag{1.49}$$

in this case $W(\mathbf{x}, \mathbf{k}, t)$ is a 4×4 Hermitian matrix but not necessarily positive definite. It can be seen as the inverse Fourier transform of the (symmetrized) autocorrelation function of the wave field $\mathbf{u}(\mathbf{x})$ (Bal, 2005). Its integral over $\mathbf{k}$ is always positive:

$$\int_{\mathbb{R}^3} W(\mathbf{x}, \mathbf{k}, t) d\mathbf{k} = \mathbf{u}(\mathbf{x}, t) \mathbf{u}^*(\mathbf{x}, t) = |\mathbf{u}(\mathbf{x}, t)|^2 \tag{1.50}$$

Equations (1.46) along with the equation (1.50) lead to the following expressions for the energy density ϵ and the energy flux $\mathcal{F}$ in terms of the Wigner transform of the wave field:

$$\mathcal{E}(\mathbf{x}, t) = \frac{1}{2} \int_{\mathbb{R}^3} \text{Tr} \left(\mathcal{A}(\mathbf{x}) W(\mathbf{x}, \mathbf{k}, t) \right) d\mathbf{k} \quad ; \quad \mathcal{F}_j(\mathbf{x}, t) = \frac{1}{2} \int_{\mathbb{R}^3} \text{Tr} \left(\mathcal{D}^j W(\mathbf{x}, \mathbf{k}, t) \right) d\mathbf{k} \tag{1.51}$$

The rescaled spatial Wigner transform matrix W_ε is then defined similar to definition (1.49):

$$W_\varepsilon(\mathbf{x}, \mathbf{k}, t) = \left(\frac{1}{2\pi} \right)^3 \int_{\mathbb{R}^3} e^{i\mathbf{k}\mathbf{y}} \mathbf{u}_\varepsilon \left(\mathbf{x} - \frac{1}{2}\varepsilon\mathbf{y}, t \right) \mathbf{u}_\varepsilon^* \left(\mathbf{x} + \frac{1}{2}\varepsilon\mathbf{y}, t \right) d\mathbf{y} \tag{1.52}$$

It can be shown that the high frequency limit of W_ε is not only Hemitian but also positive definite, which is interesting as far as the interpretation of the Wigner transform as a measure of energy is concerned.

The Taylor expansion of the deterministic rescaled Wigner matrix W_ε in terms of adimensional parameter ε reads:

$$W_\varepsilon(\mathbf{x},\mathbf{k},t) = W^{(0)}(\mathbf{x},\mathbf{k},t) + \varepsilon W^{(1)}(\mathbf{x},\mathbf{k},t) + \varepsilon^2 W^{(2)}(\mathbf{x},\mathbf{k},t) + \cdots \tag{1.53}$$

Let b_+ and b_- denote respectively the polarization directions of the outgoing and incoming acoustic waves. it can then be shown that the high frequency limit of the Wigner measure, *i.e.* $W^{(0)}$, may be decomposed as:

$$W^{(0)}(\mathbf{x},\mathbf{k},t) = a_+(\mathbf{x},\mathbf{k},t)\mathsf{b}_+(\mathbf{k})\mathsf{b}_+^*(\mathbf{k}) + a_-(\mathbf{x},\mathbf{k},t)\mathsf{b}_-(\mathbf{k})\mathsf{b}_-^*(\mathbf{k}) \tag{1.54}$$

where the scalar functions a_+ and a_- are related as $a_+(\mathbf{x},\mathbf{k},t) = a_-(\mathbf{x},-\mathbf{k},t)$ and a_+ satisfies a Liouville equation which is similar to the energy conservation law in equation (1.47):

$$\frac{\partial a_+}{\partial t} + \{\omega, a_+\} = 0 \tag{1.55}$$

in which the so-called Poisson bracket $\{\}$ is defined as $\{f,g\} = \nabla_{\mathbf{k}} f \cdot \nabla_{\mathbf{x}} g - \nabla_{\mathbf{x}} f \cdot \nabla_{\mathbf{k}} g$. Since $W^{(0)}$ is a positive definite matrix, the positive scalar a_+ can be interpreted as the wave energy density in phase space. Equation (1.55) is the RTE of acoustic waves in a homogeneous medium because so far the medium parameters κ, μ and ρ are considered to be deterministic.

Insertion of randomness on medium properties and extraction of RTE: We now introduce the spatial randomness on parameters κ and μ as:

$$\kappa(\mathbf{x}) = \underline{\kappa}\left[1 + \sqrt{\varepsilon} X_\kappa\left(\frac{\mathbf{x}}{\varepsilon}\right)\right] \;;\; \mu(\mathbf{x}) = \underline{\mu}\left[1 + \sqrt{\varepsilon} X_\mu\left(\frac{\mathbf{x}}{\varepsilon}\right)\right] \;;\; \rho(\mathbf{x}) = \underline{\rho}\left[1 + \sqrt{\varepsilon} X_\rho\left(\frac{\mathbf{x}}{\varepsilon}\right)\right] \tag{1.56}$$

in which X_κ, X_μ and X_ρ are adimensional, independent, statically isotropic and second-order random functions with zero mean values and with correlation lengths comparable to the typical wavelengths (since the stochastic scattering regime is of our interest). In this equation ε is the same scaling factor defined early in this chapter. The magnitude of perturbations $\sqrt{\varepsilon}$, is chosen such that the scattering effects due to the heterogeneities and the effect of the homogeneous background medium be comparable (Ryzhik et al., 1996). However, this reduction in the amplitude of fluctuations will also prevent the waves to be in a localization regime in which the wave energy will be trapped in finite regions so that its transport might no more be possible. In all 1D and 2D random media, the (Anderson) localization is expected. In 3D random media with strong fluctuations, even when the heterogeneities are isotropic, a localization regime will be obtained (see Sheng (1995), Larose et al. (2004) and Lobkis and Weaver (2008) for example).

Using the fast space variable $\boldsymbol{\xi} = \frac{\mathbf{x}}{\varepsilon}$, a multiscale expansion of random matrix-valued W_ε is now introduced as:

$$W_\varepsilon(\mathbf{x},\boldsymbol{\xi},\mathbf{k},t) = W^{(0)}(\mathbf{x},\mathbf{k},t) + \sqrt{\varepsilon} W^{(1)}(\mathbf{x},\boldsymbol{\xi},\mathbf{k},t) + \varepsilon W^{(2)}(\mathbf{x},\boldsymbol{\xi},\mathbf{k},t) + \cdots \tag{1.57}$$

with a high frequency asymptotic $W^{(0)}$ which is assumed to be independent of the variable $\boldsymbol{\xi}$. It can be shown that the average value of the random matrix W_ε is close (in a mean-square sense)

to the positive definite $\boldsymbol{\xi}$-independent matrix $W^{(0)}$ which itself could be again decomposed as in equation (1.54), in which a_+ which is hereafter denoted simply by a satisfies the following transport equation:

$$\frac{\partial a}{\partial t} + \{\omega, a\} = \frac{\pi v^2 |\mathbf{k}|^2}{2} \int_{\mathbb{R}^3} \delta\left(\omega(\mathbf{k}) - \omega(\mathbf{k}')\right)\left(a(\mathbf{k}') - a(\mathbf{k})\right) \times \left\{(\hat{\mathbf{k}} \cdot \hat{\mathbf{k}}')^2 S_{\rho\rho}(|\mathbf{k} - \mathbf{k}'|) + 2(\hat{\mathbf{k}} \cdot \hat{\mathbf{k}}') S_{\rho\kappa}(|\mathbf{k} - \mathbf{k}'|) + S_{\kappa\kappa}(|\mathbf{k} - \mathbf{k}'|)\right\} \quad (1.58)$$

Since the local frequency is $\omega(\mathbf{x}, \mathbf{k}) = v(\mathbf{x})|\mathbf{k}|$, the Poisson bracket will be $\{\omega, a\} = v\hat{\mathbf{k}} \cdot \nabla_{\mathbf{x}} a - |\mathbf{k}| \nabla_{\mathbf{x}} v \cdot \nabla_{\mathbf{k}} a$. The right hand side of this equation can be rewritten in the following general form:

$$\frac{\partial a}{\partial t} + \{\omega, a\} = \int_{\mathbb{R}^3} \sigma(\mathbf{x}, \mathbf{k}, \mathbf{k}') a(\mathbf{k}') d\mathbf{k}' - \Sigma(\mathbf{x}, \mathbf{k}) a(\mathbf{k}) \quad (1.59)$$

which is the general form of the transport equation of scalar waves having just a single wave mode. In equation (1.58) $S_{\rho\rho}$, $S_{\rho\kappa}$ and $S_{\kappa\kappa}$ are the power spectra of the inhomogeneities (note that for example $S_{\rho\rho}$ is the PSDF of the random variable X_ρ defined in equation (1.56)) and $\hat{\mathbf{k}}$ and $\hat{\mathbf{k}}'$ are the unit wave vectors corresponding to the incident and scattered waves or vice versa. The left hand side of equation (1.59) represents the total time derivative of the angular energy density a at a point moving along a ray in phase space $(\mathbf{x}, \mathbf{k})$ and the right hand side represents the effects of scattering by random heterogeneities. The first term of the latter results from the gain of energy due to the scattering of all possible incident waves which are scattered in direction $\mathbf{k}$ and the second term is related to the loss of energy resulting from the scattering of the incident wave following $\mathbf{k}$ to all other directions. It can be pointed out that the left and right hand sides of equation (1.59) take into account respectively the parameter fluctuations at slow and fast scales. The scattering process by a localized heterogeneity is schematically shown in Figure 1.8.

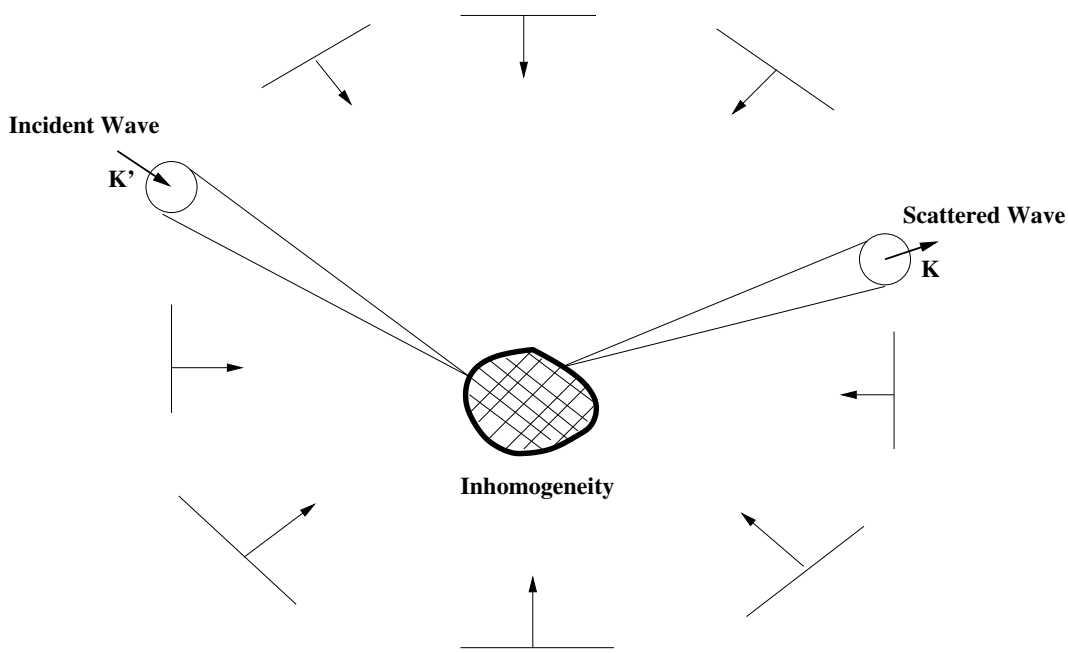

Figure 1.8: Scalar wave scattering pattern

Differential and total scattering cross-sections: In equation (1.59), the so-called differential scattering cross-section σ is given by:

$$\sigma(\mathbf{x},\mathbf{k},\mathbf{k}') = \frac{\pi v^2|\mathbf{k}|^2}{2}\left\{(\hat{\mathbf{k}}\cdot\hat{\mathbf{k}}')^2 S_{\rho\rho}(|\mathbf{k}-\mathbf{k}'|) + 2(\hat{\mathbf{k}}\cdot\hat{\mathbf{k}}')S_{\rho\kappa}(|\mathbf{k}-\mathbf{k}'|) + S_{\kappa\kappa}(|\mathbf{k}-\mathbf{k}'|)\right\}\delta\left(v|\mathbf{k}| - v|\mathbf{k}'|\right) \tag{1.60}$$

From equation (1.59), σ can be interpreted as the rate at which an incident wave with wave vector $\mathbf{k}'$ is scattered into another direction $\mathbf{k}$. As it can be observed from equation (1.60), when the material behavior is isotropic, σ is solely a function of the incident wave number $|\mathbf{k}|$ and the cosine of the scattering angle ($\cos\theta = (\hat{\mathbf{k}}\cdot\hat{\mathbf{k}}')$) which is henceforth denoted by χ:

$$\text{Isotropic Material} \rightarrow \sigma(\mathbf{x},\mathbf{k},\mathbf{k}') \equiv \sigma(\mathbf{x},|\mathbf{k}|,\chi) \tag{1.61}$$

The Dirac delta function means that the wave frequency remains unchanged during scattering process which is always true for time-independent non-dissipative media. The wave number is conserved and therefore the differential scattering cross-section is symmetric with respect to $\mathbf{k}$ and $\mathbf{k}'$, *i.e.*:

$$\sigma(\mathbf{x},\mathbf{k},\mathbf{k}') = \sigma(\mathbf{x},\mathbf{k}',\mathbf{k}) \tag{1.62}$$

which is not necessarily the case for vector waves such as electromagnetic or elastic waves.

The total scattering cross section Σ in a point $\mathbf{x}$ and following a direction $\mathbf{k}$ is defined as the sum of differential scattering cross sections for the incident (scattered) direction $\mathbf{k}$ and all possible scattered (incident) directions $\mathbf{k}'$:

$$\Sigma(\mathbf{x},\mathbf{k}) = \int_{\mathbb{R}^3} \sigma(\mathbf{x},\mathbf{k},\mathbf{k}')d\mathbf{k}' \tag{1.63}$$

σ and Σ are respectively in units of m^3s^{-1} and s^{-1}. Physically Σ can be interpreted as follows: If a plane wave packet with a wave vector $\mathbf{k}$ is considered, its directional energy density following $\mathbf{k}$ in any point $\mathbf{x}$ after a propagation time t will be decayed with a factor of $\exp(-\Sigma(\mathbf{x},\mathbf{k})t)$ (Turner, 1998). Σ specifies the wave attenuation due to the wave scattering.

1.4.2 Extension to the case of elastic waves

In this section, considering the particularities of elastic waves compared to the acoustic waves, we will extend the RTE and the scattering parameters introduces in Section 1.4.1 to the case of elastic waves. The main complexities related to the elastic waves compared to the case of acoustic waves are:

(i) The existence of multiple wave modes resulting in potential mode conversions between P and S waves during scattering events.

(ii) The state of polarization of S waves which can affect the transport equations.

The first complexity results in two strongly coupled transport equations for the directional energy densities of P and S waves and the second one leads to a modification in the total time derivative corresponding to the shear waves (LHS of the transport equation of S waves (see equation (1.68))).

Consideration of different mode conversions: Equation (1.63) is no more true for elastic waves in which multiple modes interact with each other during scatterings. In these cases, σ and Σ are matrices. If we differentiate between two S wave modes as S_1 and S_2, the 3×3 matrices corresponding to σ and Σ are as follows:

$$\begin{bmatrix} \sigma(P \to P) & \sigma(P \to S_1) & \sigma(P \to S_2) \\ \sigma(S_1 \to P) & \sigma(S_1 \to S_1) & \sigma(S_1 \to S_2) \\ \sigma(S_2 \to P) & \sigma(S_2 \to S_1) & \sigma(S_2 \to S_2) \end{bmatrix} \Longleftrightarrow \begin{bmatrix} \Sigma(P \to P) & \Sigma(P \to S_1) & \Sigma(P \to S_2) \\ \Sigma(S_1 \to P) & \Sigma(S_1 \to S_1) & \Sigma(S_1 \to S_2) \\ \Sigma(S_2 \to P) & \Sigma(S_2 \to S_1) & \Sigma(S_2 \to S_2) \end{bmatrix} \tag{1.64}$$

Different entries of the scattering matrices can be grouped as follows:

$$\begin{pmatrix} \boxed{\Sigma(P \to P)} & \boxed{\Sigma(P \to S_1) \quad \Sigma(P \to S_2)} \\ \boxed{\begin{matrix} \Sigma(S_1 \to P) \\ \Sigma(S_2 \to P) \end{matrix}} & \boxed{\begin{matrix} \Sigma(S_1 \to S_1) & \Sigma(S_1 \to S_2) \\ \Sigma(S_2 \to S_1) & \Sigma(S_2 \to S_2) \end{matrix}} \end{pmatrix} \tag{1.65}$$

in which the total scattering cross-sections corresponding to different mode conversions are defined as:

$$\Sigma_{PP} = \Sigma(P \to P) \tag{1.66a}$$

$$\Sigma_{SP} = \Sigma(P \to S_1) + \Sigma(P \to S_2) \tag{1.66b}$$

$$\Sigma_{PS} = \begin{bmatrix} \Sigma(S_1 \to P) & 0 \\ 0 & \Sigma(S_2 \to P) \end{bmatrix} \tag{1.66c}$$

$$\Sigma_{SS} = \begin{bmatrix} \Sigma(S_1 \to S_1) & \Sigma(S_2 \to S_1) \\ \Sigma(S_1 \to S_2) & \Sigma(S_2 \to S_2) \end{bmatrix} \tag{1.66d}$$

Modifications in transport equations: For random media with locally isotropic material behavior, Weaver (1990) and Ryzhik et al. (1996) derived the RTEs of elastic waves as the following coupled system of equations:

$$\begin{aligned} &\frac{\partial a^p(\mathbf{k})}{\partial t} + \{\omega^p, a^p(\mathbf{k})\} \\ &\quad = \underbrace{\int_{\mathbb{R}^3} \sigma_{\mathrm{PP}}(\mathbf{k}, \mathbf{k}') a^p(\mathbf{k}') d\mathbf{k}' - \Sigma_{\mathrm{PP}}(\mathbf{k}) a^p(\mathbf{k})}_{\text{Effect of P-to-P scattering}} + \underbrace{\int_{\mathbb{R}^3} \sigma_{\mathrm{PS}}(\mathbf{k}, \mathbf{k}') [a^s(\mathbf{k}')] d\mathbf{k}' - \Sigma_{\mathrm{PS}}(\mathbf{k}) a^p(\mathbf{k})}_{\text{Effect of S-to-P (left) and P-to-S (right) scattering}} \end{aligned} \tag{1.67}$$

$$\begin{aligned} &\frac{\partial [a^s(\mathbf{k})]}{\partial t} + \{\omega^s, [a^s(\mathbf{k})]\} + \underbrace{[a^s(\mathbf{k})]\mathbf{N} - \mathbf{N}[a^s(\mathbf{k})]}_{\text{Effect of the polarization of S waves}} \\ &\quad = \underbrace{\int_{\mathbb{R}^3} \sigma_{\mathrm{SS}}(\mathbf{k}, \mathbf{k}') [a^s(\mathbf{k}')] d\mathbf{k}' - \Sigma_{\mathrm{SS}}(\mathbf{k}) [a^s(\mathbf{k})]}_{\text{Effect of S-to-S scattering}} + \underbrace{\int_{\mathbb{R}^3} \sigma_{\mathrm{SP}}(\mathbf{k}, \mathbf{k}') a^p(\mathbf{k}') d\mathbf{k}' - \Sigma_{\mathrm{SP}}(\mathbf{k}) [a^s(\mathbf{k})]}_{\text{Effect of P-to-S (left) and S-to-P (right) scattering}} \end{aligned} \tag{1.68}$$

where $a^p(\mathbf{k})$ and $[a^s(\mathbf{k})]$ are respectively the scalar directional energy density of compressional P waves and the 2×2 coherence matrix containing the directional energy densities of the coupled

shear S waves. This coherence matrix is similar to the energy density of electromagnetic waves which can be described by four Stokes parameters, *i.e.* the intensity I, the degree of polarization Q, the plane of polarization U and the ellipticity V. We denote the S wave modes (S_1 and S_2) by plane waves as:

$$S_1(t,\mathbf{x}) = A_1(t,\mathbf{x})\exp(i\omega t) \tag{1.69a}$$
$$S_2(t,\mathbf{x}) = A_2(t,\mathbf{x})\exp(i\omega t + i\phi(t)) \tag{1.69b}$$

in which A_1 and A_2 are the respective amplitudes, ω is the wave's circular frequency and $\phi(t)$ is the phase shift between these two wave modes. The Stokes parameters are defined as (see Weaver (1990), Turner and Weaver (1994), Margerin et al. (2000), Trégourès and van Tiggelen (2002)):

$$I = \langle S_1 S_1^* + S_2 S_2^* \rangle = \langle A_1^2 \rangle + \langle A_2^2 \rangle \tag{1.70a}$$
$$Q = \langle S_1 S_1^* - S_2 S_2^* \rangle = \langle A_1^2 \rangle - \langle A_2^2 \rangle \tag{1.70b}$$
$$U = \langle S_1 S_2^* + S_2 S_1^* \rangle = \langle 2A_1 A_2 \cos\phi \rangle \tag{1.70c}$$
$$V = \langle -i(S_1 S_2^* - S_2 S_1^*) \rangle = \langle 2A_1 A_2 \sin\phi \rangle \tag{1.70d}$$

in which $\langle\rangle$ stands for the average over several periods. Note that the waves are unpolarized when $Q = U = V = 0$. The coherence matrix $[a^s(\mathbf{k})]$ is then defined as:

$$[a^s(\mathbf{k})] = \frac{1}{2}\begin{pmatrix} I+Q & U+iV \\ U-iV & I-Q \end{pmatrix} = [a^{s*}(\mathbf{k})] \tag{1.71}$$

which is Hermitian and positive definite and satisfies the Chandrasekhar's RTE (Chandrasekhar, 1960). The extra-diagonal entries of $[a^s(\mathbf{k})]$ result from the polarization of S waves and they vanish when the shear waves are depolarized which takes place in diffusion regime.

In equation (1.68) the 2×2 matrix $\mathbf{N}(\mathbf{x},\mathbf{k})$ describes the polarization effect of shear waves which will be defined later. In equations (1.67) and (1.68), differential scattering cross-section $\sigma_{ij}(\mathbf{k},\mathbf{k}')$ for $i,j \in \{P,S\}$ (with unit m^3/s), is the rate at which energy of mode type j with wave vector $\mathbf{k}'$ is converted to wave energy of mode type i with wave vector $\mathbf{k}$ at the point $\mathbf{x}$. It represents the connection between material properties (Lamé parameters and density) and transport parameters (attenuation, scattering cross-section, scattering mean free paths and diffusion constant) which will be defined further in this chapter.

Thanks to the isotropy of the constitutive behavior (elasticity) and conservation of frequency through mode conversion, one can parameterize the differential scattering operators as (Ryzhik et al., 1996):

$$\sigma_{\mathrm{PP}}(\mathbf{k},\mathbf{k}') = \sigma_{pp}(\mathbf{k},\mathbf{k}')\delta(v_p|\mathbf{k}| - v_p|\mathbf{k}'|) \tag{1.72a}$$
$$\sigma_{\mathrm{PS}}(\mathbf{k},\mathbf{k}')[\mathbb{I}_2] = \mathrm{Tr}\left[\sigma_{ps}(\mathbf{k},\mathbf{k}')\mathbf{G}(\mathbf{k},\mathbf{k}')\right]\delta(v_p|\mathbf{k}| - v_s|\mathbf{k}'|) \tag{1.72b}$$
$$\sigma_{\mathrm{SP}}(\mathbf{k},\mathbf{k}') = \sigma_{ps}(\mathbf{k}',\mathbf{k})\mathbf{G}(\mathbf{k}',\mathbf{k})\delta(v_s|\mathbf{k}| - v_p|\mathbf{k}'|) \tag{1.72c}$$
$$\begin{aligned}\sigma_{\mathrm{SS}}(\mathbf{k},\mathbf{k}')[\mathbb{I}_2] = \Big\{&\sigma_{ss}^{TT}(\mathbf{k},\mathbf{k}')\mathbf{T}(\mathbf{k},\mathbf{k}')\mathbf{T}(\mathbf{k}',\mathbf{k}) + \sigma_{ss}^{\Gamma\Gamma}(\mathbf{k},\mathbf{k}')\mathbf{\Gamma}(\mathbf{k},\mathbf{k}')\mathbf{\Gamma}(\mathbf{k}',\mathbf{k}) \\ &+\sigma_{ss}^{\Gamma T}(\mathbf{k},\mathbf{k}')\left[\mathbf{T}(\mathbf{k},\mathbf{k}')\mathbf{\Gamma}(\mathbf{k}',\mathbf{k}) + \mathbf{\Gamma}(\mathbf{k},\mathbf{k}')\mathbf{T}(\mathbf{k}',\mathbf{k})\right]\Big\}\delta(v_s|\mathbf{k}| - v_s|\mathbf{k}'|)\end{aligned} \tag{1.72d}$$

where the matrices $\mathbf{G}$, $\mathbf{T}$ and $\mathbf{\Gamma}$ will be defined in Section 1.4.3. The following self-consistency relationship between P-to-S and S-to-P scattering cross-sections is a straightforward result from

comparing the equations (1.72b) and (1.72c) which can also be shown using the fact that the Green function is symmetrical:

$$\sigma_{PS}(\mathbf{k},\mathbf{k}') = \mathrm{Tr}\ \sigma_{SP}(\mathbf{k}',\mathbf{k}) \tag{1.73a}$$

The differential, total and forward scattering cross-sections of elastic waves or the scattering parameters will be studied in the next section.

1.4.3 Scattering parameters

Differential scattering cross-sections: Let the triplet $[\hat{\mathbf{k}}, z^{(1)}(\mathbf{k}), z^{(2)}(\mathbf{k})]$ (defined in Section 1.4.1) denote respectively the orthonormal polarization directions of P and S waves in spherical coordinates:

$$\hat{\mathbf{k}} = \begin{pmatrix} \sin\theta\cos\phi \\ \sin\theta\sin\phi \\ \cos\theta \end{pmatrix} \quad ; \quad z^{(1)}(\mathbf{k}) = \begin{pmatrix} \cos\theta\cos\phi \\ \cos\theta\sin\phi \\ -\sin\theta \end{pmatrix} \quad ; \quad z^{(2)}(\mathbf{k}) = \begin{pmatrix} -\sin\phi \\ \cos\phi \\ 0 \end{pmatrix} \tag{1.74}$$

In equations (1.72b), (1.72c) and (1.72d), the 2×2 matrices $\mathbf{G}$, $\mathbf{T}$ and $\mathbf{\Gamma}$ are respectively defined as:

$$\mathrm{G}_{ij}(\mathbf{k},\mathbf{k}') = (\hat{k}\cdot z^{(i)}(\mathbf{k}'))(\hat{k}\cdot z^{(j)}(\mathbf{k}')) \tag{1.75}$$

$$\mathrm{T}_{ij}(\mathbf{k},\mathbf{k}') = z^{(i)}(\mathbf{k})\cdot z^{(j)}(\mathbf{k}') \tag{1.76}$$

$$\Gamma_{ij}(\mathbf{k},\mathbf{k}') = (\hat{\mathbf{k}}\cdot\hat{\mathbf{k}}')(z^{(i)}(\mathbf{k})\cdot z^{(j)}(\mathbf{k}')) + (\hat{\mathbf{k}}\cdot z^{(j)}(\mathbf{k}')).(\hat{\mathbf{k}}'\cdot z^{(i)}(\mathbf{k})) \tag{1.77}$$

Without any loss of generality, we assume that the incident wave is in z direction ($\theta = \phi = 0$ in equation (1.74)), so that the orthonormal propagation triplets corresponding to the incident and scattered waves can be written as:

$$\hat{\mathbf{k}} = \begin{pmatrix} 0 \\ 0 \\ 1 \end{pmatrix} \quad ; \quad z^{(1)}(\mathbf{k}) = \begin{pmatrix} 1 \\ 0 \\ 0 \end{pmatrix} \quad ; \quad z^{(2)}(\mathbf{k}) = \begin{pmatrix} 0 \\ 1 \\ 0 \end{pmatrix} \tag{1.78}$$

$$\hat{\mathbf{k}}' = \begin{pmatrix} \sin\theta'\cos\phi' \\ \sin\theta'\sin\phi' \\ \cos\theta' \end{pmatrix} \quad ; \quad z^{(1)}(\mathbf{k}') = \begin{pmatrix} \cos\theta'\cos\phi' \\ \cos\theta'\sin\phi' \\ -\sin\theta' \end{pmatrix} \quad ; \quad z^{(2)}(\mathbf{k}') = \begin{pmatrix} -\sin\phi' \\ \cos\phi' \\ 0 \end{pmatrix} \tag{1.79}$$

Hence, the scattering angle is θ' and we define $\chi = \cos\theta'$. In equations (1.72), the differential scattering cross-sections σ_{PP}, σ_{PS} and σ_{SP} are respectively (see Weaver (1990), Ryzhik et al. (1996), Turner (1998), Turner and Anugonda (2001) and Savin (2005) for instance):

$$\begin{aligned}\sigma_{PP}(\mathbf{k},\mathbf{k}') = \frac{\pi|\mathbf{k}|^2(2\underline{\mu}+\underline{\lambda})}{2\underline{\rho}}\Bigg\{&\frac{\underline{\lambda}^2}{(2\underline{\mu}+\underline{\lambda})^2}S_{\lambda\lambda}(|\mathbf{k}-\mathbf{k}'|) + \frac{4\underline{\lambda}\underline{\mu}}{(2\underline{\mu}+\underline{\lambda})^2}(\hat{\mathbf{k}}\cdot\hat{\mathbf{k}}')^2 S_{\lambda\mu}(|\mathbf{k}-\mathbf{k}'|) \\ &+\frac{4\underline{\mu}^2}{(2\underline{\mu}+\underline{\lambda})^2}(\hat{\mathbf{k}}\cdot\hat{\mathbf{k}}')^4 S_{\mu\mu}(|\mathbf{k}-\mathbf{k}'|) + (\hat{\mathbf{k}}\cdot\hat{\mathbf{k}}')^2 S_{\rho\rho}(|\mathbf{k}-\mathbf{k}'|) \\ +\frac{2\underline{\lambda}}{(2\underline{\mu}+\underline{\lambda})}(\hat{\mathbf{k}}\cdot\hat{\mathbf{k}}')S_{\lambda\rho}(|\mathbf{k}-\mathbf{k}'|) &+ \frac{4\underline{\mu}}{(2\underline{\mu}+\underline{\lambda})}(\hat{\mathbf{k}}\cdot\hat{\mathbf{k}}')^3 S_{\rho\mu}(|\mathbf{k}-\mathbf{k}'|)\Bigg\}.\delta(v_p|\mathbf{k}| - v_p|\mathbf{k}'|)\end{aligned} \tag{1.80}$$

$$\sigma_{PS}(\mathbf{k},\mathbf{k}^{'}) = \frac{\pi\underline{\mu}}{2\underline{\rho}}\Big\{|\mathbf{k}^{'}|^2 S_{\rho\rho}(|\mathbf{k}-\mathbf{k}^{'}|) + 4|\mathbf{k}|^2(\hat{\mathbf{k}}\cdot\hat{\mathbf{k}}')^2 S_{\mu\mu}(|\mathbf{k}-\mathbf{k}^{'}|)$$
$$+4|\mathbf{k}||\mathbf{k}^{'}|(\hat{\mathbf{k}}\cdot\hat{\mathbf{k}}')S_{\mu\rho}(|\mathbf{k}-\mathbf{k}^{'}|)\Big\}\left(1-(\hat{\mathbf{k}}\cdot\hat{\mathbf{k}}')^2\right).\delta(v_s|\mathbf{k}^{'}|-v_p|\mathbf{k}|) \quad (1.81)$$

$$\sigma_{SP}(\mathbf{k},\mathbf{k}^{'}) = \frac{\pi\underline{\mu}}{2\underline{\rho}}\Big\{|\mathbf{k}|^2 S_{\rho\rho}(|\mathbf{k}-\mathbf{k}^{'}|) + 4|\mathbf{k}^{'}|^2(\hat{\mathbf{k}}\cdot\hat{\mathbf{k}}')^2 S_{\mu\mu}(|\mathbf{k}-\mathbf{k}^{'}|) + 4|\mathbf{k}||\mathbf{k}^{'}|(\hat{\mathbf{k}}\cdot\hat{\mathbf{k}}')S_{\mu\rho}(|\mathbf{k}-\mathbf{k}^{'}|)\Big\}$$
$$\left(1-(\hat{\mathbf{k}}\cdot\hat{\mathbf{k}}')^2\right)\begin{bmatrix}\cos^2\phi' & 0\\ 0 & \sin^2\phi'\end{bmatrix}.\delta(v_s|\mathbf{k}|-v_p|\mathbf{k}^{'}|) \quad (1.82)$$

where $S_{ij},\ i,j \in \{\lambda,\mu,\rho\}$ are the power spectra of the underlying random medium and $\underline{\rho}$, $\underline{\mu}$ and $\underline{\lambda}$ denote the respective average values calculated over the random medium. The differential scattering cross-section corresponding to the S-to-S mode conversion σ_{SS} is a 2×2 matrix with the following components (see equation (1.72d)):

$$\sigma_{ss}^{TT}(\mathbf{k},\mathbf{k}^{'}) = \frac{1}{2}\pi v_s^2|\mathbf{k}|^2 S_{\rho\rho}(|\mathbf{k}-\mathbf{k}^{'}|) \quad (1.83a)$$
$$\sigma_{ss}^{\Gamma\Gamma}(\mathbf{k},\mathbf{k}^{'}) = \frac{1}{2}\pi v_s^2|\mathbf{k}|^2 S_{\mu\mu}(|\mathbf{k}-\mathbf{k}^{'}|) \quad (1.83b)$$
$$\sigma_{ss}^{\Gamma T}(\mathbf{k},\mathbf{k}^{'}) = \frac{1}{2}\pi v_s^2|\mathbf{k}|^2 S_{\rho\mu}(|\mathbf{k}-\mathbf{k}^{'}|) \quad (1.83c)$$

Therefore, $\sigma_{SS} = \sigma_{SS}^{TT} + \sigma_{SS}^{\Gamma\Gamma} + \sigma_{SS}^{\Gamma T}$ has the following components:

$$\sigma_{SS}^{TT}(\mathbf{k},\mathbf{k}^{'}) = \frac{1}{2}\pi v_s^2|\mathbf{k}|^2 S_{\rho\rho}(|\mathbf{k}-\mathbf{k}^{'}|).\delta(v_s|\mathbf{k}^{'}|-v_s|\mathbf{k}|)$$
$$\begin{bmatrix}\cos^2\theta'\cos^2\phi'+\sin^2\phi' & \cos\phi'\sin\phi'\left(\cos^2\theta'-1\right)\\ \cos\phi'\sin\phi'\left(\cos^2\theta'-1\right) & \cos^2\theta'\sin^2\phi'+\cos^2\phi'\end{bmatrix} \quad (1.84)$$

$$\sigma_{SS}^{\Gamma\Gamma}(\mathbf{k},\mathbf{k}^{'}) = \frac{1}{2}\pi v_s^2|\mathbf{k}|^2 S_{\mu\mu}(|\mathbf{k}-\mathbf{k}^{'}|).\delta(v_s|\mathbf{k}^{'}|-v_s|\mathbf{k}|)$$
$$\begin{bmatrix}\cos^2\phi'\left(2\cos^2\theta'-1\right)^2+\sin^2\phi'\cos^2\theta' & \sin\phi'\cos\phi'\left(4\cos^4\theta'-5\cos^2\theta'+1\right)\\ \sin\phi'\cos\phi'\left(4\cos^4\theta'-5\cos^2\theta'+1\right) & \sin^2\phi'\left(2\cos^2\theta'-1\right)^2+\cos^2\phi'\cos^2\theta'\end{bmatrix} \quad (1.85)$$

$$\sigma_{SS}^{\Gamma T}(\mathbf{k},\mathbf{k}^{'}) = \pi v_s^2|\mathbf{k}|^2 S_{\rho\mu}(|\mathbf{k}-\mathbf{k}^{'}|).\delta(v_s|\mathbf{k}^{'}|-v_s|\mathbf{k}|)$$
$$\begin{bmatrix}\cos\theta'\left(2\cos^2\theta'-1\right)\cos^2\phi'+\cos\theta'\sin^2\phi' & 2\cos\theta'\left(\cos^2\theta'-1\right)\sin\phi'\cos\phi'\\ 2\cos\theta'\left(\cos^2\theta'-1\right)\sin\phi'\cos\phi' & \cos\theta'\left(2\cos^2\theta'-1\right)\sin^2\phi'+\cos\theta'\cos^2\phi'\end{bmatrix} \quad (1.86)$$

Total scattering cross-sections: Following equation (1.63), the corresponding wave number dependent total scattering cross-sections are defined as:

$$\Sigma_{PP}(|\mathbf{k}|) = \int_{\mathbb{R}^3}\sigma_{PP}(|\mathbf{k}|,|\mathbf{k}'|,\chi)d\mathbf{k}' = \frac{2\pi}{v_p}\int_{-1}^{+1}|\mathbf{k}|^2\sigma_{PP}(|\mathbf{k}|,|\mathbf{k}'|=|\mathbf{k}|,\chi)d\chi \quad (1.87)$$

$$\Sigma_{PS}(|\mathbf{k}|) = \int_{\mathbb{R}^3} \sigma_{PS}(|\mathbf{k}|, |\mathbf{k}'|, \chi) d\mathbf{k}' = \frac{2\pi}{v_s}\left(\frac{v_p}{v_s}\right)^2 \int_{-1}^{+1} |\mathbf{k}|^2 \sigma_{PS}(|\mathbf{k}|, |\mathbf{k}'| = \frac{v_p}{v_s}|\mathbf{k}|, \chi) d\chi \tag{1.88}$$

$$\Sigma_{SP}(|\mathbf{k}|) = \int_{\mathbb{R}^3} \sigma_{SP}(|\mathbf{k}|, |\mathbf{k}'|, \chi, \phi') d\mathbf{k}' = \frac{1}{v_p}\left(\frac{v_s}{v_p}\right)^2 \int_{-1}^{+1}\int_0^{2\pi} |\mathbf{k}|^2 \sigma_{SP}(|\mathbf{k}|, |\mathbf{k}'| = \frac{v_s}{v_p}|\mathbf{k}|, \chi, \phi') d\phi' d\chi \tag{1.89}$$

$$\Sigma_{SS}(|\mathbf{k}|) = \int_{\mathbb{R}^3} \sigma_{SS}(|\mathbf{k}|, |\mathbf{k}'|, \chi, \phi') d\mathbf{k}' = \frac{1}{v_s}\int_{-1}^{+1}\int_0^{2\pi} |\mathbf{k}|^2 \sigma_{SS}(|\mathbf{k}|, |\mathbf{k}'| = |\mathbf{k}|, \chi, \phi') d\phi' d\chi \tag{1.90}$$

Integrating equations (1.80), (1.81), (1.82) and (1.84) to (1.86) respectively using equations (1.87), (1.88), (1.89) and (1.90) gives:

$$\Sigma_{PP}(|\mathbf{k}|) = \int_{-1}^{+1} \frac{\pi^2|\mathbf{k}|^4\sqrt{2\underline{\mu}+\underline{\lambda}}}{\sqrt{\underline{\rho}}} \left\{ \frac{\underline{\lambda}^2}{(2\underline{\mu}+\underline{\lambda})^2} S_{\lambda\lambda}(a) + \frac{4\underline{\lambda}\underline{\mu}}{(2\underline{\mu}+\underline{\lambda})^2}\chi^2 S_{\lambda\mu}(a) + \frac{4\underline{\mu}^2}{(2\underline{\mu}+\underline{\lambda})^2}\chi^4 S_{\mu\mu}(a) \right.$$
$$\left. + \chi^2 S_{\rho\rho}(a) + \frac{2\underline{\lambda}}{(2\underline{\mu}+\underline{\lambda})}\chi S_{\lambda\rho}(a) + \frac{4\underline{\mu}}{(2\underline{\mu}+\underline{\lambda})}\chi^3 S_{\rho\mu}(a) \right\} d\chi \tag{1.91}$$

$$\Sigma_{PS}(|\mathbf{k}|) = \int_{-1}^{+1} \frac{\pi^2(2\underline{\mu}+\underline{\lambda})}{\sqrt{\underline{\rho}}\sqrt{\underline{\mu}}}|\mathbf{k}|^4 \left\{ \frac{2\underline{\mu}+\underline{\lambda}}{\underline{\mu}} S_{\rho\rho}(b) + 4\chi^2 S_{\mu\mu}(b) + 4\sqrt{\frac{2\underline{\mu}+\underline{\lambda}}{\underline{\mu}}}\chi S_{\mu\rho}(b) \right\} \left(1-\chi^2\right) d\chi \tag{1.92}$$

$$\Sigma_{SP}(|\mathbf{k}|) = \int_{-1}^{+1} \frac{\pi^2\underline{\mu}^2}{2\sqrt{\underline{\rho}}\sqrt{(2\underline{\mu}+\underline{\lambda})^3}}|\mathbf{k}|^4 \left\{ S_{\rho\rho}(c) + \frac{4\underline{\mu}}{2\underline{\mu}+\underline{\lambda}}\chi^2 S_{\mu\mu}(c) \right.$$
$$\left. + 4\sqrt{\frac{\underline{\mu}}{2\underline{\mu}+\underline{\lambda}}}\chi S_{\mu\rho}(c) \right\} \begin{bmatrix} 1 & 0 \\ 0 & 1 \end{bmatrix} \left(1-\chi^2\right) d\chi \tag{1.93}$$

$$\Sigma_{SS}(|\mathbf{k}|) = \int_{-1}^{+1} \frac{\pi^2 v_s}{2}|\mathbf{k}|^4 S_{\rho\rho}(a) \begin{bmatrix} \chi^2+1 & 0 \\ 0 & \chi^2+1 \end{bmatrix} d\chi$$
$$+ \int_{-1}^{+1} \frac{\pi^2 v_s}{2}|\mathbf{k}|^4 S_{\mu\mu}(a) \begin{bmatrix} 4\chi^4-3\chi^2+1 & 0 \\ 0 & 4\chi^4-3\chi^2+1 \end{bmatrix} d\chi$$
$$+ \int_{-1}^{+1} \pi^2 v_s |\mathbf{k}|^4 S_{\rho\mu}(a) \begin{bmatrix} 2\chi^3 & 0 \\ 0 & 2\chi^3 \end{bmatrix} d\chi \tag{1.94}$$

in which:

$$a = |\mathbf{k}|\sqrt{2(1-\chi)}\ ;\ b = |\mathbf{k}|\sqrt{1+\frac{2\underline{\mu}+\underline{\lambda}}{\underline{\mu}} - 2\sqrt{\frac{2\underline{\mu}+\underline{\lambda}}{\underline{\mu}}}\chi}\ ;\ c = |\mathbf{k}|\sqrt{1+\frac{\underline{\mu}}{2\underline{\mu}+\underline{\lambda}} - 2\sqrt{\frac{\underline{\mu}}{2\underline{\mu}+\underline{\lambda}}}\chi} \tag{1.95}$$

The comparison of equations (1.92) and (1.93) shows that:

$$\frac{\Sigma_{SP}(\frac{v_p}{v_s}|\mathbf{k}|)}{\Sigma_{PS}(|\mathbf{k}|)} = \frac{1}{2}\left(\frac{v_s}{v_p}\right)^3 \tag{1.96}$$

in which $\Sigma_{SP}(\frac{v_p}{v_s}|\mathbf{k}|)$ is considered to be any of the diagonal entries of the corresponding matrix.

Forward scattering cross-sections: A direct result from equations (1.80), (1.81), (1.82) and (1.83) is that the scattering of elastic waves is intrinsically anisotropic and the angle dependence of the differential scattering cross-sections even in low-frequencies is inevitable (Turner, 1998). Another parameter relevant to the description of scattering preference is called the forward scattering cross-section, which is defined as the integral of the differential scattering cross-section weighted by the cosine of the scattering angle. Thus, it characterizes the degree of scattering in forward direction. Its value can be negative, zero or positive respectively for backward, non-preferential (but not necessarily isotropic) and forward scattering (Trégourès and van Tiggelen, 2002):

$$\Sigma'_{ij}(\mathbf{k}) = \int_{\mathrm{R}^3} (\hat{\mathbf{k}} \cdot \hat{\mathbf{k}}')\sigma_{ij}(\mathbf{k}, \mathbf{k}')d\mathbf{k}', \ i, j \in \{P, S\} \tag{1.97}$$

We will see further in Section 1.5 that this quantity appears to describe the parameters in a diffusion regime.

Scattering mean free time (path): The attenuation of the wave energy is due to: 1) the scattering effects due to the random heterogeneities and 2) the inelastic absorption resulting from the dissipative nature of the underlying medium. Neglecting the effects of dissipation and dividing both sides of the equations 1.67 and 1.68 respectively by $\Sigma_P = \Sigma_{PP} + \Sigma_{PS}$ and $\Sigma_S = \Sigma_{SS} + \Sigma_{SP}$, two terms appear that have units of time. These quantities are called respectively the scattering mean free time of the P and S waves. In the context of the elastic waves propagating in continuous random media, the scattering mean free time (path) is defined as the time (path) during which the scattering of the waves is effective. In the case of scalar waves propagating in discrete random media, this quantity describes the average distance traveled by the waves without being scattered. For elastic waves, the scattering mean free paths and times relative to each of the wave modes are related via the corresponding phase velocity when the background is homogeneous (see Savin (2005) for instance). We can define:

$$\tau_P(\mathbf{k}) = \frac{1}{\Sigma_{PP}(\mathbf{k}) + \Sigma_{PS}(\mathbf{k})} \Rightarrow \ell_P(\mathbf{k}) = \tau_P(\mathbf{k})v_p \tag{1.98}$$

and

$$\tau_S(\mathbf{k}) = \frac{1}{\Sigma_{SS}(\mathbf{k}) + \Sigma_{SP}(\mathbf{k})} \Rightarrow \ell_S(\mathbf{k}) = \tau_S(\mathbf{k})v_s \tag{1.99}$$

In the following section, the diffusion regime will be discussed as the limit of a transport regime at long lapse times.

1.5 Diffusion regime

In a strongly scattering medium, after long propagation paths, the energy propagation of the multiply scattered waves can be described by a simplified version of the RTEs, the so-called diffusion

equation. A diffusive regime establishes when (1) the energy radiation is almost isotropic and (2) energy between P and S waves is equipartitioned. The latter one is in general less stringent than the first condition (Margerin, 2013). When only the second condition is satisfied, an equipartition regime has set in. The transport mean free time (path) of the waves $\tau^*(l^*)$, is the typical time (distance) beyond which the waves will forget all their information about the source(s) or the initial conditions. As a result, for the propagation times (distances) greater than $\tau^*(l^*)$, the direction of propagation of the waves becomes independent of the direction of the initial pulse and the S waves become depolarized. These are some of the fundamental characteristics of the diffusion regime, which is an asymptotic limit of the transport equations. In this regime, the energy density of each mode will become independent of the propagation direction $\mathbf{k}$, and will satisfy a scalar diffusion equation which is identical to the heat conduction equation in thermal processes. For elastic waves, the energy density of P and S waves in each point $\mathbf{x}$ and at any time t are defined as the 3D integral of the corresponding directional energy densities:

$$\mathcal{E}_p(t,\mathbf{x}) = \int_{\mathbb{R}^3} a^p(t,\mathbf{x},\mathbf{k})d\mathbf{k}; \quad \mathcal{E}_s(t,\mathbf{x}) = \int_{\mathbb{R}^3} \mathrm{Tr}[a^s(t,\mathbf{x},\mathbf{k})]d\mathbf{k} \tag{1.100}$$

In diffusion regime, the energy densities in phase space will be independent of the wave vectors, therefore:

$$a^p(t,\mathbf{x},\mathbf{k}) \sim \alpha(t,\mathbf{x},|\mathbf{k}|); \quad [a^s(t,\mathbf{x},\mathbf{k}')] \sim \beta(t,\mathbf{x},|\mathbf{k}'|)\mathbf{I}_2 \tag{1.101}$$

where $\mathbf{I}_2$ is a 2×2 identity matrix and It can be shown that the scalar function $\phi(t,\mathbf{x},|\mathbf{k}|) = \alpha(t,\mathbf{x},|\mathbf{k}|) = \beta(t,\mathbf{x},|\mathbf{k}|v_p/v_s)$ satisfies the following so called diffusion equation:

$$\frac{\partial\phi}{\partial t} = \nabla_{\mathbf{x}}.[D\nabla_{\mathbf{x}}\phi] \tag{1.102}$$

which is characterized by a so called diffusion constant or diffusivity D that determines the degree of the scattering process. That is to say that lower values of D correspond to a highly scattering medium and *vice versa*.

Now if we consider an incident P wave with wave vector $\mathbf{k}$ and a scattered S wave with wave vector $\mathbf{k}'$, since the local frequency remains always constant during the scattering events, *i.e.* $v_p|\mathbf{k}| = v_s|\mathbf{k}'|$, in equilibrium (*i.e.* when an equipartitioning regime sets in) we will have $\alpha(t,\mathbf{x},|\mathbf{k}|) = \beta(t,\mathbf{x},|\mathbf{k}|v_p/v_s)$. Integrating both sides of this equation over $\mathbf{k}$ will give us the following equipartitioning law (Weaver (1982, 1990), Papanicolaou et al. (1996), Ryzhik et al. (1996), Turner (1998), Margerin (2013)):

$$\lim_{t>\tau^*} \frac{\mathcal{E}_s(t,\mathbf{x})}{\mathcal{E}_p(t,\mathbf{x})} = 2K^3 = \frac{2v_p^3}{v_s^3} \simeq 2\left(2+\frac{\underline{\lambda}}{\underline{\mu}}\right)^3 \tag{1.103}$$

which is true for times larger than the typical transport mean free time. As a result, on the one hand, each of the energies $\mathcal{E}_p$ and $\mathcal{E}_s$ are individually related to the statistical properties of the medium through the scalar diffusion equation and on the other hand, the ratio $\mathcal{E}_s/\mathcal{E}_p$ is directly related to the first order statistics of Lamé parameters. The equipartition law was first derived by Weaver (1982) by counting the number of normal wave modes. Weaver (1990), Ryzhik et al. (1996) and Papanicolaou et al. (1996) then derived mathematically, based on the transport theory of elastic waves, the law of energy partitioning between P and S wave energy densities. Margerin et al. (2001) studied the effect of anelastic absorption on the equipartitioning of elastic waves.

They found that even in dissipative media, in the coda part of the seismograms, the energies are equipartitioned between P and S waves with a slight modification which rarely differs by more than 15% from the ratio predicted in full elastic media (equation 1.103). Shapiro et al. (2000) observed the energy partitioning in the seismic coda of high-frequency local earthquakes in Mexico with the measurements of the curl and divergence parts of the ground displacement. Thus, according to the equation 1.103, at large lapse times the energy density ratio depends only upon the ratio between the mean phase velocities K and not on the details of the multiple scattering neither the source or initial conditions. For Poissonian materials, $\mathcal{E}_s/\mathcal{E}_p \simeq 10.4$ which highlights the fact that the S waves are dominant in diffusion. This dominance was observed by Aki (1992), using the analysis of the seismological data.

The transport mean free paths of P and S waves are defined as distances that are required for each wave type to travel in order to be in a diffusion regime. Derivations of the elastic diffusion equation results in the following equations for these quantities (Margerin, 2006):

$$\ell_P^*(\mathbf{k}) = \frac{v_p(\Sigma_{SS} + \Sigma_{SP} - \Sigma'_{SS}) + v_s\Sigma'_{PS}}{(\Sigma_{PP} + \Sigma_{PS} - \Sigma'_{PP})(\Sigma_{SS} + \Sigma_{SP} - \Sigma'_{SS}) - \Sigma'_{PS}\Sigma'_{SP}} \tag{1.104}$$

and

$$\ell_S^*(\mathbf{k}) = \frac{v_s(\Sigma_{PP} + \Sigma_{PS} - \Sigma'_{PP}) + v_p\Sigma'_{SP}}{(\Sigma_{PP} + \Sigma_{PS} - \Sigma'_{PP})(\Sigma_{SS} + \Sigma_{SP} - \Sigma'_{SS}) - \Sigma'_{PS}\Sigma'_{SP}} \tag{1.105}$$

The elastic diffusivity in equation (1.102) is a weighted average of the diffusion coefficients of individual P and S wave modes, *i.e.* $D_P(\mathbf{k}) = \frac{v_p\ell_P^*(\mathbf{k})}{3}$ and $D_S(\mathbf{k}) = \frac{v_s\ell_S^*(\mathbf{k})}{3}$):

$$D(\mathbf{k}) = \frac{1}{1+2K^3}(D_P(\mathbf{k}) + 2K^3 D_S(\mathbf{k})) = \frac{1}{1+2K^3}\left[\frac{v_p\ell_P^*(\mathbf{k})}{3} + 2K^3\frac{v_s\ell_S^*(\mathbf{k})}{3}\right] \tag{1.106}$$

in which the weights are determined using the equipartition equation $\mathcal{E}_s = 2K^3\mathcal{E}_p$.

The separation of the elastic energy density ϕ into the P and S wave energy densities ($\mathcal{E}_p$ and $\mathcal{E}_s$) cannot be done directly in equation (1.102) (Papanicolaou et al., 1996). However, in discrete random media with spherically symmetric scatterers, Trégourès and van Tiggelen (2002) derived a sophisticated form of the diffusion equation as a coupled system of equation for P and S wave energy densities:

$$\frac{\partial}{\partial t}\begin{pmatrix}\mathcal{E}_p(t,\mathbf{x})\\ \mathcal{E}_s(t,\mathbf{x})\end{pmatrix} - D_T.\Delta_{\mathbf{x}}\begin{pmatrix}\mathcal{E}_p(t,\mathbf{x})\\ \mathcal{E}_s(t,\mathbf{x})\end{pmatrix} = -J.\begin{pmatrix}\mathcal{E}_p(t,\mathbf{x})\\ \mathcal{E}_s(t,\mathbf{x})\end{pmatrix} \tag{1.107}$$

where D_T and J are respectively the matrix of elastic diffusivity and the collision matrix defined as:

$$D_T = \frac{1}{3\left((\Sigma_{PP} + \Sigma_{PS} - \Sigma'_{PP})(\Sigma_{SS} + \Sigma_{SP} - \Sigma'_{SS}) + \Sigma'_{PS}\Sigma'_{SP}\right)} \begin{bmatrix} v_p^2(\Sigma_{SS} + \Sigma_{SP} - \Sigma'_{SS}) & v_pv_s\Sigma'_{PS} \\ v_pv_s\Sigma'_{SP} & v_s^2(\Sigma_{PP} + \Sigma_{PS} - \Sigma'_{PP}) \end{bmatrix} \tag{1.108}$$

and

$$J = \Sigma_{PS}\begin{pmatrix}1 & -\frac{1}{K^3}\\ -1 & \frac{1}{K^3}\end{pmatrix} \tag{1.109}$$

The solution of the equation (1.107) in an unbounded medium shows an exponential decay of the P and S wave energy densities toward the steady-state solution with the same rate. This decay rate is called the global stabilization (equipartition) time τ_{eq} and is defined as the time needed to reach the global equipartiton:

$$\tau_{eq}(\mathbf{k}) = \frac{1}{\Sigma_{PS}(\mathbf{k}) + \Sigma_{SP}(\mathbf{k})} = \frac{1}{\Sigma_{PS}(\mathbf{k})\left(1 + \frac{1}{2K^3}\right)} \tag{1.110}$$

1.6 Summary and Conclusion

This chapter addressed the problem of the elastic wave propagation in randomly heterogeneous media with locally isotropic material behavior. The concept of wave scattering in random media is then introduced and the equations governing the mean wave energy densities in phase space are derived following Ryzhik et al. (1996). The demonstrations are done only for acoustic waves just for the sake of simplicity and the extension to the elastic waves is discussed. These transport equations are characterized by the so-called scattering cross-sections which are functions of the statistics of the underlying random medium. In the next chapter we will discuss in detail about the scattering parameters and specifically we will focus on the assessment of the influence of the correlation kernel of the random medium on the scattering parameters.

Chapter 2

Influence of the spatial correlation structure of an elastic random medium on its scattering properties

A correlation model is parameterized in general by a variance and a correlation length. The variance indicates an order of magnitude of the strength of the fluctuations and the correlation length an order of magnitude of the distance over which the field fluctuates significantly. However, these two numbers are not sufficient to describe completely a correlation model. Depending on the application, it is not clear when higher order moments have a significant impact on the wave behavior. The main objective of this chapter is to try and clarify this aspect. We therefore introduce several classical correlation structures (exponential, power-law, Gaussian, triangular and low-pass white noise) and study the impact of the structure on several parameters in the weakly heterogeneous scattering regime (scattering cross-sections, diffusion parameters). This impact is studied independently of the variance and correlation length, in order to compare the relative influences. The asymptotic behavior of the mentioned parameters will be also investigated.

2.1 Normalizations of parameters

The objective of this section is to normalize all scattering parameters which have been introduced in chapter 1 and represent them in terms of some adimensional parameters.

2.1.1 Phase velocity contrast parameter K

We will see further down that one of the most relevant mechanical parameter for our study is the ratio between the space-averaged values of the phase velocities defined as:

$$K = \frac{v_p}{v_s} \simeq \sqrt{2 + \frac{\underline{\lambda}}{\underline{\mu}}} \tag{2.1}$$

Guilleminot and Soize (2013) have investigated the statistical dependence of different components of the random elastic matrix using the maximum entropy principle. They have shown that for isotropic materials, the bulk and shear moduli $(\kappa(\mathbf{x}), \mu(\mathbf{x}))$ can be modeled as independent, Gamma-distributed random variables. As a result, instead of considering Lamé coefficients $(\lambda(\mathbf{x}), \mu(\mathbf{x}))$, the bulk and shear moduli are considered as two independent random fields with

Gamma distribution (see Appendix C). In this case, K can be rewritten as $\sqrt{4/3+\underline{\kappa}/\underline{\mu}}$. We define the local phase velocity ratio random field as:

$$K_\delta(\mathbf{x}) = \sqrt{\frac{4}{3} + \frac{\kappa(\mathbf{x})}{\mu(\mathbf{x})}} \tag{2.2}$$

For the sake of simplicity, the coefficients of variation of $\kappa(\mathbf{x})$ and $\mu(\mathbf{x})$ are considered to be the same, *i.e.* $\delta_\kappa = \delta_\mu = \delta$. Let $\kappa(\mathbf{x})$ and $\mu(\mathbf{x})$ be two independent Gamma random variables with parameters $(\theta_\kappa, \alpha_\kappa = 1/\delta^2)$ and $(\theta_\mu, \alpha_\mu = 1/\delta^2)$, it can be shown that the random variable $R(\mathbf{x}) = \kappa(\mathbf{x})/\mu(\mathbf{x})$ follows a beta distribution of the second kind with the following probability density:

$$f_R(r) = \frac{1}{\left(\frac{\theta_\kappa}{\theta_\mu}\right)^{\frac{1}{2\delta^2}} \mathrm{B}(\frac{1}{2\delta^2}, \frac{1}{2\delta^2})} \frac{r^{\frac{1}{2\delta^2}-1}}{\left(1+\frac{r}{\frac{\theta_\kappa}{\theta_\mu}}\right)^{\frac{2}{\delta^2}}} \mathrm{H}(r) \tag{2.3}$$

in which H and B are respectively the Heaviside and the beta function. The latter is defined as:

$$\mathrm{B}(\alpha, \beta) = \int_0^1 p^{\alpha-1}(1-p)^{\beta-1} \mathrm{d}p \tag{2.4}$$

Since $\theta_\kappa/\theta_\mu = \underline{\kappa}/\underline{\mu}$, a first-order approximation for the mean value and standard deviation of R can be evaluated respectively using $\underline{R} = \frac{1}{1-\delta^2}\frac{\underline{\kappa}}{\underline{\mu}}$ and $\sigma_R = \frac{(2-\delta^2)\delta^2}{(1-2\delta^2)(1-\delta^2)}\frac{\underline{\kappa}}{\underline{\mu}}$. Using some frequently-used values in geological media, *i.e.* $\underline{\mu} = 2\times10^9$ Pa, $\underline{\kappa} = 3.3191\times10^9$ Pa and $\delta = 0.25$, we get $\underline{R} = 1.77$ and $\sigma_R = 0.26$. Hence, the first-order approximation for the mean value and standard deviation of K will be respectively $\underline{K_\delta} = \sqrt{4/3+\underline{R}} = 1.76$ and $\sigma_{K_\delta} = \frac{\sigma_R}{2\sqrt{4/3+\underline{R}}} = 0.07$. As a result, the spatial variation of $K_\delta(\mathbf{x})$ can be approximately neglected. In geological media, the isotropic elastic material is frequently considered as a Poisson solid whose Lamé parameters are equal ($\underline{\lambda} = \underline{\mu}$), so that $K = \sqrt{3}$ will be used as a reference value in this study. Based on seismological data, the values of K for the upper mantle range between 1.65 and 1.8. In laboratory tests under pertinent pressure and temperature conditions for the geological layers, its values range between 1.7 and 2.3 (Sato, 1984). Note that the theoretical minimum of K is $\sqrt{4/3} \simeq 1.16$. This value ensures that the bulk modulus is positive but corresponds to a negative value of λ. In the next section, we briefly remind the definitions of the normalized ACF and PSDF along with some basic hypotheses made about them.

2.1.2 Random model of the mechanical parameters

Since the statistics of the Lamé parameters appear in transport equations of elastic waves rather than that of $(\kappa(\mathbf{x}), \mu(\mathbf{x}))$, a random description of the pair of random fields $(\lambda(\mathbf{x}), \mu(\mathbf{x}))$ will be considered. As before, we model them as second-order homogeneous random fields and specify their mean values $\underline{\lambda}$ and $\underline{\mu}$, autocorrelation functions (ACF) $\mathrm{R}_\lambda(\mathbf{x}-\mathbf{x}') = \mathbb{E}[(\lambda(\mathbf{x})-\underline{\lambda})(\lambda(\mathbf{x}')-\underline{\lambda})]$ and $\mathrm{R}_\mu(\mathbf{x}-\mathbf{x}') = \mathbb{E}[(\mu(\mathbf{x})-\underline{\mu})(\mu(\mathbf{x}')-\underline{\mu})]$, and cross-correlation function $\mathrm{R}_{\lambda\mu}(\mathbf{x}-\mathbf{x}') = \mathbb{E}[(\lambda(\mathbf{x})-\underline{\lambda})(\mu(\mathbf{x}')-\underline{\mu})]$. When the auto/cross-correlation functions R_κ, R_μ and $\mathrm{R}_{\kappa\mu}$ are defined, the calculation of the corresponding functions R_λ, R_μ and $\mathrm{R}_{\lambda\mu}$ is straightforward. For instance, the cross-correlation function $\mathrm{R}_{\lambda\mu}$ can be calculated via:

$$\mathrm{R}_{\lambda\mu}(\tau) = \frac{\sigma_\kappa^2 \mathrm{R}_\kappa(\tau) + \frac{4}{9}\sigma_\mu^2 \mathrm{R}_\mu(\tau)}{\sigma_\kappa^2 + \frac{4}{9}\sigma_\mu^2} \tag{2.5}$$

These models of correlation functions $\mathrm{R}(r)$ are usually introduced after normalization by the variance $\sigma^2 = \mathrm{R}(0)$ and the correlation length ℓ_c is defined as in (1.36) of chapter 1. Assuming that the correlation function is a function of the ratio between the lag distance r and the correlation length ℓ_c, *i.e.* $R(r;\ell_c) = R(r/\ell_c)$, we define the non-dimensional correlation function as:

$$\hat{\mathrm{R}}(\eta) = \frac{\mathrm{R}(\frac{r}{\ell_c})}{\sigma^2} \tag{2.6}$$

Note that the values of $\hat{\mathrm{R}}(\eta)$ theoretically belong to the interval $[-1, +1]$. For the simplicity of the presentation, we will consider from now on that all the correlation lengths are the same:

$$\frac{2}{\sigma_\lambda^2}\int_{\mathbb{R}^+} \mathrm{R}_\lambda(r)\,dr = \frac{2}{\sigma_\mu^2}\int_{\mathbb{R}^+} \mathrm{R}_\mu(r)\,dr = \frac{2}{\sigma_\lambda\sigma_\mu\rho_{\lambda\mu}}\int_{\mathbb{R}^+} \mathrm{R}_{\lambda\mu}(r)\,dr \equiv \ell_c, \tag{2.7}$$

as well as the normalized correlation functions:

$$\hat{\mathrm{R}}_\lambda(\eta) = \hat{\mathrm{R}}_\mu(\eta) = \hat{\mathrm{R}}_{\lambda\mu}(\eta) \equiv \hat{\mathrm{R}}(\eta) \tag{2.8}$$

The different correlation models therefore only differ through the variances $\sigma_\lambda^2 = \mathrm{R}_\lambda(0)$ and $\sigma_\mu^2 = \mathrm{R}_\mu(0)$ and the correlation coefficient $\rho_{\lambda\mu} = \mathrm{R}_{\lambda\mu}(0)/(\sigma_\lambda\sigma_\mu)$. Finally, we introduce the normalized power spectral density function (PSDF) $\Phi(\zeta)$ as the Fourier transform of $\hat{\mathrm{R}}(\eta)$. We consider the classical definition of the Fourier transform in spherical coordinates for isotropic functions in 3D:

$$\Phi(\zeta) = \frac{1}{2\pi^2}\int_{\mathbb{R}^+} \mathrm{sinc}(\zeta\eta)\,\eta^2\hat{R}(\eta)d\eta. \tag{2.9}$$

Note that the value of the PSDF at origin is related to the second order central moment of the non-dimensional correlation function:

$$\Phi(0) = \frac{1}{2\pi^2}\int_{\mathbb{R}^+} \eta^2\hat{R}(\eta)d\eta \tag{2.10}$$

and that the first central moment of the PSDF is related to the zeroth order central moment of the non-dimensional correlation function which is constant considering the definition of the correlation length:

$$\int_{\mathbb{R}^+} \zeta\Phi(\zeta)\;d\zeta = \frac{1}{2\pi^2}\int_{\mathbb{R}^+} \hat{R}(\eta)\;d\eta = \frac{1}{4\pi^2} \tag{2.11}$$

These last two properties will be used to investigate the asymptotic behavior of the scattering properties of the random medium throughout this chapter.

Although the effect of density variations has been shown to be influential on the attenuation of wave energy and therefore on its propagation regime (Turner and Anugonda, 2001), we neglect it here because these fluctuations are small in the geophysical media that we are interested in (Sato et al., 2012). Therefore we have:

$$\Phi_\rho = \Phi_{\rho\lambda} = \Phi_{\rho\mu} = 0 \tag{2.12}$$

Since no information is available about the power spectral densities, different assumptions can be made in order to simplify the analytical formulas in the theory of elastic wave scattering. For example Turner (1998) used the following assumption:

$$\underline{\lambda}^2\Phi_\lambda = \underline{\mu}^2\Phi_\mu = \underline{\lambda}\underline{\mu}\Phi_{\lambda\mu} \tag{2.13}$$

In this work, we assume factorizable power spectral density functions which results from the assumption that we have made in equation (2.8):

$$\Phi_\lambda = \Phi_\mu = \Phi_{\lambda\mu} \equiv \Phi \tag{2.14}$$

Obviously for the Poissonian materials ($\underline{\lambda} = \underline{\mu}$) these two assumptions are equivalent.

2.1.3 Classical correlation models

We now introduce several models of correlation that have been used in geophysics Klimeš (2002). First of all, the family of exponential correlation models with a general form as $e^{-t(x/\ell_c)^{2\alpha}}$ is considered in which t is a constant which is determined from the normalization condition and α describes the smoothness of the random field. Larger values of α correspond to smoother random fields. The models corresponding to $\alpha = 0.5$ or $\alpha = 1$ are of special interest, which are respectively called the exponential and squared exponential or Gaussian correlation models. The exponential correlation function has been used in Frankel and Clayton (1986) to explain observations of both seismic wave scattering and travel-time variations. This correlation function as well as its PSDF are:

$$\hat{R}(\eta) = \exp(-2\eta) \tag{2.15a}$$

$$\Phi(\zeta) = \frac{1}{8\pi^2\left(1 + \frac{\zeta^2}{4}\right)^2} \tag{2.15b}$$

For large wave numbers, the Gaussian correlation function tends to zero faster than exponential model so that it has a lower high-frequency content. Both the correlation function and the corresponding PSDF have a Gaussian functional form:

$$\hat{R}(\eta) = \exp(-\pi\eta^2) \tag{2.16a}$$

$$\Phi(\zeta) = \frac{1}{8\pi^3}\exp\left(-\frac{\zeta^2}{4\pi}\right) \tag{2.16b}$$

The next correlation function is called the low-pass white noise and has a constant PSDF with an upper frequency limit beyond which it vanishes. Thanks to the boundedness of the support of the PSDF of this model, it will be interesting in our numerical simulations because the discretization error in the wave number domain will be decreased (Ta et al., 2010). The corresponding random field will also be smooth because of the complete suppression of the high frequency content. This model can be written as:

$$\hat{R}(\eta) = \frac{3\left(\sin\left(\frac{3\pi}{2}\eta\right) - \frac{3\pi}{2}\eta\cos\left(\frac{3\pi}{2}\eta\right)\right)}{\left(\frac{3\pi}{2}\eta\right)^3} \tag{2.17a}$$

$$\Phi(\zeta) = \frac{2}{9\pi^4}\mathrm{H}\left(\frac{3\pi}{2} - \zeta\right) \tag{2.17b}$$

Another correlation function whose PSDF has a linearly decreasing form with an upper frequency limit is called the triangular model (see Ta et al. (2010), Soize (2000)). It has therefore the

same numerical advantages as the media with low-pass white noise PSDF. This model is formulated as:

$$\hat{R}(\eta) = \frac{12\left(2 - 2\cos(2\pi\eta) - (2\pi\eta)\sin(2\pi\eta)\right)}{(2\pi\eta)^4} \tag{2.18a}$$

$$\Phi(\zeta) = \frac{3}{8\pi^4}\left(1 - \frac{\zeta}{2\pi}\right)\mathrm{H}\left(2\pi - \zeta\right) \tag{2.18b}$$

A fundamental difference between this model and the flat correlation model is that in this model the derivative of the PSDF at the origin is not equal to zero. We will see further in this chapter that some of the factors that describe the influence of the correlation kernel on the scattering parameters are the values of $\Phi(0)$ and $\Phi'(0)$.

Finally, a so-called power-law model is introduced:

$$\hat{R}(\eta) = \frac{1}{\left(1 + \frac{\pi^2\eta^2}{4}\right)^2} \tag{2.19a}$$

$$\Phi(\zeta) = \frac{1}{\pi^4}\exp\left(-2\frac{\zeta}{\pi}\right) \tag{2.19b}$$

Table 2.1 summarizes these models in their non-dimensional form, that is to say such that $\hat{\mathrm{R}}(0) = 1$ and $2\int_{\mathbb{R}^+}\hat{\mathrm{R}}(\eta)d\eta = 1$. The ACF and PSDF for these models are drawn in Figure 2.1. One realization of a centered unit Gaussian random field with each of the correlation models is also plotted in Figure 2.2 to give an idea of the difference of texture that these correlation models imply.

Correlation model	Normalized ACF $\hat{R}(\eta)$	Normalized PSDF $\Phi(\zeta)$
Exponential	$\exp(-2\eta)$	$\frac{1}{8\pi^2\left(1+\frac{\zeta^2}{4}\right)^2}$
Power-law	$\frac{1}{\left(1+\frac{\pi^2\eta^2}{4}\right)^2}$	$\frac{1}{\pi^4}\exp\left(-2\frac{\zeta}{\pi}\right)$
Gaussian	$\exp(-\pi\eta^2)$	$\frac{1}{8\pi^3}\exp\left(-\frac{\zeta^2}{4\pi}\right)$
Triangular	$\frac{12(2-2\cos(2\pi\eta)-(2\pi\eta)\sin(2\pi\eta))}{(2\pi\eta)^4}$	$\frac{3}{8\pi^4}\left(1-\frac{\zeta}{2\pi}\right)\mathrm{H}\left(2\pi-\zeta\right)$
Low-pass white noise	$\frac{3\left(\sin\left(\frac{3\pi}{2}\eta\right)-\frac{3\pi}{2}\eta\cos\left(\frac{3\pi}{2}\eta\right)\right)}{\left(\frac{3\pi}{2}\eta\right)^3}$	$\frac{2}{9\pi^4}\mathrm{H}\left(\frac{3\pi}{2}-\zeta\right)$

Table 2.1: Definitions of the normalized correlation models.

Note that all the correlations models, except the exponential one, have a vanishing initial slope $\partial\hat{\mathrm{R}}/\partial\eta(\eta = 0) = 0$. This means that they all correspond to random fields that have almost surely continuous trajectories. The exponential correlation corresponds to random fields that are only mean-square continuous.

2.1.4 Normalization of differential scattering cross-section

In transport equations (1.67) and (1.68), one can parameterize the differential scattering operators as functions of $|\mathbf{k}|$ and the two angles $\theta = \cos^{-1}(\hat{\mathbf{k}}\cdot\hat{\mathbf{k}'})$ (or scattering angle) and $\phi = \cos^{-1}(\mathbf{z}^{(2)}(\hat{\mathbf{k}})\cdot$

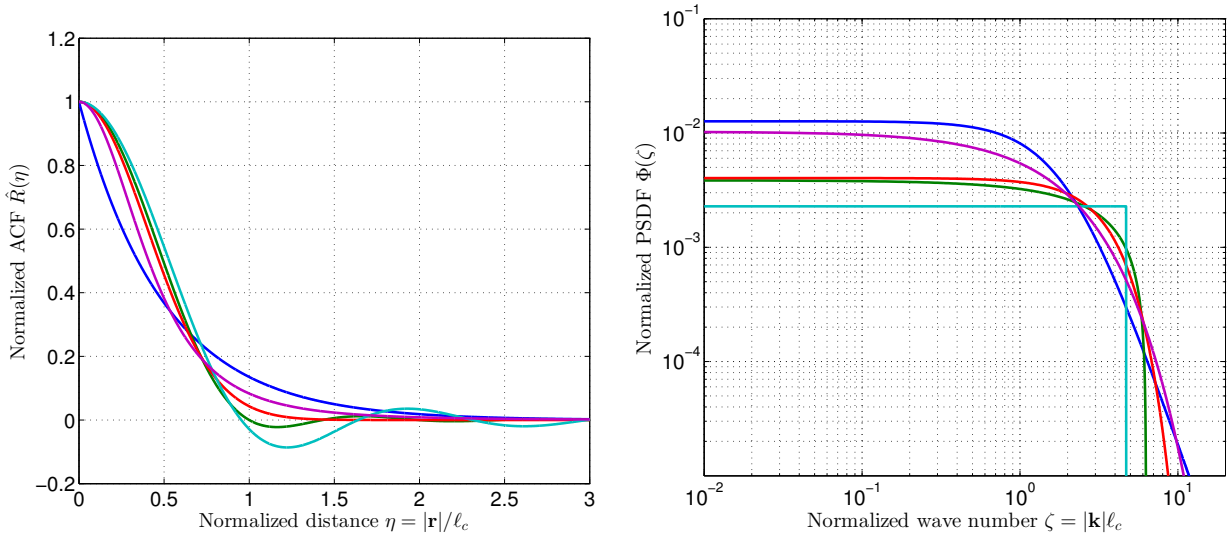

(a) (b)

Figure 2.1: Classical correlation functions (left figure) and corresponding power spectral densities (right figure), as described in Table 2.1: exponential (blue), power-law (purple), Gaussian (red), triangular (green) and low-pass white noise (cyan).

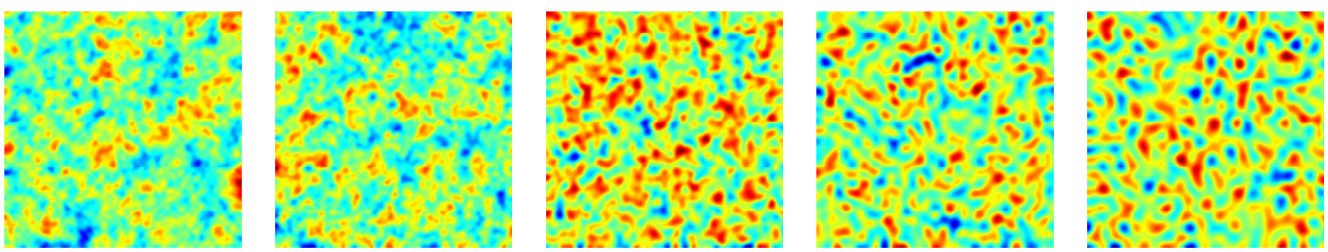

(a) (b) (c) (d) (e)

Figure 2.2: One realization of a centered unit Gaussian random field with different correlation models: (a) exponential, (b) power-law, (c) Gaussian, (d) triangular, and (e) low-pass white noise. The images are $L \times L$, where $L = 20\ell_c$ and ℓ_c is the correlation length.

$\mathbf{z}^{(2)}(\hat{\mathbf{k}}')$) of the spherical representation of $\mathbf{k}' - \mathbf{k}$:

$$\sigma_{\mathrm{PP}}(\mathbf{k},\mathbf{k}')[a^p(\mathbf{k}')] = \frac{\pi}{2} v_p \ell_c \overline{\sigma}_{pp}(|\mathbf{k}|\ell_c, \theta)\; a^p(\mathbf{k}')\; \delta(|\mathbf{k}| - |\mathbf{k}'|) \tag{2.20}$$

$$\sigma_{\mathrm{SP}}(\mathbf{k},\mathbf{k}')[a^p(\mathbf{k}')] = 2\pi v_p \ell_c \overline{\sigma}_{ps}\left(\frac{|\mathbf{k}|\ell_c}{K}, \theta\right)\; G(\phi)\; a^p(\mathbf{k}')\; \delta(\frac{|\mathbf{k}|}{K} - |\mathbf{k}'|) \tag{2.21}$$

$$\sigma_{\mathrm{PS}}(\mathbf{k},\mathbf{k}')[a^s(\mathbf{k}')] = 2\pi v_s \ell_c \overline{\sigma}_{ps}(|\mathbf{k}|\ell_c, \theta)\; \mathrm{Tr}\left(G(0) a^s(\mathbf{k}')\right) \delta(K|\mathbf{k}| - |\mathbf{k}'|) \tag{2.22}$$

$$\sigma_{\mathrm{SS}}(\mathbf{k},\mathbf{k}')[a^s(\mathbf{k}')] = \frac{\pi}{2} v_s \ell_c \overline{\sigma}_{ss}(|\mathbf{k}|\ell_c, \theta)\; R(\phi)\Gamma(\theta)[a^s(\mathbf{k}')](R(\phi)\Gamma(\theta))^T\; \delta(|\mathbf{k}| - |\mathbf{k}'|) \tag{2.23}$$

in which the non-dimensional functions $\overline{\sigma}_{ij}$ $(i, j \in \{p, s\})$ include the influence of the correlation kernel and the Dirac delta functions imply that the frequency remains unchanged during the scattering phenomenon. This also shows that the differential scattering cross-sections σ_{ij} $(i, j \in \{P, S\})$ have the unity of m^3/s.

The incident waves are assumed to be in z direction. Hence, the orthonormal basis containing the polarization directions of the P and two perpendicular S waves, respectively for incident and

scattered waves, $[\hat{\boldsymbol{\zeta}}, z^{(1)}(\hat{\boldsymbol{\zeta}}), z^{(2)}(\hat{\boldsymbol{\zeta}})]$ and $[\hat{\boldsymbol{\zeta}}', z^{(1)}(\hat{\boldsymbol{\zeta}}'), z^{(2)}(\hat{\boldsymbol{\zeta}}')]$, can be written in spherical coordinates as in the equations (1.78) and (1.79). We also have $|\boldsymbol{\zeta} - \boldsymbol{\zeta}'| = 2\zeta \sin(\theta/2)$. With the choice of angles made above, In equations (2.21) to (2.23), the functions $\Gamma(\theta)$, $G(\phi)$ and $R(\phi)$ will be:

$$G(\phi) = \begin{bmatrix} \cos^2\phi & \cos\phi\sin\phi \\ \cos\phi\sin\phi & \sin^2\phi \end{bmatrix} \tag{2.24}$$

$$\Gamma(\theta) = \begin{bmatrix} \cos 2\theta & 0 \\ 0 & \cos\theta \end{bmatrix} \tag{2.25}$$

$$R(\phi) = \begin{bmatrix} \cos\phi & -\sin\phi \\ \sin\phi & \cos\phi \end{bmatrix} \tag{2.26}$$

The analytical definitions of the non-dimensional functions $\overline{\sigma}_{pp}(\zeta,\theta)$, $\overline{\sigma}_{ps}(\zeta,\theta)$, and $\overline{\sigma}_{ss}(\zeta,\theta)$ will be introduced in Section 2.2.

2.2 Influence of the correlation function on the scattering parameters

We consider in this section the influence of the correlation function on the scattering, total scattering, and forward scattering cross sections that appear in the radiative transfer equations introduced in chapter 1.

2.2.1 Influence on the differential scattering cross-sections

For elastic waves propagating in a weakly-varying random isotropic medium, the analytical formulas for the differential scattering cross-sections are given in equations (2.20) to (2.23) in which the influence of the correlation function is summarized in the following adimensional functions (see Ryzhik et al. (1996) for instance):

$$\overline{\sigma}_{pp}(\zeta,\theta) = \zeta^2 \left\{ \left(1 - \frac{2}{K^2}\right)^2 \sigma_\lambda^2 + \frac{4}{K^2}\left(1 - \frac{2}{K^2}\right)\cos^2\theta\sigma_\lambda\sigma_\mu\rho_{\lambda\mu} + \frac{4}{K^4}\cos^4\theta\sigma_\mu^2 \right\} \Phi\left(2\zeta\sin\frac{\theta}{2}\right), \tag{2.27}$$

$$\overline{\sigma}_{ps}(\zeta,\theta) = \zeta^2\cos^2\theta\sin^2\theta\sigma_\mu^2\Phi\left(\zeta\sqrt{1 + K^2 - 2K\cos\theta}\right), \tag{2.28}$$

and

$$\overline{\sigma}_{ss}(\zeta,\theta) = \zeta^2\sigma_\mu^2\Phi\left(2\zeta\sin\frac{\theta}{2}\right), \tag{2.29}$$

From equations (2.27), (2.28) and (2.29) it implies that the adimensional differential scattering cross-sections are functions of the wavenumber of the incident wave and the cosine of the scattering angle, *i.e.* $\sigma_{ij} = \sigma_{ij}(\zeta,\chi)$, $(i,j \in \{p,s\}$ and $\chi = \cos\theta)$. Consequently, elastic wave scattering is intrinsically anisotropic (dependent on the scattering angle) even in low frequencies ($\zeta \ll 1$) in which the function Φ tends to be a constant $\Phi(0)$. Another direct result from these equations is that the scattering happens symmetrical about the incident axis since changing the scattering angle $\theta \to -\theta$ does not change the values of the differential scattering cross-section. Adding the randomness of the medium's density results in an asymmetrical scattering pattern. It should be noted that analytical solutions of the transport equations can be obtained assuming that the scattering process is isotropic, i.e. $\sigma = \overline{\sigma}(\zeta)$ (Aki (1992), Zeng (1993), Sato (1994)). In Appendix

D, we extend the analytical solutions of the transport equations of elastic waves in the case of isotropic scattering pattern given in Sato et al. (1997) for different source types.

Now that we have introduced the analytical formulas of the differential and total scattering cross-sections, we define the following normalization for the differential scattering cross-sections of elastic waves:

$$\hat{\sigma}_{ij}(\zeta,\theta) = \frac{\overline{\sigma}_{ij}(\zeta,\theta)}{\int_0^{2\pi} \overline{\sigma}_{ij}(\zeta,\theta)\ d\theta},\ i,j \in \{p,s\} \tag{2.30}$$

In general $\hat{\sigma}_{ij}$ states the angular dependence of the scattering process for j-to-i mode conversion. Figure 2.3 shows the polar plots of the function $\hat{\sigma}_{ij}$ for all different possible mode conversions. The propagation media are the random media defined with five different correlation kernels introduced in Table 2.1. The value of K is $\sqrt{3}$ and the covariance matrix is composed of $\sigma_\lambda = \sigma_\mu = \rho_{\lambda\mu} = 0.1$. The incident wave propagates in positive x direction and encounters the heterogeneity situated at the center of the polar plots which represent the relative scattered energy densities with respect to this incident angle. Each column corresponds to a different value of ζ. The first column ($\zeta = 0.1$) shows that for weak values of ζ, all different scattering patterns are symmetrical about the y axis. In other words, in low frequencies the scattering process happens non-preferentially in forward and backward directions. Nonetheless, the scattering is not isotropic (independent from the scattering angle). P-to-P and S-to-S mode conversions occur almost in the same polarization direction as the incident wave (positive and negative x direction). The P-to-S plot shows that the scattered S wave energies are almost in $\theta = \pi/4, 3\pi/4, 5\pi/4, 7\pi/4$ directions. Since in low frequencies, the influence of the correlation kernel on differential scattering cross-sections are described by $\Phi(0)$, $\hat{\sigma}_{ij}$ becomes independent from the correlation kernel as it can be seen also in the first column.

From second and third columns it implies that, irrespective from the correlation type, increasing the values of ζ results in scattering patterns with increasing trend toward the forward scattering for all different mode conversions. The second column ($\zeta = 1$) shows that all models except the low-pass white noise have a forward scattering tendency. In this case, as far as the angular distribution of the relative scattered energies corresponding to P-to-S mode conversion is concerned, the polar plot of $\hat{\sigma}_{ps}$ depicts that the amount of scattered S wave energy following $\theta = 40°$ and $\theta = 320°$ is almost 1 (for low-pass white noise model) to 4.5 (for exponential model) times the scattered S wave energy following $\theta = 130°$ and $\theta = 220°$.

The third column ($\zeta = 10$) shows that the scattering angles are tending to the exact same direction as the incident wave packet direction. This comes from the fact that higher values of ζ correspond to a more homogeneous medium which results in weak degrees of scattering. It should be pointed out that in high frequencies, the values of $\hat{\sigma}_{ps}$ for low-pass white noise and triangular correlation models vanish due to the boundedness of the spectrum. That means there is no more conversion between P and S wave energies (see Figure 2.3(f)).

2.2.2 Influence on the total scattering cross-sections

We remind from chapter 1 that the total scattering cross-section $\Sigma_{ij}(\mathbf{k})$ ($i,j \in \{P,S\}$) is defined as the integral of the differential scattering cross-section $\sigma_{ij}(\mathbf{k},\mathbf{k}')$ ($i,j \in \{P,S\}$) over all wave

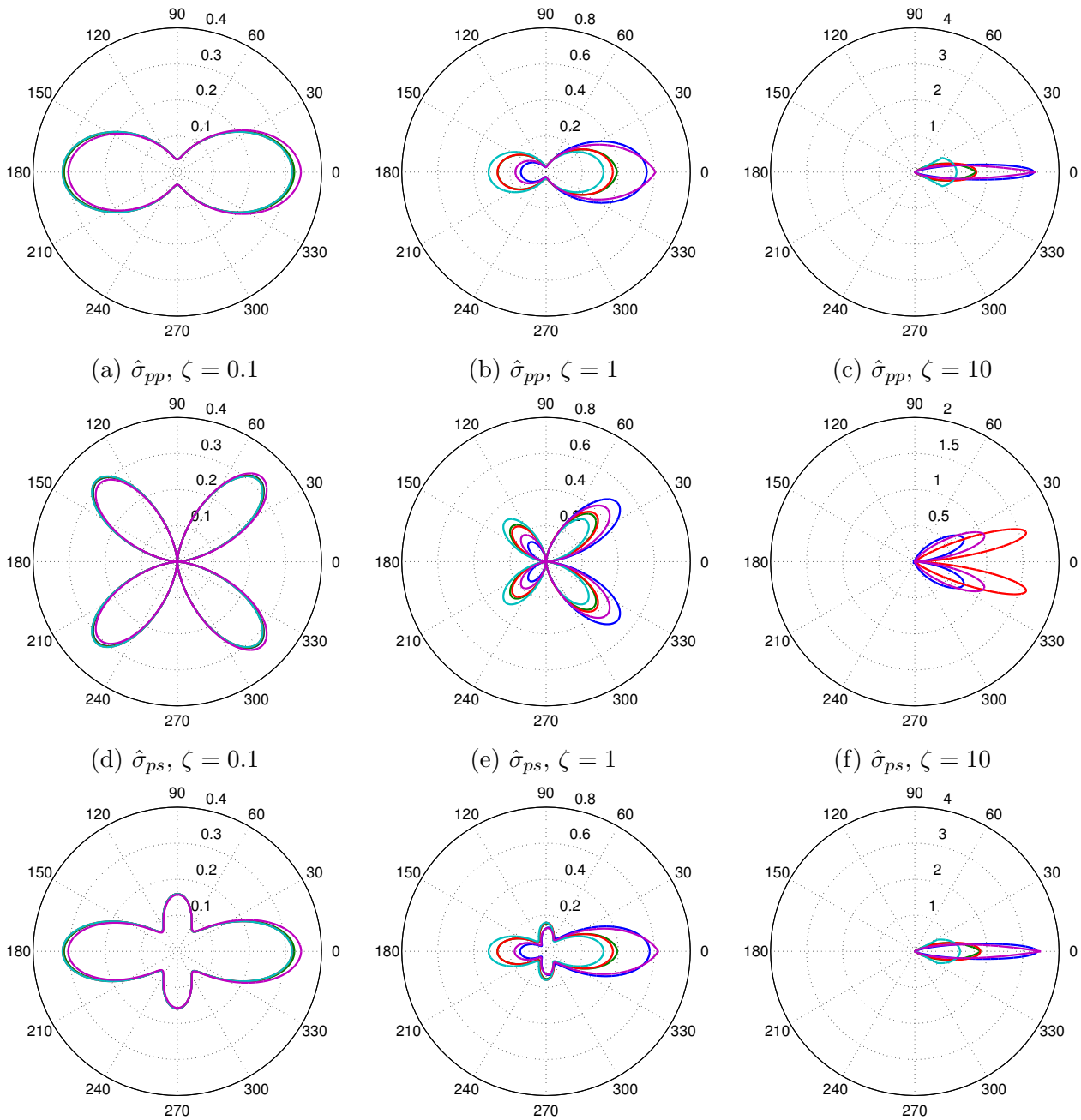

(a) $\hat{\sigma}_{pp}$, $\zeta = 0.1$ (b) $\hat{\sigma}_{pp}$, $\zeta = 1$ (c) $\hat{\sigma}_{pp}$, $\zeta = 10$

(d) $\hat{\sigma}_{ps}$, $\zeta = 0.1$ (e) $\hat{\sigma}_{ps}$, $\zeta = 1$ (f) $\hat{\sigma}_{ps}$, $\zeta = 10$

(g) $\hat{\sigma}_{ss}$, $\zeta = 0.1$ (h) $\hat{\sigma}_{ss}$, $\zeta = 1$ (i) $\hat{\sigma}_{ss}$, $\zeta = 10$

Figure 2.3: Influence of the correlation model on the scattering probability density functions $\hat{\sigma}_{ij}(\zeta, \theta)$ for $K = \sqrt{3}$ and $\sigma_\lambda = \sigma_\mu = \rho_{\lambda\mu} = 0.1$: exponential (blue), power-law (purple), Gaussian (red), triangular (green) and low-pass white noise (cyan).

vectors $\mathbf{k}'$. We define:

$$\Sigma_{PP}(\mathbf{k}) = \frac{\pi^2}{4} \frac{v_p}{\ell_c} \overline{\Sigma}_{pp}(2|\mathbf{k}|\ell_c) \tag{2.31}$$

$$\Sigma_{PS}(\mathbf{k})\mathbf{I}_2 = \pi^2 \frac{v_p}{\ell_c} \overline{\Sigma}_{ps}\left(2|\mathbf{k}|\ell_c\sqrt{K_0 K}\right)\mathbf{I}_2 = 2K^3 \Sigma_{SP}\left(\frac{\mathbf{k}}{K}\right) \tag{2.32}$$

$$\Sigma_{SS}(\mathbf{k}) = \frac{\pi^2}{8} \frac{v_s}{\ell_c} \overline{\Sigma}_{ss}(2|\mathbf{k}|\ell_c)\mathbf{I}_2 \tag{2.33}$$

where $\mathbf{I}_2$ is a 2×2 identity matrix and the influence of the correlation kernel on the total scattering cross-sections is completely included in the adimensional functions $\overline{\Sigma}_{pp}$, $\overline{\Sigma}_{ps}$ and $\overline{\Sigma}_{ss}$:

$$\overline{\Sigma}_{pp}(\zeta) = \zeta^4 \left\{ \left(1 - \frac{2}{K^2}\right)^2 \sigma_\lambda^2 I_0(\zeta) + \frac{4}{K^2}\left(1 - \frac{2}{K^2}\right)\sigma_\lambda \sigma_\mu \rho_{\lambda\mu} I_2(\zeta) + \frac{4}{K^4}\sigma_\mu^2 I_4(\zeta) \right\} \tag{2.34}$$

$$\overline{\Sigma}_{ps}(\zeta) = \zeta^4 \frac{1}{K K_0^2}\sigma_\mu^2 \left\{ J_2(\zeta) - J_4(\zeta) \right\} \tag{2.35}$$

$$\overline{\Sigma}_{ss}(\zeta) = \zeta^4 \sigma_\mu^2 \left\{ I_0(\zeta) - 3I_2(\zeta) + 4I_4(\zeta) \right\} \tag{2.36}$$

in which

$$I_n(\zeta) = \int_0^1 \left(1 - 2\chi^2\right)^n \chi \Phi(\zeta\chi) d\chi \tag{2.37}$$

and

$$J_n(\zeta) = K_0^{n+1} \int_{K_1}^{K_2} \left(1 - 2\chi^2\right)^n \chi \Phi(\zeta\chi) d\chi, \tag{2.38}$$

and where $K_0 = (K + 1/K)/2$, $K_1 = \sqrt{(1 - 1/K_0)/2}$ and $K_2 = \sqrt{(1 + 1/K_0)/2}$. The behavior of the functions $I_n(\zeta)$ and $J_n(\zeta)$ is studied in Appendix A.

Using the asymptotic results for I_n and J_n in Appendix A, we get the low-frequency behavior of the $\overline{\Sigma}_{ij}$ $(i, j \in \{p, s\})$:

$$\overline{\Sigma}_{pp}(\zeta \ll 1) = \left\{ \left(1 - \frac{2}{K^2}\right)^2 \sigma_\lambda^2 + \frac{4}{3K^2}\left(1 - \frac{2}{K^2}\right)\sigma_\lambda \sigma_\mu \rho_{\lambda\mu} + \frac{4}{5K^4}\sigma_\mu^2 \right\} \frac{\Phi(0)}{2}\zeta^4 + \mathrm{O}(\zeta^6) \tag{2.39}$$

$$\overline{\Sigma}_{ps}(\zeta \ll 1) = \frac{1}{K K_0^2}\sigma_\mu^2 \frac{\Phi(0)}{15}\zeta^4 + \mathrm{O}(\zeta^5) \tag{2.40}$$

$$\overline{\Sigma}_{ss}(\zeta \ll 1) = \frac{2}{5}\sigma_\mu^2 \Phi(0)\zeta^4 + \mathrm{O}(\zeta^6) \tag{2.41}$$

Two main results can be extracted from these equations:

- In low frequencies, the total scattering cross-sections increase with fourth power of the frequency.
- The influence of the correlation kernel in this limit can be described by the second central moment of the ACF or the value of the PSDF at origin $\Phi(0)$ (equation (2.10)). Figure 2.4 also shows that correlation models with higher values of $\Phi(0)$ have higher values of total scattering cross-sections.

The high-frequency behavior of the P-to-P and S-to-S total scattering cross-sections is:

$$\overline{\Sigma}_{pp}(\zeta \gg 1) = \frac{1}{4\pi^2} \left\{ \left(1 - \frac{2}{K^2}\right)^2 \sigma_\lambda^2 + \frac{4}{K^2}\left(1 - \frac{2}{K^2}\right)\sigma_\lambda \sigma_\mu \rho_{\lambda\mu} + \frac{4}{K^4}\sigma_\mu^2 \right\} \zeta^2 + \mathrm{O}(\zeta), \tag{2.42}$$

$$\overline{\Sigma}_{ss}(\zeta \gg 1) = \frac{1}{2\pi^2}\sigma_\mu^2 \zeta^2 + \mathrm{O}(\zeta). \tag{2.43}$$

In high frequencies the influence of the correlation kernel on P-to-P and S-to-S total scattering cross-sections is the zeroth-order central moment of the ACF or equivalently the first-order central moment of the PSDF (equation (2.11)) that is $1/(4\pi^2)$ based on our normalization condition for the correlation length (equation (1.36)). In this limit, $\overline{\Sigma}_{pp}$ and $\overline{\Sigma}_{ss}$ increase with second power of frequency and as it can be seen in figure 2.4, different correlation models result in the same values for $\overline{\Sigma}_{pp}$ and $\overline{\Sigma}_{ss}$. Contrarily, the P-S total scattering coefficient is extremely dependent on the correlation model. For the case of power spectra with bounded support, the values of $\overline{\Sigma}_{ps}$ cancel at a frequency ζ^* so that the high-frequency limit will be zero (see Figure 2.4(b)):

$$\zeta^* = \frac{\zeta_c}{K_1} = \frac{\sqrt{2(K^2+1)}}{K-1}\zeta_c \tag{2.44}$$

Therefore, we have $\overline{\Sigma}_{ps}(\zeta \geq \zeta^*) = \Sigma_{PS}(2|\mathbf{k}|\ell_c \geq \zeta^*) = 0$. Consequently, for the low-pass white-noise and triangular correlation models for which ζ_c is respectively $3\pi/2$ and 2π as in table 2.1, and for $K = \sqrt{3}$ ($K_0 = \frac{2}{\sqrt{3}}$), the values of $\overline{\Sigma}_{ps}$ and Σ_{PS} cancel at $\zeta^* \simeq 18.21$ and $\zeta^* \simeq 24.28$ respectively (see figure 2.4).

Using equation (A.18) in Appendix A.4, we can also show that in high frequencies, $\overline{\Sigma}_{ps}$ for a random medium with an exponential correlation kernel tends to a constant (see the stabilization of the blue curve at high frequencies in Figure 2.4(b)):

$$\overline{\Sigma}_{ps}^{\exp}(\zeta \gg 1) = \frac{2}{\pi^2 K K_0^2}\sigma_\mu^2\left[V_2^{-4}(K) - V_4^{-4}(K)\right] + \mathrm{O}(\zeta^{-1}) \tag{2.45}$$

in which the function $V_n^p(K)$ is defined in Appendix A. As a result, the only model among those studied in this presentation for which even in high frequencies the exchange between body wave energies takes place is the exponential correlation model. Contrary to the case of exponential correlation, for Gaussian and power-law models in which the PSDFs are exponential functions, the high-frequency values of $\overline{\Sigma}_{ps}$ tend to zero exponentially so that a polynomial representation is impossible.

Finally, for the regime $\zeta \sim 1$, Figure 2.4 shows that the influence of the correlation model seems to be limited for all three total scattering coefficients P-P, S-S and P-S.

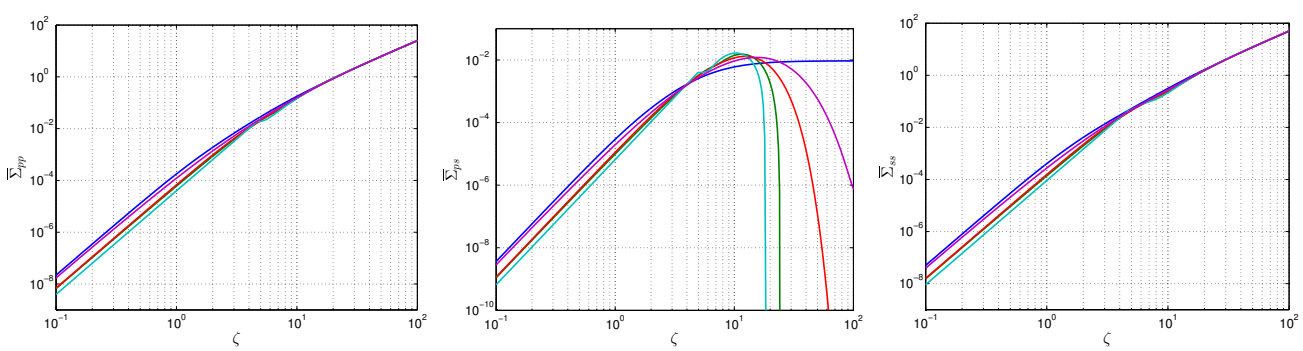

(a) (b) (c)

Figure 2.4: $\overline{\Sigma}_{pp}$, $\overline{\Sigma}_{ps}$ and $\overline{\Sigma}_{ss}$ in terms of ζ for $K = \sqrt{3}$ and $\sigma_\lambda = \sigma_\mu = \rho_{\lambda\mu} = 0.1$: exponential (blue), power-law (purple), Gaussian (red), triangular (green) and low-pass white noise (cyan).

2.2.3 Influence on the forward scattering cross-sections

We remind from chapter 1 that forward scattering cross-sections characterize the degree of scattering in forward direction. Assuming the same normalizations for the forward scattering cross sections as for the total scattering cross-sections, that is to say:

$$\Sigma'_{PP}(\mathbf{k}) = \frac{\pi^2}{4}\frac{v_p}{\ell_c}\overline{\Sigma}'_{pp}(2|\mathbf{k}|\ell_c) \tag{2.46}$$

$$\Sigma'_{PS}(\mathbf{k})\mathbf{I}_2 = \pi^2\frac{v_p}{\ell_c}\overline{\Sigma}'_{ps}\left(2|\mathbf{k}|\ell_c\sqrt{K_0K}\right)\mathbf{I}_2 = 2K^3\Sigma'_{SP}\left(\frac{\mathbf{k}}{K}\right) \tag{2.47}$$

$$\Sigma'_{SS}(\mathbf{k}) = \frac{\pi^2}{8}\frac{v_s}{\ell_c}\overline{\Sigma}'_{ss}(2|\mathbf{k}|\ell_c)\mathbf{I}_2 \tag{2.48}$$

Hence, we get:

$$\overline{\Sigma}'_{pp}(\zeta) = \zeta^4\left\{\left(1-\frac{2}{K^2}\right)^2\sigma_\lambda^2 I_1(\zeta) + \frac{4}{K^2}\left(1-\frac{2}{K^2}\right)\sigma_\lambda\sigma_\mu\rho_{\lambda\mu}I_3(\zeta) + \frac{4}{K^4}\sigma_\mu^2 I_5(\zeta)\right\} \tag{2.49}$$

$$\overline{\Sigma}'_{ps}(\zeta) = \zeta^4\frac{1}{KK_0^2}\sigma_\mu^2\left\{J_3(\zeta) - J_5(\zeta)\right\} \tag{2.50}$$

$$\overline{\Sigma}'_{ss}(\zeta) = \zeta^4\sigma_\mu^2\left\{I_1(\zeta) - 3I_3(\zeta) + 4I_5(\zeta)\right\} \tag{2.51}$$

in which the functions I_n and J_n are defined in equations (2.37) and (2.38). Function I for odd n values cancels when the correlation model is low-pass white noise and $\zeta \leq \zeta_c = 3\pi/2$. As a result, for this particular correlation model, the values of $\overline{\Sigma}'_{pp}$ and $\overline{\Sigma}'_{ss}$ vanish for $\zeta < 3\pi/2 \simeq 4.7$ which implies that P-to-P and S-to-S scatterings occur non-preferentially in this case (see the first two columns of figure 2.3). It can also be shown that for the correlation models whose PSDF have bounded support and for the values of $\zeta \geq \frac{\sqrt{2(K^2+1)}}{K-1}\zeta_c$, Σ'_{ps} vanishes.

Since the randomness in density is neglected, all of differential scattering cross-section are functions of pair powers of $\chi = \cos\theta$. This implies that $\Sigma'_{ij} \geq 0$ $(i, j \in \{P, S\}$ is always true so that the plots of these parameters can be done in a logarithmic scale. Polar plots in figure 2.3 also showed that the scattering patterns in this case are always symmetrical (about the y axis) or have a forward trend.

The limit behavior of the functions $I_n(\zeta)$ and $J_n(\zeta)$ for $\zeta \ll 1$ and $\zeta \gg 1$ implies that the limit behavior of the forward scattering cross-sections in the low frequency range is:

$$\begin{aligned}\overline{\Sigma}'_{pp}(\zeta \ll 1) = &\left\{\left(1-\frac{2}{K^2}\right)^2\sigma_\lambda^2 W_1^1 + \frac{4}{K^2}\left(1-\frac{2}{K^2}\right)\sigma_\lambda\sigma_\mu\rho_{\lambda\mu}W_3^1 + \frac{4}{K^4}\sigma_\mu^2 W_5^1\right\}\Phi'(0)\zeta^5 \\ &- \left\{\frac{1}{24}\left(1-\frac{2}{K^2}\right)^2\sigma_\lambda^2 + \frac{1}{10K^2}\left(1-\frac{2}{K^2}\right)\sigma_\lambda\sigma_\mu\rho_{\lambda\mu} + \frac{1}{14K^4}\sigma_\mu^2\right\}\Phi''(0)\zeta^6 + \mathrm{O}(\zeta^7)\end{aligned} \tag{2.52}$$

$$\overline{\Sigma}'_{ps}(\zeta \ll 1) = \frac{1}{KK_0^2}\sigma_\mu^2(V_3^1 - V_5^1)\Phi'(0)\zeta^5 - \frac{1}{140KK_0^3}\sigma_\mu^2\Phi''(0)\zeta^6 + \mathrm{O}(\zeta^7) \tag{2.53}$$

$$\overline{\Sigma}'_{ss}(\zeta \ll 1) = \sigma_\mu^2(W_1^1 - 3W_3^1 + 4W_5^1)\Phi'(0)\zeta^5 - \frac{4}{105}\sigma_\mu^2\Phi''(0)\zeta^6 + \mathrm{O}(\zeta^7) \tag{2.54}$$

in which W_n^p and V_n^p are defined in Appendix A. Hence, the influence of the correlation kernel in this limit can be described by the first and second derivatives of the PSDF in origin. Consequently, in a low-frequency regime, forward scattering cross-sections are *a priori* proportional to the fifth power of frequency. However, for correlation models whose first derivative in origin is zero ($\Phi'(0) = 0$) (for instance the exponential and Gaussian spatial correlation models) the low-frequency limits of forward scattering cross-sections vary in sixth power of frequency. Nonetheless, since for the case of the low-pass white noise correlation for all $n \geq 1$ we have $\Phi^{(n)}(0) = 0$, the low-frequency limit tends to zero. For instance, figure 2.5(b) shows that in low frequencies we can distinguish three groups: The exponential and Gaussian models with a slope of 6, the triangular and power-law models with a slope of 5. It should be pointed out that $\overline{\Sigma}'_{ps}$ for the low-pass white noise model is defined within the interval $[3\pi/(2K_2), 3\pi/(2K_1)]$ since the functions $J_3(\zeta)$ and $J_5(\zeta)$ are defined in this interval (see Appendix A.4).

The high-frequency behavior of the $\overline{\Sigma}'_{pp}$ and $\overline{\Sigma}'_{ss}$:

$$\overline{\Sigma}'_{pp}(\zeta \gg 1) = \frac{1}{4\pi^2}\left\{\left(1 - \frac{2}{K^2}\right)^2\sigma_\lambda^2 + \frac{4}{K^2}\left(1 - \frac{2}{K^2}\right)\sigma_\lambda\sigma_\mu\rho_{\lambda\mu} + \frac{4}{K^4}\sigma_\mu^2\right\}\zeta^2 + \mathrm{O}(\zeta^1) \tag{2.55}$$

$$\overline{\Sigma}'_{ss}(\zeta \gg 1) = \frac{1}{2\pi^2}\sigma_\mu^2\zeta^2 + \mathrm{O}(\zeta^1) \tag{2.56}$$

In high frequencies, similar to the case of total scattering cross-sections, $\overline{\Sigma}'_{pp}$ and $\overline{\Sigma}'_{ss}$ are proportional to the second power of frequency. It should be pointed out that high frequency limits of $\overline{\Sigma}_{pp}$ and $\overline{\Sigma}'_{pp}$ and likewise $\overline{\Sigma}_{ss}$ and $\overline{\Sigma}'_{ss}$ are equal. The influence of the correlation model can be described by the second central moment of the ACF or the first central moment of the PSDF which is a constant for different models based on the normalization condition defined in equation (1.36). Figures 2.5(a) and 2.5(c) show the convergence of different correlation models together in this limit.

Contrary to the P-to-P and S-to-S forward scattering cross-sections which are increasing in high frequencies, $\overline{\Sigma}'_{ps}$ decreases and tends to zero regardless of the medium's correlation structure. As it can be seen in figure 2.5(b) and similar to the case of $\overline{\Sigma}_{ps}$, the high-frequency behavior of $\overline{\Sigma}'_{ps}$ is correlation-dependent. For bounded power spectra, the cut-off frequency follows the equation (2.44) and we have $\overline{\Sigma}'_{ps}(\zeta \geq \zeta^*) = 0$. For an exponential correlation model, we can show that the high-frequency behavior of $\overline{\Sigma}'_{ps}$ can be approximated by a constant (see Figure 2.5(b)):

$$\overline{\Sigma}'^{\exp}_{ps}(\zeta \gg 1) = \frac{2}{\pi^2 K K_0^2}\sigma_\mu^2\left[V_3^{-4}(K) - V_5^{-4}(K)\right] + \mathrm{O}(\zeta^{-1}) \tag{2.57}$$

For Gaussian and power-law models, the high-frequency values of $\overline{\Sigma}'_{ps}$ tends to zero exponentially so that a polynomial approximation is impossible.

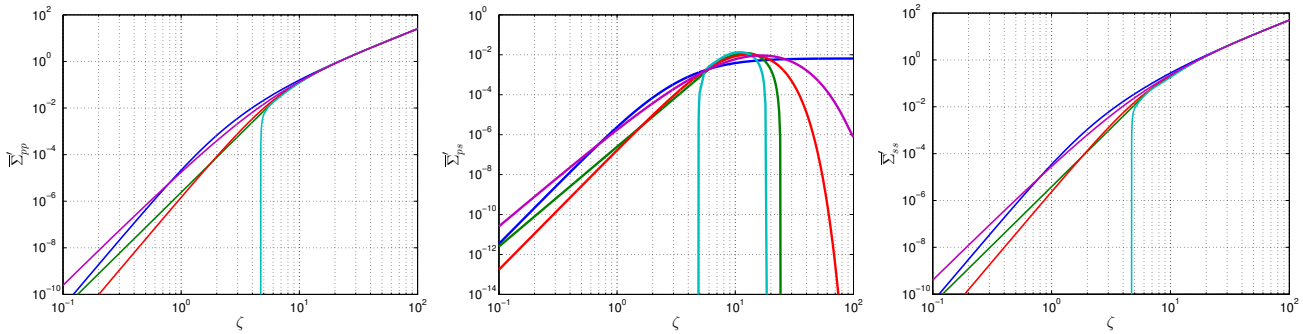

(a) (b) (c)

Figure 2.5: $\overline{\Sigma}'_{pp}$, $\overline{\Sigma}'_{ps}$ and $\overline{\Sigma}'_{ss}$ in terms of ζ for $K = \sqrt{3}$ and $\sigma_\lambda = \sigma_\mu = \rho_{\lambda\mu} = 0.1$: exponential (blue), power-law (purple), Gaussian (red), triangular (green) and low-pass white noise (cyan).

2.3 Influence of the correlation function on the diffusion regime

2.3.1 Normalized scattering mean free time (path), $\overline{\tau}$ ($\overline{\ell}$)

The scattering mean free time (path) is defined in Section 1.4.3 of chapter 1. Following equations (1.98) and (1.99) we can define:

$$\tau_P(\mathbf{k}) = \frac{1}{\Sigma_{PP}(\mathbf{k}) + \Sigma_{PS}(\mathbf{k})} = \frac{4}{\pi^2}\frac{\ell_c}{v_p}\overline{\tau}_p(2|\mathbf{k}|\ell_c) \Rightarrow \ell_P(\mathbf{k}) = \tau_P(\mathbf{k})v_p \tag{2.58}$$

and

$$\tau_S(\mathbf{k}) = \frac{1}{\Sigma_{SS}(\mathbf{k}) + \Sigma_{SP}(\mathbf{k})} = \frac{8}{\pi^2}\frac{\ell_c}{v_s}\overline{\tau}_s(2|\mathbf{k}|\ell_c) \Rightarrow \ell_S(\mathbf{k}) = \tau_S(\mathbf{k})v_s \tag{2.59}$$

with the non-dimensional functions $\overline{\tau}_p$ and $\overline{\tau}_s$ including the influences of the correlation model:

$$\begin{aligned}\overline{\tau}_p(\zeta) &= \frac{1}{\overline{\Sigma}_{pp}(\zeta) + 4\overline{\Sigma}_{ps}(\zeta\sqrt{KK_0})} \\ &= \frac{\zeta^{-4}}{\left(1-\frac{2}{K^2}\right)^2\sigma_\lambda^2 I_0(\zeta) + \frac{4}{K^2}\left(1-\frac{2}{K^2}\right)\sigma_\lambda\sigma_\mu\rho_{\lambda\mu}I_2(\zeta) + \frac{4}{K^4}\sigma_\mu^2\left(I_4(\zeta) + K^5(J_2(\zeta\sqrt{KK_0}) - J_4(\zeta\sqrt{KK_0}))\right)}\end{aligned} \tag{2.60}$$

and

$$\begin{aligned}\overline{\tau}_s(\zeta) &= \frac{1}{\overline{\Sigma}_{ss}(\zeta) + \frac{4}{K^2}\overline{\Sigma}_{ps}(\zeta K\sqrt{KK_0})} \\ &= \frac{1}{\sigma_\mu^2}\frac{\zeta^{-4}}{I_0(\zeta) - 3I_2(\zeta) + 4I_4(\zeta) + \frac{4}{K^3K_0^2}(J_2(\zeta K\sqrt{KK_0}) - J_4(\zeta K\sqrt{KK_0}))}\end{aligned} \tag{2.61}$$

The influence of the correlation kernel on $\overline{\tau}_p$ and $\overline{\tau}_s$ can now be investigated using the asymptotics for $\overline{\Sigma}_{pp}(\zeta)$, $\overline{\Sigma}_{ps}(\zeta)$ and $\overline{\Sigma}_{ss}(\zeta)$. The low-frequency limits of the scattering mean free time of P and S waves read:

$$\overline{\tau}_p(\zeta \ll 1) = \frac{\zeta^{-4}}{\left\{\left(1-\frac{2}{K^2}\right)^2\sigma_\lambda^2 + \frac{4}{3K^2}\left(1-\frac{2}{K^2}\right)\sigma_\lambda\sigma_\mu\rho_{\lambda\mu} + \frac{4}{5K^4}\left(1+\frac{2K^5}{3}\right)\sigma_\mu^2\right\}\frac{\Phi(0)}{2}} + \mathrm{O}(\zeta^{-3}) \tag{2.62}$$

and

$$\overline{\tau}_s(\zeta \ll 1) = \frac{15\zeta^{-4}}{2(3+2K^3)\sigma_\mu^2\Phi(0)} + \mathrm{O}(\zeta^{-3}) \tag{2.63}$$

Consequently, in low frequencies, the decay of the scattering mean free times occurs inversely proportional to the fourth power of the frequency. In addition, the influence of the correlation kernel appears in $1/\Phi(0)$, *i.e.* in this asymptotic regime, models with lower values of $\Phi(0)$ have higher values of scattering mean free paths and vice versa.

The high-frequency behavior of these quantities are independent form the correlation model since the function $\overline{\Sigma}_{ps}$ becomes negligible compared to $\overline{\Sigma}_{pp}$ and $\overline{\Sigma}_{ss}$ respectively in equations (2.60) and (2.61) (see Figure 2.6). The corresponding high-frequency limits of the P and S scattering mean free paths read:

$$\overline{\tau}_p(\zeta \gg 1) = \frac{1}{\overline{\Sigma}_{pp}(\zeta \gg 1)} = \frac{\zeta^{-2}}{\frac{1}{4\pi^2}\left\{\left(1-\frac{2}{K^2}\right)^2\sigma_\lambda^2 + \frac{4}{K^2}\left(1-\frac{2}{K^2}\right)\sigma_\lambda\sigma_\mu\rho_{\lambda\mu} + \frac{4}{K^4}\sigma_\mu^2\right\}} + \mathrm{O}(\zeta^{-1}) \tag{2.64}$$

and

$$\overline{\tau}_s(\zeta \gg 1) = \frac{1}{\overline{\Sigma}_{ss}(\zeta \gg 1)} = \frac{\zeta^{-2}}{\frac{1}{2\pi^2}\sigma_\mu^2} + \mathrm{O}(\zeta^{-1}) \tag{2.65}$$

As a result, for instance the high-frequency limit of the scattering mean free time of shear waves τ_S propagating in random media with any type of correlation model, can be simplified as:

$$\tau_S(|\mathbf{k}|\ell_c \gg 1) \simeq \frac{4}{v_s\sigma_\mu^2|\mathbf{k}|^2\ell_c} \tag{2.66}$$

Figure 2.6 shows the variations of $\bar{\tau}_p$ and $\bar{\tau}_s$ in terms of ζ in which the transition between the slopes -4 to -2 from low to high frequencies can be observed.

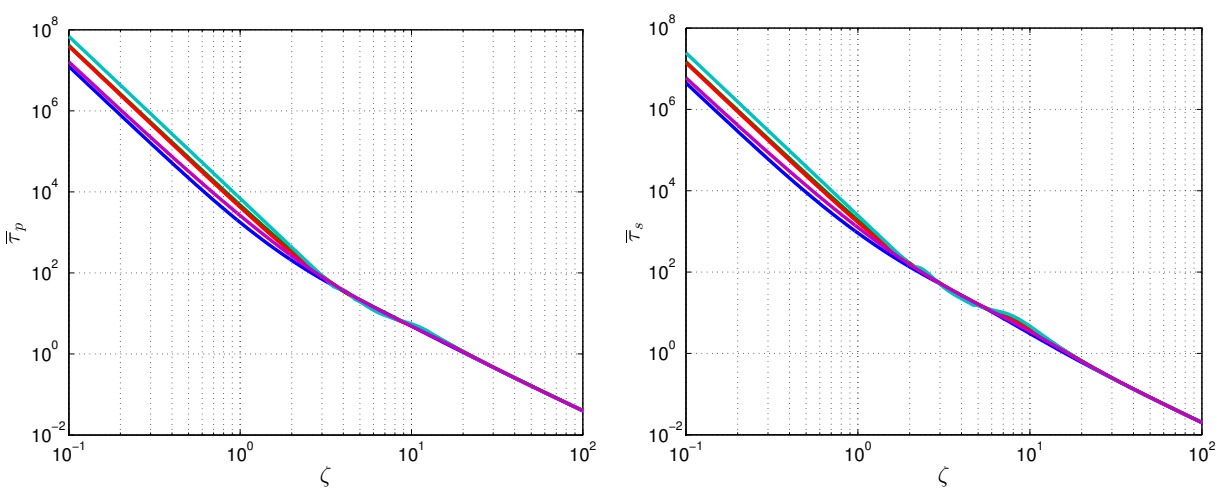

Figure 2.6: $\bar{\tau}_p$ (left plot) and $\bar{\tau}_s$ (right plot) in terms of ζ for $K = \sqrt{3}$ and $\sigma_\lambda = \sigma_\mu = \rho_{\lambda\mu} = 0.1$: exponential (blue), power-law (purple), Gaussian (red), triangular (green) and low-pass white noise (cyan).

2.3.2 Normalized transport mean free path (time), $\overline{\ell}^*$ ($\overline{\tau}^*$)

In chapter 1 we defined the transport mean free path/time as the distance/time beyond which each wave mode reaches a diffusion regime. We define:

$$\ell_P^*(\mathbf{k}) = \frac{v_p(\Sigma_{SS} + \Sigma_{SP} - \Sigma'_{SS}) + v_s\Sigma'_{PS}}{(\Sigma_{PP} + \Sigma_{PS} - \Sigma'_{PP})(\Sigma_{SS} + \Sigma_{SP} - \Sigma'_{SS}) - \Sigma'_{PS}\Sigma'_{SP}} = \frac{4}{\pi^2}\ell_c\overline{\ell}_p^*(2|\mathbf{k}|\ell_c) \tag{2.67}$$

and

$$\ell_S^*(\mathbf{k}) = \frac{v_s(\Sigma_{PP} + \Sigma_{PS} - \Sigma'_{PP}) + v_p\Sigma'_{SP}}{(\Sigma_{PP} + \Sigma_{PS} - \Sigma'_{PP})(\Sigma_{SS} + \Sigma_{SP} - \Sigma'_{SS}) - \Sigma'_{PS}\Sigma'_{SP}} = \frac{8}{\pi^2}\ell_c\overline{\ell}_s^*(2|\mathbf{k}|\ell_c) \tag{2.68}$$

in which the normalized functions $\overline{\ell}_p^*$ and $\overline{\ell}_s^*$, which include the influence of the correlation model on the transport mean free paths, are defined as:

$$\overline{\ell}_p^*(\zeta) = \frac{\overline{\Sigma}_{ss}(\zeta) + \frac{4}{K^2}\overline{\Sigma}_{ps}(\zeta K\sqrt{KK_0}) - \overline{\Sigma}'_{ss}(\zeta) + 8\overline{\Sigma}'_{ps}(\zeta\sqrt{KK_0})}{\left(\overline{\Sigma}_{pp}(\zeta) + 4\overline{\Sigma}_{ps}(\zeta\sqrt{KK_0}) - \overline{\Sigma}'_{pp}(\zeta)\right)\left(\overline{\Sigma}_{ss}(\zeta) + \frac{4}{K^2}\overline{\Sigma}_{ps}(\zeta K\sqrt{KK_0}) - \overline{\Sigma}'_{ss}(\zeta)\right) - \frac{16}{K^2}\overline{\Sigma}'_{ps}(\zeta\sqrt{KK_0})\overline{\Sigma}'_{ps}(\zeta K\sqrt{KK_0})} \tag{2.69}$$

and

$$\overline{\ell}_s^*(\zeta) = \frac{\overline{\Sigma}_{pp}(\zeta) + 4\overline{\Sigma}_{ps}(\zeta\sqrt{KK_0}) - \overline{\Sigma}'_{pp}(\zeta) + \frac{2}{K^2}\overline{\Sigma}'_{ps}(\zeta K\sqrt{KK_0})}{\left(\overline{\Sigma}_{pp}(\zeta) + 4\overline{\Sigma}_{ps}(\zeta\sqrt{KK_0}) - \overline{\Sigma}'_{pp}(\zeta)\right)\left(\overline{\Sigma}_{ss}(\zeta) + \frac{4}{K^2}\overline{\Sigma}_{ps}(\zeta K\sqrt{KK_0}) - \overline{\Sigma}'_{ss}(\zeta)\right) - \frac{16}{K^2}\overline{\Sigma}'_{ps}(\zeta\sqrt{KK_0})\overline{\Sigma}'_{ps}(\zeta K\sqrt{KK_0})} \tag{2.70}$$

A direct result of the equations 2.67 and 2.68 is that in the special case of non-preferential scattering between all wave modes, *i.e.* $\Sigma'_{ij} = 0$ $(i, j \in \{P, S\})$, the forward scattering cross-sections cancel and the transport mean free paths will become equivalent to the corresponding scattering mean free paths defined earlier in section 2.3.1.

The low-frequency limit of the normalized functions $\overline{\ell}_p^*$ and $\overline{\ell}_s^*$ are:

$$\overline{\ell}_p^*(\zeta \ll 1) = \frac{\zeta^{-4}}{\left\{\left(1 - \frac{2}{K^2}\right)^2\sigma_\lambda^2 + \frac{4}{3K^2}\left(1 - \frac{2}{K^2}\right)\sigma_\lambda\sigma_\mu\rho_{\lambda\mu} + \frac{4}{15K^4}\left(3 + 2K^5\right)\sigma_\mu^2\right\}\frac{\Phi(0)}{2}} + \mathrm{O}(\zeta^{-3}) \tag{2.71}$$

and

$$\overline{\ell}_s^*(\zeta \ll 1) = \frac{15\zeta^{-4}}{2\left(3 + 2K^3\right)\sigma_\mu^2\Phi(0)} + \mathrm{O}(\zeta^{-3}) \tag{2.72}$$

Therefore, the transport mean free paths of elastic waves in low frequencies is inversely proportional to the fourth power of frequency and the influence of the correlation model appears in $1/\Phi(0)$.

The high-frequency limits can be simplified as following equations (since $\overline{\Sigma}_{ps}$ and $\overline{\Sigma}'_{ps}$ are negligible compared to other terms in equations (2.69) and (2.70)):

$$\overline{\ell}_p^*(\zeta \gg 1) = \frac{1}{\overline{\Sigma}_{pp}(\zeta) - \overline{\Sigma}'_{pp}(\zeta)} \tag{2.73}$$

and

$$\overline{\ell}_s^*(\zeta \gg 1) = \frac{1}{\overline{\Sigma}_{ss}(\zeta) - \overline{\Sigma}'_{ss}(\zeta)} \tag{2.74}$$

which means that in this case, the transport mean free paths are a simple modification of the corresponding scattering mean free paths. We can show that these limits are as follows:

$$\overline{\ell}_p^*(\zeta \gg 1) = \frac{1}{2\left[\left(1-\frac{2}{K^2}\right)^2\sigma_\lambda^2 + \frac{4}{K^2}\left(1-\frac{2}{K^2}\right)\sigma_\lambda\sigma_\mu\rho_{\lambda\mu} + \frac{4}{K^4}\sigma_\mu^2\right]\left[\lim_{\zeta\to\infty}\int_0^\zeta p^3\Phi(p)dp\right]} \tag{2.75}$$

and

$$\overline{\ell}_s^*(\zeta \gg 1) = \frac{1}{4\sigma_\mu^2\left[\lim_{\zeta\to\infty}\int_0^\zeta p^3\Phi(p)dp\right]} \tag{2.76}$$

Hence, the influence of the correlation kernel on the diffusion lengths in high frequencies can be described by the third central moment of the PSDF, *i.e.*:

$$\lim_{\zeta\to\infty}\int_0^\zeta p^3\Phi(p)dp \tag{2.77}$$

We can verify simply that this integral converges for all correlation models except the exponential model. For the latter, the behavior of this integral cannot be described via polynomial functions. In other words, a polynomial representation of the high-frequency limits of the transport mean free paths of a random medium with exponential correlation is impossible. Figure (2.7) shows the variations of the adimensional functions $\overline{\ell}_p^*(\zeta)$ and $\overline{\ell}_s^*(\zeta)$. In high frequencies, the latter tend to constant values for all models except the exponential model according to equations (2.75) and (2.76). This stabilization of the transport mean free paths in high frequencies can be observed from this figure. The integral of the equation (2.77) converges to $\frac{3}{8}$, $\frac{1}{\pi}$, $\frac{3}{10}$ and $\frac{9}{32}$ respectively for power-law, Gaussian, triangular and low-pass white noise correlations. For instance, the transport mean free path of shear waves for a random medium with low-pass white noise correlation model reads:

$$\ell_S^*\left(|\mathbf{k}|\ell_c \gg 1\right) = \frac{64}{9\pi^2}\frac{\ell_c}{\sigma_\mu^2} \tag{2.78}$$

so that the ratio between the correlation length and the variance of the shear modulus of the underlying random medium will determine the transport mean free path of shear waves.

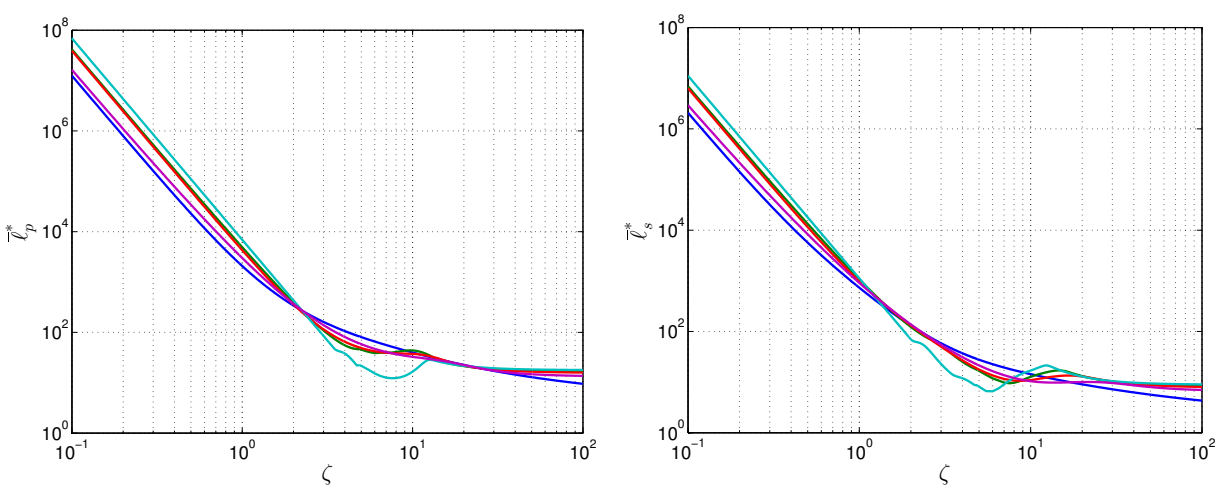

Figure 2.7: $\overline{\ell}_p^*$ (left plot) and $\overline{\ell}_s^*$ (right plot) in terms of ζ for $K = \sqrt{3}$ and $\sigma_\lambda = \sigma_\mu = \rho_{\lambda\mu} = 0.1$: exponential (blue), power-law (purple), Gaussian (red), triangular (green) and low-pass white noise (cyan).

2.3.3 Normalized diffusion constant, $\overline{D}$

We normalize the elastic diffusivity as:

$$D(\mathbf{k}) = \frac{1}{1+2K^3}(D_P(\mathbf{k})+2K^3 D_S(\mathbf{k})) = \frac{1}{1+2K^3}\left[\frac{v_p \ell_P^*(\mathbf{k})}{3} + 2K^3 \frac{v_s \ell_S^*(\mathbf{k})}{3}\right] = \frac{4}{3\pi^2}\frac{\ell_c v_p}{1+2K^3}\overline{D}(2|\mathbf{k}|\ell_c) \tag{2.79}$$

in which the non-dimensional function $\overline{D}$ is defined as:

$$\overline{D}(\zeta) = \overline{\ell}_p^*(\zeta) + 4K^2 \overline{\ell}_s^*(\zeta) \tag{2.80}$$

introducing the equations 2.69 and 2.70 into 2.80 and then into the equation 2.79 gives:

$$D(\zeta) = \frac{4}{3\pi^2}\frac{\ell_c v_p}{1+2K^3} \frac{4K^2\overline{\Sigma}_{pp}(\zeta) + \frac{4}{K^2}\overline{\Sigma}_{ps}(\zeta K\sqrt{KK_0}) + 16K^2\overline{\Sigma}_{ps}(\zeta\sqrt{KK_0}) + \overline{\Sigma}_{ss}(\zeta) - 4K^2\overline{\Sigma}'_{pp}(\zeta) + 8\left(\overline{\Sigma}'_{ps}(\zeta\sqrt{KK_0}) + \overline{\Sigma}'_{ps}(\zeta K\sqrt{KK_0})\right) - \overline{\Sigma}'_{ss}(\zeta)}{\left(\overline{\Sigma}_{pp}(\zeta) + 4\overline{\Sigma}_{ps}(\zeta\sqrt{KK_0}) - \overline{\Sigma}'_{pp}(\zeta)\right)\left(\overline{\Sigma}_{ss}(\zeta) + \frac{4}{K^2}\overline{\Sigma}_{ps}(\zeta K\sqrt{KK_0}) - \overline{\Sigma}'_{ss}(\zeta)\right) - \frac{16}{K^2}\overline{\Sigma}'_{ps}(\zeta\sqrt{KK_0})\overline{\Sigma}'_{ps}(\zeta K\sqrt{KK_0})} \tag{2.81}$$

Using the asymptotic functions describing the low-frequency limits of the non-dimensional functions $\overline{\ell}_p^*$ and $\overline{\ell}_s^*$ gives:

$$\overline{D}(\zeta \ll 1) = \left[\frac{2}{\left\{\left(1-\frac{2}{K^2}\right)^2\sigma_\lambda^2 + \frac{4}{3K^2}\left(1-\frac{2}{K^2}\right)\sigma_\lambda\sigma_\mu\rho_{\lambda\mu} + \frac{4}{15K^4}\left(3+2K^5\right)\sigma_\mu^2\right\}} + \frac{4K^2}{\frac{2}{15}\left(3+2K^3\right)\sigma_\mu^2}\right]\frac{\zeta^{-4}}{\Phi(0)} + \mathrm{O}(\zeta^{-3}) \tag{2.82}$$

which shows that the low-frequency limit of the diffusion constant is inversely proportional to the fourth power of frequency and the influence of the correlation kernel is the term $1/\Phi(0)$.

The high-frequency behavior is model-dependent. For all correlation models except the exponential model, the elastic constant converges as follows:

$$\overline{D}(\zeta \gg 1) = \left[\frac{1}{2\left[\left(1-\frac{2}{K^2}\right)^2\sigma_\lambda^2 + \frac{4}{K^2}\left(1-\frac{2}{K^2}\right)\sigma_\lambda\sigma_\mu\rho_{\lambda\mu} + \frac{4}{K^4}\sigma_\mu^2\right]} + \frac{K^2}{\sigma_\mu^2}\right]\frac{1}{\lim_{\zeta\to\infty}\int_0^\zeta p^3\Phi(p)dp} \tag{2.83}$$

Similar to the case of transport mean free paths, for a random medium with exponential correlation model, the elastic constant cannot be represented polynomially. The left plot in Figure 2.8 depicts the variation of the normalized elastic constant for different models from which the exponential correlation can be simply differentiated from other models.

2.3.4 Normalized equipartitioning time

We define the global equipartitioning time as:

$$t_{eq}(\mathbf{k}) = \frac{1}{\Sigma_{PS}(\mathbf{k}) + \Sigma_{SP}(\mathbf{k})} = \frac{1}{\Sigma_{PS}(\mathbf{k})\left(1+\frac{1}{2K^3}\right)} = \frac{1}{\pi^2\frac{v_p}{\ell_c}\left(1+\frac{1}{2K^3}\right)\overline{\Sigma}_{ps}(2|\mathbf{k}|\ell_c\sqrt{K_0K})} = \frac{1}{\pi^2\frac{v_p}{\ell_c}\left(1+\frac{1}{2K^3}\right)}\overline{t}_{eq}(2|\mathbf{k}|\ell_c\sqrt{K_0K}) \tag{2.84}$$

in which $\bar{t}_{eq}(\zeta) = 1/\overline{\Sigma}_{ps}(\zeta)$ is the adimensional function including the effects of the correlation model. Equation (2.84) shows the importance of the P-to-S total scattering cross-section on the global equilibrium time. The low-frequency limit of $\bar{t}_{eq}$ is a decreasing function by the fourth power of frequency. In this regime, $1/\Phi(0)$ determines the effects of the correlation kernel:

$$\bar{t}_{eq}(\zeta \ll 1) = \frac{\zeta^{-4}}{\frac{\pi^2 \sigma_\mu^2 v_p}{15 K K_0^2 \ell_c}\left(1 + \frac{1}{2K^3}\right)\Phi(0)} + \mathrm{O}(\zeta^{-3}) \tag{2.85}$$

The high-frequency limit of $\bar{t}_{eq}$ for correlations whose PSDF has a bounded support, will be undefined since $\Sigma_{ps}(\zeta)$ for $\zeta > \zeta^*$ vanishes. For Gaussian and power-law models a polynomial representation of $\bar{t}_{eq}$ in high frequencies is impossible. However, following equation (2.45), the high-frequency limit of the global equipartitioning time of a random medium with exponential ACF converges to the following constant:

$$\bar{t}_{eq}^{\exp}(\zeta \gg 1) = \frac{1}{\overline{\Sigma}_{ps}^{\exp}(\zeta \gg 1)} = \frac{1}{\frac{2}{\pi^2 K K_0^2}\sigma_\mu^2 \left[V_2^{-4}(K) - V_4^{-4}(K)\right]} + \mathrm{O}(\zeta^{-1}) \tag{2.86}$$

The right plot in Figure 2.8 shows the variation of $\bar{t}_{eq}(\zeta)$ in terms of adimensional parameter ζ in which three correlation groups can be distinguished: (1) low-pass white noise and triangular models having PSDFs with bounded support for which the high frequency values of $\bar{t}_{eq}$ are undefined; (2) power-law and Gaussian models for which a polynomial representation of $\bar{t}_{eq}$ in high frequencies is impossible and (3) exponential model which converges at high frequencies.

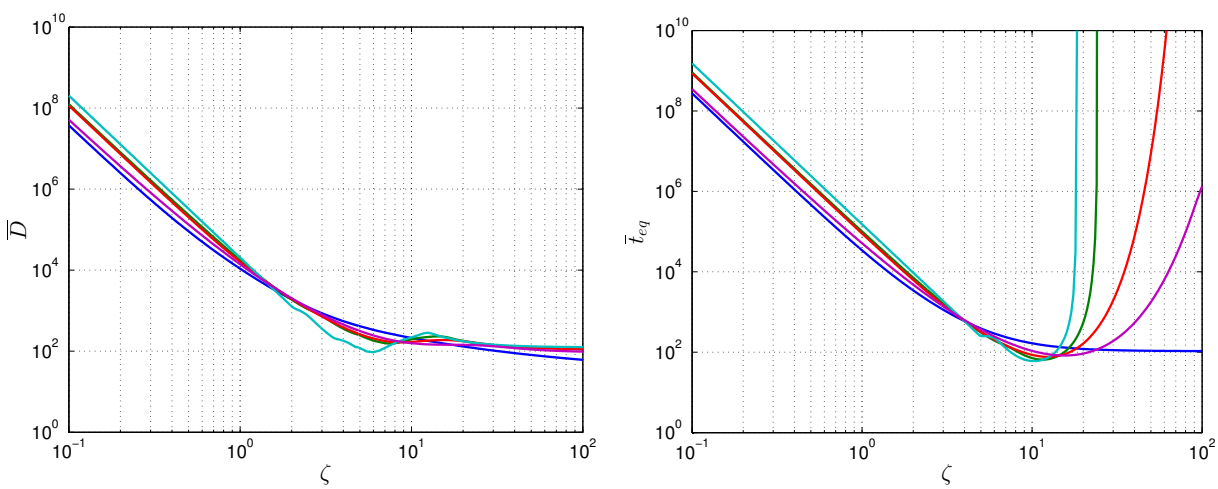

Figure 2.8: $\bar{D}$ (left plot) and $\bar{t}_{eq}$ (right plot) in terms of ζ for $K = \sqrt{3}$ and $\sigma_\lambda = \sigma_\mu = \rho_{\lambda\mu} = 0.1$: exponential (thick solid line), power-law (thin dashed-dotted line), Gaussian (thick dashed line), triangular (thin solid line) and low-pass white noise (thin dashed line).

2.4 Summary and Conclusion

Scattering parameters of the elastic waves propagating in weakly heterogeneous media depend on four key parameters *i.e.* the medium fluctuation level δ, the ratio between the averages of phase velocities K, the adimensional frequency $\zeta = |\mathbf{k}_p| l_c$ and the correlation kernel of the random medium $\hat{R}$. The assessment of their influence on the values of scattering parameters is studied in this chapter. We proved that the value of PSDF at origin ($\Phi(0)$) appears in low frequencies for

all different mode conversions. In high frequencies, for P-to-P and S-to-S mode conversions, no influence of the correlation kernel is observed. On the contrary, in this limit, the P-to-S (or S-to-P) scattering parameters are extremely dependent on the correlation kernel. The limits corresponding to all models are zero except the exponential model which converges to a constant. As a result, in low frequencies, the required time to reach a global equipartitioning regime is described by $1/\Phi(0)$. Moreover, the high frequency limit of the equipartitioning time is model-dependent. For models with bounded support of PSDF, the corresponding limit is undefined. For power-law and Gaussian models, the limits tend to infinity and a polynomial representation is impossible. Finally, for exponential model, the values of equipartitioning time in high frequencies tend to a constant.

Chapter 3

Elastic wave propagation in an isotropic randomly heterogeneous medium

3.1 The Spectral Element Code SPEC3D

3.1.1 Numerical methods in elastodynamics

Since the principal objective of this work is the analysis of elastic wave propagation through a randomly heterogeneous medium subjected to a given source, several numerical approaches could be employed such as: *finite difference*, *finite elements*, *boundary elements*, *spectral elements*, etc. The dimension of the medium, the complexity of its boundaries, the fluctuation level of the heterogeneities, the Sommerfeld radiation condition at infinity (for unbounded media) and the linear (small deformations) or nonlinear (large deformations) behavior of the underlying medium are some of the influential factors on the efficiency and accuracy of these numerical methods. The advantages and drawbacks of the specified numerical methods highly depend on these factors. For a detailed review and comparison between these methods in elastodynamics see Semblat (2010). In the next paragraphs, we will succinctly discuss the above-mentioned numerical methods.

The finite difference method (FDM) is based on the solution of the wave equation (equation (1.1)) by replacing the spatial and temporal partial derivatives by their finite difference approximations (Frankel, 1989). This method has been widely used to model the wave propagation in 2D and 3D media (Frankel and Clayton (1984), Virieux (1986) and Moczo et al. (2002)). It is mostly adapted to simple geometries. In classical FDM, in order to reduce the numerical dispersion [1] related to the finite difference grid, at least 15 grid points per shortest wavelength should be used. This implies considerable numerical costs compared to other numerical methods (at typical propagation lengths considered in this study). However, using the fourth-order finite difference scheme proposed by Levander (1988), allows to use 5 grid points per shortest wavelength which decreases significantly the calculation costs. Despite this improvement, there is still a fundamental inconvenience in this type of methods which is the difficulty to implement the free surface boundary condition with the same precision as the interior of the domain for complicated geometries (see for instance Virieux (1986), Levander (1988) Moczo et al. (2002) and Bohlen and Saenger (2006)).

[1] The numerical dispersion means that the wave's velocity depends on frequency which causes the distortion of the waveforms.

The boundary element method (BEM) is based on the solution of the partial differential equation (1.1) written in the form of a so-called boundary integral equation. The BEM is derived from the Maxwell-Betti reciprocity work theorem which enables us to calculate the displacement field within a domain Ω in terms of the displacement and stress fields calculated over its boundary $\partial\Omega$. This method has been used since long time in acoustics and seismology. For more details about this group of methods the readers are invited to see Dangla (1989), Clouteau (1990) and Sanchez-Sesma and Luzon (1995) for applications in elastodynamics and seismology. The main drawback of this approach is its limitation to the problems for which the Green's function is known analytically as in linear homogeneous media. Therefore, the BEM is mostly adapted to weakly heterogeneous media with linear material behavior (Semblat, 2010). The strong points of the BEM are its natural capacity to model the unbounded media and the reduced dimension of the space discretization (the search space has always one dimension less than the domain).

The finite element method (FEM) which is based on the weak form of wave equation, allows for more natural consideration of the boundary conditions compared to the FDM (in particular the free surface condition). Despite the fact that the FEM is well adapted to the complex geometries as well as the heterogeneous materials, it is not frequently used in seismology because of the numerical dispersion and damping along with high numerical costs in 3D problems (Toshinawa and Ohmachi (1992), Semblat et al. (2008)). The lower-order FEM ($p < 4$, p being the order of the shape function which will be discussed later in this chapter) is less accurate and have more numerical dispersion in elastodynamics. Even the classical higher-order FEM will give rise to other problems such as the occurrence of spurious waves which are nonphysical and make elements of high order useless for accurate computation (Mulder, 1999). Different aspects of this method in the context of wave propagation in elastic media are discussed in Andersen (2006).

The spectral element method (SEM) is a high-order variational discretization of the partial differential equations based on the original ideas of Patera (1984) for the Chebyshev polynomials. It is then developed by Maday and Patera (1988) for Legendre polynomial basis, in which we are interested in this study. This method results in a diagonal representation of the mass matrix which reduces significantly the computational costs. As in higher-order FEM, numerical wave dispersion which depends highly on the order of the finite elements shape functions will be reduced. Applications of the SEM in 2D and 3D elastodynamics have shown high accuracies and weak numerical dispersions (see Faccioli et al. (1997), Komatitsch and Vilotte (1998) and Paolucci et al. (1999) for instance). Hence, this method is increasingly used in multidimensional problems in elastodynamics notably due to its exponential convergence rate (Chaljub et al. (2007)). The SEM could be related to the hp-FEM (Hörlin, 2005) in which the mesh is refined using a suitable combination of h and p-refinements (subdivision of the elements into smaller ones and increasing their polynomial degree) that will result in an exponentially convergent method. The numerical code which will be used in this study is developed base on the SEM.

In the next section, we briefly introduce the SEM in elastodynamics.

3.1.2 An introduction to the spectral elements

In this section, a brief introduction to the mathematical formulation of the spectral elements will be given (see Komatitsch (1997) and Festa and Vilotte (2005) for detailed discussion). An inhomogeneous medium occupying an open region $\Omega \in \mathbb{R}^3$ over a time domain $T \in (0, t)$ is under

study. The displacement and velocity vector fields are denoted respectively by $\mathbf{u}(\mathbf{x},t)$ and $\mathbf{v}(\mathbf{x},t)$. The weak or variational form of the elastodynamic equilibrium equations can be written as the following equation for any test function $\mathbf{w}$ (Komatitsch et al., 1999):

$$\begin{cases} (\mathbf{w}, \rho\dot{\mathbf{v}})_\Omega = (\mathbf{w}, \mathbf{f})_\Omega - \mathcal{A}_\Omega(\mathbf{w}, \mathbf{u}) \\ (\mathbf{w}, \dot{\mathbf{u}})_\Omega = (\mathbf{w}, \mathbf{v})_\Omega \end{cases} \tag{3.1}$$

along with initial conditions:

$$(\mathbf{w}, \mathbf{u}(\mathbf{x}, t=0))_\Omega = (\mathbf{w}, \mathbf{u}_0)_\Omega \quad ; \quad (\mathbf{w}, \mathbf{v}(\mathbf{x}, t=0))_\Omega = (\mathbf{w}, \mathbf{v}_0)_\Omega \tag{3.2}$$

in which ρ and $\mathbf{f}$ are respectively the density and the external forces. The classical inner product $(\cdot,\cdot)_\Omega$ and $\mathcal{A}_\Omega(\mathbf{w},\mathbf{u})$ are defined as:

$$(\mathbf{w}, \mathbf{u})_\Omega = \int_\Omega \mathbf{w} \cdot \mathbf{u} dV \tag{3.3}$$

$$\mathcal{A}_\Omega(\mathbf{w}, \mathbf{u}) = \int_\Omega \nabla_\mathbf{x}\mathbf{w} \colon C \colon \mathrm{sym}(\nabla_\mathbf{x}\mathbf{u}) dV \tag{3.4}$$

Two types of discretizations should be done: discretization in space and time. They will be separately discussed in the following sections.

Spatial discretization

Spatial discretization consists of partitioning the physical domain Ω into a finite ensemble of non-overlapping elements $\Omega_e \subset \Omega$ such that $\bigcup_{e=1}^{n_{\mathrm{el}}} \Omega_e = \Omega$ with n_{el} being the total number of elements. In this study the hexahedral elements with 8 nodes are adopted. The integrals over the whole domain will be subdivided in terms of smaller integrals over the elements Ω_e. For example:

$$(\mathbf{w}, \mathbf{u})_\Omega = \sum_{e=1}^{n_{\mathrm{el}}} (\mathbf{w}^e, \mathbf{u}^e)_{\Omega_e} = \sum_{e=1}^{n_{\mathrm{el}}} \int_{\Omega_e} \mathbf{w}^e \cdot \mathbf{u}^e dV^e \tag{3.5}$$

in which $\mathbf{w}^e$ and $\mathbf{u}^e$ and dV^e are the restrictions of the corresponding parameters to the element number e, *i.e.* $\mathbf{w}^e(\mathbf{x},t) = \mathbf{w}(\mathbf{x},t)\,|_{\mathbf{x}\in\Omega_e}$ for instance. Let $\square_\Omega = [-1,+1]^3$ be a hexahedral reference element for the whole domain Ω. As it can be observed in Figure 3.1, each element in physical domain Ω_e is the image of the reference element by means of a geometrical transformation $\mathcal{F}_e$ corresponding to Ω_e defined as $\mathcal{F}_e \colon \square_\Omega \to \Omega_e$ such that $\mathbf{x}(\boldsymbol{\xi}) = \mathcal{F}_e(\boldsymbol{\xi})$. $\boldsymbol{\xi}$ is the Cartesian coordinates defined over the 8-node hexahedron reference element which is used in this study (see Figure 3.1). A classical way to define the function $\mathcal{F}_e$ is to interpolate $\mathbf{x}$ using n_p control points $\mathbf{a}^i$ in each element Ω_e ($e = 1, 2, ..., n_{\mathrm{el}}$). These geometrical interpolation functions which are also called the shape functions are chosen as the product of the Lagrange polynomials following each of the three axes. The point $\mathbf{x}$ in element Ω_e is uniquely related to the point $\boldsymbol{\xi}$ in the reference element $\square_\Omega$ via the invertible mapping:

$$\mathbf{x}(\boldsymbol{\xi}) = \mathcal{F}_e(\boldsymbol{\xi}) = \sum_{i=1}^{n_p} \mathbf{a}^i N_{\mathbf{a}^i}(\boldsymbol{\xi}) = \sum_{i=1}^{n_p} \mathbf{a}^i \prod_{j=1}^{3} l^n_{\mathbf{a}^i}(\xi_j) \tag{3.6}$$

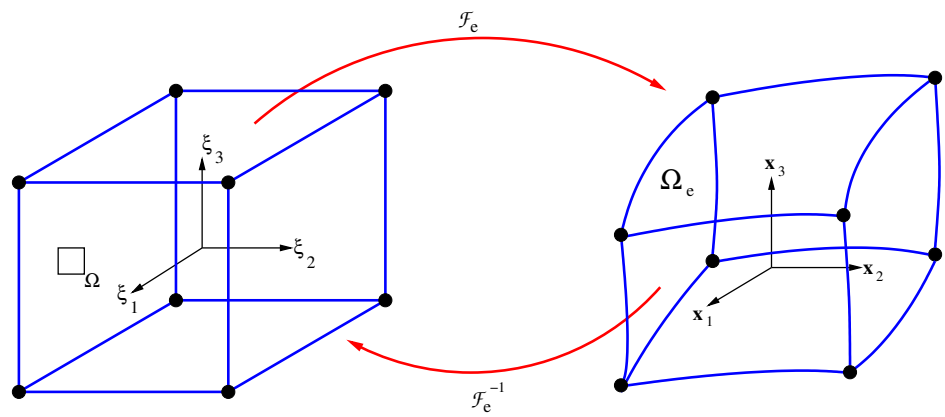

Figure 3.1: 8-node hexahedron reference element and the mapping function

in which $l^n_{\mathbf{a}^i}(\xi_j)$ $(i \in \{1, 2, ..., n_p\}, j \in \{1, 2, 3\}, \xi_j \in [-1, +1])$ is the nth order Lagrange polynomial associated to the ith control point following jth direction. The Jacobian of the mapping $\mathbf{J} = \nabla_{\boldsymbol{\xi}}\mathbf{x}$ will be therefore related to the derivatives of the shape functions:

$$\mathbf{J} = \nabla_{\boldsymbol{\xi}}\mathbf{x} = \sum_{i=1}^{n_p} \mathbf{a}^i \frac{\partial N_{\mathbf{a}^i}(\boldsymbol{\xi})}{\partial \boldsymbol{\xi}} \tag{3.7}$$

The choice of the Lagrange polynomials guarantees that the Jacobian of the coordinate transformation will not be singular which means that its determinant does not cancel over the entire domain. It should be also pointed out that n is often considered to be 1 or 2 (linear and quadratic) and that the shape functions N is defined as:

$$N_{\mathbf{a}^i}(\boldsymbol{\xi}(\mathbf{a}^j)) = \delta_{ij} \tag{3.8}$$

where δ_{ij} is the Kronecker's delta function. In general, for n_p control points, the Lagrange polynomials of degree $n_p - 1$ following each direction are defined as:

$$l^{n_p}_{\alpha}(\xi) = \frac{(\xi - \xi_1)(\xi - \xi_2)\cdots(\xi - \xi_{\alpha-1})(\xi - \xi_{\alpha+1})\cdots(\xi - \xi_{n_p})}{(\xi_\alpha - \xi_1)(\xi_\alpha - \xi_2)\cdots(\xi_\alpha - \xi_{\alpha-1})(\xi_\alpha - \xi_{\alpha+1})\cdots(\xi_\alpha - \xi_{n_p})} \tag{3.9}$$

in which $\alpha = 1, 2, ..., n_p$ and $-1 \leq \xi_\alpha \leq 1$.

In isoparametric finite elements, the basis functions which are used to interpolate the wavefield (the displacement $\mathbf{u}(\mathbf{x}, t)$) are the same as the shape functions N. In SEM, typically Lagrange interpolation functions (defined in equation (3.9)) of degree 4-10 are used. The best trade-off between accuracy and computation time (due to stability condition) could be obtained using Legendre polynomials of order 4 or 5 (Seriani and Priolo (1994) and Tromp et al. (2008)). In numerical simulations of wave propagation which will be carried out in this study, Lagrange polynomials are of order 7. The control points on each direction ξ_i where i is the number of the control point $(i \in \{1, 2, ..., n\})$ are chosen to be the n Gauss-Lobatto-Legendre (GLL) points which are the solutions of the following equation (Canuto et al., 1988):

$$(1 - \xi^2)\frac{dP_n(\xi)}{d\xi} = 0 \tag{3.10}$$

in which $\frac{dP_n(\xi)}{d\xi}$ is the derivative of the Legendre polynomial of order n (Abramowitz and Stegun, 2012):

$$P_n(\xi) = \frac{1}{2^n n!} \frac{d^n}{d\xi^n} \left((\xi^2 - 1)^n \right) \tag{3.11}$$

Using n control points in each direction results in n^3 degrees of freedom over each element which are not uniformly spaced. Figure 3.2a depicts the Lagrange polynomials of degree 4 all of which passing through the GLL points which are the five roots of the equation $(1 - \xi^2)P_4'(\xi) = 0$, *i.e.* $\xi_{GLL} = \{-1, -0.65, 0, +0.65, +1\}$. These points create the mesh which is shown in Figure 3.2b.

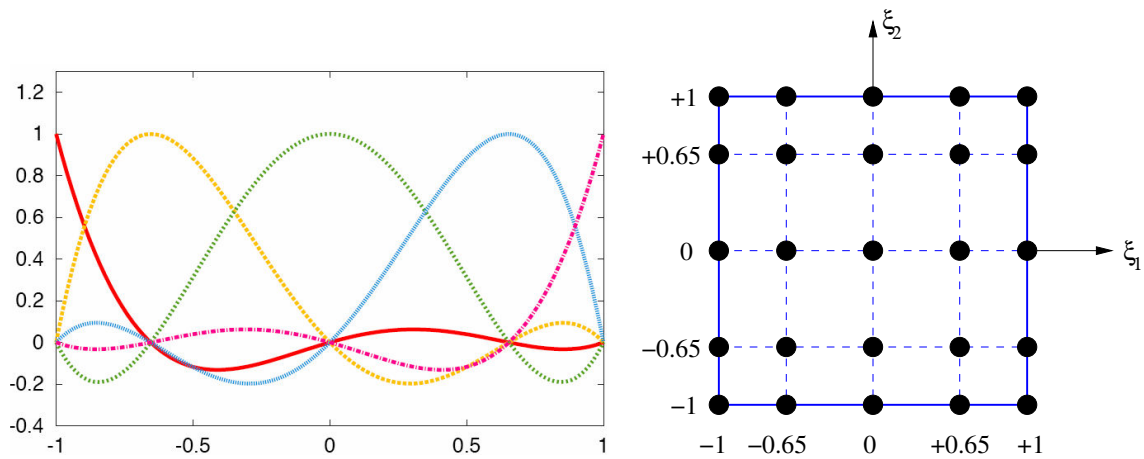

(a) (b)

Figure 3.2: (a) Five Lagrange polynomials of order 4. (b) GLL points of degree 4

The displacement field $\mathbf{u}(\mathbf{x})$ or the response of the medium can now be expanded in terms of Lagrange polynomials:

$$\mathbf{u}(\mathbf{x}(\xi_1, \xi_2, \xi_3)) = \sum_{\alpha=0}^{n} \sum_{\beta=0}^{n} \sum_{\gamma=0}^{n} \mathbf{u}(\mathbf{x}(\xi_\alpha^n, \xi_\beta^n, \xi_\gamma^n)) l_\alpha^n(\xi_1) l_\beta^n(\xi_2) l_\gamma^n(\xi_3) \tag{3.12}$$

where $(\xi_1, \xi_2, \xi_3) = \mathcal{F}_e^{-1}(\mathbf{x})$ is the coordinates in the reference element corresponding to the point $\mathbf{x}$, ξ_α^n is the coordinates of a node in the reference element $\square_\Omega$ associated with the polynomial $l_\alpha^n(\xi)$, $n+1$ is the number of GLL points used in each direction (hereafter we suppose that the number of GLL points is the same in each direction) and $\mathbf{u}(\mathbf{x}(\xi_\alpha^n, \xi_\beta^n, \xi_\gamma^n))$ is the value of the desired field $\mathbf{u}$ at GLL points. The next step will be the evaluation of the integrals over the elements (the integral in equation (3.5) for instance). For this purpose, in the framework of the SEM, a Gauss-Lobatto integration rule (see for example Abramowitz and Stegun (2012)) is used which leads to a diagonal mass matrix (this will be shown further down in this section). The integral of any function $f(\mathbf{x})$ over the element Ω_e is related to that over the reference element which itself could be approximated as:

$$\begin{aligned} \int_{\Omega_e} f(\mathbf{x}) dV^e &= \int_{-1}^{+1} \int_{-1}^{+1} \int_{-1}^{+1} f(\mathbf{x}(\xi_1, \xi_2, \xi_3)) |\mathbf{J}(\xi_1, \xi_2, \xi_3)| d\xi_1 d\xi_2 d\xi_3 \\ &\simeq \sum_{\alpha=0}^{n} \sum_{\beta=0}^{n} \sum_{\gamma=0}^{n} f(\mathbf{x}(\xi_\alpha^n, \xi_\beta^n, \xi_\gamma^n)) |\mathbf{J}(\mathbf{x}(\xi_\alpha^n, \xi_\beta^n, \xi_\gamma^n))| \omega_\alpha^n \omega_\beta^n \omega_\gamma^n \end{aligned} \tag{3.13}$$

in which for instance ω_α^n ($\alpha = 0, 1, \cdots, n$) represent the quadrature weights associated with the Gauss-Lobatto integration scheme (Tromp et al., 2008):

$$\omega_\alpha^n = \frac{2}{n(n+1)} \frac{1}{\left(P_n(\xi_\alpha^n)\right)^2} \tag{3.14}$$

The corresponding integral over the whole medium can therefore be written as:

$$\begin{aligned}\int_\Omega f(\mathbf{x}) dV = \sum_{e=1}^{n_{\text{el}}} \int_{\Omega_e} f(\mathbf{x}) dV^e &= \sum_{e=1}^{n_{\text{el}}} \int_{-1}^{+1} \int_{-1}^{+1} \int_{-1}^{+1} f(\mathbf{x}(\xi_1, \xi_2, \xi_3)) |\mathbf{J}(\xi_1, \xi_2, \xi_3)| d\xi_1 d\xi_2 d\xi_3 \\ &\simeq \sum_{e=1}^{n_{\text{el}}} \sum_{\alpha=0}^{n} \sum_{\beta=0}^{n} \sum_{\gamma=0}^{n} f(\mathbf{x}(\xi_\alpha^n, \xi_\beta^n, \xi_\gamma^n)) |\mathbf{J}(\mathbf{x}(\xi_\alpha^n, \xi_\beta^n, \xi_\gamma^n))| \omega_\alpha^n \omega_\beta^n \omega_\gamma^n \end{aligned} \tag{3.15}$$

Matrix form of the semi-discrete initial value problem

As in classical finite elements, the procedure of the spatial discretization mentioned in previous section leads to a coupled system of first-order ordinary differential equations in time:

$$\begin{cases} \mathcal{M} \dot{\mathbf{v}}(t) = \mathcal{F}^{\text{ext}}(t) - \mathcal{F}^{\text{int}}(\mathbf{u}, t) \\ \dot{\mathbf{u}}(t) = \mathbf{v}(t) \end{cases} \tag{3.16}$$

where $\mathbf{u}$ is now the vector of nodal values resulting from the spatial discretization with polynomials of order n. The mass matrix $\mathcal{M}$ along with the vectors corresponding to the external and internal forces, $\mathcal{F}^{\text{ext}}$ and $\mathcal{F}^{\text{int}}$ in equation (3.16), are assembled from the corresponding elementary parameters:

$$\mathcal{M} = \biguplus_{e=1}^{n_{\text{el}}} \mathcal{M}^e \quad ; \quad \mathcal{F}^{\text{ext}} = \biguplus_{e=1}^{n_{\text{el}}} \mathcal{F}^{\text{ext,e}} \quad ; \quad \mathcal{F}^{\text{int}} = \biguplus_{e=1}^{n_{\text{el}}} \mathcal{F}^{\text{int,e}} \tag{3.17}$$

where $\biguplus$ denotes the assembling operator. It can be shown that in a SEM framework, the elementary mass matrix $\mathcal{M}^e$ is the tensor product of the identity matrix $\mathbf{Id}_3$ (in 3D problems) and a matrix $\hat{\mathcal{M}}^e$ which is characteristic of the SEM, *i.e.* $\mathcal{M}^e = \mathbf{Id}_3 \otimes \hat{\mathcal{M}}^e$ in which using $n+1$ GLL points in each direction, $\hat{\mathcal{M}}^e$ becomes a $(n+1)^3 \times (n+1)^3$ matrix. Using a Gauss-Lobatto integration rule we have (see Festa and Vilotte (2005) or Delavaud (2007) for instance):

$$\hat{\mathcal{M}}_{ij}^e = \int_{\Omega_e} \rho(\boldsymbol{\xi}) N_{\mathbf{a}^i}(\boldsymbol{\xi}) N_{\mathbf{a}^j}(\boldsymbol{\xi}) d\boldsymbol{\xi} = \rho(\xi_\alpha^n, \xi_\beta^n, \xi_\gamma^n) |\mathbf{J}(\mathbf{x}(\xi_\alpha^n, \xi_\beta^n, \xi_\gamma^n))| \omega_\alpha^n \omega_\beta^n \omega_\gamma^n \delta_{ij} \tag{3.18}$$

which is obviously a diagonal matrix. This diagonal representation of the mass matrix allows a straightforward calculation of its inverse, an efficient parallel implementation and reduces the computational costs drastically (Komatitsch et al. (1999) or Tromp et al. (2008)).

Time discretization

In order to solve the system of equations (3.16), one should discretize the time interval $(0, t)$ using a time step Δt. For this purpose, a modified Newmark scheme with three control parameters $\{\alpha, \beta, \gamma\} \in [0, 1]$ will be used. For a complete review about the family of Newmark numerical schemes see Hughes (2012). Let $\mathbf{u}_m$, $\mathbf{v}_m$ and $\mathbf{a}_m$ be respectively the time-discrete approximations of the displacement, velocity and acceleration fields in mth time step, *i.e.* $\mathbf{u}_m = \mathbf{u}(t_m)$, $\mathbf{v}_m = \mathbf{v}(t_m)$

and $\mathbf{a}_m = \mathbf{a}(t_m)$ with $t_m = m\Delta t$. The semi-discrete momentum equation at the time $t_{n+\alpha}$ (a time which varies between t_n and t_{n+1} depending on the value of α) reads (see Simo et al. (1992) or Komatitsch (1997) for example):

$$\begin{cases} \dfrac{1}{\Delta t}\mathcal{M}(\mathbf{v}_{n+1} - \mathbf{v}_n) = \mathcal{F}^{\text{ext}}_{n+\alpha} - \mathcal{F}^{\text{int}}(\mathbf{u}_{n+\alpha}, \mathbf{v}_{n+\alpha}) \\ \mathbf{u}_{n+1} = \mathbf{u}_n + \Delta t \left[\left(1 - \dfrac{\beta}{\gamma}\right)\mathbf{v}_n + \dfrac{\beta}{\gamma}\mathbf{v}_{n+1}\right] + (\Delta t)^2 \left(\dfrac{1}{2} - \dfrac{\beta}{\gamma}\right)\mathbf{a}_n \\ \mathbf{a}_{n+1} = \dfrac{1}{\gamma\Delta t}(\mathbf{v}_{n+1} - \mathbf{v}_n) + \left(1 - \dfrac{1}{\gamma}\right)\mathbf{a}_n \end{cases} \tag{3.19}$$

in which:

$$\begin{cases} \mathbf{u}_{n+\alpha} = (1-\alpha)\mathbf{u}_n + \alpha\mathbf{u}_{n+1} \\ \mathbf{v}_{n+\alpha} = (1-\alpha)\mathbf{v}_n + \alpha\mathbf{v}_{n+1} \\ \mathcal{F}^{\text{ext}}_{n+\alpha} = (1-\alpha)\mathcal{F}^{\text{ext}}_n + \alpha\mathcal{F}^{\text{ext}}_{n+1} \end{cases} \tag{3.20}$$

Finally a predictor-multicorrector scheme will be used in which the state of the system at each time step will be completely determined by that of the previous time step. Following Komatitsch and Vilotte (1998), different steps of this scheme can be summarized as follows:

1. **Predictor phase:** Between each two time steps n and $n+1$, the iterations (denoted with iteration counter i) will be done until the convergence occurs. At first, the iteration counter i is set to zero. The field values at the time step $n+1$ for the iteration number i are supposed to be known. The schemes based on velocity and acceleration correspond respectively to the cases in which the predictor of the corresponding parameters is set to zero. In this study we adopt a velocity-based scheme which is the time integration scheme implemented in our numerical code. The predictors are therefore:

$$\mathbf{u}^{(i)}_{n+1} = \tilde{\mathbf{u}}_{n+1} \quad ; \quad \mathbf{v}^{(i)}_{n+1} = \mathbf{0} \quad ; \quad \mathbf{a}^{(i)}_{n+1} = \tilde{\mathbf{a}}_{n+1} \tag{3.21}$$

in which $\tilde{\mathbf{u}}_{n+1}$ and $\tilde{\mathbf{a}}_{n+1}$ are defined as:

$$\begin{cases} \tilde{\mathbf{u}}_{n+1} = \mathbf{u}_n + \Delta t \left(1 - \dfrac{\beta}{\gamma}\right)\mathbf{v}_n + (\Delta t)^2 \left(\dfrac{1}{2} - \dfrac{\beta}{\gamma}\right)\mathbf{a}_n \\ \tilde{\mathbf{a}}_{n+1} = \left(1 - \dfrac{1}{\gamma}\right)\mathbf{a}_n - \dfrac{1}{\gamma\Delta t}\mathbf{v}_n \end{cases} \tag{3.22}$$

2. **Solution phase:** At each iteration i, the state of the system in time t_{n+1} is related to that in time t_n via:

$$\frac{1}{\Delta t}\mathcal{M}\Delta\mathbf{v}^{(i)} = \mathcal{F}^{\text{ext}}_{n+\alpha} - \mathcal{F}^{\text{int}}(\mathbf{u}^{(i)}_{n+\alpha}, \mathbf{v}^{(i)}_{n+\alpha}) - \frac{1}{\Delta t}\mathcal{M}\left[\mathbf{v}^{(i)}_{n+1} - \mathbf{v}_n\right] \tag{3.23}$$

3. **Corrector phase:** At the next iteration $i+1$, the corrections which should be applied to the fields are:

$$\begin{cases} \mathbf{v}^{(i+1)}_{n+1} = \mathbf{v}^{(i)}_{n+1} + \Delta\mathbf{v}^{(i)} \\ \mathbf{u}^{(i+1)}_{n+1} = \tilde{\mathbf{u}}_{n+1} + \dfrac{\beta\Delta t}{\gamma}\mathbf{v}^{(i+1)}_{n+1} \\ \mathbf{a}^{(i+1)}_{n+1} = \tilde{\mathbf{a}}_{n+1} - \dfrac{1}{\gamma\Delta t}\mathbf{v}^{(i+1)}_{n+1} \end{cases} \tag{3.24}$$

If the convergence does not occur yet, the iteration counter i is replaced by $i+1$ and the procedure will be repeated from the equation (3.23). In all numerical simulations performed in this study, the values $\alpha = \frac{1}{2}$ (corresponding to a central differencing scheme), $\beta = \frac{1}{2}$ and $\gamma = 1$ will be used which result in a conditionally stable scheme (Simo et al., 1992). The accuracy and stability of the numerical method is ensured when both following conditions are satisfied (Cupillard et al., 2012):

(1) In order to properly estimate the wavefields ($\mathbf{u}$, $\mathbf{v}$, $\mathbf{a}$), based on experience, at least five GLL points per wavelength are needed (see Faccioli et al. (1997) and Fichtner and Trampert (2011) for instance). This means that the shortest wavelength λ_{min} constrains both the size of the elements d, and the polynomial order n. These parameters form the following heuristic criteria:

$$d \leq \frac{n}{5}\lambda_{min} \tag{3.25}$$

(2) The stability of the solving method is ensured with Courant-Friedrichs-Lewy (CFL) condition which depends on the minimum grid spacing between GLL points. The time integration scheme is stable if the time step Δt, satisfies the following CFL condition:

$$\Delta t \leq C \left[\frac{\Delta x}{v_p}\right]_{min} \tag{3.26}$$

in which C is the Courant number which takes empirically (depending on the geometry of the problem and the frequencies involved) the values of 0.4 and 0.6 and 0.8 for 3D, 2D and 1D media. $\left[\frac{\Delta x}{v_p}\right]_{min}$ is the minimum value of the ratio between the grid spacing and the P-wave speed.

In the simulations performed in this work, the size of each element is taken to be $d = 50$(m) being compatible with the correlation length of the order $\ell_c = 100$(m). Typical dominant wavelength for the P and S waves lengths are respectively $\lambda_p = 173$(m) and $\lambda_s = 100$(m). For a Ricker pulse with a central frequency of $f_0 = 10$Hz, the minimum wavelength of S waves can be calculated considering the maximum frequency of $f_{\max} \simeq 2.5 f_0 = 25$Hz which gives a minimum value of 40(m). As a result, following equation (3.25), for $d = 50$(m) and $\lambda_{\min} = 40$(m), the minimum polynomial order should be $n_{min} = 7$ which is used in this study.

In the next section, we introduce the numerical tool that will be used further in this chapter to carry out the simulations of elastic waves propagation in random heterogeneous media.

3.1.3 An introduction to the software SPEC3D

SPEC3D is a parallel computing code which is used in this presentation to simulate the propagation of elastic waves in randomly heterogeneous media. This code is written in Fortran 90 and parallelized using MPI and was initially developed at *Institut de Physique du Globe de Paris* (Cupillard et al., 2012). It can be run on a single processor as well as multi-core machines or large clusters. The software package SPEC3D performs the 3D numerical simulations of seismic wave propagation at the scale of a few kilometers (in each direction). Most simulations were performed using 100 to 200 processors and the elapsed walltime was roughly half of a day (note that the dominant shear wavelength is considered to be $100(m)$). SPEC3D is developed with initial works of Festa and

Vilotte (2005), Delavaud (2007), Cupillard (2008), Cottereau et al. (2007) and Ta et al. (2010) (see also Cupillard et al. (2012)). It is based on the SEM that has been already elaborated in Section 3.1.2. We also cite SPECFEM3D [2] (Komatitsch et al., 2010) and SPEED [3] (Stupazzini et al., 2009) and (Mazzieri et al., 2013) as other examples of spectral element based computational codes.

The only discretization that is done by SPEC3D is that of the reference elements. The meshing process is done in two steps. At first, a mesh containing the 8-nodes hexahedral elements is generated. Subsequently the mesh is partitioned into various subdomains via METIS which is a software package based on multilevel graph partitioning (Karypis and Kumar, 1998). It should be pointed out that this mesh partitioning is done via a non-parallelized Fortran code.

Roughly speaking, SPEC3D is a code with linear growth of resource requirements, that is to say that the simulation time varies almost linearly in function of the number of degrees of freedom per processor. The scalability of SPEC3D is studied and the main results are depicted in Figure 3.3. Figure 3.3a shows the variation of the ratio between the number of degrees of freedom in the propagation medium and the number of processors in terms of the simulation time per each time step which is almost a line passing through the origin. This implies that the code is highly scalable. Figure 3.3b depicts, in a logarithmic scale, the variation of the simulation time per each time step in terms of the number of processors for constant degrees of freedom (each color represents a certain number of degrees of freedom). Increasing the number of the degrees of freedom necessitates using more processors. Because of too few degrees of freedom per processor, the simulations in this thesis are typically performed using 96 processors. They are executed over the processors in *Mesocentre de calcul de Centrale Paris*[4]. The *ultimate simulation* performed in this work is a medium whose random elastic matrix has a flat PSDF and its dimensions are 3km $\times$ 3km $\times$ 3km or in terms of shear wavelength $30\lambda_s \times 30\lambda_s \times 30\lambda_s$ and has about 7.5×10^7 degrees of freedom.

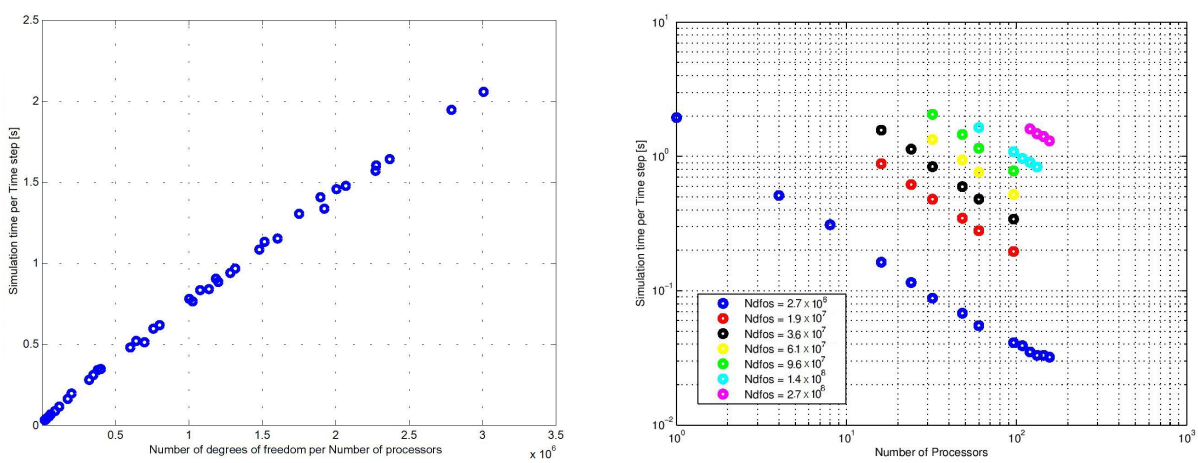

(a) (b)

Figure 3.3: (a) Variation of the number of degrees of freedom in the propagation medium over the number of processors in terms of the simulation time per each time step. (b) The variation of the simulation time per each time step in terms of the number of processors for constant degrees of freedom

[2] http://geodynamics.org/cig/software/specfem3d

[3] https://mox.polimi.it/it/progetti/speed/

[4] More relevant information about this center of parallel calculations can be found at http://www.mesocentre.ecp.fr/.

3.1.4 Adaptations of SPEC3D for different correlation models with isotropic structure

The implementation of the elastic matrix random field modeled with the probabilistic law defined in Soize (2000) (see Appendix C) in locally isotropic materials using the spectral representation method (Shinozuka and Deodatis, 1988) was initially done in SPEC3D by Régis Cottereau. Then, Ta (2011) decoupled the statistical fluctuation level of the elastic random field in Soize's model by introducing a new so-called anisotropy index which is defined as the random variable of the distance between local elastic matrices and the isotropic matrix and is therefore restricted to the *a priori* description of the isotropic elastic matrix (Ta et al., 2010). He then implemented the random elastic matrix in the general case of anisotropic material behavior. In both of these developments, the correlation kernel of the underlying random medium was considered to have an anisotropic structure: Φ was assumed to be spatially separable following 3 directions:

$$\Phi(k_x, k_y, k_z) = \Phi_x(k_x) \cdot \Phi_y(k_y) \cdot \Phi_z(k_z) \tag{3.27}$$

By contrast, since the analytical formulas of elastic wave scattering are valid only for isotropic correlation structures (chapter 2), the code SPEC3D was adapted in this work to the case of random media whose PSDF depends solely on the radial wavenumber $|\mathbf{k}| = \sqrt{k_x^2 + k_y^2 + k_z^2}$:

$$\Phi(k_x, k_y, k_z) = \Phi(|\mathbf{k}|) \tag{3.28}$$

Moreover, different correlation kernels were implemented in the code to observe numerically the theoretical results obtained in chapter 2.

In this section, at first the numerical generation of the random elastic matrix field is discussed. Subsequently, the structure of the underlying power spectrum/correlation of the random media will be of our interest. The implementations in SPEC3D will be also expressed.

Generation of the elasticity random field: In this section, numerical simulation of the random matrix $\mathbf{C}(\theta, \mathbf{x})$ which is defined in chapter 1 will be investigated. θ characterizes the randomness in $\mathbf{C}$. Therefore, the main objective is to separate the spatial ($\mathbf{x}$) and the random (θ) dimensions of the random field $\mathbf{C}(\theta, \mathbf{x})$ and to approximate its random dimension, which is *a priori* infinite, using a projection over a basis with finite dimension. For this purpose, several approaches are proposed in the literature which are summarized in Puig (2003). In this dissertation, the *spectral representation method* (Shinozuka and Deodatis (1988, 1991)) will be used to simulate the Gaussian stochastic germs and then a so-called *inverse transform sampling technique* (Devroye, 1986) is employed to generate the stochastic germs following any prescribed first-order marginal probability density function. One of the main reasons to use this method is based on the simplicity of implementation. The main steps to follow in order to create *a single realization* of the random elasticity matrix with local material isotropy are summarized below (see Arnst (2007) or Ta (2011) for more details):

- **Initialization:**

  (1) Choose the mean model which is described with the average values of the compressibility and shear moduli $(\underline{\kappa}, \underline{\mu})$. The mean value of the random matrix $\mathbf{C}$ will be $\underline{\mathbf{C}} = 3\underline{\kappa}\mathbf{S} + 2\underline{\mu}\mathbf{D}$ in which $\mathbf{S}$ and $\mathbf{D}$ are the so-called *spherical* and *deviatoric* matrices

(see Appendix C). In the framework of this study, the mean model is assumed to be space-independent.

(2) Choose the correlation kernel $\Phi(\zeta)$ of the random medium. The support of this function is a key parameter to calculate the necessary wave number discretization steps.

(3) Choose the correlation distance of the medium ℓ_c. In this study, both of the random fields (κ, μ) are assumed to have the same correlation lengths, *i.e.* ${\ell_c}^{\kappa} = {\ell_c}^{\mu} = {\ell_c}^{\kappa\mu} \equiv \ell_c$. Following Shinozuka and Deodatis (1988), the number of degrees of freedoms that should be considered in wave number space in each direction will be $n_x = c_x L_x/\ell_c$, $n_y = c_y L_y/\ell_c$ and $n_z = c_z L_z/\ell_c$ where L_x, L_y and L_z are the medium's lengths in corresponding directions. c_x/ℓ_c, c_y/ℓ_c and c_z/ℓ_c are the cut-off frequencies following each direction which are related to the support of the function Φ. For instance, the value of c for triangular and low-pass white noise correlation models are respectively $3\pi/2$ and 2π as indicated already in Table 2.1. For correlation models with unbounded frequency content, c is chosen such that in the interval $\zeta \in [0, c]$ at least 99% of the total area under the function Φ is covered (see Shinozuka and Deodatis (1991) for more details):

$$\int_0^c \Phi(\zeta) d\zeta = 0.99 \int_0^\infty \Phi(\zeta) d\zeta \tag{3.29}$$

It should be noted that using values less than n_x, n_y and n_z will result in the generation of periodic realizations of the random field.

(4) Choose the dispersion parameter of the medium δ which is simultaneously the fluctuation parameter of the underlying random matrix $\mathbf{C}$ and the coefficient of variation of the random fields κ and μ, *i.e.* $\delta = \delta_{|\mathbf{C}|} = \delta_\kappa = \delta_\mu$ (see Appendix C).

- **Simulation of the samples of random amplitudes and phases:**

The idea is inspired from the *Box-Muller* transform in which the cosine function with independent and uniformly distributed random phase and amplitude will be used to generate two independent random variables with standard normal distributions (see Poirion and Soize (1989) for example). The steps are summarized bellow:

(1) The random amplitudes: Generate a set of $2 \times n_x \times n_y \times n_z$ mutually independent and identically distributed (iid) real random numbers $\mathbb{X}$ derived from a uniform random variable $\mathbb{Z} \sim \mathrm{U}[0, 1]$ as:

$$\mathbb{X} = \sqrt{-\log \mathbb{Z}} \tag{3.30}$$

(2) The random phases: Generate a set of $2 \times n_x \times n_y \times n_z$ iid real random numbers following a uniform distribution $\mathbb{Y} \sim \mathrm{U}[0, 1]$. The random variables $\mathbb{X}$ and $\mathbb{Y}$ are independent.

- **Construction of the samples of the 2-subsets of Gaussian stochastic germs:**

In each point of the finite element mesh, two stochastic germs for κ and μ is required. Following a spectral representation scheme, a realization of the Gaussian stochastic germ in

3D will be:

$$\mathbb{G}_k(\mathbf{x}, \ell_c, \Phi) = \sqrt{2\left(\frac{\pi}{\ell_c}\right)^3} \sum_{l=1}^{\frac{c_x}{\ell_c}} \sum_{m=1}^{\frac{c_y}{\ell_c}} \sum_{n=1}^{\frac{c_z}{\ell_c}} \sqrt{\Phi(|\mathbf{k}_{lmn}|\ell_c)}\mathbb{X}_k \cos(k_{xl}x + k_{y_m}y + k_{zn}z + 2\pi\mathbb{Y}_k) \quad (3.31)$$

in which $\mathbf{x} = (x, y, z)$, $\mathbf{k}_{lmn} = (k_{xl}, k_{y_m}, k_{zn})$ and $k \in \{1, 2\}$. In general, the term $k_{xl}x + k_{y_m}y + k_{zn}z$ should be replaced by the scalar product $(\mathbf{k}, \mathbf{x})$. Equation (3.31) can be rewritten in an equivalent form using the Fast Fourier Transform (FFT) which results in a significant decrease on the computational costs (Cottereau, 2007). For large number of terms in the sum, thanks to the central limit theorem, the generated random field will follow a Gaussian distribution. A discussion about the error occurring by using the approximation resulting from the finite series in equation (3.31) to generate Gaussian random germs can be found in Hu and Schiehlen (1997).

- **Construction of the samples of the elasticity matrix:**

  (1) Generating Gamma stochastic germs:

  We recall from chapter 1 that the stochastic fields κ and μ are independent Gamma random fields. The following Gamma-distributed independent random germs g_k could be generated by using the inverse transform sampling method:

$$g_k = F_k^{-1}(F_{\mathbb{G}}(\mathbb{G}_k)) \quad (3.32)$$

  in which F_k and $F_{\mathbb{G}}$ are respectively the cumulative distribution functions of either κ or μ and $\mathbb{G}$. It should be pointed out that using equation (3.32) will slightly change the target spatial correlation function of the random field $\mathbb{G}_k$ (see Grigoriu (1998) or Puig (2003) for instance).

  (2) Generating the samples of random matrix C:

  We have:

$$\mathbf{C}(\mathbf{x}, \ell_c, \Phi) = 3\kappa(g_1)\mathbf{S} + 2\mu(g_2)\mathbf{D} \quad (3.33)$$

Different correlation models with isotropic structure: Since the assessment of the influence of the correlation model on the scattering parameters of the medium is of our interest (chapter 2), different types of isotropic correlation models are implemented in the code SPEC3D. The ACF and PSDF of the corresponding random media are therefore only functions of the lag distance and the wave number respectively. These models are already introduced in Table 2.1 of chapter 2. For each model, the maximum adimensional frequency ζ or the cut-off frequency which is used in SPEC3D are obtained from equation (3.29). As an example, for exponential correlation model:

$$\int_0^c \Phi^{\exp}(x)dx = 0.99 \int_0^\infty \Phi^{\exp}(x)dx \Rightarrow \tan^{-1}\left(\frac{c}{2}\right) + \frac{2c}{c^2+4} = 0.99 \times \frac{\pi}{2} \Rightarrow c \simeq 3.7 \quad (3.34)$$

Table 3.1 shows the values of the cut-off frequencies for different correlation types. It should be noted that the computational cost of the spectral representation method is largely influenced by the value of c.

In the following section, at first some theoretical aspects of the equipartitioning of elastic waves will be introduced. Subsequently, we will observe this phenomenon via numerical simulations performed using the code SPEC3D.

Table 3.1: Cut-off frequencies used for different correlation models.

Correlation model	Normalized PSDF $\Phi(\zeta)$	Cut-off Frequency $\zeta_{\max} = c/\ell_c$
Exponential	$\frac{1}{8\pi^2\left(1+\frac{\zeta^2}{4}\right)^2}$	$\frac{6.7}{\ell_c}$
Gaussian	$\frac{1}{8\pi^3}\exp\left(-\frac{\zeta^2}{4\pi}\right)$	$\frac{6.45}{\ell_c}$
Power-law	$\frac{1}{\pi^4}\exp\left(-2\frac{\zeta}{\pi}\right)$	$\frac{7.23}{\ell_c}$
Triangular	$\frac{3}{8\pi^4}\left(1-\frac{\zeta}{2\pi}\right)\mathrm{H}\left(2\pi-\zeta\right)$	$\frac{2\pi}{\ell_c}$
Low-pass white noise	$\frac{2}{9\pi^4}\mathrm{H}\left(\frac{3\pi}{2}-\zeta\right)$	$\frac{3\pi}{2\ell_c}$

3.2 Numerical observation of equipartitioning regime in random elastic media

As it has been discussed in chapter 1, at large lapse times the mode conversions between compressional and shear waves during the scatterings result in a stable partition of the energy between these body wave modes irrespective of the initial conditions (location and magnitude of the source) and the details of the scatterings. For full elastic media, the equipartitioned energy ratio is shown to be a function of the ratio between the average speed of P and S waves propagating through the random medium. According to the equation (1.96), the stabilization ratio is also equal to the ratio between P-to-S and S-to-P total scattering cross-sections:

$$\frac{\mathcal{E}_s(t)}{\mathcal{E}_p(t)} = \frac{\Sigma_{PS}(|\mathbf{k}|)}{\Sigma_{SP}(\frac{v_s}{v_p}|\mathbf{k}|)} = 2\left(\frac{v_p}{v_s}\right)^3 = 2K^3 \tag{3.35}$$

A ratio of about 10.4 is expected for crustal materials ($K = \sqrt{3}$) when an equipartitioning regime sets in. Moreover, the global equipartitioning time τ_{eq} which is the time necessary to reach an equipartitioning regime was defined as (see chapters 1 and 2):

$$\tau_{eq} = \frac{1}{\Sigma_{PS} + \Sigma_{SP}} = \frac{1}{\Sigma_{PS}\left(1 + \frac{1}{2K^3}\right)} \tag{3.36}$$

Shapiro et al. (2000) observed the stabilization of energies between P and S waves calculated in coda parts of the seismograms recorded from local earthquakes in Mexico. The stabilization value was about 7 which is different from the expected value of 10.4. This discrepancy can be explained as:

(1) The effects of the anelastic dissipation is in favor of the mode P, meaning that the medium dissipates the S waves more than P wave energy (Margerin et al., 2000).

(2) The free surface over which the energy calculations is done is dominated by the surface Rayleigh waves so that the analytical value corresponding to the full elastic media is not observed.

The second reason will be the subject of Section 3.2.2 where the energies will be calculated using the recorded wavefields at the surface and subsequently the effect of the existence of surface wave modes will be investigated.

3.2.1 Equipartitioning without free surface

The calculation of the energy densities of wave modes requires the information about the local values of the medium parameters. The objective of this section is therefore to express the equipartitioning law in terms of the recorded wavefield in the case of an open medium in which the surface waves do not appear.

The total energy density of elastic waves $\mathcal{E}(\mathbf{x},t)$ is the sum of the kinetic and potential energies. It can be written in terms of the wavefield and the medium parameters (Ryzhik et al., 1996):

$$\mathcal{E}(\mathbf{x},t) = \frac{1}{2}\rho(\mathbf{x})\left|\frac{\partial \mathbf{u}(\mathbf{x},t)}{\partial t}\right|^2 + \frac{1}{2}\lambda(\mathbf{x})(\text{div } \mathbf{u}(\mathbf{x}))^2 + \frac{1}{2}\mu(\mathbf{x})\text{Tr}(\nabla\mathbf{u}(\mathbf{x},t) + \nabla^{\text{T}}\mathbf{u}(\mathbf{x},t))^2 \tag{3.37}$$

in which the first term represents the kinetic energy and the sum of the last two terms corresponds to the strain energy ($\frac{1}{2}\sigma_{kl}\epsilon_{kl}$). The decomposition of the total energy into the P and S wave energies can also be done (see Shapiro et al. (2000) or Hennino et al. (2001) for instance). The total energy can be expressed as:

$$\begin{aligned}\mathcal{E}(\mathbf{x},t) &= \mathcal{E}_k(\mathbf{x},t) + \mathcal{E}_p(\mathbf{x},t) + \mathcal{E}_s(\mathbf{x},t) + \mu(\mathbf{x})\ \mathbf{I}(\mathbf{x},t) \\ &= \frac{1}{2}\rho(\mathbf{x})\left|\frac{\partial \mathbf{u}(\mathbf{x},t)}{\partial t}\right|^2 + \frac{\lambda(\mathbf{x}) + 2\mu(\mathbf{x})}{2}(\text{div } \mathbf{u}(\mathbf{x}))^2 + \frac{\mu(\mathbf{x})}{2}||\nabla \times \mathbf{u}(\mathbf{x})||^2 + \mu(\mathbf{x})\ \mathbf{I}(\mathbf{x},t)\end{aligned} \tag{3.38}$$

where $\mathcal{E}_k(\mathbf{x},t)$ is the kinetic energy density. In this equation the cross term $\mathbf{I}$ reads:

$$\mathbf{I}(\mathbf{x},t) = 2\left(\frac{\partial u_x}{\partial y}\frac{\partial u_y}{\partial x} + \frac{\partial u_x}{\partial z}\frac{\partial u_z}{\partial x} + \frac{\partial u_y}{\partial z}\frac{\partial u_z}{\partial y}\right) - 2\left(\frac{\partial u_x}{\partial x}\frac{\partial u_y}{\partial y} + \frac{\partial u_x}{\partial x}\frac{\partial u_z}{\partial z} + \frac{\partial u_y}{\partial y}\frac{\partial u_z}{\partial z}\right) \tag{3.39}$$

Let us now consider the coda part of a wavefield $\mathbf{u}(\mathbf{x},t)$ which is assumed to be diffuse, meaning that its energy is governed by a diffusion equation. This implies that the local energy fluxes are isotropic and the total energy is equipartitioned. In this case, the wavefield can be assumed to be a superposition of *a priori* uncorrelated plane P and S waves coming from different directions (Shapiro et al., 2000):

$$\mathbf{u}(\mathbf{x},t) = \sum_i \mathbf{u}_{p_i}^{\text{Plane}}(\mathbf{x},t) + \sum_j \mathbf{u}_{s_j}^{\text{Plane}}(\mathbf{x},t) \tag{3.40}$$

Therefore, the total energy densities of P and S waves could be written as the sum of their individual components:

$$\mathcal{E}_p(\mathbf{x},t) = \sum_i \mathcal{E}_{p_i}(\mathbf{x},t) = \sum_i \frac{\lambda(\mathbf{x}) + 2\mu(\mathbf{x})}{2}(\text{div } \mathbf{u}_{p_i}(\mathbf{x}))^2 \tag{3.41}$$

$$\mathcal{E}_s(\mathbf{x},t) = \sum_j \mathcal{E}_{s_j}(\mathbf{x},t) = \sum_j \frac{\mu(\mathbf{x})}{2}||\text{curl } \mathbf{u}_{s_j}(\mathbf{x})||^2 \tag{3.42}$$

At long lapse times, since the wavefield is diffuse, the displacement components will be uncorrelated. As a result, the space-average of the cross term $\mathbf{I}$ will cancel. The average of the total

energy density of the P waves will be:

$$\begin{aligned}\langle \mathcal{E}_p \rangle &= \left\langle \frac{\lambda(\mathbf{x}) + 2\mu(\mathbf{x})}{2} (\text{div } \mathbf{u}(\mathbf{x}))^2 \right\rangle \\ &= \sum_i \left\langle \frac{\lambda(\mathbf{x}) + 2\mu(\mathbf{x})}{2} (\text{div } \mathbf{u}_{p_i}(\mathbf{x}))^2 \right\rangle + 2 \sum_{\ell,m} \left\langle \frac{\lambda(\mathbf{x}) + 2\mu(\mathbf{x})}{2} (\text{div } \mathbf{u}_{p_\ell}(\mathbf{x}))(\text{div } \mathbf{u}_{p_m}(\mathbf{x})) \right\rangle \\ &= \sum_i \left\langle \frac{\lambda(\mathbf{x}) + 2\mu(\mathbf{x})}{2} (\text{div } \mathbf{u}_{p_i}(\mathbf{x}))^2 \right\rangle = \sum_i \langle \mathcal{E}_{p_i} \rangle \end{aligned} \tag{3.43}$$

and similarly

$$\langle \mathcal{E}_s \rangle = \left\langle \frac{\mu(\mathbf{x})}{2} ||\text{curl } \mathbf{u}(\mathbf{x})||^2 \right\rangle = \sum_j \langle \mathcal{E}_{sj} \rangle \tag{3.44}$$

in which $\langle\rangle$ denotes a spatial averaging (further in this chapter, we use $\langle\rangle_t$ to specify a time averaging). Since the individual plane waves are uncorrelated, the averages of the terms $(\text{div } \mathbf{u}_{p_\ell}(\mathbf{x}))(\text{div } \mathbf{u}_{p_m}(\mathbf{x}))$ and $||\text{curl } \mathbf{u}_{s\ell}(\mathbf{x})|| \cdot ||\text{curl } \mathbf{u}_{sm}(\mathbf{x})||$ vanish so that the average of the total energy of the P and S waves are respectively the sum of the average of their components as expressed in equations (3.43) and (3.44). Since the average value of $\mathbf{I}$ is zero, the average of the total energy density will become the sum of the averages of the P and S wave energy densities:

$$\langle \mathcal{E} \rangle = \langle \mathcal{E}_p \rangle + \langle \mathcal{E}_s \rangle = \left\langle \frac{\lambda(\mathbf{x}) + 2\mu(\mathbf{x})}{2} (\text{div } \mathbf{u}(\mathbf{x}))^2 \right\rangle + \left\langle \frac{\mu(\mathbf{x})}{2} ||\text{curl } \mathbf{u}(\mathbf{x})||^2 \right\rangle \tag{3.45}$$

The assessment of the stabilization ratio R can now be done using a grid of closely spaced sensors which enable us to calculate the derivatives of the displacement vector following all three spatial coordinates (divergence and curl of $\mathbf{u}$ in equation (3.45)):

$$R = \frac{\langle \mathcal{E}_s \rangle}{\langle \mathcal{E}_p \rangle} = \frac{\left\langle \frac{\mu(\mathbf{x})}{2} ||\text{curl } \mathbf{u}(\mathbf{x})||^2 \right\rangle}{\left\langle \frac{\lambda(\mathbf{x})+2\mu(\mathbf{x})}{2} (\text{div } \mathbf{u}(\mathbf{x}))^2 \right\rangle} = \frac{\underline{\mu}}{\underline{\lambda} + 2\underline{\mu}} \cdot \frac{\langle ||\text{curl } \mathbf{u}(\mathbf{x})||^2 \rangle}{\langle (\text{div } \mathbf{u}(\mathbf{x}))^2 \rangle} = \frac{1}{K^2} \cdot \frac{\langle ||\text{curl } \mathbf{u}(\mathbf{x})||^2 \rangle}{\langle (\text{div } \mathbf{u}(\mathbf{x}))^2 \rangle} \tag{3.46}$$

in which the first equation is based on the assumption that the pairs of the random variables $(\mu(\mathbf{x}), ||\text{curl } \mathbf{u}(\mathbf{x})||^2)$ and $(\lambda(\mathbf{x}) + 2\mu(\mathbf{x}), (\text{div } \mathbf{u}(\mathbf{x}))^2)$ are independent so that the average of their product is the product of the respective averages. This assumption will be verified via numerical simulations performed in Section 3.2.3. In the last equation, we made use of the equation (2.1). Since in an open medium at long lapse times we have $R = 2K^3$, the equipartitioning law in terms of the spatial derivatives of the recorded wavefield reads:

$$\frac{\langle ||\text{curl } \mathbf{u}(\mathbf{x})||^2 \rangle}{\langle (\text{div } \mathbf{u}(\mathbf{x}))^2 \rangle} = 2K^5 \tag{3.47}$$

At the end of this section and before starting to discuss the equipartitioning with the presence of a free surface, we define the kinetic energy density $\bar{K}$ as:

$$\bar{K} = \int \frac{1}{2} \rho(\mathbf{x}) \left| \frac{\partial \mathbf{u}(\mathbf{x}, t)}{\partial t} \right|^2 d\mathbf{x} \tag{3.48}$$

In an equipartitioning regime on an open Poissonian medium (full-space with $K = \sqrt{3}$), the energies are equally distributed between $\bar{K}$ and $\overline{\mathcal{E}}_p + \overline{\mathcal{E}}_s$ so that the value of the ratio $\bar{K} / \left(\overline{\mathcal{E}}_p + \overline{\mathcal{E}}_s\right)$ tends to 1. The corresponding stabilization values for this ratio with different hypotheses for Poissonian materials are summarized in Hennino et al. (2001). In sections 3.2.3 and 3.3 this stabilization is investigated via numerical simulations.

3.2.2 Equipartitioning with a free surface

In practice, the equipartitioning regime can be observed only using seismic sensors on the Earth's surface. Therefore, the calculation of the derivative of the wavefield in z direction is rather difficult because it requires to install the seismic receivers in depth. Hence, the free surface boundary condition (equation (1.17)) will be used as a tool to simplify the calculation of the stabilization ratio R over the surface of the Earth. The components of the stress tensor in z direction should vanish *i.e.* $\sigma_{xz} = \sigma_{yz} = \sigma_{zz} = 0$. These equations result in the following relations between vertical derivatives of the wavefield and horizontal ones:

$$\begin{cases} \dfrac{\partial \mathbf{u}_y}{\partial z} = -\dfrac{\partial \mathbf{u}_z}{\partial y} \\ \dfrac{\partial \mathbf{u}_x}{\partial z} = -\dfrac{\partial \mathbf{u}_z}{\partial x} \\ \dfrac{\partial \mathbf{u}_z}{\partial z} = -\dfrac{1}{2+\frac{\lambda}{\mu}}\left(\dfrac{\partial \mathbf{u}_x}{\partial x} + \dfrac{\partial \mathbf{u}_y}{\partial y}\right) \end{cases} \tag{3.49}$$

Substituting equation (3.49) into equation (3.46) gives the following relation for the stabilization ratio R only in terms of horizontal derivatives of the wavefield.:

$$R = \frac{\langle \mathcal{E}_s \rangle}{\langle \mathcal{E}_p \rangle} = \frac{1}{4}K^2 \frac{\left\langle 4\left(\dfrac{\partial \mathbf{u}_z}{\partial x}\right)^2 + 4\left(\dfrac{\partial \mathbf{u}_z}{\partial y}\right)^2 + \left(\dfrac{\partial \mathbf{u}_x}{\partial y} - \dfrac{\partial \mathbf{u}_y}{\partial x}\right)^2 \right\rangle}{\left\langle \left(\dfrac{\partial \mathbf{u}_x}{\partial x} + \dfrac{\partial \mathbf{u}_y}{\partial y}\right)^2 \right\rangle} \tag{3.50}$$

This equation can be used to calculate the equipartitioning ratio over the free surface using an array of seismic sensors installed only over the free surface of the Earth. We remind that the wavefield on the surface is a Rayleigh plane wave as (see equation (1.22)):

$$\begin{cases} \mathbf{u}_y(z=0) = 0 \\ \mathbf{u}_x(z=0) = -\sin(\omega t - k\mathbf{x}) \\ \mathbf{u}_z(z=0) = \varrho \cos(\omega t - k\mathbf{x}) \end{cases} \tag{3.51}$$

in which ϱ is the vertical-to-horizontal axis ratio on the free surface which can be obtained by:

$$\varrho = \frac{K_r^2\sqrt{1-\frac{K_r^2}{K^2}}}{2-K_r^2-2\sqrt{1-K_r^2}\sqrt{1-\frac{K_r^2}{K^2}}} \tag{3.52}$$

Introducing equations (3.51) into the equipartitioning ratio (3.50) will result in the following equipartitioning law on the surface:

$$R_{\text{surface}} = \frac{\langle \mathcal{E}_s \rangle_{\text{surface}}}{\langle \mathcal{E}_p \rangle_{\text{surface}}} = \frac{1}{4}K^2 \frac{\left\langle 4\left(\dfrac{\partial \mathbf{u}_z}{\partial x}\right)^2 \right\rangle}{\left\langle 4\left(\dfrac{\partial \mathbf{u}_x}{\partial x}\right)^2 \right\rangle} = K^2\varrho^2 = \frac{K^2K_r^4\left(1-\frac{K_r^2}{K^2}\right)}{\left(2-K_r^2-2\sqrt{1-K_r^2}\sqrt{1-\frac{K_r^2}{K^2}}\right)^2} \tag{3.53}$$

K	K_r^2	$\frac{v_r}{v_s}$	ϱ	R	R_{surface}
$\sqrt{\frac{4}{3}} \simeq 1.16$	0.49	0.7	1.06	3.12	1.5
1.5	0.80	0.89	1.34	6.75	4.02
$\sqrt{3} \simeq 1.73$	0.85	0.92	1.47	10.4	6.44
2	0.87	0.93	1.57	16	9.80
2.5	0.89	0.94	1.67	31.25	17.37

Table 3.2: Analytical values of the equipartitioning ratio for unbounded media and over the medium's traction-free surface for different values of K

The equation (3.47) in this case becomes:

$$\frac{\langle ||\text{curl } \mathbf{u}(\mathbf{x})||^2 \rangle_{\text{surface}}}{\langle (\text{div } \mathbf{u}(\mathbf{x}))^2 \rangle_{\text{surface}}} = K^2 R_{\text{surface}} = \frac{K^4 K_r^4 \left(1 - \frac{K_r^2}{K^2}\right)}{\left(2 - K_r^2 - 2\sqrt{1 - K_r^2}\sqrt{1 - \frac{K_r^2}{K^2}}\right)^2} \tag{3.54}$$

As an example, for Poissonian materials ($K^2 = 3$), the characteristic Rayleigh equation (1.18) has three roots for K_r^2:

$$K_r^2 = 4 \ , \quad 2 + \frac{2}{\sqrt{3}} \ , \quad 2 - \frac{2}{\sqrt{3}} \tag{3.55}$$

in which the first two roots result in imaginary values for q/k and s/k following equations (1.21) and hence they will be rejected. The value of $K_r^2 = 2 - \frac{2}{\sqrt{3}}$ gives the propagation velocity of Rayleigh waves $v_r \simeq 0.92 v_s$. Inserting $K_r^2 = 2 - \frac{2}{\sqrt{3}}$ in equation (3.52) gives $\varrho \simeq 1.47$ and a stabilization ratio of $R \simeq 6.5$ that is consistent with 7 which is reported by Shapiro et al. (2000) from the studies of the energy ratios in the Coda waves observed from local earthquakes in Mexico. Table 3.2 shows the analytical values for the stabilization of the S to P energy ratio in an unbounded medium as well as over the free surface for different values of K.

3.2.3 Numerical observation of equipartitioning regime

The objective of this section is to investigate the equipartitioning phenomenon via the numerical simulations carried out using SPEC3D. For this purpose, three types of measurements are available:

(1) The values of the divergence free and curl free parts of the displacement field ($||\text{curl } \mathbf{u}(\mathbf{x})||, \text{div } \mathbf{u}(\mathbf{x})$). Theoretically in an equipartitioning regime, the ratio between the space-averaged of the squared of these fields converges to the values indicated in equations (3.47) and (3.54) respectively for an open unbounded medium and over a free surface.

(2) The mean values of the P and S wave energy densities over the entire medium, ($\overline{\mathcal{E}}_p^{\Omega}, \overline{\mathcal{E}}_s^{\Omega}$):

$$\overline{\mathcal{E}}_p^{\Omega}(t) = \int_{\Omega} \mathcal{E}_p(\mathbf{x}, t) d\mathbf{x} = \int_{\Omega} \frac{\lambda(\mathbf{x}) + 2\mu(\mathbf{x})}{2} \left(\text{div } \mathbf{u}(\mathbf{x})\right)^2 d\mathbf{x} \tag{3.56a}$$

$$\overline{\mathcal{E}}_s^{\Omega}(t) = \int_{\Omega} \mathcal{E}_s(\mathbf{x}, t) d\mathbf{x} = \int_{\Omega} \frac{\mu(\mathbf{x})}{2} ||\text{curl } \mathbf{u}(\mathbf{x})||^2 d\mathbf{x} \tag{3.56b}$$

in which Ω is the whole propagation medium including its boundaries. Since in a half-space this value accounts simultaneously for the energies corresponding to the surface and body waves, the stabilization value in this case should lie between R_{surface} and R depending on the depth of surface Rayleigh waves.

(3) The mean value of the kinetic energy density over the entire medium $\overline{K}^{\Omega}$ calculated using equation (3.48). As discussed in Section 3.2.1, in an equipartitioning regime, the ratio $\overline{K}^{\Omega}/(\overline{\mathcal{E}}_p^{\Omega} + \overline{\mathcal{E}}_s^{\Omega})$ converges.

Problem description: The numerical example in this section consists of a propagation medium as a cube defined by $\Omega = \{\mathbf{x} \in \mathbb{R}^3 | -1500 \text{ m} \leq x, y \leq 1500 \text{ m}; -3000 \text{ m} \leq z \leq 0 \text{ m}\}$ with continuous random heterogeneities in elastic moduli and a constant density of 2000 kg/m^3. The average value of μ is assumed to be $\bar{\mu} = 2 \times 10^9$ Pa. Hence, for a given value of $K = v_p/v_s$, the average value of κ and the average phase velocities will be:

$$\bar{\kappa} = \left(K^2 - \frac{4}{3}\right)\bar{\mu} \quad ; \quad v_s = \sqrt{\bar{\mu}/\rho} = 1000 \text{ m/s} \quad ; \quad v_p = 1000K \tag{3.57}$$

The components of the covariance matrix for different values of δ and K used henceforth in this work are summarized in Table 3.3 (see Appendix B for more discussion). Tables 3.4 and 3.5 also show the values of different scattering parameters for two different correlation kernels in terms of different values of δ, K and ℓ_c used in this study. These tables list the different configurations that will be considered along the course of this chapter.

δ	K	σ_λ^2	σ_μ^2	$\text{cov}(\lambda, \mu)$
0.15	1.73	0.21	0.02	-0.02
0.4	1.16	0.27	0.24	0.25
0.4	1.73	20	0.24	-0.01
0.6	1.73	43.6	1.1	0.26

Table 3.3: Components of the covariance matrix in terms of the values of δ and K

Config.	ℓ_c $[m]$	δ	K	Σ_{PS}/Σ_{SP}	Σ_{PP}/Σ_{PS}	Σ_{SS}/Σ_{SP}	ℓ_S^* $[m]$	ℓ_P^* $[m]$
Reference	100	0.4	1.16	0.32	0.5	3.2	450	435
Localization	100	0.6	1.73	0.10	16	33	130	25
Inefficient mixture	100	0.4	1.73	0.10	32	33	580	60
Large $\ell_{p/s}^*$	100	0.15	1.73	0.10	3.3	33	6500	4000

Table 3.4: Scattering parameters for a random medium with a low-pass white noise correlation kernel

Config.	ℓ_c $[m]$	δ	K	Σ_{PS}/Σ_{SP}	Σ_{PP}/Σ_{PS}	Σ_{SS}/Σ_{SP}	ℓ_S^* $[m]$	ℓ_P^* $[m]$
Reference-exp	100	0.4	1.16	0.32	1.73	8	530	520

Table 3.5: Scattering parameters for a random medium with an exponential correlation kernel

Configuration: Reference and Reference-exp The half-space Ω with a dispersion level of $\delta = 0.40$ is subjected to an explosion source at its central point $(x, y, z) = (0, 0, -1500)$(m). The source is characterized by a Ricker pulse time function. The delay time t_0 and central frequency f_0 of the source are considered to be respectively 0.3 s and 10 Hz (see Figure 3.4). Figure 3.5 depicts a typical half-space surrounded with PML layers except over the free surface.

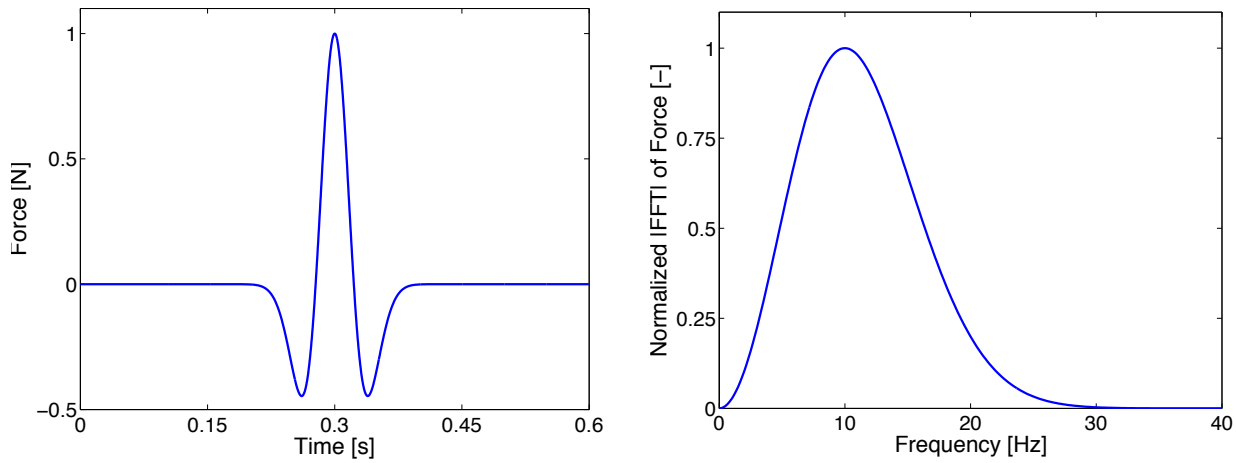

(a) (b)

Figure 3.4: Ricker pulse with $t_0 = 0.3$(s) and $f_0 = 10$(Hz) in time (a) and frequency (b) domains

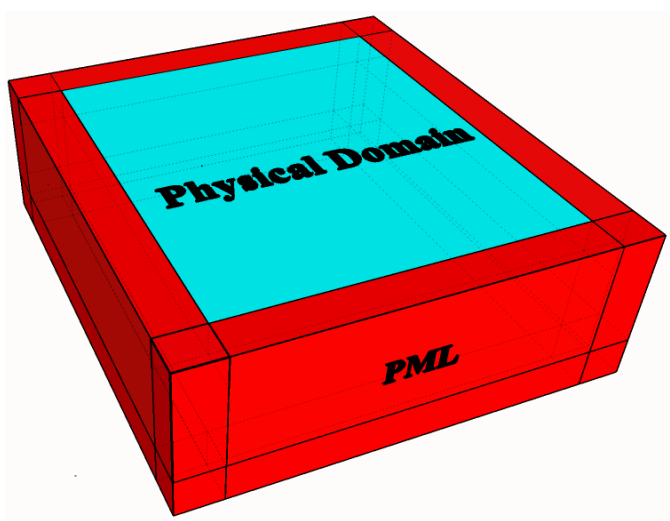

Figure 3.5: A half-space with PML layers at boundaries

The spatial correlation function of the random elastic moduli is considered to be either low-pass white noise or exponential. The value of K is 1.16 and the correlation length is $\ell_c = 100$ m which is equal to the shear wavelength. The simulation is performed over $t = 5$ s. Figure 3.6 shows the temporal variation of the space-averaged body wave energies $\overline{\mathcal{E}}_p^{\Omega}$ and $\overline{\mathcal{E}}_s^{\Omega}$ calculated via the equations (3.56) along with their ratio. The individual variation of $\overline{\mathcal{E}}_p^{\Omega}$ (red curves) and $\overline{\mathcal{E}}_s^{\Omega}$ (blue curves) are depicted in the top plot. The solid and dashed curves in both plots indicate the results corresponding respectively to the medium with low-pass white noise and exponential correlation model. At the beginning, the source injects only the P wave energy into the medium (explosion source). For the case of medium with low-pass white noise ACF, following Table 3.4,

we have $\Sigma_{PS} = 2\Sigma_{PP}$, which implies that the chance of the P-to-S mode conversion is twice the chance of the P-to-P mode conversion. Therefore, the wave scattering results in the generation of S waves. The contrast between the average phase velocities is not significant (for instance in comparison with the case where $K = \sqrt{3}$). We observe therefore that the space-averaged P and S wave energies begin to decay more or less at the same time.

From now on, all figures depicting the temporal evolution of the whole space-averaged energies include a shaded window indicating the time interval during which the decay of the energies $\overline{\mathcal{E}}_p^{\Omega}$ and $\overline{\mathcal{E}}_s^{\Omega}$ begins. The starting and end points of this window specify respectively the lapse times corresponding to the first arrivals of the direct P and S waves (the waves traveling in the homogeneous background) to the boundaries of the medium. The lower plot of the Figure 3.6 shows that the energy ratio $\overline{\mathcal{E}}_s^{\Omega}/\overline{\mathcal{E}}_p^{\Omega}$ converges to 2.9 and 3.1 respectively for the low-pass white noise and exponential models. These stabilization values lie between $R_{\text{surface}} = 1.5$ (thin black line) and $R = 3.12$ (thick black line) (see Table 3.2) and are closer to the analytical value for an open unbounded medium.

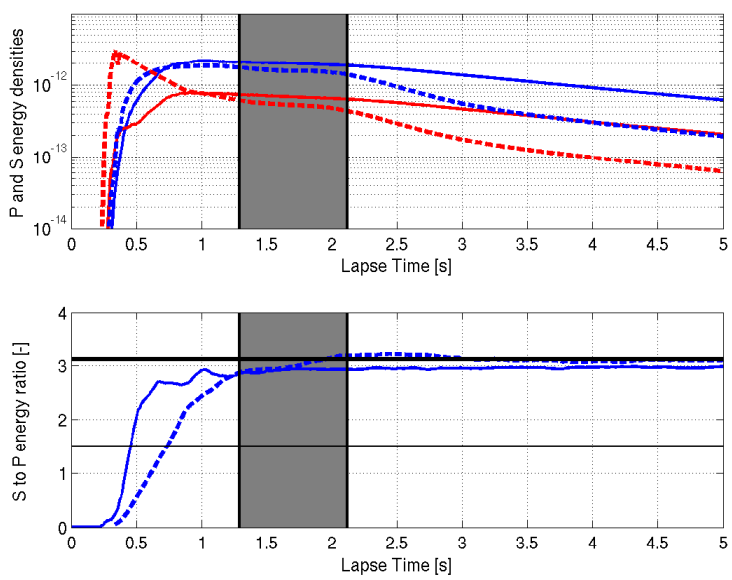

Figure 3.6: Top: temporal variation of $\overline{\mathcal{E}}_p^{\Omega}$ (red curves) and $\overline{\mathcal{E}}_s^{\Omega}$ (blue curves). Bottom: temporal variation of $\overline{\mathcal{E}}_s^{\Omega}/\overline{\mathcal{E}}_p^{\Omega}$. Solid and dashed curves correspond respectively to the low-pass white noise and exponential correlation models. The starting and end points of the shaded window indicate respectively the lapse times in which the direct P and S waves propagating in homogeneous background arrive to the boundaries.

The top plot in Figure 3.7 shows that the space-averaged kinetic energy densities $\bar{K}^{\Omega}$ (blue curves) reach their maximum value at the source's delay time $t = t_0 = 0.3$ s. From the bottom plot, stabilization values of 0.8 and 1.1 are observed respectively for the low-pass white noise and exponential correlation models. The corresponding stabilization times are observed to be highly dependent on the correlation model. As a result, in this case, both of the ratios $\overline{\mathcal{E}}_s^{\Omega}/\overline{\mathcal{E}}_p^{\Omega}$ and $\bar{K}^{\Omega}/(\overline{\mathcal{E}}_p^{\Omega} + \overline{\mathcal{E}}_s^{\Omega})$ are stabilized for both correlation types.

The equipartitioning regime can also be visualized more locally via the films showing the propagation of the energies through the medium. For this purpose, the snapshots of the squared curl-free and squared divergence-free parts of the displacement field will be plotted at two different horizontal slices situated at the depths $z = 0$ m (surface) and $z = -1000$ m (at a distance of

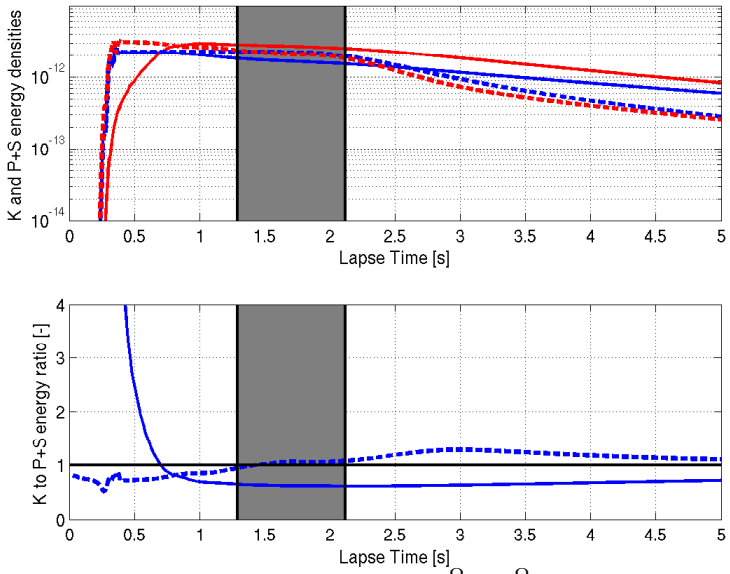

Figure 3.7: Top: temporal variation of $\bar{K}^{\Omega}$ (blue curves) and $\overline{\mathcal{E}}_p^{\Omega} + \overline{\mathcal{E}}_s^{\Omega}$ (red curves). Bottom: temporal variation of $\bar{K}^{\Omega}/(\overline{\mathcal{E}}_p^{\Omega} + \overline{\mathcal{E}}_s^{\Omega})$. Solid and dashed curves correspond respectively to the low-pass white noise and exponential correlation models. The starting and end points of the shaded window indicate respectively the lapse times in which the direct P and S waves propagating in homogeneous background arrive to the boundaries.

about a transport mean free path from the source), and at two different lapse times $t = 2$ s and $t = 4$ s. Figure 3.8 shows the snapshots corresponding to (div $\mathbf{u}(\mathbf{x}))^2$ (normalized by its average value calculated over the slice) (top row) along with $||\text{curl } \mathbf{u}(\mathbf{x})||^2$ (normalized by its average over the slice) (bottom row), both represented in percent. The plots show the results of the random medium with low-pass white noise correlation model. At $t = 4$ s, the P and S wave energies are almost distributed uniformly within both of the slices (see the low ranges of the plot's colorbars at $t = 4$ s compared to $t = 2$ s for both slices).

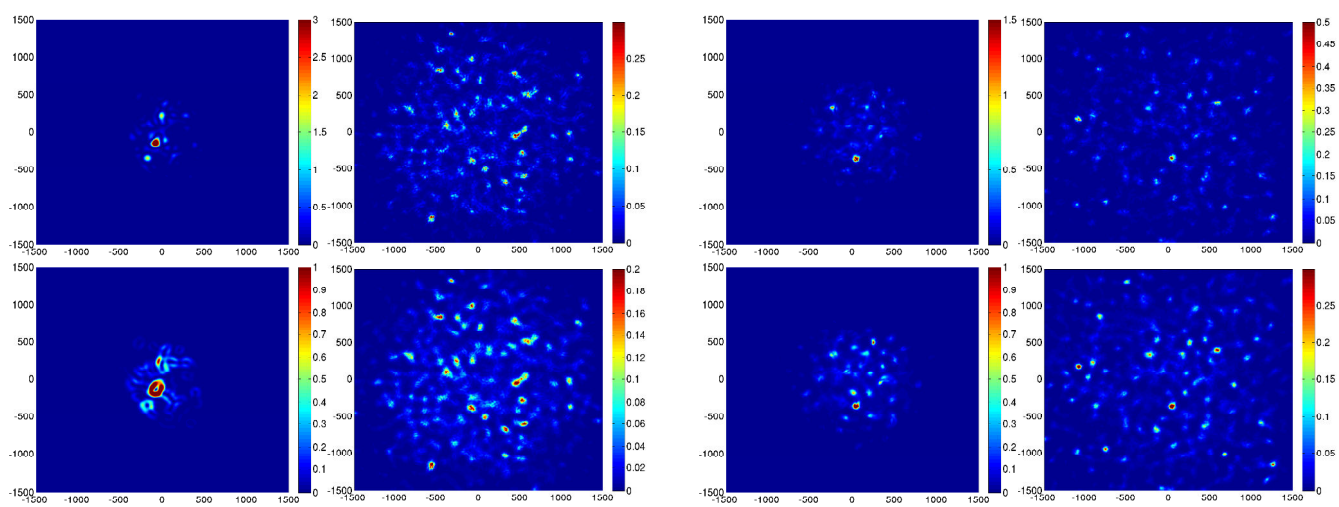

$z = 0$ m, $t = 2$ s $\quad$ $z = 0$ m, $t = 4$ s $\quad$ $z = -1000$ m, $t = 2$ s $\quad$ $z = -1000$ m, $t = 4$ s

Figure 3.8: Snapshots of the ratio (div $\mathbf{u}(\mathbf{x}))^2/\langle(\text{div } \mathbf{u}(\mathbf{x}))^2\rangle_{\text{slice}}$ (top row) and $||\text{curl } \mathbf{u}(\mathbf{x})||^2/\langle||\text{curl } \mathbf{u}(\mathbf{x})||^2\rangle_{\text{slice}}$ (bottom row) in percent for two different lapse times ($t = 2$ s and $t = 4$ s) and two different depths ($z = 0$ m and $z = -1000$ m). The random heterogeneities have a low-pass white noise correlation kernel.

The objective of this paragraph is to investigate the equipartitioning regime more locally. For

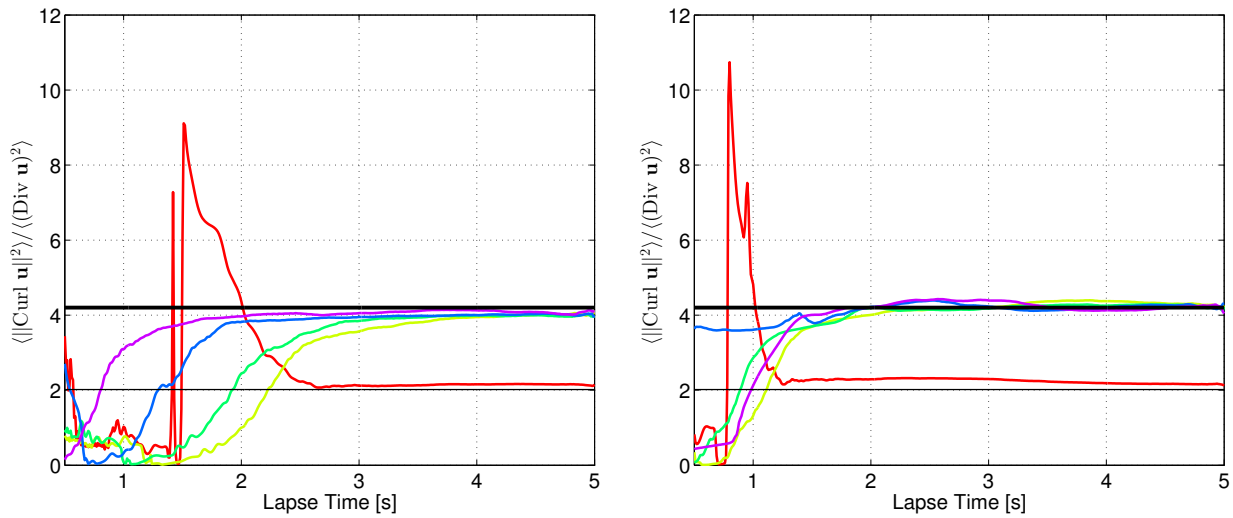

Figure 3.9: Temporal variation of $\langle ||\text{curl } \mathbf{u}(\mathbf{x})||^2\rangle/\langle(\text{div } \mathbf{u}(\mathbf{x}))^2\rangle$ calculated over the whole slices. Red, green, cyan and purple colors correspond respectively to the slices at $z = 0$ m, $z = -250$ m, $z = -500$ m and $z = -1000$ m. The thick and thin black lines correspond respectively to the analytical values on full space and over the free surface. Left and right plots correspond respectively to the low-pass white noise and exponential correlation models.

this purpose, an energy analysis is done over some horizontal slices at five different depths of $z = 0, -250, -500, -1000$ m. The results are depicted in Figure 3.9 for both low-pass white noise (left plot) and exponential (right plot) correlations. This figure shows the temporal variation of the space-averaged ratio $\langle ||\text{curl } \mathbf{u}(\mathbf{x})||^2\rangle/\langle(\text{div } \mathbf{u}(\mathbf{x}))^2\rangle$ where $\langle\rangle$ denotes a spatial averaging over the slice only. It can be observed that for the slice in the free surface (red curve), the energy ratio converges to the analytical value of $K^2 R_{\text{surface}} = 2$ (thin black line). For the other slices, the stabilization occurs at a value lying between $K^2 R_{\text{surface}} = 2$ and $2K^5 = 4.2$ (thick black line) but closer to the full-space stabilization value.

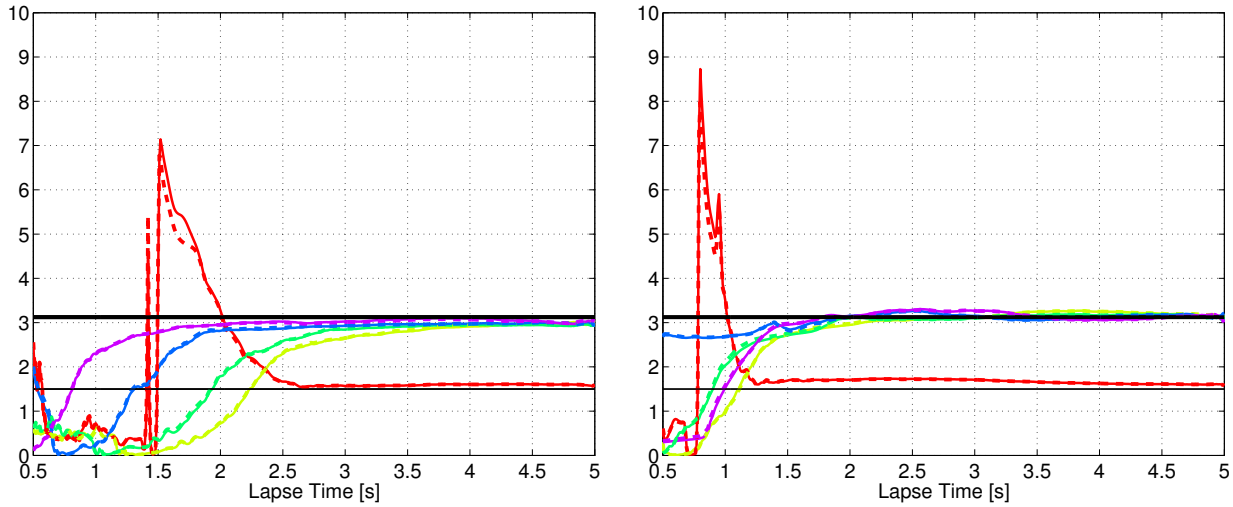

Figure 3.10: Temporal variation of $\frac{\left\langle \frac{\mu(\mathbf{x})}{2} ||\text{curl } \mathbf{u}(\mathbf{x})||^2 \right\rangle}{\left\langle \frac{\lambda(\mathbf{x})+2\mu(\mathbf{x})}{2} (\text{div } \mathbf{u}(\mathbf{x}))^2 \right\rangle}$ (solid curves) and $\frac{\underline{\mu}}{\underline{\lambda}+2\underline{\mu}} \cdot \frac{\left\langle ||\text{curl } \mathbf{u}(\mathbf{x})||^2 \right\rangle}{\langle(\text{div } \mathbf{u}(\mathbf{x}))^2\rangle}$ (dashed curves) calculated over the whole slices. Red, green, cyan and purple colors correspond respectively to the slices at $z = 0$ m, $z = -250$ m, $z = -500$ m and $z = -1000$ m. The thick and thin black lines correspond respectively to the analytical values on full space and over the free surface. Note that the dashed curves are almost hidden by the solid ones. Left and right plots correspond respectively to the low-pass white noise and exponential correlation models.

At the end of this section, the hypothesis behind the equation (3.46) will be verified. In this equation, we have made the following assumption:

$$\frac{\langle \mathcal{E}_s \rangle}{\langle \mathcal{E}_p \rangle} = \frac{\left\langle \frac{\mu(\mathbf{x})}{2} ||\text{curl } \mathbf{u}(\mathbf{x})||^2 \right\rangle}{\left\langle \frac{\lambda(\mathbf{x})+2\mu(\mathbf{x})}{2} (\text{div } \mathbf{u}(\mathbf{x}))^2 \right\rangle} = \frac{\underline{\mu}}{\underline{\lambda} + 2\underline{\mu}} \cdot \frac{\langle ||\text{curl } \mathbf{u}(\mathbf{x})||^2 \rangle}{\langle (\text{div } \mathbf{u}(\mathbf{x}))^2 \rangle} \tag{3.58}$$

in which the pairs of random variables $(\mu(\mathbf{x}), ||\text{curl } \mathbf{u}(\mathbf{x})||^2)$ and $(\lambda(\mathbf{x}) + 2\mu(\mathbf{x}), (\text{div } \mathbf{u}(\mathbf{x}))^2)$ are assumed to be independent. Knowing the local values of the Lamé parameters, we plot the variations of $\frac{\left\langle \frac{\mu(\mathbf{x})}{2} ||\text{curl } \mathbf{u}(\mathbf{x})||^2 \right\rangle}{\left\langle \frac{\lambda(\mathbf{x})+2\mu(\mathbf{x})}{2} (\text{div } \mathbf{u}(\mathbf{x}))^2 \right\rangle}$ and $\frac{\underline{\mu}}{\underline{\lambda}+2\underline{\mu}} \cdot \frac{\left\langle ||\text{curl } \mathbf{u}(\mathbf{x})||^2 \right\rangle}{\langle (\text{div } \mathbf{u}(\mathbf{x}))^2 \rangle}$. Figure 3.10 depicts the temporal variation of these two quantities, respectively with solid and dashed curves, for low-pass white noise (left plot) and exponential correlation model (right plot). We observe from this figure that there is no significant discrepancy between the results. Hence, the mentioned hypothesis is numerically validated.

In conclusion, for low values of K an equipartitioning regime is established at global and local scales for two different correlation models. We remind the ratio between P-to-S and S-to-P total scattering cross-sections:

$$\frac{\Sigma_{PS}}{\Sigma_{SP}} = 2K^3 \tag{3.59}$$

According to this equation, lower values of K lead to lower contrasts between Σ_{PS} and Σ_{SP} which means that during the scattering process the normal modes exchanges occur with closer probabilities compared to the case of higher values of K. Moreover, in this case, the values of the ratios Σ_{PP}/Σ_{PS} and Σ_{SS}/Σ_{SP} are not significantly different from unity contrary to the other case studies (see Table 3.4). These two reasons favor the onset of an equipartitioning regime in this case. We will study less favorable cases in Section 3.3.

3.3 Limitations to reaching numerically the equipartitioning regime

For the Reference case studied in Section 3.2.3, as indicated in Table 3.4, the values of the transport mean free paths of P and S waves are respectively $\ell_P^* = 435(m)$ and $\ell_S^* = 450(m)$ so that:

(1) The P and S waves reach a diffusion regime almost simultaneously since $\ell_P^* \simeq \ell_S^*$,

(2) They can reach an equipartitioning regime before leaving the medium (since $\ell_P^*, \ell_S^* < 1500(m)$) and at enough distances (at least a transport mean free path) from the boundaries which can *a priori* pollute the wave energies by the unwanted reflections toward the physical medium.

In the simulations discussed in this section, either a transport regime is established but the above-mentioned conditions are not satisfied or a localization regime is dominant both of which imply the inability to observe an equipartitioning regime. Next section introduces a case in which a strong localization regime is dominant.

3.3.1 Setting of a localization regime

In this section we increase the value of the mean phase velocity contrast to $K = \sqrt{3}$ (third row in Table 3.4). The most favorable case to reach an equipartitioning regime is *a priori* the case with

maximum value of δ ($\delta = 0.6$). The differences between the values of ℓ_P^* and ℓ_S^* in this case and the corresponding values for the cases with the same K and lower δ (0.4 or 0.15) is remarkable. In the following paragraph, the case of a propagation medium with $K = \sqrt{3}$ and $\delta = 0.6$ will be treated.

Configuration: Localization The half-space Ω is excited during $t = 5$ s with two different source types: an explosion and a unidirectional force both of which have the Ricker pulse time function. A low-pass white noise model is used as the correlation kernel of the heterogeneities.

In Figure 3.11, the top left plot depicts the temporal variations of $\overline{\mathcal{E}}_p^\Omega$ and $\overline{\mathcal{E}}_s^\Omega$ respectively in red and blue. For each of these cases, the solid and dashed curves correspond respectively to the explosion and unidirectional sources. The unidirectional source which creates initially the S wave energies more than the P waves, results at first (before arriving to the gray shaded area) in higher values of $\overline{\mathcal{E}}_s^\Omega$ and lower values of $\overline{\mathcal{E}}_p^\Omega$ compared to the case of explosion source. However, at longer lapse times, the body wave energy densities become source-independent. We observe from the top plot of the Figure 3.11 that regardless of the source type, even before the complete evacuation of the direct wave energies, both of the phase energies are almost stabilized at a lapse time of $t = 2$ s and their decay rate tend to zero at longer lapse times. This is in contradiction with a transport regime in which $\overline{\mathcal{E}}_p^\Omega$ and $\overline{\mathcal{E}}_s^\Omega$ decay in time because of the existence of PML layers around the medium.

The lower plot of the Figure 3.11 shows the stabilization of the space-averaged energy ratio for both source types. We guess that this stabilization is related to the fact that a major part of the wave energy is trapped within the propagation medium so that it does not touch the boundaries. To verify this hypothesis, we do the same simulation (with an explosion source) but with Neumann boundary conditions all around the medium and the corresponding results are shown with dashed-dotted curves. From the top left plot, we observe a slight increase in $\overline{\mathcal{E}}_p^\Omega$ and $\overline{\mathcal{E}}_s^\Omega$ in Neumann case, resulting in a small change in the stabilization value (dashed-dotted blue curve in lower left plot). The latter is observed to be more than twice the analytical value in full-space. As it has been already discussed, this ratio must be even less than the analytical value $2K^3$ which is not the case here. The right plots also show the evolution of $\bar{K}^\Omega$, $\overline{\mathcal{E}}_p^\Omega + \overline{\mathcal{E}}_s^\Omega$ and their ratio for all above-mentioned cases. The top right figure shows that after a certain time, the values of $\bar{K}^\Omega$ and $\overline{\mathcal{E}}_p^\Omega + \overline{\mathcal{E}}_s^\Omega$ become time-independent for all three cases.

This regime is called the *localization regime* in which the random heterogeneities of the medium are too strong ($\delta = 0.6$) so that the wave energy is trapped before it reaches the boundaries. In this regime, the transport equations introduced in chapter 2 are no more valid. There is no theoretical formula which relates the stabilization value in a localization regime to the statistical parameters of the medium.

The visualization of the energy snapshots will help to observe the localization phenomenon. The snapshots of $\langle ||\text{curl } \mathbf{u}(\mathbf{x})||^2 \rangle$ and $\langle (\text{div } \mathbf{u}(\mathbf{x}))^2 \rangle$ normalized by their corresponding average values calculated over the corresponding slice at the given lapse times of $t = 2$ s and $t = 4$ s are shown in Figure 3.12. The pattern of these fields is similar to a collection of points distributed over the slices containing the essential part of the slice's average energy. According to the Table 3.4, the transport mean free paths of the P and S waves are respectively $\ell_P^* = 25$ m and $\ell_S^* = 130$ m. The main point in these figures is that the body wave energies are localized within almost the same

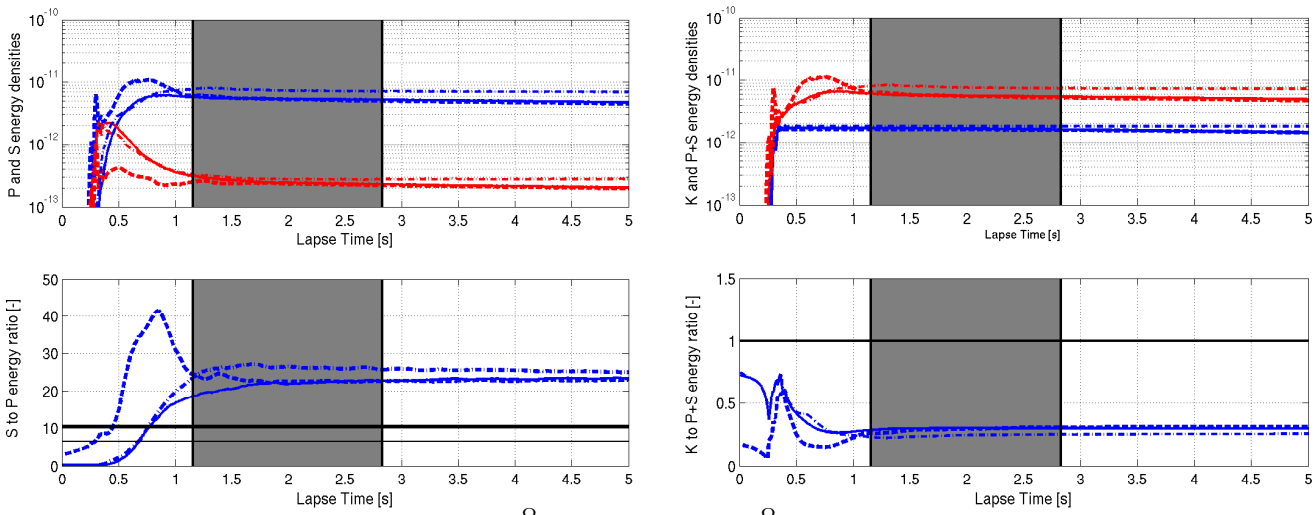

Figure 3.11: Top left: temporal variation of $\overline{\mathcal{E}}_p^{\Omega}$ (red curves) and $\overline{\mathcal{E}}_s^{\Omega}$ (blue curves). Bottom left: temporal variation of $\overline{\mathcal{E}}_s^{\Omega}/\overline{\mathcal{E}}_p^{\Omega}$. Top right: temporal variation of $\bar{K}^{\Omega}$ (blue curves) and $\overline{\mathcal{E}}_p^{\Omega}+\overline{\mathcal{E}}_s^{\Omega}$ (red curves). Bottom right: temporal variation of $\bar{K}^{\Omega}/(\overline{\mathcal{E}}_p^{\Omega}+\overline{\mathcal{E}}_s^{\Omega})$. Solid, dashed and dashed-dotted curves correspond respectively to half-space with explosion source, half-space with unidirectional source and Neumann boundary conditions with explosion source. The starting and end points of the shaded window indicate respectively the lapse times in which the direct P and S waves propagating in homogeneous background arrive to the boundaries.

zone over each slice between the lapse times $t = 2$ s and $t = 4$ s. The results of the slice-average energy ratio calculated over the slices gives similar information as in the lower left plot of the Figure 3.11.

The objective of the next section is to deal with a simulation in which we keep the value of $K = \sqrt{3}$ but we decrease δ to 0.15 with the aim of getting rid of the localization regime which was dominant in this section.

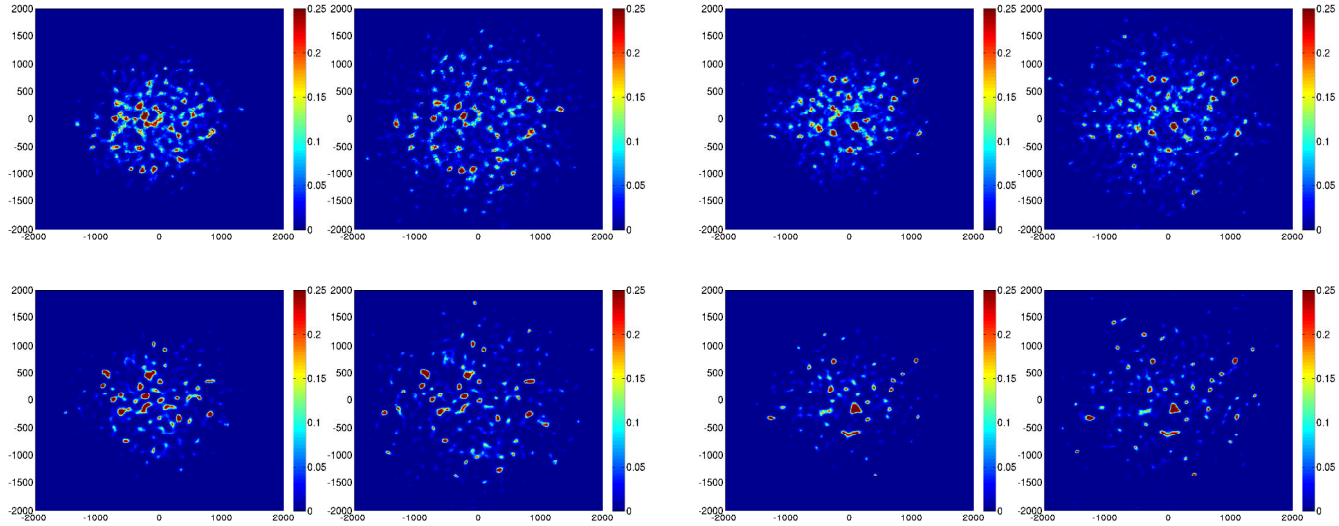

$z = 0(m)$, $t = 2(s)$ $\quad$ $z = 0(m)$, $t = 4(s)$ $\quad$ $z = -1000(m)$, $t = 2(s)$ $\quad$ $z = -1000(m)$, $t = 4(s)$

Figure 3.12: Snapshots of the ratio $(\text{div } \mathbf{u}(\mathbf{x}))^2/\langle(\text{div } \mathbf{u}(\mathbf{x}))^2\rangle_{\text{slice}}$ (top row) and $||\text{curl } \mathbf{u}(\mathbf{x})||^2/\langle||\text{curl } \mathbf{u}(\mathbf{x})||^2\rangle_{\text{slice}}$ (bottom row) in percent for two different lapse times ($t = 2(s)$ and $t = 4(s)$) and two different depths ($z = 0(m)$ and $z = -1000(m)$).

3.3.2 Influence of mean free path

Configuration: Large $\ell^*_{p/s}$ The propagation medium Ω is again subjected to an explosion source and the simulation time is considered to be $t = 5$ s. The random propagation medium has a low-pass white noise ACF, the values of K and δ are respectively $\sqrt{3}$ and 0.15, and the medium is a half-space. Left plots in Figure 3.13 show the temporal variations of $\overline{\mathcal{E}}^{\Omega}_p$ and $\overline{\mathcal{E}}^{\Omega}_s$ and their ratio. From the lower left plot, it can be observed that until about $t = 2(s)$ (the end of the gray shaded area), the ratio $\overline{\mathcal{E}}^{\Omega}_s/\overline{\mathcal{E}}^{\Omega}_p$ tends to increase. At this time, both of the direct P and S waves have already arrived to the boundaries and the role of the boundary conditions begins.

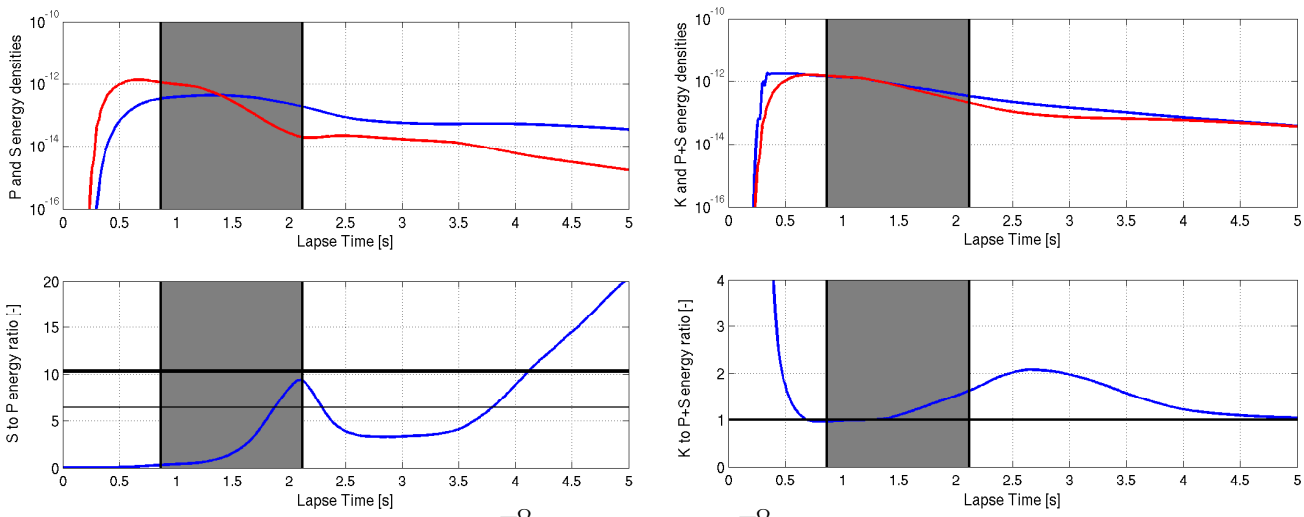

Figure 3.13: Top left: temporal variation of $\overline{\mathcal{E}}^{\Omega}_p$ (red curves) and $\overline{\mathcal{E}}^{\Omega}_s$ (blue curves). Bottom left: temporal variation of $\overline{\mathcal{E}}^{\Omega}_s/\overline{\mathcal{E}}^{\Omega}_p$. Top right: temporal variation of $\bar{K}^{\Omega}$ (blue curves) and $\overline{\mathcal{E}}^{\Omega}_p + \overline{\mathcal{E}}^{\Omega}_s$ (red curves). Bottom right: temporal variation of $\bar{K}^{\Omega}/(\overline{\mathcal{E}}^{\Omega}_p + \overline{\mathcal{E}}^{\Omega}_s)$. The starting and end points of the shaded window indicate respectively the lapse times in which the direct P and S waves propagating in homogeneous background arrive to the boundaries.

The top right plot of Figure 3.13 shows the temporal variations of the kinetic energy density $\bar{K}^{\Omega}$ and the sum of the averages of the P and S wave energy densities $\overline{\mathcal{E}}^{\Omega}_p + \overline{\mathcal{E}}^{\Omega}_s$. From the bottom right plot a stabilization is observed at first around $t = 1$ s and then at the end of simulation ($t = 5$ s). However, even if the ratio $\bar{K}^{\Omega}/(\overline{\mathcal{E}}^{\Omega}_p + \overline{\mathcal{E}}^{\Omega}_s)$ is globally stabilized over the entire medium in some time intervals, a global equipartitioning regime does not occur (as already seen in the lower left plot of Figure 3.13).

The snapshots of $(\text{div } \mathbf{u}(\mathbf{x}))^2$ and $||\text{curl } \mathbf{u}(\mathbf{x})||^2$ normalized by their corresponding average values are plotted in Figure 3.14. From these figures it can be observed that over the free surface ($z = 0$ m) at $t = 2$ s both P and S energies are more concentrated around the boundaries. However, at longer lapse times ($t = 4$ s) and near the source ($z = -1000$ m), the pattern of both of the energies does not look like a localization.

From Table 3.4, the values of the transport mean free paths of P and S waves are respectively $\ell^*_P = 4000$ m and $\ell^*_S = 6500$ m. These distances cannot be achieved by the waves before reaching the boundaries in this simulation. A medium whose sides are at least $2\ell^*_S = 13000$ m which is more than 4 times bigger (in each side) than the propagation medium in this case, is required in order to observe the equipartitioning of the energies.

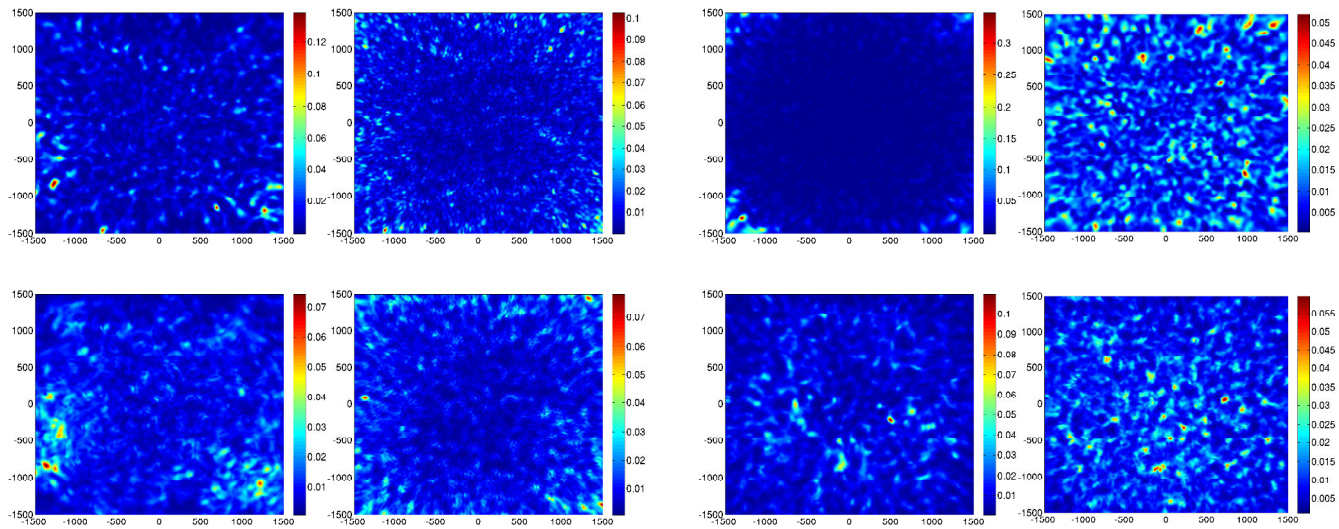

$z = 0$ m, $t = 2$ s $z = 0$ m, $t = 4$ s $z = -1000$ m, $t = 2$ s $z = -1000$ m, $t = 4$ s

Figure 3.14: Snapshots of the ratio $(\text{div } \mathbf{u}(\mathbf{x}))^2/\langle(\text{div } \mathbf{u}(\mathbf{x}))^2\rangle_{\text{slice}}$ (top row) and $||\text{curl } \mathbf{u}(\mathbf{x})||^2/\langle||\text{curl } \mathbf{u}(\mathbf{x})||^2\rangle_{\text{slice}}$ (bottom row) in percent for two different lapse times ($t = 2$ s and $t = 4$ s) and two different depths ($z = 0$ m and $z = -1000$ m).

In conclusion, for Poissonian materials ($K = \sqrt{3}$) with low degrees of fluctuation ($\delta = 0.15$ in this case), the equipartitioning regime was not observed because of the small propagation lengths compared to the transport mean free paths. In the next section, we increase the value of δ from 0.15 to 0.4 with the aim of decreasing the transport mean free paths and make them less than the propagation length.

3.3.3 Influence of inefficient mixture of body waves

In this section, we will be concerned with the influence of inefficient mixture between the body wave energies during the scattering events in the numerical observation of the equipartitioning establishment. For this purpose, the dispersion level of the elasticity matrix is hold to be the same as in the Reference case ($\delta = 0.4$) and the same value of $K = \sqrt{3}$ will be used.

Configuration: Inefficient mixture The propagation medium Ω is subjected to three different sources: explosion, unidirectional and their combination all of which having a Ricker pulse time function. The medium is a half-space and has a low-pass white noise correlation kernel. The simulation is performed over $t = 5$ s. The top left plot in Figure 3.15 show the temporal variation of $\overline{\mathcal{E}}_p^{\Omega}$ (red curved) and $\overline{\mathcal{E}}_s^{\Omega}$ (blue curves) where the solid, dashed and dashed-dotted curves represent respectively the results relative to the explosion, unidirectional and combined sources. This plot shows that the waves are not localized since both of the body wave energies are temporally decaying. The lower left plot shows the corresponding S-to-P energy ratios which states no global equipartitioning for all source types. From Table 3.4, the values of the transport mean free paths of P and S waves are respectively $\ell_P^* = 60$ m and $\ell_S^* = 580$ m. Hence, both wave modes can travel at least a transport mean free path before the arrival of the direct waves to the boundaries.

Following Table 3.4 we have $\Sigma_{PP}/\Sigma_{PS} = 32$ and $\Sigma_{SS}/\Sigma_{SP} = 33$ from which it implies that the P wave energies have much more tendency to scatter into P waves and likewise the initial S wave energies are more likely to scatter into S waves. For the sake of comparison, we remind the values

of the ratios Σ_{PP}/Σ_{PS} and Σ_{SS}/Σ_{SP} being respectively 0.5 and 3.2 for the Reference case. These values are closer to 1 and imply a faster apparition of an equipartitioning regime (Margerin et al., 2000). Moreover, the ratio Σ_{PS}/Σ_{SP} is farther from 1 compared to the Reference case where it is 0.32. As a consequence, the asymmetry between the P-to-S and S-to-P mode exchanges is higher. The fact that the values of these three ratios are not as close to 1 as in the Reference case, can be imagined as another reason of discrepancy between the observed and the analytical stabilization values.

As a result, for $K = \sqrt{3}$ and $\delta = 0.4$ even if the transport mean free paths are small compared to the propagation length, large values of the ratios Σ_{PP}/Σ_{PS} and Σ_{SS}/Σ_{SP} and the ratio Σ_{PS}/Σ_{SP} being not enough close to 1 prevent the establishment of an equipartitioning regime.

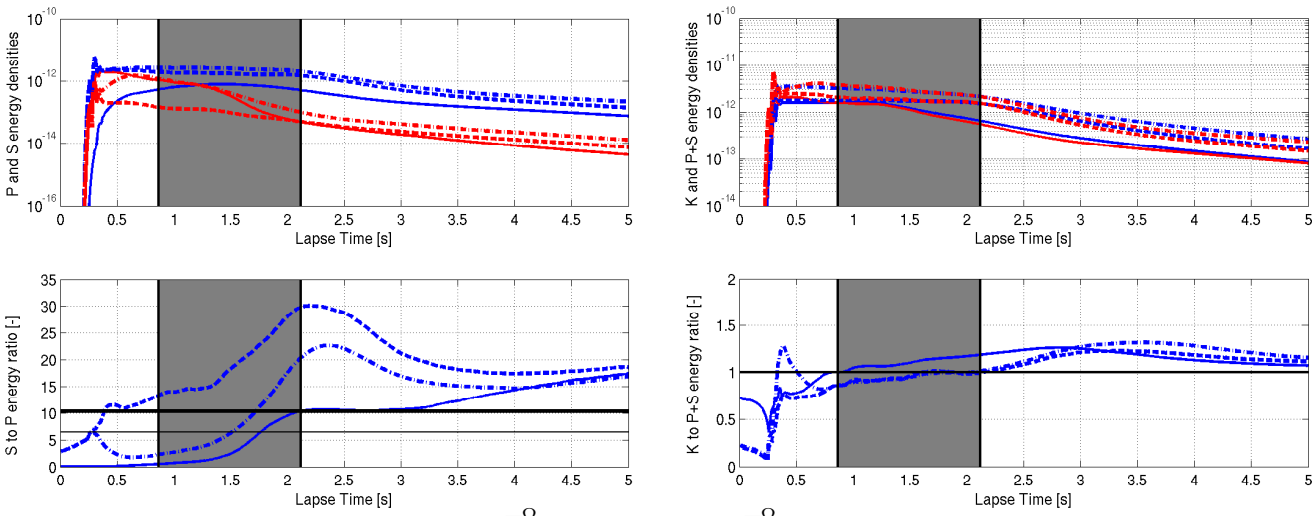

Figure 3.15: Top left: temporal variation of $\overline{\mathcal{E}}_p^{\Omega}$ (red curves) and $\overline{\mathcal{E}}_s^{\Omega}$ (blue curves). Bottom left: temporal variation of $\overline{\mathcal{E}}_s^{\Omega}/\overline{\mathcal{E}}_p^{\Omega}$. Top right: temporal variation of $\bar{K}^{\Omega}$ (blue curves) and $\overline{\mathcal{E}}_p^{\Omega} + \overline{\mathcal{E}}_s^{\Omega}$ (red curves). Bottom right: temporal variation of $\bar{K}^{\Omega}/(\overline{\mathcal{E}}_p^{\Omega} + \overline{\mathcal{E}}_s^{\Omega})$. Solid, dashed and dashed-dotted curves correspond respectively to explosion, unidirectional and combined source. The starting and end points of the shaded window indicate respectively the lapse times in which the direct P and S waves propagating in homogeneous background arrive to the boundaries.

In previous sections, no attention has been paid to the influence of the boundary conditions to the stabilization values. In the following section, we discuss this influence via numerical simulations.

3.3.4 Influence of the PML layers

The propagation domain being subjected to an explosion has now three different boundary conditions of types half-space (PML layers all around the medium except over the free surface), full-space (PML layers surrounding the propagation medium) and Neumann (reflecting or stress-free boundaries). Figure 3.16 summarizes all the results regarding the spatially-averaged energy densities. In the top left plot, the red and blue curves represent $\overline{\mathcal{E}}_p^{\Omega}$ and $\overline{\mathcal{E}}_s^{\Omega}$ respectively. The results corresponding to the half-space, full-space and Neumann cases are also differentiated by solid, dashed and dashed-doted curves. The lower left plot shows the corresponding stabilization values. A direct result that can be drawn from this plot is that the existence of the PML layers implies an increase in the stabilization values. This is assumed to be the effect of PML boundary conditions which behave in favor of the S wave energy. The stabilization values are about 14.5, 14 and 12 respectively for half-space, full-space and Neumann boundary condition cases. These

values are not theoretically acceptable since they do not belong to the interval $[6.44, 10.4]$.

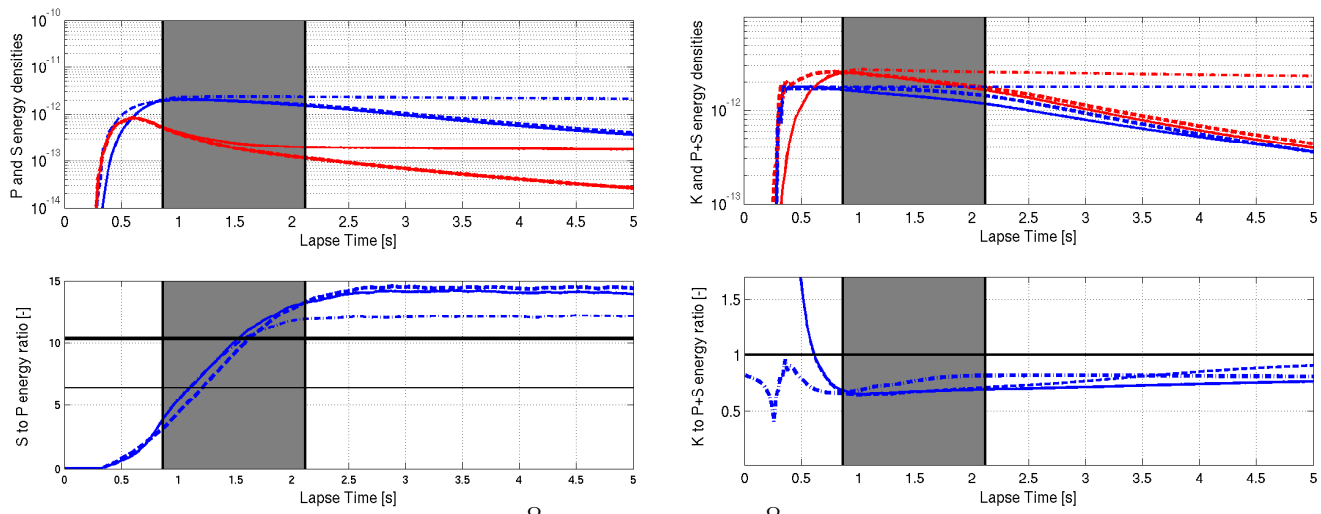

Figure 3.16: Top left: temporal variation of $\overline{\mathcal{E}}_p^{\Omega}$ (red curves) and $\overline{\mathcal{E}}_s^{\Omega}$ (blue curves). Bottom left: temporal variation of $\overline{\mathcal{E}}_s^{\Omega}/\overline{\mathcal{E}}_p^{\Omega}$. Top right: temporal variation of $\bar{K}^{\Omega}$ (blue curves) and $\overline{\mathcal{E}}_p^{\Omega} + \overline{\mathcal{E}}_s^{\Omega}$ (red curves). Bottom right: temporal variation of $\bar{K}^{\Omega}/(\overline{\mathcal{E}}_p^{\Omega} + \overline{\mathcal{E}}_s^{\Omega})$. Solid, dashed and dashed-dotted curves correspond respectively to half-space, full-space and Neumann boundary conditions. The starting and end points of the shaded window indicate respectively the lapse times in which the direct P and S waves propagating in homogeneous background arrive to the boundaries.

In this section, we have observed that the existence of the PML layers can slightly change the stabilization value in numerical observations of equipartitioning. This observation also revealed that this influence is in favor of the shear wave energy so that the stabilization ratio will be increased in the presence of PML layers.

In Sections 3.2.3 and 3.3 we investigated the numerical observation of an equipartitioning regime and also discussed the influence of some key factors in the onset of this regime at long lapse times. Thus, so far no particular attention has been paid to the statistical identification problem. In the following section we propose a preliminary identification process of the spatial correlation of a random medium. This identification is based on measures of the curl and divergence of the displacement field of a random medium.

3.4 Identification of the correlation structure of the medium properties

The objective of this section is to use the curl-free and divergence-free parts of the seismograms at long lapse times in order to invert for the some statistical information of the propagation medium. In the following section, the theory which will be used in our inversion problem is introduced.

3.4.1 Theory

In previous sections we investigated the convergence of the spatially-averaged ratio $\langle ||\text{curl}\, \mathbf{u}(\mathbf{x})||^2 \rangle / \langle (\text{div}\, \mathbf{u}(\mathbf{x}))^2$ at long lapse times to the analytical values of $2K^5$ and $K^2 R_{\text{surface}}$ respectively in an open medium and over the free surface. Now, we will discuss about the local information that can be extracted

from solely time-averaged (and not spatially-averaged) ratio $\langle||\text{curl } \mathbf{u}(\mathbf{x})||^2\rangle_t/\langle(\text{div } \mathbf{u}(\mathbf{x}))^2\rangle_t$. The basic equation is:

$$\frac{\langle\mathcal{E}_s(\mathbf{x})\rangle_t}{\langle\mathcal{E}_p(\mathbf{x})\rangle_t} = \frac{\mu(\mathbf{x})}{\lambda(\mathbf{x})+2\mu(\mathbf{x})}\frac{\langle||\text{curl } \mathbf{u}(\mathbf{x})||^2\rangle_t}{\langle(\text{div } \mathbf{u}(\mathbf{x}))^2\rangle_t} = \frac{1}{(K_\delta(\mathbf{x}))^2}\frac{\langle||\text{curl } \mathbf{u}(\mathbf{x})||^2\rangle_t}{\langle(\text{div } \mathbf{u}(\mathbf{x}))^2\rangle_t} \tag{3.60}$$

in which $K_\delta(\mathbf{x})$ is the ratio between local phase velocities in the case of a random medium with a given fluctuation level $\delta_{|C|} = \delta_\kappa = \delta_\mu = \delta$. Since in an equipartitioning regime, the local time-averaged ratio $\langle\mathcal{E}_s(\mathbf{x})\rangle_t/\langle\mathcal{E}_p(\mathbf{x})\rangle_t$ will tend to a global average value $2K^3$ for an open medium, we will have:

$$\frac{\langle||\text{curl } \mathbf{u}(\mathbf{x})||^2\rangle_t}{\langle(\text{div } \mathbf{u}(\mathbf{x}))^2\rangle_t} = 2K^3(K_\delta(\mathbf{x}))^2 \tag{3.61}$$

As a result, the correlation structure of the time-averaged field $\langle||\text{curl } \mathbf{u}(\mathbf{x})||^2\rangle_t/\langle(\text{div } \mathbf{u}(\mathbf{x}))^2\rangle_t$ (which is calculable in our numerical simulations and also over the free surface in real situations) tends to be the same as the correlation structure of the adimensional local value $(K_\delta(\mathbf{x}))^2$ which has itself a structure similar to that of the local value of the P to S wave speed ratio $K_\delta(\mathbf{x}) = v_p(\mathbf{x})/v_s(\mathbf{x})$. We will discuss about these relations in the next paragraphs. The basic hypotheses of the calculations are: **1)** $\kappa(\mathbf{x})$ and $\mu(\mathbf{x})$ are two independent random fields with the same coefficient of variation δ. Note that the independence implies that their correlation coefficient vanishes or: $\langle\kappa\mu\rangle - \langle\kappa\rangle\langle\mu\rangle = 0$. **2)** The mean values of all random fields are space-independent. In other words, the average background medium is deterministic. and **3)** The correlation kernels of the random fields $\kappa(\mathbf{x})$ and $\mu(\mathbf{x})$ are assumed to be the same:

$$\hat{R}_{\kappa\kappa}(\tau) = \hat{R}_{\mu\mu}(\tau) \tag{3.62}$$

it should be noted that if this relation is not valid, the final result will be a function of different correlation distances.

We start by calculating the cross-correlation function of the random fields $\lambda(\mathbf{x})$ and $\mu(\mathbf{x})$. The correlation coefficient between the random variables λ and μ is:

$$\rho(\lambda,\mu) = \frac{\text{cov}(\lambda,\mu)}{\sigma_\lambda\sigma_\mu} = \frac{\langle\kappa\mu\rangle - \langle\kappa\rangle\langle\mu\rangle - \frac{2}{3}\left(\langle\mu^2\rangle - \langle\mu\rangle^2\right)}{\sqrt{\sigma_\kappa^2 + \frac{4}{9}\sigma_\mu^2}\sigma_\mu} = \frac{-2\sigma_\mu}{3\sqrt{\sigma_\kappa^2 + \frac{4}{9}\sigma_\mu^2}} \tag{3.63}$$

The normalized cross-correlation kernel of $\lambda(\mathbf{x})$ and $\mu(\mathbf{x})$ reads:

$$\hat{R}_{\lambda\mu}(\tau) = \frac{\langle\lambda(\mathbf{x}+\boldsymbol{\tau})\mu(\mathbf{x})\rangle - \langle\lambda\rangle\langle\mu\rangle}{\sigma_\lambda\sigma_\mu\rho(\lambda,\mu)} = \frac{\langle\kappa(\mathbf{x}+\boldsymbol{\tau})\mu(\mathbf{x})\rangle - \langle\kappa\rangle\langle\mu\rangle - \frac{2}{3}\left(\langle\mu(\mathbf{x}+\boldsymbol{\tau})\mu(\mathbf{x})\rangle - \langle\mu\rangle^2\right)}{\sqrt{\sigma_\kappa^2 + \frac{4}{9}\sigma_\mu^2}\sigma_\mu\rho(\lambda,\mu)} \tag{3.64}$$

Given that $\langle\mu(\mathbf{x}+\boldsymbol{\tau})\mu(\mathbf{x})\rangle - \langle\mu\rangle^2 = \sigma_\mu^2\hat{R}_{\mu\mu}(\tau)$ and inserting the equation 3.63 into the equation 3.64 results in:

$$\hat{R}_{\lambda\mu}(\tau) = \hat{R}_{\mu\mu}(\tau) \tag{3.65}$$

Using also the equation 3.62 gives:

$$\hat{R}_{\lambda\mu}(\tau) = \hat{R}_{\kappa\kappa}(\tau) = \hat{R}_{\mu\mu}(\tau) \tag{3.66}$$

Now we derive the ACF of the random field λ in terms of the ACF of κ and μ:

$$\hat{R}_{\lambda\lambda}(\tau) = \frac{\langle \lambda(\mathbf{x}+\boldsymbol{\tau})\lambda(\mathbf{x})\rangle - \langle\lambda\rangle^2}{\sigma_\lambda^2} = \frac{\sigma_\kappa^2 \hat{R}_{\kappa\kappa}(\tau) + \frac{4}{9}\sigma_\mu^2 \hat{R}_{\mu\mu}(\tau)}{\sigma_\kappa^2 + \frac{4}{9}\sigma_\mu^2} \tag{3.67}$$

Consequently we have:

$$\hat{R}_{\lambda\mu}(\tau) = \hat{R}_{\lambda\lambda}(\tau) = \hat{R}_{\kappa\kappa}(\tau) = \hat{R}_{\mu\mu}(\tau) \tag{3.68}$$

Let $A(\mathbf{x}) = (K_\delta(\mathbf{x}))^2 = \frac{4}{3} + \frac{\kappa(\mathbf{x})}{\mu(\mathbf{x})}$, a second-order approximation for its mean and variance will be:

$$\langle A\rangle \simeq \frac{4}{3} + \frac{\langle\kappa\rangle}{\langle\mu\rangle}(1+\delta^2) \quad ; \quad \sigma_A^2 = 2\delta^2 \frac{\langle\kappa\rangle^2}{\langle\mu\rangle^2} \tag{3.69}$$

The ACF of A will be therefore:

$$\begin{aligned} R_{AA}(\tau) &= \frac{\langle A(\mathbf{x}+\boldsymbol{\tau})A(\mathbf{x})\rangle - \langle A\rangle^2}{\sigma_A^2} \\ &= \frac{\left\langle \frac{\kappa(\mathbf{x}+\boldsymbol{\tau})\kappa(\mathbf{x})}{\mu(\mathbf{x}+\boldsymbol{\tau})\mu(\mathbf{x})}\right\rangle + \frac{4}{3}\left\langle\frac{\kappa(\mathbf{x})}{\mu(\mathbf{x})}\right\rangle + \frac{4}{3}\left\langle\frac{\kappa(\mathbf{x}+\boldsymbol{\tau})}{\mu(\mathbf{x}+\boldsymbol{\tau})}\right\rangle + \frac{16}{9} - \left(\frac{4}{3} + \frac{\langle\kappa\rangle}{\langle\mu\rangle}(1+\delta^2)\right)^2}{2\delta^2\frac{\langle\kappa\rangle^2}{\langle\mu\rangle^2}} \end{aligned} \tag{3.70}$$

Inserting second-order approximations for the terms $\left\langle \frac{\kappa(\mathbf{x}+\boldsymbol{\tau})\kappa(\mathbf{x})}{\mu(\mathbf{x}+\boldsymbol{\tau})\mu(\mathbf{x})}\right\rangle$ and $\left\langle\frac{\kappa(\mathbf{x})}{\mu(\mathbf{x})}\right\rangle = \left\langle\frac{\kappa(\mathbf{x}+\boldsymbol{\tau})}{\mu(\mathbf{x}+\boldsymbol{\tau})}\right\rangle$ into 3.71 and simplifying the terms results in:

$$R_{AA}(\tau) = \frac{1+R(\tau)}{(1+\delta^2 R(\tau))^2} - \frac{(1+\delta^2)^2}{2\delta^2} \tag{3.71}$$

Assuming that δ^2 is small compared to 1, we can use the following approximation:

$$\frac{1}{1+\delta^2 R(\tau)} \simeq 1 - \delta^2 R(\tau) + \delta^4 R^2(\tau) + \mathrm{O}(\delta^6) \tag{3.72}$$

replacing this equation into the equation (3.71) gives:

$$R_{AA}(\tau) \simeq (1-2\delta^2)R(\tau) + \delta^2(3\delta^2-2)R^2(\tau) - \frac{\delta^2}{2} - \frac{1}{2\delta^2} \tag{3.73}$$

Integrating both sides of this equation in terms of τ will result in:

$$\int_{\mathbb{R}} R_{AA}(\tau)d\tau \simeq (1-2\delta^2)\int_{\mathbb{R}} R(\tau)d\tau + \delta^2(3\delta^2-2)\int_{\mathbb{R}} R^2(\tau)d\tau \tag{3.74}$$

Knowing that the correlation length of the Lamé parameters are defined as:

$$2\int_{\mathbb{R}} R(\tau)d\tau = \ell_c^\lambda = \ell_c^\mu = \ell_c^{\lambda\mu} = \ell_c \tag{3.75}$$

As a result:

$$\frac{\ell_c^A}{2} \simeq (1-2\delta^2)\frac{\ell_c}{2} + \delta^2(3\delta^2-2)\int_{\mathbb{R}} R^2(\tau)d\tau \tag{3.76}$$

Let $\tilde{\ell}_c$ denote the correlation length of $(K_\delta(\mathbf{x}))^2$ or $\frac{\langle ||\text{curl } \mathbf{u}(\mathbf{x})||^2\rangle_t}{\langle (\text{div } \mathbf{u}(\mathbf{x}))^2\rangle_t}$. Since for the correlation models used in this work we have $\int_{\mathbb{R}} R^2(\tau)d\tau \ll \ell_c$, we approximately have:

$$\tilde{\ell}_c \simeq (1 - 2\delta^2)\ell_c \tag{3.77}$$

Therefore, the correlation length of the time-averaged ratio $\frac{\langle ||\text{curl } \mathbf{u}(\mathbf{x})||^2\rangle_t}{\langle (\text{div } \mathbf{u}(\mathbf{x}))^2\rangle_t}$ is directly proportional to the correlation length of the medium via a factor which depends on its dispersion level. In the following paragraphs the numerical simulations to verify the convergence of the correlation structure of $\langle ||\text{curl } \mathbf{u}(\mathbf{x})||^2\rangle_t / \langle (\text{div } \mathbf{u}(\mathbf{x}))^2\rangle_t$ to that of $(K_\delta(\mathbf{x}))^2$ are presented.

3.4.2 Identification of the correlation structure

Two of the numerical case studies introduced in Table 3.4 will be discussed in this section with the aim of inversion for the statistical parameters of the medium.

Configuration: Influence of inefficient mixture of body waves In this simulation $\ell_c = 100(m)$, $K = \sqrt{3}$, $\delta = 0.40$ and the heterogeneities are considered to have either the low-pass white noise or the exponential correlation model. The correlation length of the local parameter $(K_\delta(\mathbf{x}))^2$ can be estimated using equation (3.77):

$$\tilde{\ell}_c \simeq (1 - 2(0.4)^2)(100) = 68(m) \tag{3.78}$$

A first-order approximation for the variance of the random field $(K_\delta(\mathbf{x}))^2$ in the right hand side of the equation (3.61) is:

$$\text{Var}\left((K_\delta(\mathbf{x}))^2\right) \simeq 2\delta^2 \left(K^2 - \frac{4}{3}\right)^2 = 0.88 \tag{3.79}$$

As a result, its standard deviation 0.94 is not negligible compared to its mean value 3.26. The results of the simulations are summarized in Figures 3.17 and 3.18 respectively for random medium with low-pass white noise and exponential correlation model. The calculations are done at the lapse time $t = 4(s)$. These figures show the convergence of the estimated correlation function of the time-averaged ratio $\langle ||\text{curl } \mathbf{u}(\mathbf{x})||^2\rangle_t / \langle (\text{div } \mathbf{u}(\mathbf{x}))^2\rangle_t$ (blue curve) toward the correlation function of the corresponding slice (R_{AA} in equation (3.73)) (black curve). It should be pointed out that the time-averagings are done over the windows of 1s. Subsequently, the correlation length defined as twice the area under the correlation function is converged toward the value $68(m)$ (see the value of ℓ_c indicated over the plots in third columns).

Tables 3.6 summarizes the correlation coefficients between the fields $\frac{\langle ||\text{curl } \mathbf{u}(\mathbf{x})||^2\rangle_t}{\langle (\text{div } \mathbf{u}(\mathbf{x}))^2\rangle_t}$ and $(K_\delta(\mathbf{x}))^2$ at different depths and lapse times for the random medium with low-pass white noise correlation model. Significant correlations are therefore observed between the random fields. We also emphasize on the fact that the correlation over the slice in the free surface at all lapse times is higher than in the other slices.

We discussed in this section the identification of the correlation structure of a random medium by calculating the time-averaged ratio between the square curl and divergence of the displacement wavefield. In the next section we introduce a limit in which our method does not give a proper identification of the correlation function.

	$t = 2(s)$	$t = 4(s)$
$z = 0(m)$	0.73	0.84
$z = -250(m)$	0.68	0.74
$z = -500(m)$	0.70	0.75

Table 3.6: Correlation coefficients of the fields $\frac{\langle ||\text{curl } \mathbf{u}(\mathbf{x})||^2 \rangle_t}{\langle (\text{div } \mathbf{u}(\mathbf{x}))^2 \rangle_t}$ and $(K_\delta(\mathbf{x}))^2$ at different depths and lapse times.

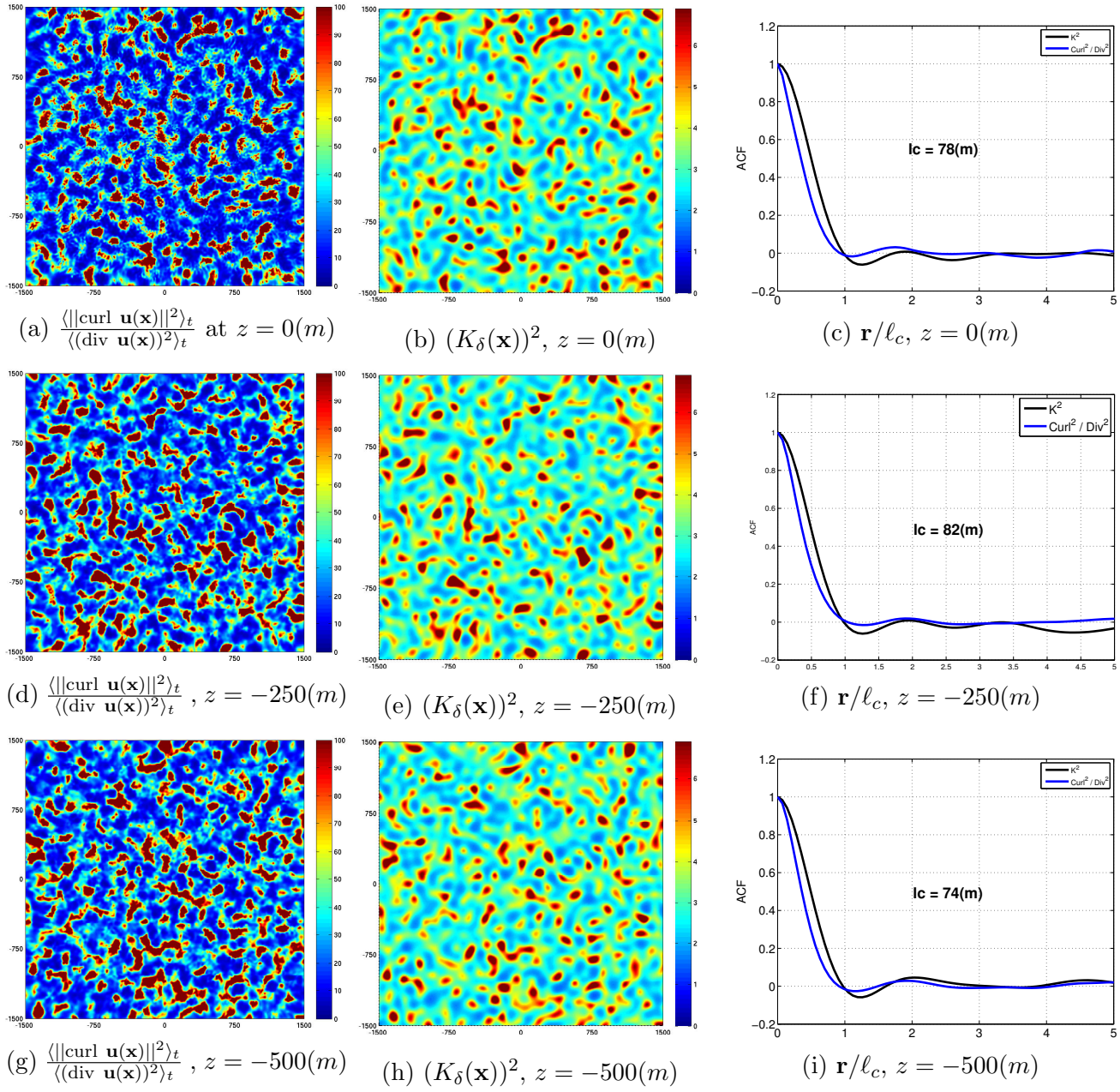

(a) $\frac{\langle ||\text{curl } \mathbf{u}(\mathbf{x})||^2 \rangle_t}{\langle (\text{div } \mathbf{u}(\mathbf{x}))^2 \rangle_t}$ at $z = 0(m)$ (b) $(K_\delta(\mathbf{x}))^2$, $z = 0(m)$ (c) $\mathbf{r}/\ell_c$, $z = 0(m)$

(d) $\frac{\langle ||\text{curl } \mathbf{u}(\mathbf{x})||^2 \rangle_t}{\langle (\text{div } \mathbf{u}(\mathbf{x}))^2 \rangle_t}$, $z = -250(m)$ (e) $(K_\delta(\mathbf{x}))^2$, $z = -250(m)$ (f) $\mathbf{r}/\ell_c$, $z = -250(m)$

(g) $\frac{\langle ||\text{curl } \mathbf{u}(\mathbf{x})||^2 \rangle_t}{\langle (\text{div } \mathbf{u}(\mathbf{x}))^2 \rangle_t}$, $z = -500(m)$ (h) $(K_\delta(\mathbf{x}))^2$, $z = -500(m)$ (i) $\mathbf{r}/\ell_c$, $z = -500(m)$

Figure 3.17: Identification results for a half-space with low-pass white noise correlation model. Left column: the time-averaged ratio $\frac{\langle ||\text{curl } \mathbf{u}(\mathbf{x})||^2 \rangle_t}{\langle (\text{div } \mathbf{u}(\mathbf{x}))^2 \rangle_t}$ at 3 different horizontal slices at the time lapse $t = 4(s)$; Middle column: local values of the field $(K_\delta(\mathbf{x}))^2$; Right column: the correlation functions corresponding to the left and the middle columns.

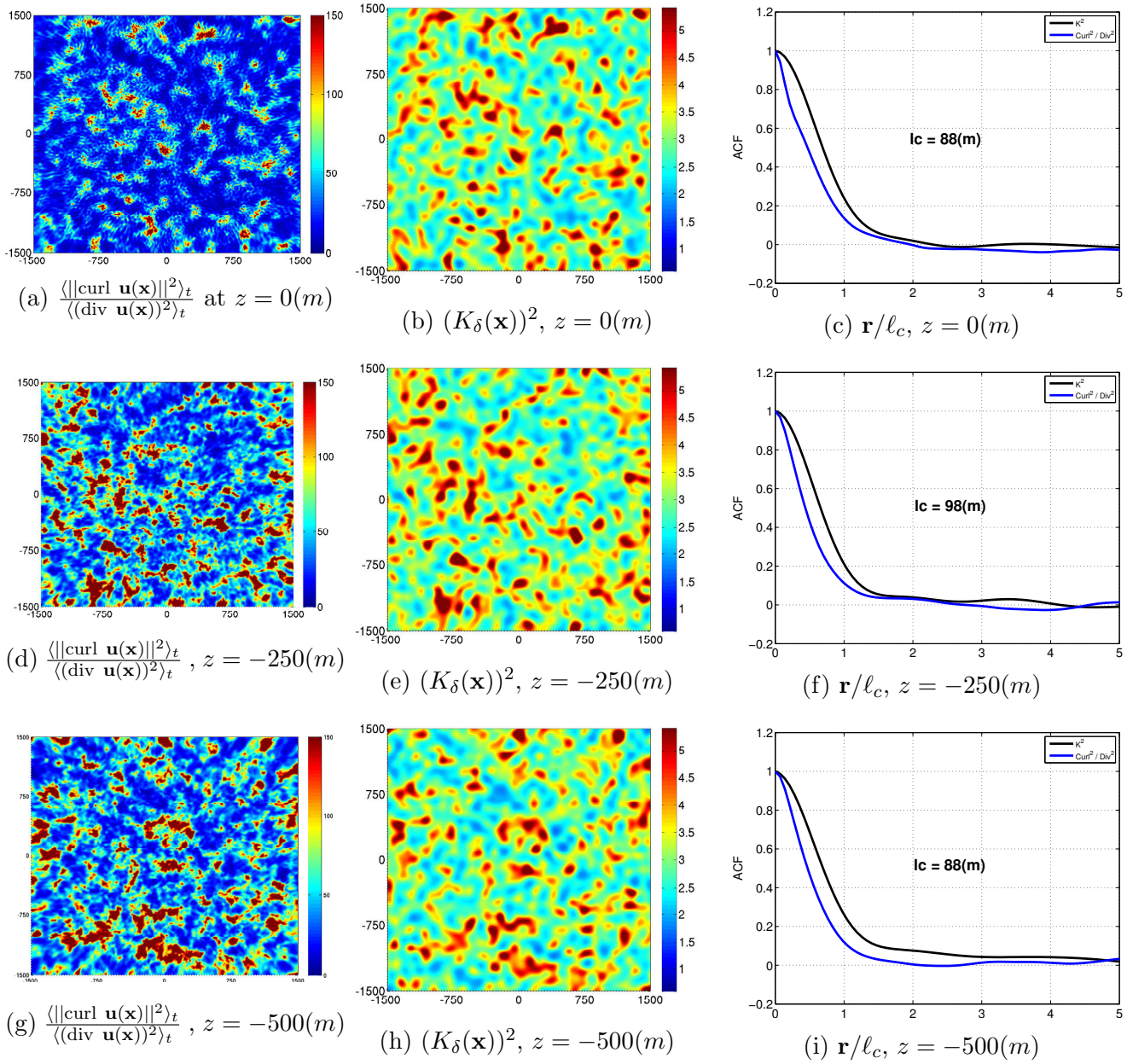

(a) $\frac{\langle ||\text{curl } \mathbf{u}(\mathbf{x})||^2\rangle_t}{\langle (\text{div } \mathbf{u}(\mathbf{x}))^2\rangle_t}$ at $z = 0(m)$ (b) $(K_\delta(\mathbf{x}))^2$, $z = 0(m)$ (c) $\mathbf{r}/\ell_c$, $z = 0(m)$

(d) $\frac{\langle ||\text{curl } \mathbf{u}(\mathbf{x})||^2\rangle_t}{\langle (\text{div } \mathbf{u}(\mathbf{x}))^2\rangle_t}$, $z = -250(m)$ (e) $(K_\delta(\mathbf{x}))^2$, $z = -250(m)$ (f) $\mathbf{r}/\ell_c$, $z = -250(m)$

(g) $\frac{\langle ||\text{curl } \mathbf{u}(\mathbf{x})||^2\rangle_t}{\langle (\text{div } \mathbf{u}(\mathbf{x}))^2\rangle_t}$, $z = -500(m)$ (h) $(K_\delta(\mathbf{x}))^2$, $z = -500(m)$ (i) $\mathbf{r}/\ell_c$, $z = -500(m)$

Figure 3.18: Identification results for a half-space with exponential correlation model. Left column: the time-averaged ratio $\frac{\langle ||\text{curl } \mathbf{u}(\mathbf{x})||^2\rangle_t}{\langle (\text{div } \mathbf{u}(\mathbf{x}))^2\rangle_t}$ at 3 different horizontal slices at the time lapse $t = 4(s)$; Middle column: local values of the field $(K_\delta(\mathbf{x}))^2$; Right column: the correlation functions corresponding to the left and the middle columns.

3.4.3 Limitation to the identification of the correlation structure

Configuration: Reference and Reference-exp A random medium characterized with $K = 1.16$, $\delta = 0.40$ with either low-pass white noise or exponential correlation model is considered. The correlation length of the random elastic moduli is set to be $\ell_c = 100(m)$. Contrary to the previous case study, the variance of the random field $(K_\delta(\mathbf{x}))^2$ will be:

$$\text{Var}\left((K_\delta(\mathbf{x}))^2\right) \simeq 0.00005 \tag{3.80}$$

The corresponding standard deviation will be thus 0.007 which is negligible compared to its average value being 1.35. This means that the random field $(K_\delta(\mathbf{x}))^2$ is almost deterministic despite

the fact that the elastic moduli (κ, μ) have a coefficient of variation of 40%. This implies in particular that the ratio in the left hand side of the equation (3.61) is almost deterministic. It also means that the information about the correlation structure of the medium cannot be extracted from the ratio $\frac{\langle ||\text{curl } \mathbf{u}(\mathbf{x})||^2 \rangle_t}{\langle (\text{div } \mathbf{u}(\mathbf{x}))^2 \rangle_t}$. Figures 3.19 and 3.20 show the plots of the random fields $\langle ||\text{curl } \mathbf{u}(\mathbf{x})||^2 \rangle_t / \langle (\text{div } \mathbf{u}(\mathbf{x}))^2 \rangle_t$ and $(K_\delta(\mathbf{x}))^2$ along with their respective spatial correlation functions in 3 different slices at the depths $z = 0(m), -250(m), -500(m)$, respectively for low-pass white noise and exponential correlation models. The considered lapse time is $t = 4(s)$. The random field $\langle ||\text{curl } \mathbf{u}(\mathbf{x})||^2 \rangle_t / \langle (\text{div } \mathbf{u}(\mathbf{x}))^2 \rangle_t$ at longer lapse times (see Figures 3.19 and 3.20) is similar to a white noise random process with no spatial correlation. The reason is the fact that $(K_\delta(\mathbf{x}))^2$ is almost not spatially varying.

Table 3.7 summarizes the correlation coefficients between the fields $\frac{\langle ||\text{curl } \mathbf{u}(\mathbf{x})||^2 \rangle_t}{\langle (\text{div } \mathbf{u}(\mathbf{x}))^2 \rangle_t}$ and $(K_\delta(\mathbf{x}))^2$ at different depths and lapse times for the random medium with low-pass white noise correlation model. This table confirms the decorrelation between the random fields independent of the lapse time and the depth of the slice.

	$t = 2(s)$	$t = 4(s)$
$z = 0(m)$	-0.002	0.004
$z = -250(m)$	0.056	0.102
$z = -500(m)$	0.072	0.107

Table 3.7: Correlation coefficients of the fields $\frac{\langle ||\text{curl } \mathbf{u}(\mathbf{x})||^2 \rangle_t}{\langle (\text{div } \mathbf{u}(\mathbf{x}))^2 \rangle_t}$ and $(K_\delta(\mathbf{x}))^2$ at different depths and lapse times.

In this section we proposed a method for identification of the spatial correlation of a random medium. This method was based on the local version of the equipartitioning law written in terms of the curl and divergence of the displacement wavefield. The numerical simulations for two different correlation models revealed appropriate estimations of the analytical correlation functions. Other complementary researches should be done in order to verify this identification technique.

3.5 Summary and Conclusion

In this chapter, the numerical simulations of elastic wave propagation in random media are performed using the computational code SPEC3D. The numerical observation of the equipartitioning regime at long lapse times is investigated as a tool to identify the ratio between the space-averaged elastic moduli. We observed that for lower values of K in which the body waves are not highly differentiated, the energy is equipartitioned between the body waves. Using typical values of K and large values of δ results in a strong localization regime being dominant and thus the equipartitioning regime is not observed. For typical values of K and lower variances, the localization does not appear. However, an equipartitioning regime is not observed because:

(i) for average δ, the mixture between the body wave energies is inefficient,

(ii) for low δ, the transport mean free paths of the body waves become too large compared to the size of the domain, so that the waves go into the PML before an equipartitioning regime sets in.

The latter is related to limitations in modeling sufficiently big propagation domains. At the end of this chapter, using the time-averaged ratio between the squared curl and divergence of the

displacement wavefield, a relation is developed between the spatial correlation function of this medium and the correlation and dispersion level of the random medium under study.

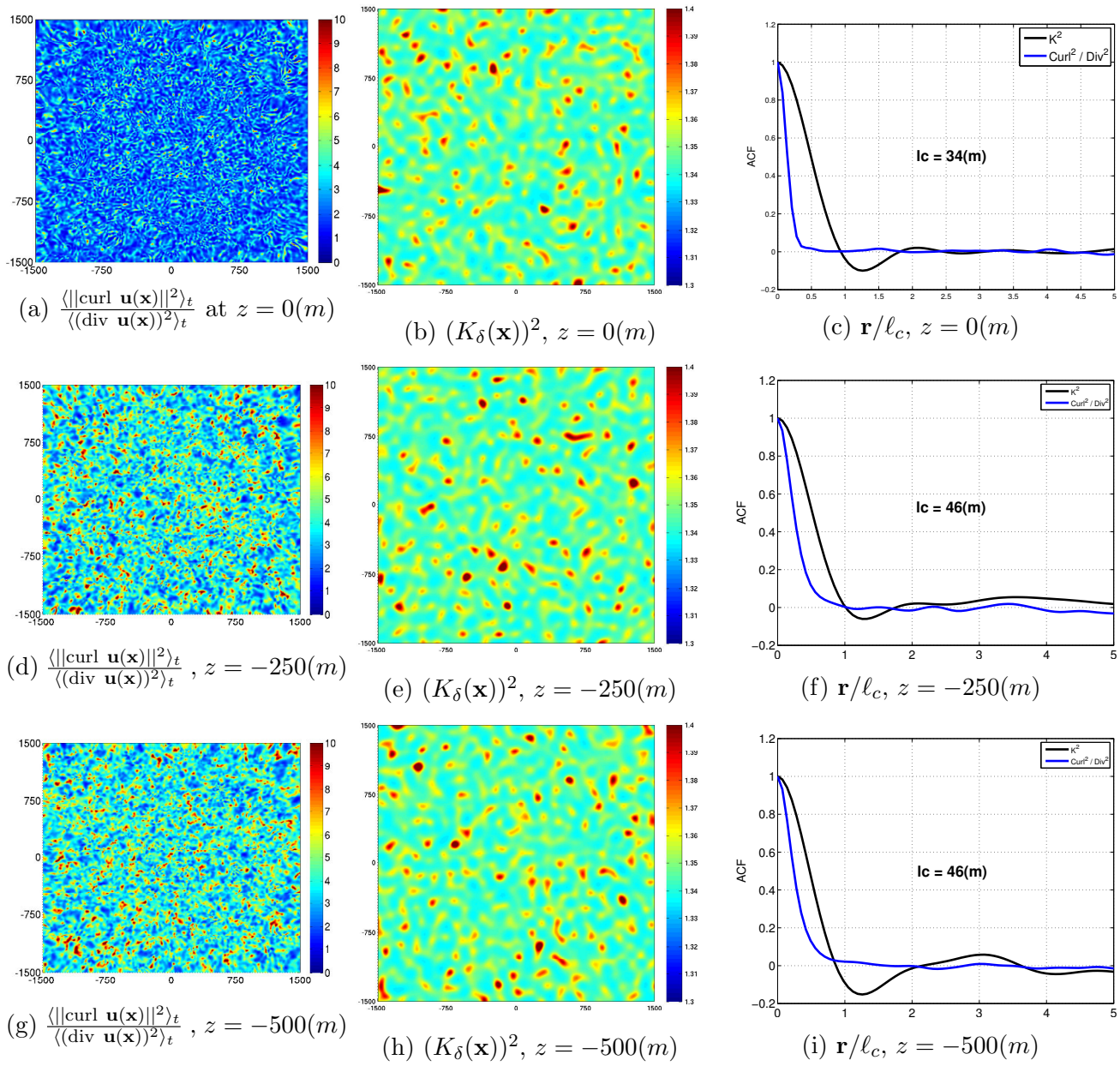

(a) $\frac{\langle ||\text{curl } \mathbf{u}(\mathbf{x})||^2 \rangle_t}{\langle (\text{div } \mathbf{u}(\mathbf{x}))^2 \rangle_t}$ at $z = 0(m)$ (b) $(K_\delta(\mathbf{x}))^2$, $z = 0(m)$ (c) $\mathbf{r}/\ell_c$, $z = 0(m)$

(d) $\frac{\langle ||\text{curl } \mathbf{u}(\mathbf{x})||^2 \rangle_t}{\langle (\text{div } \mathbf{u}(\mathbf{x}))^2 \rangle_t}$, $z = -250(m)$ (e) $(K_\delta(\mathbf{x}))^2$, $z = -250(m)$ (f) $\mathbf{r}/\ell_c$, $z = -250(m)$

(g) $\frac{\langle ||\text{curl } \mathbf{u}(\mathbf{x})||^2 \rangle_t}{\langle (\text{div } \mathbf{u}(\mathbf{x}))^2 \rangle_t}$, $z = -500(m)$ (h) $(K_\delta(\mathbf{x}))^2$, $z = -500(m)$ (i) $\mathbf{r}/\ell_c$, $z = -500(m)$

Figure 3.19: Identification results for a half-space with low-pass white noise correlation model. Left column: the time-averaged ratio $\frac{\langle ||\text{curl } \mathbf{u}(\mathbf{x})||^2 \rangle_t}{\langle (\text{div } \mathbf{u}(\mathbf{x}))^2 \rangle_t}$ at 3 different horizontal slices at the time lapse $t = 4(s)$; Middle column: local values of the field $(K_\delta(\mathbf{x}))^2$; Right column: the correlation functions corresponding to the left and the middle columns.

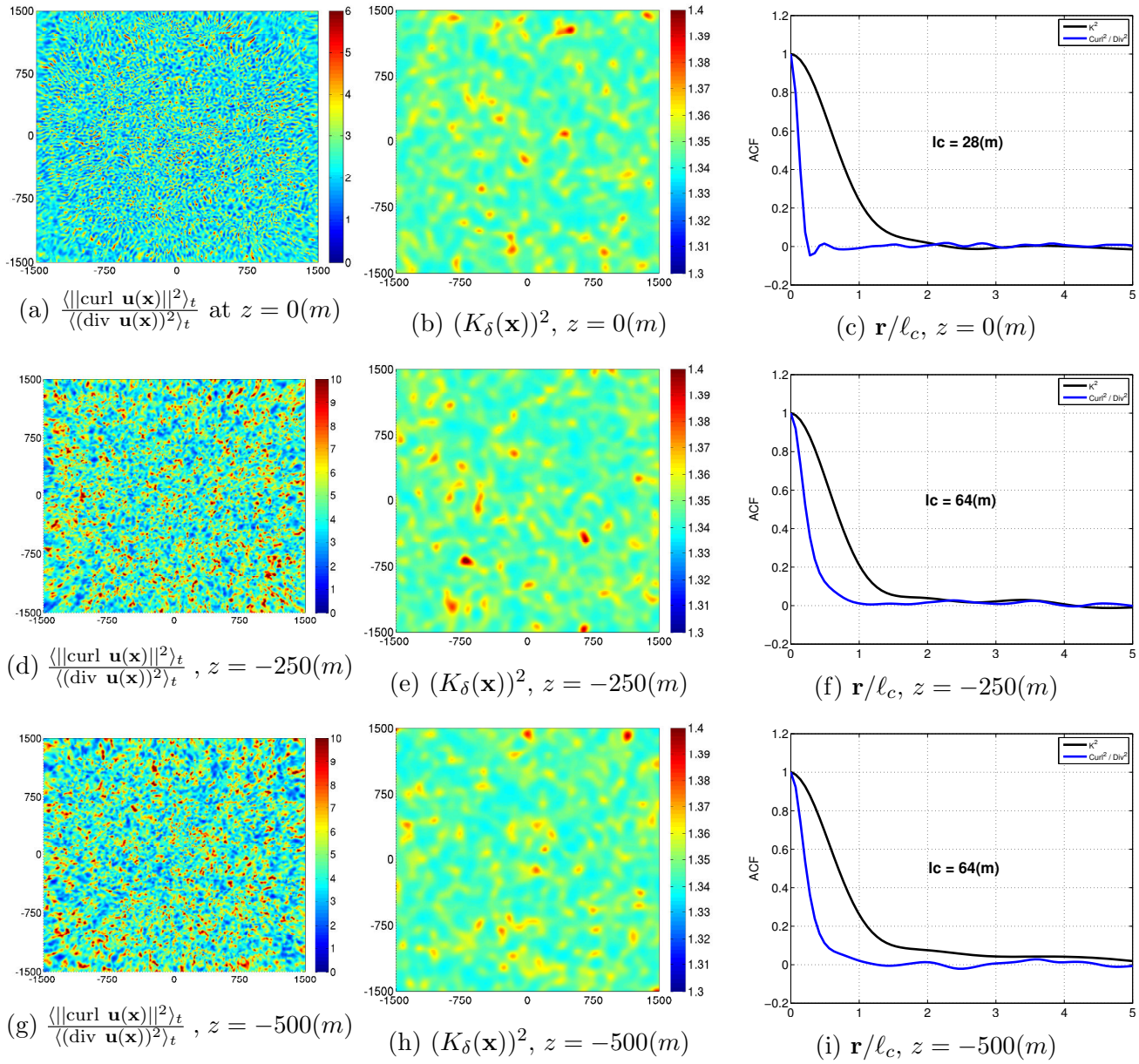

(a) $\frac{\langle ||\text{curl } \mathbf{u}(\mathbf{x})||^2\rangle_t}{\langle (\text{div } \mathbf{u}(\mathbf{x}))^2\rangle_t}$ at $z = 0(m)$ (b) $(K_\delta(\mathbf{x}))^2$, $z = 0(m)$ (c) $\mathbf{r}/\ell_c$, $z = 0(m)$

(d) $\frac{\langle ||\text{curl } \mathbf{u}(\mathbf{x})||^2\rangle_t}{\langle (\text{div } \mathbf{u}(\mathbf{x}))^2\rangle_t}$, $z = -250(m)$ (e) $(K_\delta(\mathbf{x}))^2$, $z = -250(m)$ (f) $\mathbf{r}/\ell_c$, $z = -250(m)$

(g) $\frac{\langle ||\text{curl } \mathbf{u}(\mathbf{x})||^2\rangle_t}{\langle (\text{div } \mathbf{u}(\mathbf{x}))^2\rangle_t}$, $z = -500(m)$ (h) $(K_\delta(\mathbf{x}))^2$, $z = -500(m)$ (i) $\mathbf{r}/\ell_c$, $z = -500(m)$

Figure 3.20: Identification results for a half-space with exponential correlation model. Left column: the time-averaged ratio $\frac{\langle ||\text{curl } \mathbf{u}(\mathbf{x})||^2\rangle_t}{\langle (\text{div } \mathbf{u}(\mathbf{x}))^2\rangle_t}$ at 3 different horizontal slices at the time lapse $t = 4(s)$; Middle column: local values of the field $(K_\delta(\mathbf{x}))^2$; Right column: the correlation functions corresponding to the left and the middle columns.

Conclusions and Perspectives

The general focus of this work was the analysis of the coda waves and their relation with the statistical parameters of the heterogeneous propagation medium. These incoherent waves are originated from the multiple scattering of elastic waves (Aki and Chouet, 1975). Hence, a profound understanding of the scattering of elastic waves and its effects on the wave propagation regime is a fundamental step in the statistical identification of the medium properties. For this purpose, a particular attention has been paid to the kinetic approaches describing the elastic waves propagating through heterogeneous media based on the works of Ryzhik et al. (1996). The particular aspect of this study is taking into account the full elastic nature of elastic waves rather than the acoustic approximation which is typically used in the literature. The parameters describing the scattering of elastic waves (such as differential, total and forward scattering cross-sections) are functions of the first and second order statistics of the medium parameters. They were normalized and expressed in terms of the following four key parameters being influential in the determination of the scattering mechanism:

(i) The ratio ζ between the correlation length and the wavelength,

(ii) The ratio K between the mean values of P and S wave velocities,

(iii) The fluctuation levels δ of elastic moduli (the covariance matrix),

(iv) The spatial correlation model $\hat{R}$.

A special focus has been given to the evaluation of the influence of spatial correlation model of the random medium on the scattering parameters. In low ζ, the influence of the correlation model can be described via the value of the PSDF at origin. In medium ζ ($\zeta \sim 1$), the influence of the correlation model is limited. However, for large values of ζ, there is no influence on the P-P and S-S total scattering cross-sections. On the contrary, a drastic influence is observed in P-S scattering coefficient. The latter along with K are the crucial parameters in the establishment of an equipartitioning regime. In high ζ, the correlation kernel has a noticeable influence on the onset of an equipartitioning regime. As a consequence, among the classical correlation models used in Geophysics, in low and high ζ, the exponential model results in quicker global apparition of a diffusion regime. However, in medium ζ, a low-pass white noise model minimizes the equipartitioning time.

The influence of the above-mentioned parameters in setting up an equipartitioning regime were also studied via numerical simulations. Analytical formulas of the stabilization ratio between the P and S wave energies were derived for both cases of propagation media with and without a free surface. The former were formulated in terms of the curl and divergence of the displacement wavefield rather than the energies. For low values of K, a global equipartitioning regime was

observed. Several less favorable situations were also studied, where we could not observe the onset of equipartition between the energies. This was either due to localization, inefficient exchange of energy between P and S waves or the fact that the propagation length was too small compared to the mean free paths.

As far as the statistical identification problem is concerned, we used a local version of the equipartitioning law in which the ratio between the time-averaged squared curl and divergence of the displacement wavefields at each point is related to the local values of the P to S wave speed ratio. We showed that the spatial correlation of the mentioned time-averaged ratio tends to $(1-2\delta)\ell_c$ at long lapse times and illustrated on a first example the effectiveness of the identification. This can be a first step towards the statistical identification problem especially over the free surface.

With regard to the future works, the following aspects could be treated in order to improve the results provided in this work:

(i) Consideration of the spatial variability of the density since it has been shown that it can significantly increase the wave attenuation and therefore facilitate the apparition of a diffusion regime (Turner and Anugonda, 2001).

(ii) The generation of the random medium properties notably in large-scales is one of the main limitations in numerical simulations of the wave propagation. This implies the necessity of optimization of the random field generation procedure. This work is recently carried out theoretically and is also implemented by Victor Bouvier and Luciano de Carvalho in MSSMat.

(iii) Recently the radiative transfer equations of elastic waves were rigorously developed for the case of a random medium with locally anisotropic behavior (Baydoun et al., 2014). Since Ta (2011) observed that the anisotropy favors significantly quicker onset of the diffusion regime, it would be interesting to validate the results of the simulations performed over anisotropic media via the corresponding analytical formulas.

(iv) In order to be capable of observing a diffusion regime in low-variance random media with Poissonian materials, one should use a more efficient computational code which allows to use a few thousand processors and thus enables us to model sufficiently large media. Lately, a couple of students and researchers started to develop another calculation code called SEM3D in the framework of the SINAPS@ project. Luciano de Carvalho is adding random field capabilities in SEM3D. Filippo Gatti is treating the case of nonlinear constitutive law with the aim of evaluating the influence of the non-linearities in the wave propagation regime. Angkeara Svay uses SEM3D to analyze different influencing parameters on the spatial variation of seismic ground motions. The purpose of his work is to distinguish the deterministic effects (site geometries,...) as well as the effects of the spatial variabilities in the medium parameters on the formulation of the coherency model.

Appendices

Appendix A

Behavior of functions I_n and J_n

A.1 Integral W_n^p

We introduce, because it will be useful in understanding the behavior of the function I_n, the integral

$$W_n^p = \int_0^1 \left(1 - 2\chi^2\right)^n \chi^{p+1} d\chi, \tag{A.1}$$

for $n \geq 0$ and $p \geq -1$. It can be shown that $W_n^0 = (1 + (-1)^n)/4(n+1)$. Also, for $p \geq 1$, the following recurrence relation holds $(2n + p + 2)W_n^p = 2nW_{n-1}^p + (-1)^n$. Using the initial value $W_0^p = 1/(p+2)$, this means that the values W_n^p can be computed for any pair (n, p). In particular, we have $W_n^2 = (1 + (-1)^n(2n+3))/8(n+1)(n+2)$.

Table A.1: Values of W_n^p for the first values of n and p.

	W_n^0	W_n^1	W_n^2	W_n^3	W_n^4
W_0^p	1/2	1/3	1/4	1/5	1/6
W_1^p	0	-1/15	-1/12	-3/35	-1/12
W_2^p	1/6	11/105	1/12	23/315	1/15
W_3^p	0	-13/315	-1/20	-59/1155	-1/20
W_4^p	1/10	211/3465	1/20	683/15015	3/70
W_5^p	0	-271/9009	-1/28	-1637/45045	-1/28

A.2 Integral V_n^p

Similarly, we introduce for the understanding of J_n

$$V_n^p(K) = K_0^{n+1} \int_{K_1}^{K_2} \left(1 - 2\chi^2\right)^n \chi^{p+1} d\chi, \tag{A.2}$$

for $n \geq 0$ and $p \geq -1$. We remind that $K_0 = (K + 1/K)/2$, $K_1 = (K-1)/\sqrt{2(K^2+1)}$ and $K_2 = (K+1)/\sqrt{2(K^2+1)}$. Note that $V_n^p(1) = W_n^p$. The values of V_n^p could be calculated via:

$$V_n^p(K) = K_0^{n+1} \sum_{j=0}^{n} \frac{(-2)^j \binom{n}{j}}{p + 2j + 2} \left(K_2^{p+2j+2} - K_1^{p+2j+2}\right) \tag{A.3}$$

In particular, we have $V_n^0 = (1+(-1)^n)/4(n+1)$ and $V_0^p = K_0(K_2^{p+2} - K_1^{p+2})/(p+2)$. Also, for $p \geq 1$, the following recurrence relation holds $(2n+p+2)V_n^p/K_0 = 2nV_{n-1}^p - (K_2^{p+2} + (-1)^n K_1^{p+2})$. We also have $V_{n+1}^p = K_0(V_n^p - 2V_n^{p+2})$. These two relations can be used to compute the values V_n^p for any pair (n, p). They yield in particular $V_n^0 = (1+(-1)^n)/(4(n+1))$ and $V_{2n}^2 = (1+(-1)^n)/(8(n+1))$. Observe that for these two examples, V_n^p is independent of K. This is however not true in general. Note also that, although it depends on the value of K, this family of parameters V_n^p does not depend on the correlation kernel.

A.3 Behavior of function I_n

We consider the following integral function (see Figure A.1 for its behavior for different correlation functions and values of n):

$$I_n(\zeta) = \int_0^1 \left(1 - 2\chi^2\right)^n \chi \Phi(\zeta\chi) d\chi \tag{A.4}$$

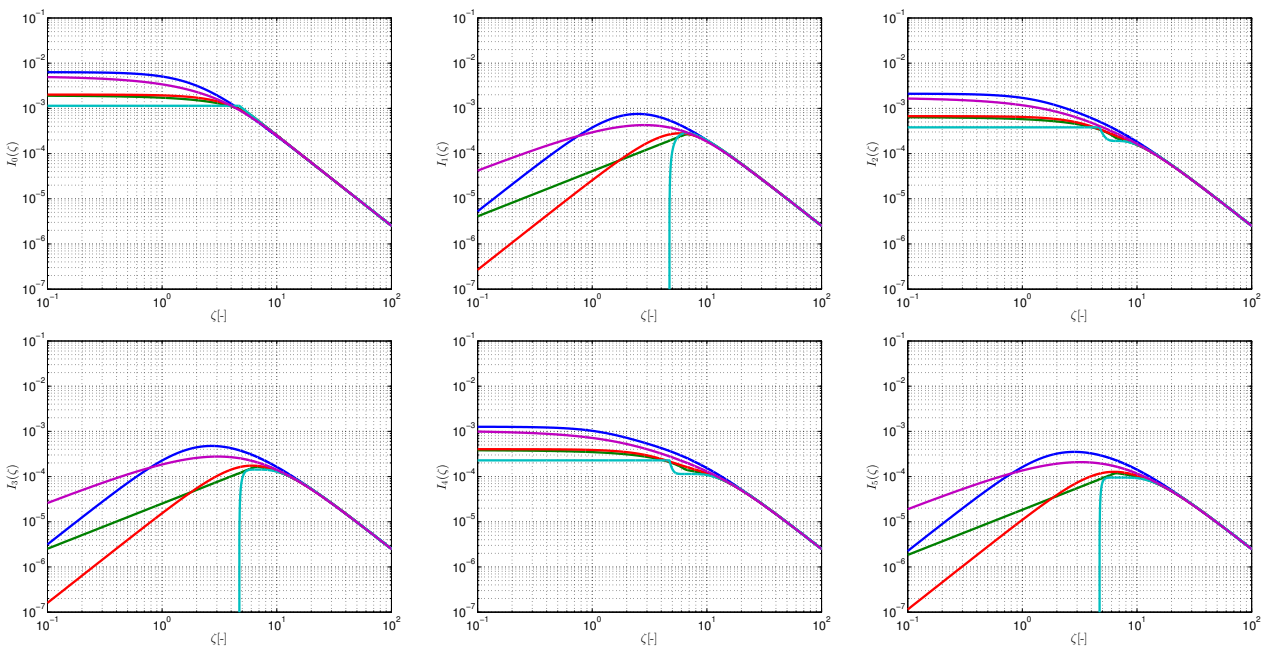

Figure A.1: Functions $I_n(\zeta)$ for different correlation kernels and different values of n ($K = \sqrt{3}$): exponential (thick solid line), power-law (thin dashed-dotted line), Gaussian (thick dashed line), triangular (thin solid line) and low-pass white noise (thin dashed line).

Using a Taylor expansion of the function $\Phi(\zeta\chi)$ for low frequencies, we get:

$$I_n(\zeta) = \sum_{p=0}^{\infty} \frac{\Phi^{(p)}(0)\zeta^p W_n^p}{p!} \tag{A.5}$$

so that the limit behavior of $I_n(\zeta)$ is:

$$I_n(\zeta) = \frac{\Phi(0)}{2(n+1)} + \mathrm{O}(\zeta) \quad \text{for even } n, \tag{A.6}$$

and

$$I_n(\zeta) = W_n^1 \Phi'(0)\zeta - \frac{\Phi''(0)}{8(n+2)}\zeta^2 + \mathrm{O}(\zeta^3) \quad \text{for odd } n. \tag{A.7}$$

Depending on the correlation model (see Table 2.1), $\Phi'(0)$ sometimes cancels, so the expansion has to be continued up to second order. For the low-pass white noise model, for which the spectrum is flat and all its derivatives cancel, the expansion is not correct. However, in that case, we can compute explicitly $I_n^{\text{noise}}(\zeta)$:

$$I_n^{\text{noise}}(\zeta \leq 3\pi/2) = \frac{1}{18\pi^2(n+1)}(1 + (-1)^n), \tag{A.8}$$

and

$$I_n^{\text{noise}}(\zeta \geq 3\pi/2) = \frac{1}{18\pi^2(n+1)}\left(1 - \left(1 - \frac{9\pi^2}{2\zeta^2}\right)^{n+1}\right). \tag{A.9}$$

The high-frequency behavior of the function $I_n(\zeta)$ can be investigated through the change of variable $\zeta\chi = p$:

$$I_n(\zeta \gg 1) = \zeta^{-2}\int_0^{\zeta}(1 - 2\frac{p^2}{\zeta^2})^n p\Phi(p)dp = \frac{1}{4\pi^2}\zeta^{-2} + \mathrm{O}(\zeta^{-3}) \tag{A.10}$$

This limit is hence independent from the correlation kernel. The results obtained from the asymptotic analysis are summarized in Table A.2.

Table A.2: Asymptotic values of $I_n(\zeta)$ and $J_n(\zeta; K)$ for different correlation kernels

Integral	Low frequency $\zeta \ll 1$	High frequency $\zeta \gg 1$
$I_n(\zeta)$, even n	$\frac{\Phi(0)}{2(n+1)}$	$\frac{1}{4\pi^2}\zeta^{-2}$
$I_n(\zeta)$, odd n	$W_n^1\Phi'(0)\zeta - \frac{\Phi''(0)}{8(n+2)}\zeta^2$	
$J_n(\zeta; K)$, even n	$\frac{\Phi(0)}{2(n+1)}$	0 for white noise and triangular
$J_n(\zeta; K)$, odd n	$V_n^1\Phi'(0)\zeta - \frac{\Phi''(0)}{8(n+2)K_0}\zeta^2$	$\frac{2}{\pi^2}V_n^{-4}\zeta^{-4}$ for exponential
		faster than polynomial for power-law and Gaussian

A.4 Behavior of function J_n

We finally consider the following integral function (see Figure A.2 for its behavior for different correlation functions and values of n):

$$J_n(\zeta; K) = K_0^{n+1}\int_{K_1}^{K_2}\left(1 - 2\chi^2\right)^n \chi\Phi(\zeta\chi)d\chi \tag{A.11}$$

Note that this function is related to the previous one through $J_n(\zeta; 1) = I_n(\zeta)$.

As before we use the Taylor expansion:

$$J_n(\zeta; K) = \sum_{p=0}^{\infty}\frac{\Phi^{(p)}(0)\zeta^p V_n^p}{p!} \tag{A.12}$$

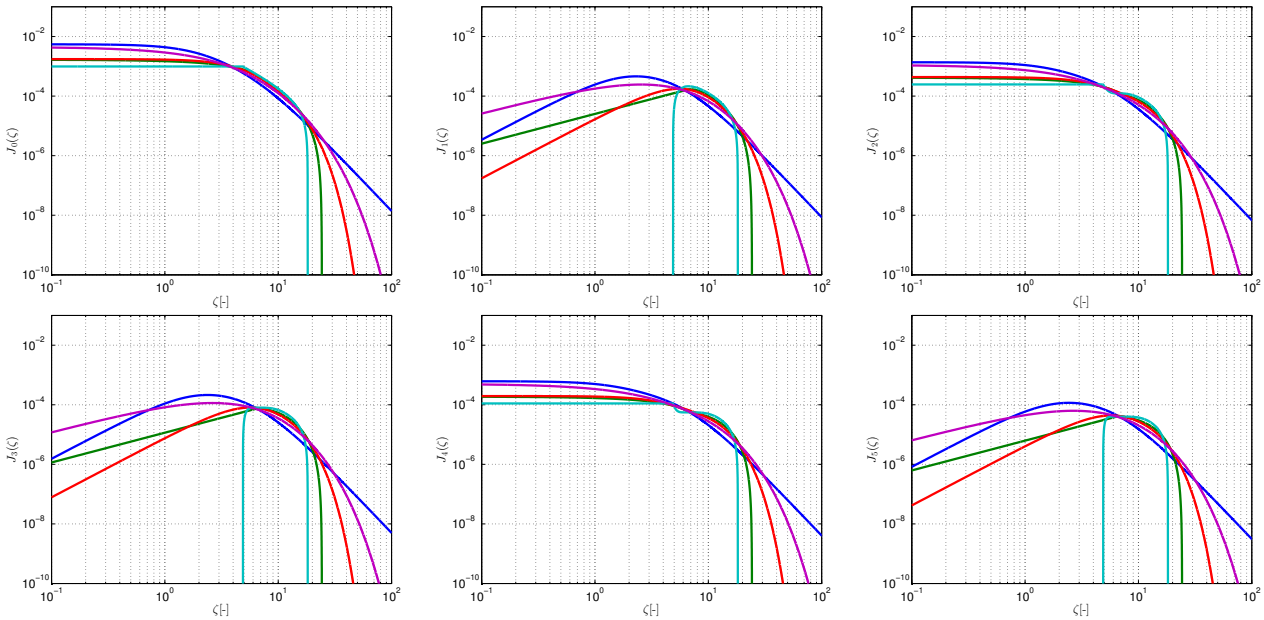

Figure A.2: Functions $J_n(\zeta)$ for different correlation kernels and different values of n ($K = \sqrt{3}$). : exponential (thick solid line), power-law (thin dashed-dotted line), Gaussian (thick dashed line), triangular (thin solid line) and low-pass white noise (thin dashed line).

and hence derive the low-frequency behavior:

$$J_n(\zeta; K) = \frac{\Phi(0)}{2(n+1)} + \mathrm{O}(\zeta) \quad \text{for even } n, \tag{A.13}$$

and

$$J_n(\zeta; K) = V_n^1 \Phi'(0)\zeta - \frac{\Phi''(0)}{8(n+2)K_0}\zeta^2 + \mathrm{O}(\zeta^3) \quad \text{for odd } n. \tag{A.14}$$

These expansions do not apply to the white noise case, but this case can be computed explicitly:

$$J_n^{\text{noise}}\left(\zeta \leq \frac{3\pi}{2K_2}\right) = \frac{1}{18\pi^4(n+1)}(1 + (-1)^n), \tag{A.15}$$

and

$$J_n^{\text{noise}}\left(\frac{3\pi}{2K_2} \leq \zeta \leq \frac{3\pi}{2K_1}\right) = \frac{1}{18\pi^4(n+1)}\left(1 - K_0^{n+1}\left(1 - \frac{9\pi^2}{2\zeta^2}\right)^{n+1}\right), \tag{A.16}$$

and $J_n^{\text{noise}}(\zeta \geq 3\pi/2K_1) = 0$ which also provides the high-frequency behavior of J for a low-pass white noise correlation model. Note that, for odd n, J_n^{noise} vanishes both in the low and high frequency ranges (outside the interval $[3\pi/2K_2, 3\pi/2K_1]$).

Likewise, for the case of a random medium with triangular correlation, one can compute explicitly the values of the integral for the low and high frequency ranges:

$$J_n^{\text{tri}}\left(\zeta \leq \frac{2\pi}{K_2}\right) = \frac{3}{8\pi^4}\left(V_n^0 - \frac{\zeta}{2\pi}V_n^1\right) \tag{A.17}$$

and $J_n^{\text{tri}}(\zeta \geq 2\pi/K_1) = 0$. Note that $V_n^0 = 0$ for odd n so that the asymptotic is then given by the linear term. The slope is positive because $V_n^1 > 0$ for odd n.

For the exponential model, we have in the high frequency range $\Phi(\zeta\chi) = 2\zeta^{-4}\chi^{-4}/\pi^2 + \mathrm{o}(\zeta^{-4})$ so that

$$J_n^{\exp}(\zeta \gg 1) = \frac{2}{\pi^2} V_n^{-4} \zeta^4 + \mathrm{O}(\zeta^5) \tag{A.18}$$

Finally, for both the power-law and Gaussian models, the $J_n(\zeta; K)$ goes to zero exponentially fast.

Appendix B

Derivation of the correlation matrix

B.1 Weakly varying random media

In order to reduce the number of parameters, one assumption that we will make is that the coefficient of variation of the shear and bulk moduli are both equal, *i.e.* $\delta_\mu = \delta_\kappa$. As a result, the global fluctuation level of the medium (the coefficient of variation of the random elastic tensor) will be $\delta = \delta_\mu = \delta_\kappa$. The objective of this part is to derive the correlation matrix of the variables $\delta\frac{1}{\lambda}$ and $\delta\frac{1}{\rho}$ in terms of the medium dispersion level δ and the ratio K. We can simply obtain the following formulas relating the variances of $(\delta\frac{1}{\lambda}, \delta\frac{1}{\mu})$ to the coefficients of variation of the variables $(\frac{1}{\lambda}, \frac{1}{\mu})$:

$$\sigma^2_{\delta\frac{1}{\lambda}} = \delta^2_{\frac{1}{\lambda}}; \qquad \sigma^2_{\delta\frac{1}{\mu}} = \delta^2_{\frac{1}{\mu}} \tag{B.1}$$

in which δ_X is the coefficients of variation of the random variable X.

If we consider the random variable X as a sum of a weak zero-mean perturbation Z and its mean $X = \bar{X} + Z$ when $|Z| \ll |\bar{X}|$ (remember that in this study, we are supposed to consider media with weak fluctuations in order to avoid the localization regime), we get:

$$\frac{1}{X} = \frac{1}{\bar{X} + Z} = \frac{1}{\bar{X}}\frac{1}{1 + \frac{Z}{\bar{X}}} = \frac{1}{\bar{X}}\left(1 - \frac{Z}{\bar{X}} + \frac{Z^2}{\bar{X}^2} - \cdots\right) \tag{B.2}$$

Taking the average and variance from both sides of equation (B.2) results in:

$$E\left(\frac{1}{X}\right) \simeq \frac{1}{\bar{X}}\left(1 + \frac{Var(X)}{\bar{X}^2}\right) \quad ; \quad Var\left(\frac{1}{X}\right) \simeq \frac{Var(X)}{\bar{X}^4} \tag{B.3}$$

As a result, the following approximation is adopted relating the coefficient of variation of a variable to that of its inverse:

$$\delta_{\frac{1}{X}} \simeq \frac{\delta_X}{1 + \delta_X^2} \tag{B.4}$$

The coefficient of variation of λ, δ_λ, can be calculated using:

$$\lambda = \kappa - \frac{2}{3}\mu \Rightarrow \sigma^2_\lambda = \sigma^2_\kappa + \frac{4}{9}\sigma^2_\mu \Rightarrow (\bar{\lambda})^2\delta^2_\lambda = \left((\bar{\kappa})^2 + \frac{4}{9}(\bar{\mu})^2\right)\delta^2 \Rightarrow \delta_\lambda = \sqrt{\frac{(\bar{\kappa})^2 + \frac{4}{9}(\bar{\mu})^2}{(\bar{\lambda})^2}}\delta \tag{B.5}$$

Now we can simplify the previous equation knowing that $\bar{\kappa} = \bar{\lambda} + \frac{2}{3}\bar{\mu}$ and considering the fact that the P to S wave speed ratio is $K^2 = 2 + \frac{\lambda}{\mu}$:

$$\delta_\lambda = \sqrt{1 + \frac{4}{3(K^2-2)} + \frac{8}{9(K^2-2)^2}}\delta \tag{B.6}$$

Another important assumption is that in our software, SPEC, we have supposed that two random fields κ and μ are independent, *i.e.* $\mathrm{cov}(\kappa, \mu) = 0$. As mentioned throughout the paper, the covariance which should be calculated is the covariance of $\delta\frac{1}{\lambda}$ and $\delta\frac{1}{\mu}$. Using approximations introduced in equations (B.2):

$$\mathrm{cov}\left(\delta\frac{1}{\lambda}, \delta\frac{1}{\mu}\right) = E\left(\delta\frac{1}{\lambda}\delta\frac{1}{\mu}\right) = \frac{\mathrm{cov}\left(\frac{1}{\lambda}, \frac{1}{\mu}\right)}{\bar{\frac{1}{\lambda}}\bar{\frac{1}{\mu}}} \tag{B.7}$$

Now, using equations (B.2), we can calculate $\mathrm{cov}\left(\frac{1}{\lambda}, \frac{1}{\mu}\right)$ in terms of the statistics of κ and μ:

$$\begin{aligned}
\mathrm{cov}\left(\frac{1}{\lambda}, \frac{1}{\mu}\right) &= \mathrm{cov}\left(\frac{1}{\kappa - \frac{2}{3}\mu}, \frac{1}{\mu}\right) = E\left(\frac{1}{\kappa\mu - \frac{2}{3}\mu^2}\right) - E\left(\frac{1}{\kappa - \frac{2}{3}\mu}\right)E\left(\frac{1}{\mu}\right) \\
&\simeq \frac{1 + \frac{\sigma^2_{\kappa\mu - 2/3\mu^2}}{\left(\bar{\kappa}\bar{\mu} - \frac{2}{3}(\sigma^2_\mu + \bar{\mu}^2)\right)^2}}{\bar{\kappa}\bar{\mu} - \frac{2}{3}(\sigma^2_\mu + \bar{\mu}^2)} - \frac{1}{\bar{\kappa} - \frac{2}{3}\bar{\mu}}\left(1 + \frac{\sigma^2_{\kappa - 2/3\mu}}{(\bar{\kappa} - \frac{2}{3}\bar{\mu})^2}\right).\frac{1}{\bar{\mu}}\left(1 + \frac{\sigma^2_\mu}{\bar{\mu}^2}\right) \\
&= \frac{1 + \frac{\frac{4}{9}\sigma^4_\mu}{\left(\bar{\kappa}\bar{\mu} - \frac{2}{3}(\sigma^2_\mu + \bar{\mu}^2)\right)^2}}{\bar{\kappa}\bar{\mu} - \frac{2}{3}(\sigma^2_\mu + \bar{\mu}^2)} - \frac{1 + \frac{\sigma^2_\mu}{\bar{\mu}^2} + \frac{\sigma^2_{\kappa - \frac{2}{3}\mu}}{(\bar{\kappa} - \frac{2}{3}\bar{\mu})^2} + \frac{\sigma^2_\mu . \sigma^2_{\kappa - \frac{2}{3}\mu}}{\bar{\mu}^2 . (\bar{\kappa} - \frac{2}{3}\bar{\mu})^2}}{\bar{\mu}(\bar{\kappa} - \frac{2}{3}\bar{\mu})} \\
&= \frac{1 + \frac{\frac{4}{9}\bar{\mu}^4}{\left(\bar{\kappa}\bar{\mu} - \frac{2}{3}\bar{\mu}^2(1+\delta^2)\right)^2}\delta^4}{\bar{\kappa}\bar{\mu} - \frac{2}{3}\bar{\mu}^2(1+\delta^2)} - \frac{1 + (1 + \frac{\bar{\kappa}^2 + \frac{4}{9}\bar{\mu}^2}{(\bar{\kappa} - \frac{2}{3}\bar{\mu})^2})\delta^2 + \frac{\bar{\kappa}^2 + \frac{4}{9}\bar{\mu}^2}{(\bar{\kappa} - \frac{2}{3}\bar{\mu})^2}\delta^4}{\bar{\mu}(\bar{\kappa} - \frac{2}{3}\bar{\mu})}
\end{aligned} \tag{B.8}$$

combining equations (B.7) and (B.8), the covariance between $\delta\frac{1}{\lambda}$ and $\delta\frac{1}{\mu}$ can be calculated in terms of first and second moments of κ and μ:

$$\mathrm{cov}\left(\delta\frac{1}{\lambda}, \delta\frac{1}{\mu}\right) = \frac{\bar{\mu}(\bar{\kappa} - \frac{2}{3}\bar{\mu})\left(1 + \frac{\frac{4}{9}\bar{\mu}^4}{\left(\bar{\kappa}\bar{\mu} - \frac{2}{3}\bar{\mu}^2(1+\delta^2)\right)^2}\delta^4\right)}{\left(\bar{\kappa}\bar{\mu} - \frac{2}{3}\bar{\mu}^2(1+\delta^2)\right)(1+\delta^2)\left(1 + \frac{\bar{\kappa}^2 + \frac{4}{9}\bar{\mu}^2}{(\bar{\kappa} - \frac{2}{3}\bar{\mu})^2}\delta^2\right)} - 1 \tag{B.9}$$

The covariance matrix of two random fields $(\delta\frac{1}{\lambda}, \delta\frac{1}{\mu})$ can be constructed as follows:

$$\begin{aligned}
R_{(\delta\frac{1}{\lambda}, \delta\frac{1}{\mu})} &= \begin{bmatrix} \sigma^2_{\delta\frac{1}{\lambda}} & \mathrm{cov}(\delta\frac{1}{\lambda}, \delta\frac{1}{\mu}) \\ \mathrm{cov}(\delta\frac{1}{\lambda}, \delta\frac{1}{\mu}) & \sigma^2_{\delta\frac{1}{\mu}} \end{bmatrix} \\
&= \begin{bmatrix} \frac{(\bar{k} - \frac{2}{3}\bar{\mu})^2(\bar{k}^2 + \frac{4}{9}\bar{\mu}^2)\delta^2}{\left[(1+\delta^2)(\bar{k}^2 + \frac{4}{9}\bar{\mu}^2) - \frac{4}{3}\bar{\kappa}\bar{\mu}\right]^2} & \frac{\bar{\mu}(\bar{\kappa} - \frac{2}{3}\bar{\mu})\left(1 + \frac{\frac{4}{9}\bar{\mu}^4}{\left(\bar{\kappa}\bar{\mu} - \frac{2}{3}\bar{\mu}^2(1+\delta^2)\right)^2}\delta^4\right)}{\left(\bar{\kappa}\bar{\mu} - \frac{2}{3}\bar{\mu}^2(1+\delta^2)\right)(1+\delta^2)\left(1 + \frac{\bar{\kappa}^2 + \frac{4}{9}\bar{\mu}^2}{(\bar{\kappa} - \frac{2}{3}\bar{\mu})^2}\delta^2\right)} - 1 \\ \frac{\bar{\mu}(\bar{\kappa} - \frac{2}{3}\bar{\mu})\left(1 + \frac{\frac{4}{9}\bar{\mu}^4}{\left(\bar{\kappa}\bar{\mu} - \frac{2}{3}\bar{\mu}^2(1+\delta^2)\right)^2}\delta^4\right)}{\left(\bar{\kappa}\bar{\mu} - \frac{2}{3}\bar{\mu}^2(1+\delta^2)\right)(1+\delta^2)\left(1 + \frac{\bar{\kappa}^2 + \frac{4}{9}\bar{\mu}^2}{(\bar{\kappa} - \frac{2}{3}\bar{\mu})^2}\delta^2\right)} - 1 & \frac{\delta^2}{(1+\delta^2)^2} \end{bmatrix}
\end{aligned} \tag{B.10}$$

it seems that the covariance matrix depends on the mean values of the elastic isotropic parameters, $(\bar{\kappa}, \bar{\mu})$ and the degree of fluctuations, δ. However, we can rewrite this matrix only in terms of δ and the mean value of P-to-S wave speed ratio K, defined earlier:

$$R_{(\delta\frac{1}{\lambda},\delta\frac{1}{\mu})} = \begin{bmatrix} \frac{(K^2-2)^2\left((K^2-\frac{4}{3})^2+\frac{4}{9}\right)\delta^2}{\left[(1+\delta^2)\left((K^2-\frac{4}{3})^2+\frac{4}{9}\right)-\frac{4}{3}(K^2-\frac{4}{3})\right]^2} & \frac{(K^2-2)\left[1+\frac{\frac{4}{9}\delta^4}{\left(K^2-\frac{4}{3}-\frac{2}{3}(1+\delta^2)\right)^2}\right]}{\left(K^2-\frac{4}{3}-\frac{2}{3}(1+\delta^2)\right)(1+\delta^2)\left(1+\frac{K^4-\frac{8}{3}K^2+\frac{20}{9}}{(K^2-2)^2}\delta^2\right)}-1 \\ \text{Sym} & \frac{\delta^2}{(1+\delta^2)^2} \end{bmatrix} \tag{B.11}$$

B.2 Highly varying random media

When δ does not necessarily tend to zero (which is often the case in simulations done in this study), the correlation matrix will be extracted using the joint probability density function of the random variables $\frac{1}{\lambda}$ and $\frac{1}{\mu}$. The variables κ and μ are assumed to be Gamma-distributed random fields with an equal coefficient of variation δ and mean values of $\underline{\kappa}$ and $\underline{\mu}$ respectively:

$$\kappa \sim \text{Gamma}\left(\frac{1}{\delta^2}; \underline{\kappa}\delta = \left(K^2 - \frac{4}{3}\right)\underline{\mu}\delta\right) \quad ; \quad \mu \sim \text{Gamma}\left(\frac{1}{\delta^2}; \underline{\mu}\delta\right) \tag{B.12}$$

The change of variables $u = \frac{1}{\lambda} = \frac{1}{\kappa - \frac{2}{3}\mu}$ and $v = \frac{1}{\mu}$ gives $\mu = \frac{1}{v}$ and $\kappa = \frac{1}{u} + \frac{2}{3v}$ which leads to the following Jacobian transformation matrix:

$$\mathbf{J} = \begin{bmatrix} \frac{\partial\mu}{\partial u} & \frac{\partial\mu}{\partial v} \\ \frac{\partial\kappa}{\partial u} & \frac{\partial\kappa}{\partial v} \end{bmatrix} = \begin{bmatrix} 0 & -\frac{1}{v^2} \\ -\frac{1}{u^2} & -\frac{2}{3v^2} \end{bmatrix} \tag{B.13}$$

Since the variables κ and μ are independent, the joint probability density function of the random variables $U \equiv \frac{1}{\lambda}$ and $V \equiv \frac{1}{\mu}$ will then be given by:

$$f_{UV}(u, v) = |\det(\mathbf{J})| f_\kappa(\kappa) f_\mu(\mu) \tag{B.14}$$

in which $f_\kappa(\kappa)$ and $f_\mu(\mu)$ are respectively the probability density function of the corresponding random variables. Then:

$$\begin{aligned} f_{UV}(u, v) &= \frac{1}{(uv)^2} \frac{\left(\frac{1}{u} + \frac{2}{3v}\right)^{\frac{1}{\delta^2}-1} \cdot e^{-\frac{\frac{1}{u}+\frac{2}{3v}}{\left(K^2-\frac{4}{3}\right)\underline{\mu}\delta}}}{\Gamma\left(\frac{1}{\delta^2}\right)\left(\left(K^2 - \frac{4}{3}\right)\underline{\mu}\delta\right)^{\frac{1}{\delta^2}}} \cdot \frac{\left(\frac{1}{v}\right)^{\frac{1}{\delta^2}-1} \cdot e^{-\frac{\frac{1}{v}}{\underline{\mu}\delta}}}{\Gamma\left(\frac{1}{\delta^2}\right)\left(\underline{\mu}\delta\right)^{\frac{1}{\delta^2}}} \\ &= \frac{1}{\Gamma^2\left(\frac{1}{\delta^2}\right)\left(\left(K^2 - \frac{4}{3}\right)\underline{\mu}^2\delta^2\right)^{\frac{1}{\delta^2}}} \cdot \frac{1}{(uv)^2}\left(\frac{1}{uv} + \frac{2}{3v^2}\right)^{\frac{1}{\delta^2}-1} e^{-\frac{1}{\underline{\mu}\delta}\left[\frac{1}{K^2-\frac{4}{3}}\left(\frac{1}{u}+\frac{2}{3v}\right)-\frac{1}{v}\right]} \end{aligned} \tag{B.15}$$

It should be noted that in this equation, for a fixed value of v, u varies in $]-\infty, -3v/2] \bigcup [0, \infty[$.

The variance of the random variables $X_{\frac{1}{\lambda}}$ and $X_{\frac{1}{\mu}}$ in terms of the statistics of the random variables $\frac{1}{\lambda}$ and $\frac{1}{\mu}$ are:

$$\text{var}\left(X_{\frac{1}{\lambda}}\right) = \frac{\text{var}\left(\frac{1}{\lambda}\right)}{\mathbb{E}^2\left(\frac{1}{\lambda}\right)} = \delta^2_{\frac{1}{\lambda}} \quad ; \quad \text{var}\left(X_{\frac{1}{\mu}}\right) = \frac{\text{var}\left(\frac{1}{\mu}\right)}{\mathbb{E}^2\left(\frac{1}{\mu}\right)} = \delta^2_{\frac{1}{\mu}} \tag{B.16}$$

Similarly, the covariance of the random variables $X_{\frac{1}{\lambda}}$ and $X_{\frac{1}{\mu}}$ reads:

$$\begin{aligned}\operatorname{cov}\left(X_{\frac{1}{\lambda}}, X_{\frac{1}{\mu}}\right) &= \mathbb{E}\left(X_{\frac{1}{\lambda}} \cdot X_{\frac{1}{\mu}}\right) - \mathbb{E}\left(X_{\frac{1}{\lambda}}\right) \cdot \mathbb{E}\left(X_{\frac{1}{\mu}}\right) = \mathbb{E}\left(X_{\frac{1}{\lambda}} \cdot X_{\frac{1}{\mu}}\right) \\ &= \mathbb{E}\left[\left(\frac{\frac{1}{\lambda}}{\mathbb{E}\left(\frac{1}{\lambda}\right)} - 1\right) \cdot \left(\frac{\frac{1}{\mu}}{\mathbb{E}\left(\frac{1}{\mu}\right)} - 1\right)\right] = \frac{\mathbb{E}\left(\frac{1}{\lambda}\frac{1}{\mu}\right) - \mathbb{E}\left(\frac{1}{\lambda}\right)\mathbb{E}\left(\frac{1}{\mu}\right)}{\mathbb{E}\left(\frac{1}{\lambda}\right)\mathbb{E}\left(\frac{1}{\mu}\right)} = \frac{\operatorname{cov}\left(\frac{1}{\lambda}, \frac{1}{\mu}\right)}{\mathbb{E}\left(\frac{1}{\lambda}\right)\mathbb{E}\left(\frac{1}{\mu}\right)}\end{aligned} \tag{B.17}$$

The desired covariance matrix in terms of the statistics of the variables $\frac{1}{\lambda}$ and $\frac{1}{\mu}$ will therefore be:

$$R_{(X_{\frac{1}{\lambda}}, X_{\frac{1}{\mu}})} = \begin{bmatrix} \operatorname{var}(X_{\frac{1}{\lambda}}) & \operatorname{cov}(X_{\frac{1}{\lambda}}, X_{\frac{1}{\mu}}) \\ \operatorname{cov}(X_{\frac{1}{\lambda}}, X_{\frac{1}{\mu}}) & \operatorname{var}(X_{\frac{1}{\mu}}) \end{bmatrix} = \begin{bmatrix} \frac{\operatorname{var}\left(\frac{1}{\lambda}\right)}{\mathbb{E}^2\left(\frac{1}{\lambda}\right)} & \frac{\operatorname{cov}\left(\frac{1}{\lambda}, \frac{1}{\mu}\right)}{\mathbb{E}\left(\frac{1}{\lambda}\right)\mathbb{E}\left(\frac{1}{\mu}\right)} \\ \frac{\operatorname{cov}\left(\frac{1}{\lambda}, \frac{1}{\mu}\right)}{\mathbb{E}\left(\frac{1}{\lambda}\right)\mathbb{E}\left(\frac{1}{\mu}\right)} & \frac{\operatorname{var}\left(\frac{1}{\mu}\right)}{\mathbb{E}^2\left(\frac{1}{\mu}\right)} \end{bmatrix} \tag{B.18}$$

Appendix C

Probabilistic modeling of random heterogeneities

In this section, the so-called maximum entropy principle will be discussed. This method allows us to construct a probability distribution model for a random variable only based on the use of the available information about it.

C.1 Maximum Entropy Principle

The Shannon measure of entropy for a real random variable X characterized with a probability density function (PDF) $f_X(\mathbf{x})$ is defined as:

$$\mathcal{S}(f_X) = -\int_{\mathbb{R}^n} f_X(\mathbf{x}) \ln f_X(\mathbf{x}) d\mathbf{x} \tag{C.1}$$

For instance, let X follows a Gamma distribution with α and θ as parameters, *i.e.*:

$$X \sim \text{Gamma}(\alpha, \theta) \Rightarrow f_X(x) = \frac{1}{\theta^\alpha \Gamma(\alpha)} x^{\alpha-1} e^{-\frac{x}{\theta}} \mathrm{H}(x) \tag{C.2}$$

in which H and Γ are respectively the Heaviside and Gamma functions. Using equation (C.1) one can show that the entropy of a Gamma random variable is $\alpha + \ln\theta + \ln[\Gamma(\alpha)] + (1-\alpha)\psi(\alpha)$ in which ψ is the digamma function which is defined as the derivative of the natural logarithm of the Gamma function. This entropy can be rewritten in terms of the mean $\mu = \alpha\theta$ and standard deviation $\sigma = \sqrt{\alpha}\theta$ of the random variable X as:

$$\mathcal{S}(X) = \frac{\mu^2}{\sigma^2} + 2\ln\sigma + \ln\mu + \ln\left[\Gamma\left(\frac{\mu^2}{\sigma^2}\right)\right] + \left(1 - \frac{\mu^2}{\sigma^2}\right)\psi\left(\frac{\mu^2}{\sigma^2}\right) \tag{C.3}$$

Table C.1 summarizes the entropy measures corresponding to some random variables in terms of their standard deviation σ. Dirac distribution which is a completely deterministic law has a zero entropy measure which means that there is no uncertainty. For other distributions, like the Gamma random variable, it can be observed that $\mathcal{S}(X)$ is an increasing function of σ which itself is an indicator of the uncertainties in random variable X. As a consequence, the Shannon measure of entropy can also be considered as a measure of uncertainty. The maximum entropy principle which is defined by Jaynes for the first time in the context of statistical physics and quantum mechanics

Random variable's type	Probability density function, $f_X(x)$	Entropy measure, $\mathcal{S}(X)$
Dirac delta	$\delta(x-x_0)\mathbb{1}_{\mathbb{R}}(x)$	0
Uniform	$\frac{1}{b-a}\mathbb{1}_{(a,b)}(x)$	$\ln(\sqrt{12}\sigma)$
Exponential	$\lambda\exp(-\lambda x)\mathbb{1}_{\mathbb{R}^+}(x)$	$\ln(e\sqrt{\sigma})$
Gaussian	$\frac{1}{\sigma\sqrt{2\pi}}\exp\left(-\frac{(x-\alpha)^2}{2\sigma^2}\right)\mathbb{1}_{\mathbb{R}}(x)$	$\ln(\sqrt{2\pi e}\sigma)$
Log-normal	$\frac{1}{x\sqrt{2\pi}\beta}\exp\left(-\frac{(x-\alpha)^2}{2\beta^2}\right)\mathbb{1}_{\mathbb{R}^+}(x)$	$\frac{1}{2}+\alpha+\frac{1}{2}\ln\left(2\pi\ln\left(\frac{1+\sqrt{1+4e^{-2\alpha}\sigma^2}}{2}\right)\right)$
Rayleigh	$\frac{x}{\beta^2}\exp(-\frac{x^2}{2\beta^2})\mathbb{1}_{\mathbb{R}^+}(x)$	$1+\frac{\gamma}{2}^{1}+\ln\left(\frac{\sigma}{\sqrt{4-\pi}}\right)$

Table C.1: Entropy measure of some random variables in terms of their standard deviation σ

for discrete probability distributions, states that among all probability distributions which satisfy a given set of constraints, one that maximizes the entropy measure, is the best choice. As a simple example, using the maximum entropy principle, we try to derive the PDF of a random variable given these available information:

(i) $X \in \mathbb{R}$ almost surly.

(ii) The mean value of X is known: $\mathbb{E}(X) = \mu_X$.

(iii) The mean value of the natural logarithm of X is also given: $\mathbb{E}(\ln X) = c$.

The desired PDF f_X is the solution of the following functional maximization problem:

$$f_X = \arg\max \mathcal{S}(f_X) \tag{C.4}$$

in which the function f_X which is defined from $\mathbb{R}$ to $\mathbb{R}^+$ should fulfill the following constraints:

$$\int_{\mathbb{R}} f_X(x)dx = 1 \tag{C.5a}$$

$$\int_{\mathbb{R}} x f_X(x)dx = \mathbb{E}(X) \tag{C.5b}$$

$$\int_{\mathbb{R}} (\ln x)\, f_X(x)dx = \mathbb{E}(\ln X) \tag{C.5c}$$

Using the Lagrange multipliers method to solve this maximization problem, one can obtain a Gamma probability density function for the PDF of the random variable X (see equation (C.2)).

C.2 Probabilistic modeling of matrix-valued random fields

A natural approach to make a matrix as random is to randomize its individual elements and to use the methods to model scalar random fieldes. However, the physical as well as the mathematical properties of the corresponding matrix, for example its invertibility, shall not be necessarily satisfied using this type of approach, specially in the case of random elastic matrix which consists of *a priori* 21 mutually independent components. In general, the random elastic matrix should satisfy these conditions: *symmetricity*, *positive definiteness* and *invertibility* (the system response should be of

[1] the Euler - Mascheroni constant

the second-order). It should also satisfy all of the *a priori* information that might be available, for instance its mean value, its variance, its correlation structure etc. Soize (2000, 2001) derived a stochastic model for the random elastic matrix using the maximum entropy principle from the essential physical and mathematical properties that the probabilistic model should possess. This probabilistic model consists of the minimal set of essential parameters needed to describe a random matrix which satisfies some *a priori* given conditions. The main steps to construct a random matrix using a non-parametric probabilistic approach with minimal parameterization which fulfills all the mentioned conditions are:

1. Application of the maximum entropy principle to construct a class of normalized symmetric positive-definite real random matrices of which mean value is an identity matrix and which are invertible:
   Let $\mathbf{G}$ be the ensemble of homogeneous normalized non Gaussian positive-definite matrix-valued random fields, characterized by a mean value $\mathbb{E}(\mathbf{G}) = \mathbf{I}_6$ (identity matrix of order 6) and a parameter describing the dispersion level δ, which is a generalization of the coefficient of variation in the case of scalar random fields:

$$\delta = \sqrt{\frac{\mathbb{E}\left\{||\mathbf{G}(\delta) - \mathbf{I}_6||_F^2\right\}}{6}} \tag{C.6}$$

   where the subscript F denotes the Frobenius or Hilbert–Schmidt norm. Let $f_{\mathbf{G}}(\mathbf{G})$ be the PDF of the random matrix $\mathbf{G}$. Apart from the positivity condition $f_{\mathbf{G}}(\mathbf{G}) \geq 0$ and the normalization condition (as in equation (C.5a)), two other constraints should be imposed before starting to solve the maximization problem of equation (C.4). These constraints take into consideration from one hand the *a priori* knowledge about the mean matrix and from the other hand ensure its invertibility so that the random response of equation (1.1) $\mathbf{u}(\mathbf{x})$ will be of second order. The solution of the constrained optimization problem using the Lagrange multipliers results in the following PDF (see Soize (2000, 2001) for details):

$$f_{\mathbb{G}}(\mathbf{G}) = \mathbb{1}_{\mathbb{M}_6^+(\mathbb{R})}(\mathbf{G}) \times \gamma_G \times \det\mathbf{G} \times \frac{7(1-\delta^2)}{2\delta^2} \exp\left(-\frac{7}{2\delta^2}\mathrm{tr}(\mathbf{G})\right) \tag{C.7}$$

   in which $\mathbb{1}_{\mathbb{M}_6^+(\mathbb{R})}(\mathbf{G})$ is the characteristic function which is equal to 1 if $\mathbf{G} \in \mathbb{M}_6^+(\mathbb{R})$ and is zero when $\mathbf{G} \notin \mathbb{M}_6^+(\mathbb{R})$. $\det\mathbf{G}$ is the determinant of the matrix $\mathbf{G}$ and the dispersion parameters of the matrices $\mathbf{G}$ and $\mathbf{C}$ are related as:

$$\delta_C^2 = \frac{\delta^2}{7}\left(1 + \frac{(\mathrm{tr}(\underline{\mathbf{C}}))^2}{\mathrm{tr}(\underline{\mathbf{C}}^2)}\right) \tag{C.8}$$

2. The random matrix is then constructed as the product of the normalized random matrix pre- and post-multiplied by the Cholesky factors of the mean value of the corresponding random matrix which should be known in this type of modeling:

   Since the mean value of the random elastic matrix $\underline{\mathbf{C}}$ belongs to the ensemble $\mathbb{M}_6^+(\mathbb{R})$, there is an upper triangular matrix $\underline{L} \in \mathbb{M}_6(\mathbb{R})$ corresponding to the Cholesky factorization of the matrix $\underline{\mathbf{C}}$ such that:

$$\underline{\mathbf{C}} = \underline{\mathbf{L}}^T\underline{\mathbf{L}} \tag{C.9}$$

The random elastic matrix $\mathbf{C}$ which belongs to the set of non normalized, non homogeneous and non Gaussian positive-definite matrix-valued random fields, parametrized with a fluctuation level δ will then be constructed as:

$$\mathbf{C}(\delta) = \underline{L}^T \mathbf{G}(\delta) \underline{L} \tag{C.10}$$

provided that the random matrix $\mathbf{G}$ has a unit mean, *i.e.* $\mathbb{E}(\mathbf{G}) = \mathbf{I}_6$. As it can be observed from equation (C.10), only the normalized random matrix $\mathbf{G}$ includes the existing randomness in the random elastic tensor $\mathbf{C}$. As a result, the probabilistic model of $\mathbf{C}$ is completely obtained knowing the PDF of the random kernel $\mathbf{G}$.

C.2.1 Modifications of Soize's probabilistic model for the random elastic matrix

The given probabilistic model for $\mathbf{C}$ in section C.2 has no assumption about its degree of symmetricity. Guilleminot and Soize (2010) developed the Soize model for the case in which the material symmetries are uncertain. For this purpose, the variances of some selected random eigenvalues of the random matrix $\mathbf{C}$ should be prescribed. Adding this constraint to the Soize's optimization problem allows us to partially control the mean distance of the random matrix $\mathbf{C}$ to a given class of material symmetry. Their model has clearly a larger number of parameters and is shown to be suitable when it comes to the experimental identification under material symmetry uncertainties. Guilleminot and Soize (2011) also presented a method based on the sequential solving of least-square optimization problems for the inverse identification problem. Guilleminot et al. (2011) proposed a probabilistic model for the random elasticity matrix when it is deterministically bounded, *i.e.* $\mathbf{C}_\ell < \mathbf{C} < \mathbf{C}_u$ in which $\mathbf{C}_\ell$ and $\mathbf{C}_u$ are respectively deterministic lower and upper bounds for the random matrix $\mathbf{C}$ (see Huet (1990) for more discussion). Taking into consideration simultaneously the material symmetry uncertainties and the boundedness of the random elasticity matrix is discussed in Guilleminot and Soize (2012) and a proper probabilistic model is proposed. Independent from the works of Guilleminot and Soize (2010), Ta et al. (2010) developed the Soize's model (equation (C.7)) by adding a new parameter which controls the mean distance and projection of the matrix $\mathbf{C}$ onto the space of isotropic materials. This parameter is also called the degree of anisotropy of the underlying random medium. Since in chapter 3 of this presentation we will make use of the probabilistic model of random elasticity matrix proposed in Ta et al. (2010) for the numerical simulations of elastic wave propagation, this model will be elaborated in the next paragraphs.

Several measures can be defined as anisotropy level (see Arts (1993) and Carcione (2007) for instance) among which the usual definition which utilizes the normalized distance in the Frobenius norm between the elastic matrix $\mathbf{C}$ and the closest isotropic one denoted by $\mathbf{C}_{iso}^{eqv}$ is used in Ta et al. (2010). The latter is defined as:

$$\begin{pmatrix} C_{11} & C_{12} & C_{13} & C_{14} & C_{15} & C_{16} \\ \cdot & C_{22} & C_{23} & C_{24} & C_{25} & C_{26} \\ \cdot & \cdot & C_{33} & C_{34} & C_{35} & C_{36} \\ \mathbf{S} & \cdot & \cdot & C_{44} & C_{45} & C_{46} \\ \cdot & \mathbf{Y} & \cdot & \cdot & C_{55} & C_{56} \\ \cdot & \cdot & \mathbf{M} & \cdot & \cdot & C_{66} \end{pmatrix} \approx \begin{pmatrix} \lambda^{eqv} + 2\mu^{eqv} & \lambda^{eqv} & \lambda^{eqv} & 0 & 0 & 0 \\ \lambda^{eqv} & \lambda^{eqv} + 2\mu^{eqv} & \lambda^{eqv} & 0 & 0 & 0 \\ \lambda^{eqv} & \lambda^{eqv} & \lambda^{eqv} + 2\mu^{eqv} & 0 & 0 & 0 \\ 0 & 0 & 0 & \mu^{eqv} & 0 & 0 \\ 0 & 0 & 0 & 0 & \mu^{eqv} & 0 \\ 0 & 0 & 0 & 0 & 0 & \mu^{eqv} \end{pmatrix} \tag{C.11}$$

in which the equivalent Lamé parameters λ^{eqv} and μ^{eqv} are given by:

$$\lambda^{eqv} = \frac{C_{11} + C_{22} + C_{33} + 4(C_{12} + C_{23} + C_{13}) - 2(C_{44} + C_{55} + C_{66})}{15} \tag{C.12}$$

$$\mu^{eqv} = \frac{2(C_{11} + C_{22} + C_{33}) - (C_{12} + C_{23} + C_{13}) + 3(C_{44} + C_{55} + C_{66})}{15} \tag{C.13}$$

The anisotropy index of a matrix $\mathbf{C}$ is then defined as:

$$I_a(\mathbf{C}) = \sqrt{\frac{||\mathbf{C} - \mathbf{C}_{iso}^{eqv}||_F^2}{||\mathbf{C}||_F^2}} \tag{C.14}$$

in which the anisotropy index I_a varies in $[0, 1]$. For isotropic materials $I_a = 0$ and for a completely anisotropic elastic matrix with 21 mutually independent parameter $I_a = 1$. The extension of the Soize's problem to the case in which the mean anisotropy index is known is done and a new PDF for the random elasticity matrix is proposed (see Ta (2011) for a complete discussion). The random elastic matrix $\mathbf{C}$ will therefore be characterized by a mean value $\underline{\mathbf{C}}$, a dispersion level δ_c and an anisotropy index I_a. It can be shown that the eigenvalues of the isotropic elastic matrix, equation (1.3), are $3\lambda + 2\mu = 3\kappa$ and 2μ being respectively proportional to the bulk and shear moduli. Guilleminot and Soize (2013) investigated the statistical dependence of the elastic matrix components based on a maximum entropy principle and found that the pair of elastic coefficients (κ, μ) can be considered as statically independent. As a result, the isotropic elastic matrix is chosen to be expressed in terms of these coefficients rather than the classical Lamé parameters:

$$\mathbf{C}^{iso} = 3\kappa\mathbf{S} + 2\mu\mathbf{D} \tag{C.15}$$

where $\mathbf{S}$ and $\mathbf{D}$ are respectively the so-called *spherical* and *deviatoric* matrices which are the orthogonal eigenvectors of the isotropic elastic tensor defined as:

$$\mathbf{S} = \frac{1}{3}\left(\mathbf{I}_2 \otimes \mathbf{I}_2\right); \quad \mathbf{I}_2 = [1\ 1\ 1\ 0\ 0\ 0]^T \tag{C.16a}$$

$$\mathbf{D} = \mathbf{I}_6 - \mathbf{S} \tag{C.16b}$$

Due to the special properties of the matrices $\mathbf{S}$ and $\mathbf{D}$, *i.e.* $\mathbf{S}^2 = \mathbf{S}$, $\mathbf{D}^2 = \mathbf{D}$ and $\mathbf{SD} = 0$, equation (C.15) can be rewritten as:

$$\mathbf{C}^{iso} = \left(\sqrt{3\kappa}\mathbf{S} + \sqrt{2\mu}\mathbf{D}\right)^2 \tag{C.17}$$

Consequently, the following model is proposed for the anisotropic random elastic matrix parametrized with $\underline{\mathbf{C}}$ (the mean model which is assumed to be spatially homogeneous for the sake of simplicity), δ (the degree of statistical fluctuations) and δ_g (the degree of anisotropy) (Ta et al., 2010):

$$\mathbf{C}(\delta, \delta_g) = \left(\sqrt{3\kappa(\delta)}\mathbf{S} + \sqrt{2\mu(\delta)}\mathbf{D}\right)\mathbf{G}(\delta_g)\left(\sqrt{3\kappa(\delta)}\mathbf{S} + \sqrt{2\mu(\delta)}\mathbf{D}\right) \tag{C.18}$$

in which $\mathbf{G}(\delta_g)$ is the anisotropy kernel with a PDF as in equation (C.7) and $(\kappa(\delta), \mu(\delta))$ are assumed to be independent strictly positive scalar random variables with equal coefficients of variation δ for the sake of simplicity of the final model:

$$\delta = \frac{\sqrt{\mathbb{E}\left\{(\kappa - \underline{\kappa})^2\right\}}}{\underline{\kappa}} = \frac{\sqrt{\mathbb{E}\left\{(\mu - \underline{\mu})^2\right\}}}{\underline{\mu}} \tag{C.19}$$

Applying the maximum entropy principle for κ and μ with given mean values $\underline{\kappa}$ and $\underline{\mu}$ and given mean logarithms, results in Gamma distributions with following parameters:

$$\kappa \sim \text{Gamma}(\alpha_\kappa = \frac{1}{\delta^2}, \theta_\kappa = \underline{\kappa}\delta^2) \Rightarrow p_\kappa(\kappa) = \frac{1}{\underline{\kappa}\delta^2\Gamma\left(\frac{1}{\delta^2}\right)} \left(\frac{\kappa}{\delta^2\underline{\kappa}}\right)^{\frac{1}{\delta^2}-1} \exp\left(-\frac{\kappa}{\delta^2\underline{\kappa}}\right) \text{H}(\kappa) \tag{C.20a}$$

$$\mu \sim \text{Gamma}(\alpha_\mu = \frac{1}{\delta^2}, \theta_\mu = \underline{\mu}\delta^2) \Rightarrow p_\mu(\mu) = \frac{1}{\underline{\mu}\delta^2\Gamma\left(\frac{1}{\delta^2}\right)} \left(\frac{\mu}{\delta^2\underline{\mu}}\right)^{\frac{1}{\delta^2}-1} \exp\left(-\frac{\mu}{\delta^2\underline{\mu}}\right) \text{H}(\mu) \tag{C.20b}$$

We emphasize that the numerical simulations done in chapter 3 use a probabilistic model as in equation (C.15) which is completely characterized knowing the mean values $(\underline{\kappa}, \underline{\mu})$ and the coefficient of variations which is supposed to be the same for the sake of having a model with minimal parametrization:

$$\mathbf{C}^{iso}(\delta) = 3\kappa(\delta)\mathbf{S} + 2\mu(\delta)\mathbf{D} \tag{C.21}$$

The elastic matrix introduced in (C.18) along with its inverse are both second-order that is to say that $\mathbb{E}\left\{||C(\delta, \delta_g)||_F^2\right\} < +\infty$ and $\mathbb{E}\left\{||C^{-1}(\delta, \delta_g)||_F^2\right\} < +\infty$ if the dispersion parameters of the model satisfy (see Arnst (2007) and Soize (2006) for a detailed discussion):

$$0 < \delta < \frac{1}{\sqrt{2}} \quad ; \quad 0 < \delta_g < \sqrt{\frac{7}{11}} \tag{C.22}$$

Appendix D

Toward the analytical solution to the RTE of elastic waves propagating in discrete isotropic scattering random media

D.1 Introduction

Using the hypothesis of isotropic scattering and assuming that σ and Σ are $\mathbf{x}$-independent which is true in the case of the uniformly distributed discrete scattereres, one can solve analytically the equation (1.59) for the total energy density $E(t, \mathbf{r})$ at each point:

$$E(t, \mathbf{r}) = \int_{\mathbb{R}^3} a(t, \mathbf{r}, \mathbf{k}) d\mathbf{k} \tag{D.1}$$

Shang and Gao (1988) and Zeng et al. (1991) studied the scattering process in a random isotropic scattering medium with discrete heterogeneities for scalar waves. They derived the equation describing the energy density propagation which is the analytical solution of the equation (1.59) integrated over the wave vector $\mathbf{k}$ in this simple case. If we denote the total wave energy density in a receiver at position $\mathbf{r}$ and time t with $E(\mathbf{r}, t)$, the energy equation can be written as:

$$E(\mathbf{r}, t) = E_{in}\left(\mathbf{r}_0, \mathbf{r}, t - \frac{|\mathbf{r} - \mathbf{r}_0|}{v}\right) + \sum_{\mathbf{r}_1 \neq \mathbf{r}} E_{sc}\left(\mathbf{r}_1, \mathbf{r}, t - \frac{|\mathbf{r}_1 - \mathbf{r}|}{v}\right) \tag{D.2}$$

in which E_{in} indicates the incident wave energy directly propagated from the source at $\mathbf{r}_0$ to the receiver point $\mathbf{r}$ and E_{sc} is the sum of scattered wave energies from all possible scatterers $\mathbf{r}_1$ (the last scattering point) to the receiver $\mathbf{r}$. If the the point-like isotropic scatterers are uniformly distributed with density n_0 in a 3-D medium, E_{in} and E_{sc} can be written as follows (Zeng et al., 1991):

$$E_{in}\left(\mathbf{r}_0, \mathbf{r}, t - \frac{|\mathbf{r} - \mathbf{r}_0|}{v}\right) = E_{in}\left(t - \frac{|\mathbf{r} - \mathbf{r}_0|}{v}\right) \frac{e^{-\frac{\Sigma|\mathbf{r}-\mathbf{r}_0|}{v}}}{4\pi|\mathbf{r} - \mathbf{r}_0|^2} \tag{D.3}$$

$$E_{sc}\left(\mathbf{r}_1, \mathbf{r}, t - \frac{|\mathbf{r}_1 - \mathbf{r}|}{v}\right) = \frac{\Sigma}{n_0 v} E\left(\mathbf{r}_1, t - \frac{|\mathbf{r}_1 - \mathbf{r}|}{v}\right) \frac{e^{-\frac{\Sigma|\mathbf{r}-\mathbf{r}_0|}{v}}}{4\pi|\mathbf{r}_1 - \mathbf{r}|^2} \tag{D.4}$$

where v is the constant propagation velocity and $\Sigma = \Sigma_{sc}$ is the space-independent total cross-section which could also include the absorption effects (*i.e.* $\Sigma = \Sigma_{sc} + \Sigma_{ab}$). The exponential decay is introduced to account for energy loss due to the scattering as well as the geometrical spreading factor ($\frac{1}{|\mathbf{r}|^2}$ in 3-D media). Substituting equations (D.3) and (D.4) in (D.2) and rewriting it in a continuous form, the following so-called *scattered wave energy equation* will be obtained:

$$E(\mathbf{r},t) = E_{in}\left(t - \frac{|\mathbf{r}-\mathbf{r}_0|}{v}\right)\frac{e^{-\frac{\Sigma|\mathbf{r}-\mathbf{r}_0|}{v}}}{4\pi|\mathbf{r}-\mathbf{r}_0|^2} + \int_{\mathbb{R}^3}\frac{\Sigma}{v}E\left(\mathbf{r}_1, t - \frac{|\mathbf{r}_1-\mathbf{r}|}{v}\right)\frac{e^{-\frac{\Sigma|\mathbf{r}-\mathbf{r}_0|}{v}}}{4\pi|\mathbf{r}_1-\mathbf{r}|^2}d\mathbf{r}_1 \tag{D.5}$$

In the case of an impulsive incident wave energy described by a delta function in time at $t = \frac{|\mathbf{r}|}{v}$, $E_{in} = \frac{E_0}{4\pi|\mathbf{r}|^2}\delta\left(t - \frac{|\mathbf{r}|}{v}\right)$, Zeng et al. (1991) have separated different scattering orders and derived a complete solution for the equation (D.5) as (henceforth the source is at origin $\mathbf{r}_0 = \mathbf{0}$ and at $t = 0$):

$$\begin{aligned}
E(\mathbf{r},t) &= E_0(\mathbf{r},t) + E_1(\mathbf{r},t) + E_2(\mathbf{r},t) + \sum_{m>2}E_m(\mathbf{r},t) \\
&= \frac{\delta\left(t - \frac{|\mathbf{r}|}{v}\right)e^{-\Sigma t}}{4\pi v|\mathbf{r}|^2} + \frac{\Sigma \mathrm{H}\left(t - \frac{|\mathbf{r}|}{v}\right)e^{-\Sigma t}}{4\pi|\mathbf{r}|v^2 t}\ln\left(\frac{1+\frac{|\mathbf{r}|}{vt}}{1-\frac{|\mathbf{r}|}{vt}}\right) \\
&+ \frac{\Sigma_{sc}^2 \mathrm{H}\left(t - \frac{|\mathbf{r}|}{v}\right)e^{-\Sigma t}}{16\pi}\left[\frac{\pi^2}{vt} - \frac{3}{|\mathbf{r}|}\int_0^{\frac{|\mathbf{r}|}{vt}}\left(\ln\frac{1+\alpha}{1-\alpha}\right)^2 d\alpha\right] \\
&+ \int_{-\infty}^{+\infty}\frac{e^{i\Omega t}}{2\pi}d\Omega\int_0^{+\infty}\frac{\left(\frac{\Sigma}{vk}\right)^3\left[\tan^{-1}\left(\frac{k}{\eta+i\frac{\Omega}{v}}\right)\right]^4\sin(k|\mathbf{r}|)}{2\pi^2 v|\mathbf{r}|\left[1-\frac{\Sigma}{vk}\tan^{-1}\left(\frac{k}{\eta+i\frac{\Omega}{v}}\right)\right]}dk
\end{aligned} \tag{D.6}$$

in which E_n denotes the nth order scattered energy density, *i.e.* the incident wave energy which has been scattered $n-1$ times before arriving to the last scattering point at $\mathbf{r}_1$ and then directly travels to the receiver at $\mathbf{r}$. Obviously, the zeroth-order term corresponds to the incident wave energy. The method of discrete wave number sum can be used to solve the integral in equation (D.6). Zeng et al. (1991) have also shown that the energy corresponding to the nth order scattered wave can be calculated using:

$$E_n(t) = \int_{\mathbb{R}^3}E_n(\mathbf{r},t)d\mathbf{r} = E_0 e^{-\Sigma t}\frac{(\Sigma t)^n}{n!} \tag{D.7}$$

Equation (D.7) expresses the nth order scattered wave energy as the multiplication of the probability that the incident wave energy undergoes n scattering events before arriving at station $\mathbf{r}$, that is to say $\frac{(\Sigma t)^n}{n!}$ (this corresponds to a Poisson random process with the rate Σ), and in this interval the incident energy E_0 will be reduced by a factor $e^{-\Sigma t}$.

A general form of equation (D.5) for an impulsive point source at the origin can be written as follows (Sato et al., 1997):

$$E(\mathbf{r},t) = W\psi(\theta,\phi)G(\mathbf{r},t) + \int_{\mathbb{R}^3}d\mathbf{r}'\int_{\mathbb{R}^+}\Sigma G(\mathbf{r}-\mathbf{r}', t-t')E(\mathbf{r}', t)dt' \tag{D.8}$$

in which the Green's function G (corresponding to incident waves) is defined as:

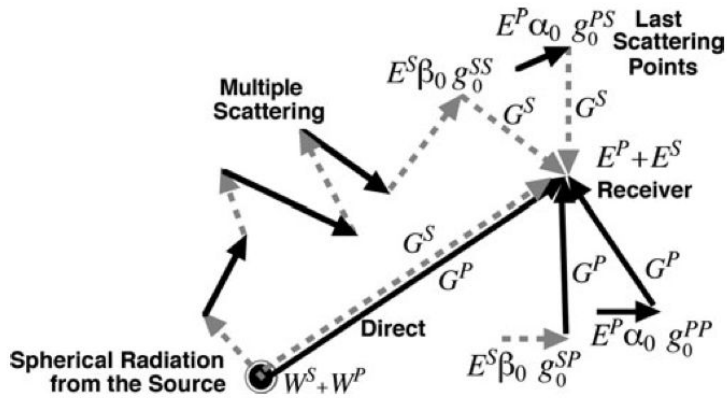

Figure D.1: Configuration of a source, a receiver and last scattering points for multiple isotropic scattering including different mode conversions (Sato et al., 2012)

$$G(\mathbf{r},t) = G(|\mathbf{r}|,t) = \frac{1}{4\pi v|\mathbf{r}|^2}\mathrm{H}(t)\delta\left(t - \frac{|\mathbf{r}|}{v}\right)e^{-\Sigma t} \tag{D.9}$$

where $\mathrm{H}(t)$ is the Heaviside step function and $\psi(\theta,\phi)$ corresponds to the source radiation pattern which is normalized as:

$$\oint \psi(\theta,\phi)d\mathbf{\Omega} = 4\pi \tag{D.10}$$

Therefore, for the case of a spherically symmetric radiation $\psi(\theta,\phi) = 1$, we will have exactly the same equation as (D.5). The equations (D.8), (D.9) and (D.10) describe completely the isotropic scattering process in a 3-D elastic medium with discrete random heterogeneities. The objective of the following two sections is to extend the scalar wave transport equation to the case of elastic waves and to derive an analytical formula for the global diffusion time of a random isotropic scattering medium. Two different point source types will be considered in the next two sections.

D.2 Isotropic (spherical) source

In this section we suppose the isotropic scattering and therefore the spherical radiation pattern $\psi(\theta,\phi) = 1$. Equation (D.8) simplifies as:

$$E(\mathbf{r},t) = WG(|\mathbf{r}|,t) + \int_{\mathbb{R}^3} d\mathbf{r}' \int_{\mathbb{R}^+} \Sigma G(|\mathbf{r}-\mathbf{r}'|,t-t')E(\mathbf{r}',t)dt' \tag{D.11}$$

The objective is to extend this scalar wave energy transport equation to the case of the elastic waves, considering the P-to-S and S-to-P mode conversions during scattering events. We emphasis again that in this section the polarization effect of S waves is neglected, so that the term $\mathbf{a}^s N - N\mathbf{a}^s$ in equation (1.68) is neglected. Furthermore, in this case the coherence matrix becomes a scalar because of the fact that in this case $Q = U = V = 0$. We assume that the P and S wave energies W^P and W^S are impulsively radiated from an isotropic source (for instance an explosion) located at the origin in a 3-D isotropic scattering medium (see Figure D.1).

The scalar energy densities of P and S waves at a given point $\mathbf{x}$ and time t, which are respectively denoted by $E^P(\mathbf{x},t)$ and $E^S(\mathbf{x},t)$, will satisfy the following integral equations which accounts for

the possible mode conversions (Sato, 1994).

$$E^P(\mathbf{x},t) = W^P G^P(\mathbf{x},t) + \int_{\mathbb{R}^3} d\mathbf{x}' \int_{\mathbb{R}^+} dt' \left[E^P(\mathbf{x}',t')\Sigma_{pp} + E^S(\mathbf{x}',t')\Sigma_{sp}\right] G^P(\mathbf{x}-\mathbf{x}',t-t') \quad \text{(D.12)}$$

$$E^S(\mathbf{x},t) = W^S G^S(\mathbf{x},t) + \int_{\mathbb{R}^3} d\mathbf{x}' \int_{\mathbb{R}^+} dt' \left[E^S(\mathbf{x}',t')\Sigma_{ss} + E^P(\mathbf{x}',t')\Sigma_{ps}\right] G^S(\mathbf{x}-\mathbf{x}',t-t') \quad \text{(D.13)}$$

where Σ_{pp}, Σ_{ps}, Σ_{sp} and Σ_{ss} are the total scattering cross-sections for P-to-P, P-to-S, S-to-P and S-to-S mode conversions due to the scattering events. G^P and G^S are P and S wave energy propagators which are characterized by the geometrical spreading factor (reciprocal of $|\mathbf{x}|$ and $|\mathbf{x}|^2$ respectively for 2-D and 3-D media) and the propagation velocities as (Nakahara and Yoshimoto, 2011):

$$G^P(\mathbf{x},t) = \frac{1}{4\pi v_p |\mathbf{x}|^2} \mathrm{H}(t)\delta\left(t - \frac{|\mathbf{x}|}{v_p}\right) e^{-(\Sigma_{pp}+\Sigma_{ps})t} \quad \text{(D.14)}$$

$$G^S(\mathbf{x},t) = \frac{1}{4\pi v_s |\mathbf{x}|^2} \mathrm{H}(t)\delta\left(t - \frac{|\mathbf{x}|}{v_s}\right) e^{-(\Sigma_{ss}+\Sigma_{sp})t} \quad \text{(D.15)}$$

Taking the Fourier-Laplace transform of the both sides of these equations respectively with respect to space and time (which are respectively denoted by tilde and hat) gives:

$$\hat{\tilde{G}}^P(\mathbf{k},s) = \int_{\mathbb{R}^3} d\mathbf{x} e^{-i\mathbf{k}.\mathbf{x}} \int_{\mathbb{R}^+} dt e^{-st} G^P(\mathbf{x},t) = \frac{1}{v_p|\mathbf{k}|} \tan^{-1}\left(\frac{|\mathbf{k}|}{\Sigma_{pp}+\Sigma_{ps}+s}\right) \quad \text{(D.16)}$$

$$\hat{\tilde{G}}^S(\mathbf{k},s) = \int_{\mathbb{R}^3} d\mathbf{x} e^{-i\mathbf{k}.\mathbf{x}} \int_{\mathbb{R}^+} dt e^{-st} G^S(\mathbf{x},t) = \frac{1}{v_s|\mathbf{k}|} \tan^{-1}\left(\frac{v_s|\mathbf{k}|}{\Sigma_{ss}+\Sigma_{sp}+s}\right) \quad \text{(D.17)}$$

The Fourier-Laplace transform of equations (D.12) and (D.13) also leads to the following equations:

$$\hat{\tilde{E}}^P(\mathbf{k},s) = \frac{W^P\hat{\tilde{G}}^P(1-\Sigma_{ss}\hat{\tilde{G}}^S) + W^S\hat{\tilde{G}}^S\Sigma_{sp}\hat{\tilde{G}}^P}{(1-\Sigma_{pp}\hat{\tilde{G}}^P)(1-\Sigma_{ss}\hat{\tilde{G}}^S) - \Sigma_{ps}\Sigma_{sp}\hat{\tilde{G}}^P\hat{\tilde{G}}^S} \quad \text{(D.18)}$$

$$\hat{\tilde{E}}^S(\mathbf{k},s) = \frac{W^S\hat{\tilde{G}}^S(1-\Sigma_{pp}\hat{\tilde{G}}^P) + W^P\hat{\tilde{G}}^P\Sigma_{ps}\hat{\tilde{G}}^S}{(1-\Sigma_{pp}\hat{\tilde{G}}^P)(1-\Sigma_{ss}\hat{\tilde{G}}^S) - \Sigma_{ps}\Sigma_{sp}\hat{\tilde{G}}^P\hat{\tilde{G}}^S} \quad \text{(D.19)}$$

Considering the case that the wave number $|\mathbf{k}|$ tends to zero, using equations (D.18) and (D.19), we will have:

$$\hat{\tilde{E}}^P(|\mathbf{k}|\to 0,s) = \int_{\mathbb{R}^3} d\mathbf{x} \int_{\mathbb{R}} dt e^{-st} E^P(\mathbf{x},t) = \frac{(W^P+W^S)\Sigma_{sp} + W^P s}{s(s+\Sigma_{ps}+\Sigma_{sp})} \quad \text{(D.20)}$$

$$\hat{\tilde{E}}^S(|\mathbf{k}|\to 0,s) = \int_{\mathbb{R}^3} d\mathbf{x} \int_{\mathbb{R}} dt e^{-st} E^S(\mathbf{x},t) = \frac{(W^P+W^S)\Sigma_{ps} + W^S s}{s(s+\Sigma_{ps}+\Sigma_{sp})} \quad \text{(D.21)}$$

The inverse Laplace transforms of the equations (D.20) and (D.21), results in following relations for the energy densities of P and S waves, integrated in the whole domain:

$$\tilde{E}^P(|\mathbf{k}|\to 0,t) = \int_{\mathbb{R}^3} E^P(\mathbf{x},t) d\mathbf{x} = \frac{(W^P+W^S)\Sigma_{sp}}{\Sigma_{ps}+\Sigma_{sp}} + \frac{W^P\Sigma_{ps} - W^S\Sigma_{sp}}{\Sigma_{ps}+\Sigma_{sp}} e^{-(\Sigma_{ps}+\Sigma_{sp})t} \quad \text{(D.22)}$$

$$\tilde{E}^S(|\mathbf{k}| \to 0, t) = \int_{\mathbb{R}^3} E^S(\mathbf{x}, t) d\mathbf{x} = \frac{(W^P + W^S)\Sigma_{ps}}{\Sigma_{ps} + \Sigma_{sp}} + \frac{W^S \Sigma_{sp} - W^P \Sigma_{ps}}{\Sigma_{ps} + \Sigma_{sp}} e^{-(\Sigma_{ps}+\Sigma_{sp})t} \tag{D.23}$$

The following important results are of special interest:

(i) Equations (D.22) and (D.23) satisfy the energy conservation, that is to say that the total energy in the medium is conserved due to wave scattering:

$$\hat{\tilde{E}}^P(|\mathbf{k}| \to 0, s) + \hat{\tilde{E}}^S(|\mathbf{k}| \to 0, s) = \int_{\mathbb{R}^3} (E^P(\mathbf{x}, t) + E^S(\mathbf{x}, t)) d\mathbf{x} = W^P + W^S \tag{D.24}$$

As a result, the sum of the P and S wave energies is conserved, meaning that the formulation is self-consistent.

(ii) The *equipartition relation* which expresses the stabilization of S to P wave energy ratio $\Gamma(t) = \frac{E^S(t)}{E^P(t)}$, when mathematically the propagation time tends to infinity:

$$\lim_{t \to \infty} \Gamma(t) = \lim_{t \to +\infty} \frac{\int_{\mathbb{R}^3} E^S(\mathbf{x}, t) d\mathbf{x}}{\int_{\mathbb{R}^3} E^P(\mathbf{x}, t) d\mathbf{x}} = \frac{\Sigma_{ps}}{\Sigma_{sp}} = 2 \left(\frac{v_p}{v_s} \right)^3 \tag{D.25}$$

in which v_p and v_s are the constant velocities of P and S wave in unperturbed background. In equation (D.25) we made use of the equation (1.96), *i.e.*:

$$\Sigma_{ps} = 2 \left(\frac{v_p}{v_s} \right)^3 \Sigma_{sp} \tag{D.26}$$

(iii) The *global diffusion time* of the elastic waves propagating in a 3-D random isotropic scattering medium with a spherical point source could be defined as the inverse of the coefficient in front of t in the exponential terms of the equations (D.22) and (D.23):

$$t_{eq} = \left[\Sigma_{ps} \left(1 + \frac{v_s^3}{2 v_p^3} \right) \right]^{-1} = \left[\Sigma_{sp} \left(1 + 2 \left(\frac{v_p}{v_s} \right)^3 \right) \right]^{-1} \tag{D.27}$$

This time is also called the *stabilization time* or the *isotropization time*, meaning that at this time the P to S wave energy ratio $\Gamma(t)$ is stabilized.

D.3 Non-isotropic (non-spherical) source

In this section the same problem as in previous section is considered, but in the case of an impulsive radiation of energy $W^P + W^S$ from a non-spherical point source located at the origin. The receiver position in spherical coordinates is $\mathbf{x} = (r, \theta, \phi)$. The matrix form of the equations (D.18) and (D.19) reads:

$$\begin{bmatrix} \hat{\tilde{E}}^P(\mathbf{k}, s) \\ \hat{\tilde{E}}^S(\mathbf{k}, s) \end{bmatrix} = \frac{1}{(1 - \Sigma_{pp}\hat{\tilde{G}}^P)(1 - \Sigma_{ss}\hat{\tilde{G}}^S) - \Sigma_{ps}\Sigma_{sp}\hat{\tilde{G}}^P\hat{\tilde{G}}^S} \begin{bmatrix} 1 - \Sigma_{ss}\hat{\tilde{G}}^S & \Sigma_{sp}\hat{\tilde{G}}^S \\ \Sigma_{ps}\hat{\tilde{G}}^P & 1 - \Sigma_{pp}\hat{\tilde{G}}^P \end{bmatrix} \tag{D.28}$$

where $\hat{\tilde{G}}^P_\psi$ and $\hat{\tilde{G}}^S_\psi$ are defined as:

$$\hat{\tilde{G}}^P_\psi = \int_{\mathbb{R}^3} d\mathbf{x} e^{-i\mathbf{kx}} \psi(\theta,\phi) \int_{\mathbb{R}^+} dt e^{-st} G^P(|\mathbf{x}|,t) \tag{D.29}$$

$$\hat{\tilde{G}}^S_\psi = \int_{\mathbb{R}^3} d\mathbf{x} e^{-i\mathbf{kx}} \psi(\theta,\phi) \int_{\mathbb{R}^+} dt e^{-st} G^S(|\mathbf{x}|,t) \tag{D.30}$$

Using the spherical harmonics, the radiation pattern ψ can be decomposed as:

$$\psi(\theta,\phi) = \sum_{l=0}^{\infty} \sum_{m=-l}^{l} \psi_{lm} Y_{lm}(\theta,\phi) \tag{D.31}$$

where $\psi_{00} = \sqrt{4\pi}$ from the normalization condition (equation (D.10)). Following Sato et al. (1997), by substituting equation (D.31) in equation (D.28), and using $j_l(-z) = (-1)^l j_l(z)$ (j_l is the l-th spherical Bessel function (Sato et al., 2012)) and the following expansion:

$$e^{ikr(\cos\theta_k \cos\theta + \sin\theta_k \sin\theta_k \cos(\phi_k - \phi))} = 4\pi \sum_{l=0}^{\infty} i^l j_l(kr) \sum_{m=-l}^{l} Y_{lm}(\theta_k,\phi_k) Y^*_{lm}(\theta,\phi) \tag{D.32}$$

We will have:

$$\begin{aligned}
\hat{\tilde{G}}^P_\psi(\mathbf{k},s) &= \sum_{l=0}^{\infty} \sum_{m=-l}^{l} \psi_{lm} \int_0^\infty |\mathbf{x}|^2 d\mathbf{x} \oint d\Omega e^{-i\mathbf{k}|\mathbf{x}|} Y_{lm}(\theta,\phi) \frac{e^{-(s+\Sigma_p)\frac{|\mathbf{x}|}{v_p}}}{4\pi v_p |\mathbf{x}|^2} \\
&= \frac{1}{v_p} \sum_{l=0}^{\infty} \sum_{m=-l}^{l} \psi_{lm} \int_0^\infty d\mathbf{x} e^{-(s+\Sigma_p)} \sum_{l'=0}^{\infty} \sum_{m=-l'}^{l'} i^{l'} j_{l'}(-k|\mathbf{x}|) Y_{l'm'}(\theta_k,\phi_k) \oint d\Omega Y^*_{l'm'}(\theta,\phi) Y_{lm}(\theta,\phi) \\
&= \frac{1}{v_p} \sum_{l=0}^{\infty} \sum_{m=-l}^{l} (-i)^l \int_0^\infty d\mathbf{x} e^{-(s+\Sigma_p)} j_l(k|\mathbf{x}|) \psi_{lm} Y_{lm}(\theta_k,\phi_k) \\
&= \sum_{l=0}^{\infty} \sum_{m=-l}^{l} (-i)^l \bar{G}^P_l(k,s) \psi_{lm} Y_{lm}(\theta_k,\phi_k)
\end{aligned} \tag{D.33}$$

in which $\mathbf{k} = (k,\theta_k,\phi_k)$ is the wave vector in spherical coordinates, $\Sigma_p = \Sigma_{pp} + \Sigma_{ps}$ and $\bar{G}^P_l(k,s)$ can be explicitly expressed using the Gauss's hypergeometric function:

$$\begin{aligned}
\bar{G}^P_l(k,s) &= \frac{1}{v_p} \int_0^\infty j_l(k|\mathbf{x}|) e^{-(s+\Sigma_p)} d\mathbf{x} \\
&= \frac{1}{v_p k} \left(\frac{k v_p}{2(s+\Sigma_p)} \right)^{l+1} \frac{\sqrt{\pi}\Gamma(l+1)}{\Gamma(l+\frac{3}{2})} {}_2F_1\left(\frac{l+1}{2}, \frac{l+2}{2}, l+\frac{3}{2}; -\left(\frac{k v_p}{s+\Sigma_p} \right)^2 \right)
\end{aligned} \tag{D.34}$$

where $k = |\mathbf{k}|$ is the wavenumber and ${}_2F_1$ is the incomplete beta function (a generalization of the beta function $B_x(p,q) = \int_0^x t^{p-1}(1-t)^{q-1} dt$) defined as:

$${}_2F_1(p, 1-q, p+1; x) = \frac{p}{x^p} B_x(p,q) \tag{D.35}$$

Taking the limit of the equation (D.28) when $k \to 0$, and using the equations (D.33) and (D.34), knowing that $\bar{G}_0^P(k,s) = \frac{1}{v_p k}\tan^{-1}\left(\frac{kv_p}{s+\Sigma_p}\right)$ and similarly $\bar{G}_0^S(k,s) = \frac{1}{v_s k}\tan^{-1}\left(\frac{kv_s}{s+\Sigma_s}\right)$, and that $\psi_{00}Y_{00} = 1$, we will have exactly the same formulation as in the case of the spherical radiation pattern and the diffusion time, which is shown to be independent from the source type, can be calculated in an isotropic scattering random medium, using the equation (D.27):

$$t_{eq} = \left[\Sigma_{ps}\left(1 + \frac{v_s^3}{2v_p^3}\right)\right]^{-1} = \left[\Sigma_{sp}\left(1 + 2\left(\frac{v_p}{v_s}\right)^3\right)\right]^{-1} \tag{D.36}$$

List of Figures

1 Seismic exploration (left) and Seismic tomography using the recorder wavefield on surface of the Earth (der Hilst et al., 2007) (right). 7
2 A typical seismogram generated by an earthquake 8

1.1 Different wave types created during a typical marine survey 11
1.2 Particle motion of Rayleigh waves (Shearer, 2009) 15
1.3 (a) Variation of P and S-wave velocity (α, β) and mass density (ρ) in depth. (b) Scattergrams showing the correlations between α, β and ρ at the same depth (Shiomi et al., 1997) 17
1.4 Left: A continuous random medium, Right: A discrete random medium consisting in point-like scatterers (heterogeneities) embedded in a homogeneous matrix 20
1.5 Schematic scattering pattern when a typical heterogeneity is illuminated by a plane wave 22
1.6 Length scales in wave propagation problems 23
1.7 Different scattering regimes in terms of the values of $k\ell_c$ 25
1.8 Scalar wave scattering pattern 29

2.1 Classical correlation functions (left figure) and corresponding power spectral densities (right figure), as described in Table 2.1: exponential (blue), power-law (purple), Gaussian (red), triangular (green) and low-pass white noise (cyan). 45
2.2 One realization of a centered unit Gaussian random field with different correlation models: (a) exponential, (b) power-law, (c) Gaussian, (d) triangular, and (e) low-pass white noise. The images are $L \times L$, where $L = 20\ell_c$ and ℓ_c is the correlation length. 45
2.3 Influence of the correlation model on the scattering probability density functions $\hat{\sigma}_{ij}(\zeta, \theta)$ for $K = \sqrt{3}$ and $\sigma_\lambda = \sigma_\mu = \rho_{\lambda\mu} = 0.1$: exponential (blue), power-law (purple), Gaussian (red), triangular (green) and low-pass white noise (cyan). 48
2.4 $\overline{\Sigma}_{pp}$, $\overline{\Sigma}_{ps}$ and $\overline{\Sigma}_{ss}$ in terms of ζ for $K = \sqrt{3}$ and $\sigma_\lambda = \sigma_\mu = \rho_{\lambda\mu} = 0.1$: exponential (blue), power-law (purple), Gaussian (red), triangular (green) and low-pass white noise (cyan). 50
2.5 $\overline{\Sigma}'_{pp}$, $\overline{\Sigma}'_{ps}$ and $\overline{\Sigma}'_{ss}$ in terms of ζ for $K = \sqrt{3}$ and $\sigma_\lambda = \sigma_\mu = \rho_{\lambda\mu} = 0.1$: exponential (blue), power-law (purple), Gaussian (red), triangular (green) and low-pass white noise (cyan). 53
2.6 $\bar{\tau}_p$ (left plot) and $\bar{\tau}_s$ (right plot) in terms of ζ for $K = \sqrt{3}$ and $\sigma_\lambda = \sigma_\mu = \rho_{\lambda\mu} = 0.1$: exponential (blue), power-law (purple), Gaussian (red), triangular (green) and low-pass white noise (cyan). 54

2.7 $\bar{\ell}_p^*$ (left plot) and $\bar{\ell}_s^*$ (right plot) in terms of ζ for $K = \sqrt{3}$ and $\sigma_\lambda = \sigma_\mu = \rho_{\lambda\mu} = 0.1$: exponential (blue), power-law (purple), Gaussian (red), triangular (green) and low-pass white noise (cyan). 56
2.8 $\bar{D}$ (left plot) and $\bar{t}_{eq}$ (right plot) in terms of ζ for $K = \sqrt{3}$ and $\sigma_\lambda = \sigma_\mu = \rho_{\lambda\mu} = 0.1$: exponential (thick solid line), power-law (thin dashed-dotted line), Gaussian (thick dashed line), triangular (thin solid line) and low-pass white noise (thin dashed line). 58

3.1 8-node hexahedron reference element and the mapping function 63
3.2 (a) Five Lagrange polynomials of order 4. (b) GLL points of degree 4 64
3.3 (a) Variation of the number of degrees of freedom in the propagation medium over the number of processors in terms of the simulation time per each time step. (b) The variation of the simulation time per each time step in terms of the number of processors for constant degrees of freedom 68
3.4 Ricker pulse with $t_0 = 0.3$(s) and $f_0 = 10$(Hz) in time (a) and frequency (b) domains 78
3.5 A half-space with PML layers at boundaries 78
3.6 Top: temporal variation of $\overline{\mathcal{E}}_p^\Omega$ (red curves) and $\overline{\mathcal{E}}_s^\Omega$ (blue curves). Bottom: temporal variation of $\overline{\mathcal{E}}_s^\Omega/\overline{\mathcal{E}}_p^\Omega$. Solid and dashed curves correspond respectively to the low-pass white noise and exponential correlation models. The starting and end points of the shaded window indicate respectively the lapse times in which the direct P and S waves propagating in homogeneous background arrive to the boundaries. 79
3.7 Top: temporal variation of $\bar{K}^\Omega$ (blue curves) and $\overline{\mathcal{E}}_p^\Omega + \overline{\mathcal{E}}_s^\Omega$ (red curves). Bottom: temporal variation of $\bar{K}^\Omega/(\overline{\mathcal{E}}_p^\Omega + \overline{\mathcal{E}}_s^\Omega)$. Solid and dashed curves correspond respectively to the low-pass white noise and exponential correlation models. The starting and end points of the shaded window indicate respectively the lapse times in which the direct P and S waves propagating in homogeneous background arrive to the boundaries. 80
3.8 Snapshots of the ratio $(\text{div}\ \mathbf{u}(\mathbf{x}))^2/\langle(\text{div}\ \mathbf{u}(\mathbf{x}))^2\rangle_{\text{slice}}$ (top row) and $||\text{curl}\ \mathbf{u}(\mathbf{x})||^2/\langle||\text{curl}\ \mathbf{u}(\mathbf{x})||^2\rangle_{\text{slice}}$ (bottom row) in percent for two different lapse times ($t = 2$ s and $t = 4$ s) and two different depths ($z = 0$ m and $z = -1000$ m). The random heterogeneities have a low-pass white noise correlation kernel. 80
3.9 Temporal variation of $\langle||\text{curl}\ \mathbf{u}(\mathbf{x})||^2\rangle/\langle(\text{div}\ \mathbf{u}(\mathbf{x}))^2\rangle$ calculated over the whole slices. Red, green, cyan and purple colors correspond respectively to the slices at $z = 0$ m, $z = -250$ m, $z = -500$ m and $z = -1000$ m. The thick and thin black lines correspond respectively to the analytical values on full space and over the free surface. Left and right plots correspond respectively to the low-pass white noise and exponential correlation models. 81
3.10 Temporal variation of $\frac{\left\langle \frac{\mu(\mathbf{x})}{2}||\text{curl}\ \mathbf{u}(\mathbf{x})||^2\right\rangle}{\left\langle \frac{\lambda(\mathbf{x})+2\mu(\mathbf{x})}{2}(\text{div}\ \mathbf{u}(\mathbf{x}))^2\right\rangle}$ (solid curves) and $\underline{\mu}\ \lambda + 2\ \mu \cdot \frac{\left\langle||\text{curl}\ \mathbf{u}(\mathbf{x})||^2\right\rangle}{\langle(\text{div}\ \mathbf{u}(\mathbf{x}))^2\rangle}$ (dashed curves) calculated
3.11 Top left: temporal variation of $\overline{\mathcal{E}}_p^\Omega$ (red curves) and $\overline{\mathcal{E}}_s^\Omega$ (blue curves). Bottom left: temporal variation of $\overline{\mathcal{E}}_s^\Omega/\overline{\mathcal{E}}_p^\Omega$. Top right: temporal variation of $\bar{K}^\Omega$ (blue curves) and $\overline{\mathcal{E}}_p^\Omega + \overline{\mathcal{E}}_s^\Omega$ (red curves). Bottom right: temporal variation of $\bar{K}^\Omega/(\overline{\mathcal{E}}_p^\Omega + \overline{\mathcal{E}}_s^\Omega)$. Solid, dashed and dashed-dotted curves correspond respectively to half-space with explosion source, half-space with unidirectional source and Neumann boundary conditions with explosion source. The starting and end points of the shaded window indicate respectively the lapse times in which the direct P and S waves propagating in homogeneous background arrive to the boundaries. 84

3.12 Snapshots of the ratio $(\text{div } \mathbf{u}(\mathbf{x}))^2/\langle(\text{div } \mathbf{u}(\mathbf{x}))^2\rangle_{\text{slice}}$ (top row) and $||\text{curl } \mathbf{u}(\mathbf{x})||^2/\langle||\text{curl } \mathbf{u}(\mathbf{x})||^2\rangle_{\text{slice}}$ (bottom row) in percent for two different lapse times ($t = 2(s)$ and $t = 4(s)$) and two different depths ($z = 0(m)$ and $z = -1000(m)$). 84
3.13 Top left: temporal variation of $\overline{\mathcal{E}}_p^{\Omega}$ (red curves) and $\overline{\mathcal{E}}_s^{\Omega}$ (blue curves). Bottom left: temporal variation of $\overline{\mathcal{E}}_s^{\Omega}/\overline{\mathcal{E}}_p^{\Omega}$. Top right: temporal variation of $\bar{K}^{\Omega}$ (blue curves) and $\overline{\mathcal{E}}_p^{\Omega} + \overline{\mathcal{E}}_s^{\Omega}$ (red curves). Bottom right: temporal variation of $\bar{K}^{\Omega}/(\overline{\mathcal{E}}_p^{\Omega} + \overline{\mathcal{E}}_s^{\Omega})$. The starting and end points of the shaded window indicate respectively the lapse times in which the direct P and S waves propagating in homogeneous background arrive to the boundaries. 85
3.14 Snapshots of the ratio $(\text{div } \mathbf{u}(\mathbf{x}))^2/\langle(\text{div } \mathbf{u}(\mathbf{x}))^2\rangle_{\text{slice}}$ (top row) and $||\text{curl } \mathbf{u}(\mathbf{x})||^2/\langle||\text{curl } \mathbf{u}(\mathbf{x})||^2\rangle_{\text{slice}}$ (bottom row) in percent for two different lapse times ($t = 2$ s and $t = 4$ s) and two different depths ($z = 0$ m and $z = -1000$ m). 86
3.15 Top left: temporal variation of $\overline{\mathcal{E}}_p^{\Omega}$ (red curves) and $\overline{\mathcal{E}}_s^{\Omega}$ (blue curves). Bottom left: temporal variation of $\overline{\mathcal{E}}_s^{\Omega}/\overline{\mathcal{E}}_p^{\Omega}$. Top right: temporal variation of $\bar{K}^{\Omega}$ (blue curves) and $\overline{\mathcal{E}}_p^{\Omega} + \overline{\mathcal{E}}_s^{\Omega}$ (red curves). Bottom right: temporal variation of $\bar{K}^{\Omega}/(\overline{\mathcal{E}}_p^{\Omega} + \overline{\mathcal{E}}_s^{\Omega})$. Solid, dashed and dashed-dotted curves correspond respectively to explosion, unidirectional and combined source. The starting and end points of the shaded window indicate respectively the lapse times in which the direct P and S waves propagating in homogeneous background arrive to the boundaries. 87
3.16 Top left: temporal variation of $\overline{\mathcal{E}}_p^{\Omega}$ (red curves) and $\overline{\mathcal{E}}_s^{\Omega}$ (blue curves). Bottom left: temporal variation of $\overline{\mathcal{E}}_s^{\Omega}/\overline{\mathcal{E}}_p^{\Omega}$. Top right: temporal variation of $\bar{K}^{\Omega}$ (blue curves) and $\overline{\mathcal{E}}_p^{\Omega} + \overline{\mathcal{E}}_s^{\Omega}$ (red curves). Bottom right: temporal variation of $\bar{K}^{\Omega}/(\overline{\mathcal{E}}_p^{\Omega} + \overline{\mathcal{E}}_s^{\Omega})$. Solid, dashed and dashed-dotted curves correspond respectively to half-space, full-space and Neumann boundary conditions. The starting and end points of the shaded window indicate respectively the lapse times in which the direct P and S waves propagating in homogeneous background arrive to the boundaries. 88
3.17 Identification results for a half-space with low-pass white noise correlation model. Left column: the time-averaged ratio $\frac{\langle||\text{curl } \mathbf{u}(\mathbf{x})||^2\rangle_t}{\langle(\text{div } \mathbf{u}(\mathbf{x}))^2\rangle_t}$ at 3 different horizontal slices at the time lapse $t = 4(s)$; Middle column: local values of the field $(K_\delta(\mathbf{x}))^2$; Right column: the correlation functions corresponding to the left and the middle columns. 92
3.18 Identification results for a half-space with exponential correlation model. Left column: the time-averaged ratio $\frac{\langle||\text{curl } \mathbf{u}(\mathbf{x})||^2\rangle_t}{\langle(\text{div } \mathbf{u}(\mathbf{x}))^2\rangle_t}$ at 3 different horizontal slices at the time lapse $t = 4(s)$; Middle column: local values of the field $(K_\delta(\mathbf{x}))^2$; Right column: the correlation functions corresponding to the left and the middle columns. 93
3.19 Identification results for a half-space with low-pass white noise correlation model. Left column: the time-averaged ratio $\frac{\langle||\text{curl } \mathbf{u}(\mathbf{x})||^2\rangle_t}{\langle(\text{div } \mathbf{u}(\mathbf{x}))^2\rangle_t}$ at 3 different horizontal slices at the time lapse $t = 4(s)$; Middle column: local values of the field $(K_\delta(\mathbf{x}))^2$; Right column: the correlation functions corresponding to the left and the middle columns. 95
3.20 Identification results for a half-space with exponential correlation model. Left column: the time-averaged ratio $\frac{\langle||\text{curl } \mathbf{u}(\mathbf{x})||^2\rangle_t}{\langle(\text{div } \mathbf{u}(\mathbf{x}))^2\rangle_t}$ at 3 different horizontal slices at the time lapse $t = 4(s)$; Middle column: local values of the field $(K_\delta(\mathbf{x}))^2$; Right column: the correlation functions corresponding to the left and the middle columns. 96

@

A.1 Functions $I_n(\zeta)$ for different correlation kernels and different values of n ($K = \sqrt{3}$): exponential (thick solid line), power-law (thin dashed-dotted line), Gaussian (thick dashed line), triangular (thin solid line) and low-pass white noise (thin dashed line). 101
A.2 Functions $J_n(\zeta)$ for different correlation kernels and different values of n ($K = \sqrt{3}$). : exponential (thick solid line), power-law (thin dashed-dotted line), Gaussian (thick dashed line), triangular (thin solid line) and low-pass white noise (thin dashed line). 103

@
D.1 Configuration of a source, a receiver and last scattering points for multiple isotropic scattering including different mode conversions (Sato et al., 2012) 117

List of Tables

2.1 Definitions of the normalized correlation models. 44

3.1 Cut-off frequencies used for different correlation models. 72
3.2 Analytical values of the equipartitioning ratio for unbounded media and over the medium's traction-free surface for different values of K 76
3.3 Components of the covariance matrix in terms of the values of δ and K 77
3.4 Scattering parameters for a random medium with a low-pass white noise correlation kernel 77
3.5 Scattering parameters for a random medium with an exponential correlation kernel 77
3.6 Correlation coefficients of the fields $\frac{\langle ||\text{curl } \mathbf{u}(\mathbf{x})||^2\rangle_t}{\langle (\text{div } \mathbf{u}(\mathbf{x}))^2\rangle_t}$ and $(K_\delta(\mathbf{x}))^2$ at different depths and lapse times. 92
3.7 Correlation coefficients of the fields $\frac{\langle ||\text{curl } \mathbf{u}(\mathbf{x})||^2\rangle_t}{\langle (\text{div } \mathbf{u}(\mathbf{x}))^2\rangle_t}$ and $(K_\delta(\mathbf{x}))^2$ at different depths and lapse times. 94

A.1 Values of W_n^p for the first values of n and p. 100
A.2 Asymptotic values of $I_n(\zeta)$ and $J_n(\zeta; K)$ for different correlation kernels 102

C.1 Entropy measure of some random variables in terms of their standard deviation σ . 110

Bibliography

Abramowitz, M. and Stegun, I. A. (2012). *Handbook of mathematical functions: with formulas, graphs, and mathematical tables.*

Aki, K. (1969). Analysis of the seismic coda of local earthquakes as scattered waves. *J. Geophys. Res.*, 74(2):615–631.

Aki, K. (1992). Scattering conversions P to S versus S to P. *Bull. Seismological Soc. Am.*, 82(4):1969–1972.

Aki, K. and Chouet, B. (1975). Origin of coda waves: Source, attenuation, and scattering effects. *J. Geophys. Res.*, 80(23):3322–3342.

Aki, K. and Richards, P. (2002). *Quantitative Seismology.* Geology (University Science Books).: Seismology. University Science Books.

Andersen, L. (2006). *Linear Elastodynamic Analysis.* DCE Lecture Notes. Department of Civil Engineering, Aalborg University.

Ang, A. H.-S. and Tang, W. H. (2007). *Probability Concepts in Engineering Planning and Design: Emphasis on Applications in Civil & Environmental Engineering.* Wiley.

Arnst, M. (2007). *Inversion of probabilistic models of structures using measured transfer function.* These, Ecole Centrale Paris.

Arts, R. J. (1993). *Étude de lélasticité anisotrope générale dans les roches par propagation des ondes.* These, Université de Pierre et Marie Curie.

Auld, B. A. (1973). *Acoustic fields and waves in solids.* Wiley.

Bal, G. (2005). Kinetics of scalar wave fields in random media. *Wave Motion*, (43):132–157.

Bal, G., Papanicolaou, G., and Ryzhik, L. (2000). Probabilistic theory of transport processes with polarization. *SIAM J. Appl. Math.*, 60(5):1639–1666.

Bal, G. and Ryzhik, L. (2002). Wave transport for a scalar model of the love waves. *Wave motion*, 36(1):49–66.

Baydoun, I., Savin, E., Cottereau, R., Clouteau, D., and Guilleminot, J. (2014). Kinetic modeling for transport of elastic waves in anisotropic heterogeneous media. *Wave Motion.* In preparation.

Bihan, N. L. and Margerin, L. (2009). Nonparametric estimation of the heterogeneity of a random medium using compound poisson process modeling of wave multiple scattering. *Phys. Rev. E*, 80(016601):1–9.

Bohlen, T. and Saenger, E. H. (2006). Accuracy of heterogeneous staggered-grid finite-difference modeling of rayleigh waves. *Geophysics*, 71(4):109–115.

Born, M. and Wolf, E. (1965). *Principles of Optics: Electromagnetic theory of propagation, interference and diffraction of light*. Cambridge University Press, 7th (expanded) edition.

Brenguier, F., Campillo, M., Hadziioannou, C., Shapiro, N. M., Nadeau, R. M., and Larose, E. (2008). Postseismic relaxation along the san andreas fault at parkfield from continuous seismological observations. *Science*, 321(5895):1478–1481.

Cambardella, C. A., Moorman, T. B., Novak, J. M., Parkin, T. B., Karlen, D. L., Turco, R. F., and Konopka, A. E. (1994). Field-scale variability of soil properties in central iowa soils. *Soil Science Society of America Journal*, 58(5):1501–1511.

Canuto, C., Hussaini, M. Y., Quarteroni, A., and Zang, T. A. (1988). Spectral methods in fluid dynamics.

Capdeville, Y., Guillot, L., and Marigo, J. J. (2010). 1-d non-periodic homogenization for the seismic wave equation. *Geophys. J. Int.*, 2(181):897–910.

Carcione, J. (2007). *Wave Fields in Real Media: Wave Propagation in Anisotropic, Anelastic, Porous and Electromagnetic Media*. Handbook of Geophysical Exploration: Seismic Exploration. Elsevier Science.

Chaljub, E., Komatitsch, D., Vilotte, J. P., Capdeville, Y., Valette, B., and Festa, G. (2007). Spectral element analysis in seismology. *Advances in Geophysics*, 48:365–419.

Chandrasekhar, S. (1960). *Radiative transfer*. Dover Publications.

Chemingui, N. (1994). Modeling 3-D anisotropic fractal media. In *Stanford Exploration Project report*, volume 80, pages 603–616.

Clouteau, D. (1990). *Propagation d'ondes dans les milieux hétérogèn, application à la tenue des ouvrages sous séismes*. These, École Centrale Paris.

Cottereau, R. (2007). *Probalilistic models of impedance matrices : application to dynamic soil-structure interaction*. These, Ecole Centrale Paris.

Cottereau, R., Clouteau, D., Vilotte, J.-P., and Madariaga, R. (2007). Validation of software for 3d propagation of waves in heterogeneous and random media. *9th US National Congress on Computational Mechanics (USNCCM)*.

Crossley, D. J. and Jensen, O. G. (1989). Fractal velocity models in refraction seismology. *Pure Appl. Geophys.*, 131(1-2):61–76.

Cupillard, P. (2008). *Simulation par la méthode des éléments spectraux des formes d'onde obtenues par corrélation de bruit sismique*. PhD thesis, Institut de Physique du Globe de Paris.

Cupillard, P., Delavaud, E., Burgos, G., Festa, G., Vilotte, J.-P., Capdeville, Y., and Montagner, J.-P. (2012). RegSEM: a versatile code based on the spectral element method to compute seismic wave propagation at the regional scale. *Geophys. J. Int.*, 188(3):1203–1220.

Dangla, P. (1989). *Couplage éléments finis - équations intégrales en élastodynamiques et intéraction sol-structures*. These, École Nationale des Ponts et Chaussées.

Delavaud, E. (2007). *Simulation numérique de la propagation d'ondes en milieu géologique complexe: application à l'évaluation de la réponse sismique du bassin de Caracas (Venezuela)*. PhD thesis, Institut de Physique du Globe de Paris.

der Hilst, R. V., Hoop, M. V. D., Wang, P., Shim, S.-H., Tenorio, L., Ma, P., and Tenorio, L. (2007). Seismo-stratigraphy and thermal structure of earths core-mantle boundary region. *PScience*, 315:18131817.

Devroye, L. (1986). *Non-Uniform Random Variate Generation*. New York: Springer-Verlag.

Faccioli, E., Maggio, F., Paolucci, R., and Quarteroni, A. (1997). 2D and 3D elastic wave propagation by a pseudo-spectral domain decomposition method. *Journal of seismology*, 1(3):237–251.

Festa, G. and Vilotte, J. P. (2005). The newmark scheme as velocity–stress time-staggering: an efficient pml implementation for spectral element simulations of elastodynamics. *gji*, 161(3):789–812.

Fichtner, A. and Trampert, J. (2011). Resolution analysis in full waveform inversion. *Geophysical Journal International*, 187(3).

Fish, J. and Chen, W. (2004). Spacetime multiscale model for wave propagation in heterogeneous media. *Computer Methods in Applied Mechanics and Engineering*, 193(45-47):4837 – 4856.

Foley, J. C. and Rehbein, D. K. (2000). In-situ nondestructive evaluation methods for characterizing sintering of aluminum powder metallurgy compacts. *P/M Science and Technology Briefs*, 2(1):10–13.

Foti, S. (2000). *Multistation methods for geotechnical characterization using surface waves*. These, Politecnico di Torino.

Fouque, J.-P., Garnier, J., and Papanicolaou, G. (2007). *Wave Propagation and Time Reversal in Randomly Layered Media*. Stochastic Modelling and Applied Probability. Springer, Dordrecht.

Frankel, A. (1989). A review of numerical experiments on seismic wave scattering. *Pure and applied geophysics*, 131(4):639–685.

Frankel, A. and Clayton, R. (1986). Finite difference simulations of seismic scattering: Implications for the propagation of short-period seismic waves in the crust and models of crustal heterogeneity. *J. Geophys. Res.*, 91(B6):6465–6489.

Frankel, A. and Clayton, R. W. (1984). A finite-difference simulation of wave propagation in two-dimensional random media. *bssa*, 74(6):2167–2186.

Frisch, U. (1968). Wave propagation in random media. In Bharucha-Reid, A. T., editor, *Probabilistic Methods in Applied Mathematics*, volume 1, pages 75–198.

Gallardo, A. (2003). Spatial variability of soil properties in a floodplain forest in northwest spain. *Ecosystems*, 6(6):564–576.

Grêt, A., Snieder, R., Aster, R. C., and Kyle, P. R. (2005). Monitoring rapid temporal change in a volcano with coda wave interferometry. *Geophysical Research Letters*, 32(6).

Grigoriu, M. (1998). Simulation of stationary non-gaussian translation processes. *Journal of engineering mechanics*, 124(2):121–126.

Guilleminot, J., Noshadravan, A., Soize, C., and Ghanem, R. (2011). A probabilistic model for bounded elasticity tensor random fields with application to polycrystalline microstructures. *Computer Methods in Applied Mechanics and Engineering*, 200(17):1637–1648.

Guilleminot, J. and Soize, C. (2010). A stochastic model for elasticity tensors with uncertain material symmetries. *International Journal of Solids and Structures*, 47(22):3121–3130.

Guilleminot, J. and Soize, C. (2011). Non-gaussian positive-definite matrix-valued random fields with constrained eigenvalues: Application to random elasticity tensors with uncertain material symmetries. *International Journal for Numerical Methods in Engineering*, 88(11):1128–1151.

Guilleminot, J. and Soize, C. (2012). Probabilistic modeling of apparent tensors in elastostatics: A maxent approach under material symmetry and stochastic boundedness constraints. *Probabilistic Engineering Mechanics*, 28:118–124.

Guilleminot, J. and Soize, C. (2013). On the statistical dependence for the components of random elasticity tensors exhibiting material symmetry properties. *J. Elasticity*, 111(2):109–130.

Hennino, R., Trégoures, N., Shapiro, N. M., Margerin, L., Campillo, M., Tiggelen, B. A. V., and Weaver, R. L. (2001). Observation of equipartition of seismic waves. *Physical Review Letters*, 86(15):3447.

Hörlin, N.-E. (2005). 3d hierarchical hp-fem applied to elasto-acoustic modelling of layered porous media. *Journal of Sound and Vibration*, 285(1):341–363.

Hu, B. and Schiehlen, W. (1997). On the simulation of stochastic processes by spectral representation. *Probabilistic engineering mechanics*, 12(2):105–113.

Huet, C. (1990). Application of variational concepts to size effects in elastic heterogeneous bodies. *Journal of the Mechanics and Physics of Solids*, 38(6):813–841.

Hughes, T. J. R. (2012). *The finite element method: linear static and dynamic finite element analysis*. Courier Dover Publications.

Jaynes, E. T. (1957). Information theory and statistical mechanics. *pr*, 106:620–630.

Karypis, G. and Kumar, V. (1998). A software package for partitioning unstructured graphs, partitioning meshes, and computing fill-reducing orderings of sparse matrices. *University of Minnesota, Department of Computer Science and Engineering, Army HPC Research Center, Minneapolis, MN*.

Klimeš, L. (2002). Correlation functions of random media. *Pure Appl. Geophys.*, 159(7-8):1811–1831.

Komatitsch, D. (1997). *Méthodes spectrales et éléments spectraux pour l'équation de l'élastodynamique 2D et 3D en milieu hétérogène (Spectral and spectral-element methods for the 2D and 3D elastodynamics equations in heterogeneous media).* PhD thesis, Institut de Physique du Globe de Paris, France.

Komatitsch, D., Göddeke, D., Erlebacher, G., and Michéa, D. (2010). Modeling the propagation of elastic waves using spectral elements on a cluster of 192 gpus. *Computer Science-Research and Development*, 25(1-2):75–82.

Komatitsch, D. and Vilotte, J. P. (1998). The spectral element method: An efficient tool to simulate the seismic response of 2D and 3D geological structures. *bssa*, 88(2):368–392.

Komatitsch, D., Vilotte, J. P., Vai, R., Castillo-Covarrubias, J. M., and Sanchez-Sesma, F. J. (1999). The spectral element method for elastic wave equations-application to 2-D and 3-D seismic problems. *International Journal for Numerical Methods in Engineering*, 45(9):1139–1164.

Kulkarni, N., Moudgil, B., and Bhardwaj, M. (1994). Ultrasonic characterization of green and sintered ceramics; 1: Time domain. *American Ceramic Society Bulletin*, 73(6).

Larose, E., L. Margerin, B. A. V. T., and Campillo, M. (2004). Weak localization of seismic waves. *Physical Review Letters*, 93(4).

Levander, R. A. (1988). Fourth-order finite-difference P-SV seismograms. *Geophysics*, 53(11):1425–1436.

Liu, D. and Turner, J. A. (2008). Influence of spatial correlation function on attenuation of ultrasonic waves in two-phase materials. *J. Acoust. Soc. Am.*, 123(5):2570–2576.

Lobkis, O. I. and Weaver, R. L. (2008). Anderson localization of ultrasound in plates: Further experimental results. *J. Acoust. Soc. Am.*, 124(6):35283533.

Maday, Y. and Patera, A. (1988). *Spectral element methods for the Navier-Stokes equations.* In A.K. Noor and J.T. Oden, editors, State-of-the-Art-Survey in Computational Fluid Mechanics, chapter 3. ASME.

Maeda, T., Sato, H., and Nishimura, T. (2008). Synthesis of coda wave envelopes in randomly inhomogeneous elastic media in a half-space: single scattering model including rayleigh waves. *gji*, 172(1):130–154.

Margerin, L. (2006). Attenuation, transport and diffusion of scalar waves in textured random media. *Tectonophys.*, 416(1-4):229 – 244.

Margerin, L. (2013). Diffusion approximation with polarization and resonance effects for the modelling of seismic waves in strongly scattering small-scale media. *Geophys. J. Int.*, 192(1):326–345.

Margerin, L., Campillo, M., and van Tiggelen, B. A. (2000). Monte carlo simulation of multiple scattering of elastic waves. *J. Geophys. Res.*, 105(B4):7873–7892.

Margerin, L., van Tiggelen, B. A., and Campillo, M. (2001). Effect of absorption on energy partition of elastic waves in the seismic coda. *Bull. Seismological Soc. Am.*, 91(3):624–627.

Mazzieri, I., Stupazzini, M., Guidotti, R., and Smerzini, C. (2013). Speed: Spectral elements in elastodynamics with discontinuous galerkin: a non-conforming approach for 3D multi-scale problems. *International Journal for Numerical Methods in Engineering*, 95(12):991–1010.

Meunier, J., Huguet, F., and Meynier, P. (2001). Reservoir monitoring using permanent sources and vertical receiver antennae: The céré-la-ronde case study. *The Leading Edge*, 20(6):622–629.

Moczo, P., Kristek, J., Vavryčuk, V., Archuleta, R. J., and Halada, L. (2002). 3D heterogeneous staggered-grid finite-difference modeling of seismic motion with volume harmonic and arithmetic averaging of elastic moduli and densities. *bssa*, 92(8):3042–3066.

Mulder, W. A. (1999). Spurious modes in finite-element discretizations of the wave equation may not be all that bad. *Applied Numerical Mathematics*, 30(4):425–445.

Nakahara, H. and Yoshimoto, K. (2011). Radiative transfer of elastic waves in two-dimensional isotropic scattering media: Semi-analytical approach for isotropic source radiation. *Earth, Planets and Space*, 63(6):459–468.

Paolucci, R., Faccioli, E., and Maggio, F. (1999). 3D response analysis of an instrumented hill at matsuzaki, japan, by a spectral method. *Journal of Seismology*, 3(2):191–209.

Papanicolaou, G. (1998). Mathematical problems in geophysical wave propagation.

Papanicolaou, G., Bal, G., and Ryzhik, L. (2000). Probabilistic theory of transport processes with polarization. *SIAM J. Appl. Math.*, 60(5):1639–1666.

Papanicolaou, G., Ryzhik, L., and Keller, J. B. (1996). Stability of the P to S energy ratio in the diffusive regime. *Bull. Seismological Soc. Am.*, 86(4):1107–1115.

Papoulis, A. (1991). *Probability, Random Variables, and Stochastic Processes*. Communications and signal processing. Mcgraw-Hill, Incorporated.

Patera, A. T. (1984). A spectral element method for fluid dynamics: laminar flow in a channel expansion. *Journal of computational Physics*, 54(3):468–488.

Pilkington, M. and Todoeschuck, J. P. (1990). Stochastic inversion for scaling geology. *Geophys. J. Int.*, 102(1):205–217.

Poirion, F. and Soize, C. (1989). Numerical simulation of homogeneous and inhomogeneous gaussian stochastic vector fields. *La recherche aérospatiale*, -(1):41–61.

Puig, B. (2003). *Modélisation et simulation de processus stochastiques non gaussiens*. PhD thesis, Université Pierre et Marie Curie-Paris VI.

Ramamoorthy, S. K., Kane, Y., and Turner, J. A. (2004). Ultrasound diffusion for crack depth determination in concrete. *The Journal of the Acoustical Society of America*, 115(2):523–529.

Ryzhik, L., Papanicolaou, G., and Keller, J. B. (1996). Transport equations for elastic and other waves in random media. *Wave Motion*, 24(4):327–370.

Sanchez-Sesma, F. J. and Luzon, F. (1995). Seismic response of three-dimensional alluvial valleys for incident P, S, and rayleigh waves. *bssa*, 85(1):269–284.

Sato, H. (1984). Attenuation and envelope formation of three-component seismograms of small local earthquakes in randomly inhomogeneous lithosphere. *J. Geophys. Res.*, 89(B2):1221–1241.

Sato, H. (1994). Multiple isotropic scattering model including P-S conversions for the seismogram envelope formation. *Geophys. J. Int.*, 117(2):487–494.

Sato, H., Fehler, M., and Maeda, T. (2012). *Seismic Wave Propagation and Scattering in the Heterogeneous Earth: Second Edition*. SpringerLink : Bücher. Springer Berlin Heidelberg.

Sato, H., Nakahara, H., and Ohtake, M. (1997). Synthesis of scattered energy density for non-spherical radiation from a point shear-dislocation source based on the radiative transfer theory. *Phys. Earth Planet. Interiors*, 104(1-3):1–13.

Savin, E. (2005). Radiative transfer theory for high-frequency power flows in fluid-saturated, poro-visco-elastic media. *J. Acoust. Soc. Am.*, 117(3):1020–1031.

Savin, E. (2010). *propagation d'ondes élastiques hautes fréquences en milieux hétérogène: Application en dynamiques des structures et vibro-acoustiques*. Habilitation à diriger des recherches en mathématiques et en informatique, Université Paris XI.

Savin, E. (2012). Transient vibrational power flows in slender random structures: Theoretical modeling and numerical simulations. *Probabilistic Engineering Mechanics*, 28(0):194 – 205.

Semblat, J. F. (2010). Modeling seismic wave propagation and amplification in 1D/2D/3D linear and nonlinear unbounded media. *ijg*, 11(6):440–448.

Semblat, J. F., Kham, M., and Bard, P. Y. (2008). Seismic-wave propagation in alluvial basins and influence of site-city interaction. *bssa*, 98(6):2665–2678.

Seriani, G. and Priolo, E. (1994). Spectral element method for acoustic wave simulation in heterogeneous media. *Finite elements in analysis and design*, 16(3):337–348.

Shang, T. and Gao, L. (1988). Transportation theory of multiple scattering and its application to seismic coda waves of impulsive source. *Scientia Sinica*, 31(12):1503–1514.

Shannon, C. (1948). A mathematical theory of communications. *Bell System Technical Journal*, 27:379–423.

Shapiro, N. M., Campillo, M., Margerin, L., Singh, S. K., Kostoglodov, V., and Pacheco, J. (2000). The energy partitioning and the diffusive character of the seismic coda. *Bull. Seismological Soc. Am.*, 90(3):655–665.

Shearer, P. M. (2009). *Introduction to seismology*. Cambridge University Press.

Sheng, P. (1995). *Introduction to Wave Scattering, Localization, and Mesoscopic Phenomena*. Academic Press, San Diego.

Shinozuka, M. and Deodatis, G. (1988). Response variability of stochastic finite element systems. *J. Engr. Mech.*, 114(3):499–519.

Shinozuka, M. and Deodatis, G. (1991). Simulation of stochastic processes by spectral representation. *Applied Mechanics Reviews*, 44(4):191–204.

Shiomi, K., Sato, H., and Ohtake, M. (1997). Broad-band power-law spectra of well-log data in japan. *Geophys. J. Int.*, 130:5764.

Simo, J. C., Tarnow, N., and Wong, K. K. (1992). Exact energy-momentum conserving algorithms and symplectic schemes for nonlinear dynamics. *Computer methods in applied mechanics and engineering*, 100(1):63–116.

Smith, R. L. (1987). Ultrasonic materials characterization. *NDT International*, 20(1):43–48.

Soize, C. (2000). A nonparametric model of random uncertainties for reduced matrix models in structural dynamics. *Probabilistic Engineering Mechanics*, 15(3):277–294.

Soize, C. (2001). Maximum entropy approach for modeling random uncertainties in transient elastodynamics. *J. Acoust. Soc. Am.*, 109:1979–1996.

Soize, C. (2006). Non-gaussian positive-definite matrix-valued random fields for elliptic stochastic partial differential operators. *Computer Methods in Applied Mechanics and Engineering*, 195(1-3):2664.

Solna, K. (2003). Acoustic pulse spreading in a random fractal. *SIAM J. Appl. Math.*, 63(5):17641788.

Soulie, M., Montes, P., and Silvestri, V. (1990). Modelling spatial variability of soil parameters. *Canadian Geotechnical Journal*, 27(5):617–630.

Stupazzini, M., Paolucci, R., and Igel, H. (2009). Near-fault earthquake ground-motion simulation in the grenoble valley by a high-performance spectral element code. *Bulletin of the Seismological Society of America*, 99(1):286–301.

Ta, Q. (2011). *Modélisation des propriétés mécaniques anisotropes aléatoires et impacts sur la propagation des ondes élastiques.* These, Ecole Centrale Paris.

Ta, Q.-A., Clouteau, D., and Cottereau, R. (2010). Modeling of random anisotropic elastic media and impact on wave propagation. *Europ. J. Comp. Mech.*, 19(1-3):241–253.

Telford, W., Geldart, L., Sheriff, R., and Keys, D. (1976). *Applied geophysics.* Cambridge University Press, Cambridge, UK.

Toshinawa, T. and Ohmachi, T. (1992). Love wave propagation in three-dimension sedimentary basin. *bssa*, 82:16611667.

Trégourès, N. P. and van Tiggelen, B. A. (2002). Generalized diffusion equation for multiple scattered elastic waves. *Waves Random Media*, 12(1):21–38.

Tromp, J., Komattisch, D., and Liu, Q. (2008). Spectral-element and adjoint methods in seismology. *Communications in Computational Physics*, 3(1):1–32.

Turner, J. A. (1998). Scattering and diffusion of seismic waves. *Bull. Seismological Soc. Am.*, 88(1):276–283.

Turner, J. A. (1999). Elastic wave propagation and scattering in heterogeneous, anisotropic media: Textured polycrystalline materials. *J. Acoust. Soc. Am.*, 106(2):541–552.

Turner, J. A. and Anugonda, P. (2001). Scattering of elastic waves in heterogeneous media with local isotropy. *J. Acoust. Soc. Am.*, 109(5):1787–1795.

Turner, J. A. and Weaver, R. L. (1994). Radiative transfer and multiple scattering of diffuse ultrasound in polycrystalline media. *J. Acoust. Soc. Am.*, 96(6):3675–3683.

Turner, J. A. and Weaver, R. L. (1995). Time dependence of multiply scattered diffuse ultrasound in polycrystalline media. *J. Acoust. Soc. Am.*, 97:2639–2644.

Turner, J. A. and Weaver, R. L. (1996). Diffuse energy propagation on heterogeneous plates: Structural acoustics radiative transfer theory. *J. Acoust. Soc. Am.*, 100(3):36863695.

Vanmarcke, E. (2010). *Random fields: analysis and synthesis*. World Scientific.

Virieux, J. (1986). P-SV wave propagation in heterogeneous media: Velocity-stress finite-difference method. *Geophysics*, 51(4):889–901.

Weaver, R. L. (1982). On diffuse waves in solid media. *J. Acoust. Soc. Am.*, 71(6):1608–1609.

Weaver, R. L. (1990). Diffusivity of ultrasound in polycrystals. *J. Mech. Phys. Solids*, 38(1):55–86.

Zeng, Y. (1993). Theory of scattered P-wave and S-wave energy in a random isotropic scattering medium. *Bull. Seismological Soc. Am.*, 83(4):1264–1276.

Zeng, Y., Su, F., and Aki, K. (1991). Scattering wave energy propagation in a random isotropic scattering medium: 1. Theory. *J. Geophys. Res.*, 96(B1):607–619.